



**HAL**  
open science

# Mueller polarimetry for probing supramolecular and optical chiralities

Minghao Li

► **To cite this version:**

Minghao Li. Mueller polarimetry for probing supramolecular and optical chiralities. Physics [physics]. Université de Strasbourg, 2020. English. NNT : 2020STRAF018 . tel-03619839

**HAL Id: tel-03619839**

**<https://theses.hal.science/tel-03619839>**

Submitted on 25 Mar 2022

**HAL** is a multi-disciplinary open access archive for the deposit and dissemination of scientific research documents, whether they are published or not. The documents may come from teaching and research institutions in France or abroad, or from public or private research centers.

L'archive ouverte pluridisciplinaire **HAL**, est destinée au dépôt et à la diffusion de documents scientifiques de niveau recherche, publiés ou non, émanant des établissements d'enseignement et de recherche français ou étrangers, des laboratoires publics ou privés.

*ÉCOLE DOCTORALE ED222*

UMR 7006

**THÈSE** présentée par :

**Minghao LI**

soutenue le : 18 Novembre 2020

pour obtenir le grade de : **Docteur de l'université de Strasbourg**

Discipline/ Spécialité : Physique

**Mueller polarimetry for probing  
supramolecular and optical chiralities**

Polarimétrie de Mueller pour sonder les  
chiralités supramoléculaires et optiques

**THÈSE dirigée par :**

**M. GENET Cyriaque**

Institut de Science et d'Ingénierie Supramoléculaires (ISIS),  
Université de Strasbourg, CNRS

**RAPPORTEURS :**

**M. BATTIE Yann**

Institut de Chimie Physique et Matériaux (ICPM), Université de  
Lorraine, CNRS

**M. BELLESSA Joël**

Institut Lumière Matière (ILM), Université Claude Bernard Lyon  
1, CNRS

---

**AUTRES MEMBRES DU JURY :**

**Mme. CRASSOUS Jeanne**

Institut des Sciences Chimiques de Rennes (ISCR), Université  
de Rennes 1, CNRS

**M. DARQUIE Benoît**

Laboratoire de Physique des Lasers (LPL), Université  
Sorbonne Paris Nord, CNRS







## *Acknowledgements*

This thesis would not have been possible without the guidance, help and support from several individuals who contributed and extended their valuable assistance during my PhD.

First and foremost, I would like to extend my deeply sincere gratitude to my supervisor, Dr. Cyriaque Genet, who has guided me to the world of research and inspired me greatly during this 3-years journey of PhD. His profound learning and enthusiasm for science keep encouraging me to make this work complete. His door is always open for all kinds of discussion and he has been not only an advisor but also a friend.

I am also obliged to Prof. Thomas W. Ebbesen for giving me the opportunity to work in his extraordinary laboratory, which has a good scientific atmosphere and harmonious interpersonal relationship. I would like especially thank for his support and assistance during my difficult time.

I would also like to thank Prof. Jeanne Crassous, Prof. Yann Battie, Prof. Joël Bellessa and Dr. Benoît Darquié for accepting to participate in my thesis jury and reviewing my thesis work. I appreciate a lot for the interest and constructive comments on this work.

My special thanks are also due to Dr, Eloïse Devaux and Dr. James Hutchison for the care and consideration on me, also for making our lab a nice place to work.

Next, many thanks should be attributed to all the former and current group members with whom it has been a great pleasure to be able to work and share time. For this work, I would like to specially thank Thibault Chervy, Anoop Thomas, Stefano Azzini and Jino George who has initiated this work. Without their pioneer work and their guidance, I could never achieve this level in the topic of supramolecular assembly and Mueller polarimetry. I keep in mind also tones of good time with Jérôme Gautier in exploring Mueller polarimetry. As I worked also in the Team-force, I would like to thank Oussama Sentissi, Yoseline Rosales-Cabara and Rémi Goerlich for their company, discussion and support in our team work. Besides, I would like to thank Xiaolan Zhong and Kuidong Wang for giving me many useful advices in research and career. Of course, I will not forget the tiramisu and all homemade delicious sweets from Robrecht Vergauwe. A special thanks to Marie-Claude, who was always responsible for every administration issue in order to make our laboratory life smooth. Moreover, I would also address my thanks to -Bianca Patrahau, Kripa Joseph, Gian-Lorenzo Paravicini-Bagliani, Samuel Albert, Kalaiivanan Nagarajan and Sandeep Kulangara as well as to our new colleagues: Soh Kushida, Sudipta Saha, Shahana Nizar and Luis Pires who will pump new energy into Mueller polarimetry, Chiral coupling and optical tweezer.

Finally, and most importantly, I would like to thank my parents and my family for their support, encouragement, quiet patience and unwavering love during all these years of my education.

# Contents

<b>Acknowledgements</b>	<b>iii</b>
<b>1 Introduction</b>	<b>3</b>
1.1 Interaction between polarized light and matter . . . . .	3
1.2 Motivations . . . . .	4
1.3 Outline . . . . .	9
<b>2 Polarization of light: the Stokes-Mueller formalism</b>	<b>11</b>
2.1 Polarization states of light . . . . .	11
2.1.1 Light propagation and polarization . . . . .	11
2.1.2 Jones formalism . . . . .	14
2.1.3 Stokes-Mueller formalism . . . . .	17
2.1.4 Relation between Jones and Stokes-Mueller formalisms . . . . .	21
2.2 Mueller matrix algebra . . . . .	23
2.2.1 Physical realizability of a Mueller matrix . . . . .	23
2.2.2 Sum decomposition of a Mueller matrix . . . . .	29
2.2.3 Product decomposition of a Mueller matrix . . . . .	32
2.2.4 Sum vs. Product decompositions . . . . .	36
2.3 Polarimetric properties of a transmissive medium . . . . .	37
2.3.1 Degree of polarization . . . . .	37
2.3.2 Birefringence and dichroism extracted by differential decomposition . . . . .	38
2.4 Polarimetric properties of an emissive medium . . . . .	45
2.5 Conclusion . . . . .	46
<b>3 Group-like algebraic structure of the Stokes-Mueller formalism</b>	<b>49</b>
3.1 Normal form for Mueller matrices . . . . .	49
3.2 Group-like algebraic structures . . . . .	50
3.3 $SO^+(1,3)$ Lie groups for non-singular non-depolarizing Mueller matrices . . . . .	53
3.3.1 Description of the $SO^+(1,3)$ group . . . . .	53
3.3.2 The $\mathfrak{so}^+(1,3)$ Lie algebra . . . . .	54
3.3.3 Eigenstate analysis . . . . .	58
3.3.4 Product decomposition and differential decomposition . . . . .	62



3.4	Lie Monoid for all non-singular Mueller matrices . . . . .	63
3.4.1	Non-singular depolarizing Mueller matrices . . . . .	63
3.4.2	Algebraic structure for all non-singular Mueller matrices . . . . .	69
3.4.3	constraints for constructing physically realizable non-singular Mueller matrices . . . . .	72
3.4.4	Eigenstates analysis for non-singular Mueller matrices . . . . .	74
3.5	Monoid for the ensemble of all physical Mueller matrices . . . . .	75
3.6	Applications . . . . .	76
3.6.1	Mueller matrix analysis by differential decomposition . . . . .	77
3.6.2	Stokes vector Poincaré sphere trajectory analysis . . . . .	77
3.6.3	Studying the symmetries of a medium by an eigenstate analysis of its Mueller matrix . . . . .	81
	Rotation symmetries . . . . .	82
	In-plane mirror symmetries . . . . .	83
	Reciprocity and flip operation . . . . .	84
	Time reversal and energy conservation . . . . .	87
	Optical chirality: optical activity and planar chirality . . . . .	89
	Summary . . . . .	92
3.6.4	Path for designing media with specific symmetries . . . . .	94
3.7	Conclusion . . . . .	98
<b>4</b>	<b>Mueller polarimetry</b> . . . . .	<b>99</b>
4.1	Introduction of Mueller polarimetry . . . . .	99
4.2	Dual rotating QWP broad-band Mueller polarimetry . . . . .	101
4.2.1	Optical setup . . . . .	101
4.2.2	Calibration procedure . . . . .	105
	Calibration of the horizontal linear polarizer . . . . .	105
	Calibration of the QWPs . . . . .	107
	Calibration accuracy . . . . .	110
4.2.3	Noise contributions and error estimation . . . . .	115
4.2.4	Reference correction . . . . .	117
4.3	Data processing: passive vs. emissive samples . . . . .	119
4.3.1	Passive sample . . . . .	119
4.3.2	Active sample . . . . .	121
4.4	Measurement configurations . . . . .	122
4.4.1	Transmission configuration . . . . .	122
4.4.2	Reflection configuration . . . . .	123
4.4.3	Emission . . . . .	125

4.4.4	Real and Fourier spaces imaging . . . . .	127
4.5	Conclusion . . . . .	128
<b>5</b>	<b>Mueller polarimetry of chiral supramolecular assemblies</b>	<b>129</b>
5.1	From achiral amphiphilic monomers to chiral aggregates . . . . .	130
5.2	Hierarchical aggregation analyzed by Mueller polarimetry . . . . .	132
5.2.1	Mueller polarimetry measurements . . . . .	133
5.2.2	Experimental results . . . . .	136
Emergence and evolution of chirality . . . . .	136	
Analyzing signatures of linear dichroism (LD) . . . . .	139	
Analyzing the degree of polarization . . . . .	142	
5.3	Poincaré sphere representation . . . . .	143
5.3.1	Wavelength dependence of Mueller matrix eigenvectors . . . . .	143
5.3.2	Polarization dynamics in the Poincaré sphere for light passing through a homogeneous sample . . . . .	145
5.3.3	Polarization dynamics of a reconstructed evolution of polarimetric observables along the self-assembly . . . . .	147
5.3.4	Evolution of the output Stokes vector $\mathbf{S}_{out}$ as a function of the aggregation stage . . . . .	153
5.4	Conclusion . . . . .	154
<b>6</b>	<b>Mueller matrices for molecular fluorescence polarimetry</b>	<b>157</b>
6.1	Standard polarization analysis of molecular fluorescence . . . . .	157
6.1.1	Molecular fluorescence and polarization . . . . .	158
6.1.2	Mueller polarimetry for molecular emission . . . . .	164
6.2	Internal filtering effect in supramolecular CPL measurements . . . . .	170
6.2.1	Supramolecular emission . . . . .	170
6.2.2	Measurement configuration . . . . .	171
6.2.3	Results and discussion . . . . .	173
6.3	Other results . . . . .	179
6.3.1	Poincaré sphere representation of emission polarization states . . . . .	179
6.3.2	2D Mueller matrix for polarization "action spectra" . . . . .	180
6.4	Conclusion and perspectives . . . . .	183
<b>7</b>	<b>Conclusions and perspectives</b>	<b>185</b>
7.1	Conclusions . . . . .	185
7.2	Perspectives . . . . .	187

<b>8</b>	<b>Résumé de thèse</b>	<b>189</b>
8.1	Contexte . . . . .	189
8.2	Résultat et discussion . . . . .	191
8.2.1	Analyse théorique du formalisme de Mueller . . . . .	191
8.2.2	Construction expérimentale du polarimètre de Mueller . . . . .	193
8.2.3	Expérience de transmission de polarimétrie Mueller . . . . .	194
8.2.4	Expérience d'émission . . . . .	195
8.3	Conclusion générale et perspectives . . . . .	196
<b>A</b>	<b>Matrix calculus</b>	<b>201</b>
A.1	Relations for the trace of matrices . . . . .	201
A.2	Relations for Kronecker product . . . . .	202
A.3	Baker-Campbell-Hausdorff formula . . . . .	203
A.4	Lie-Trotter-Kato formula . . . . .	203
A.5	Eigenvector of a matrix transpose . . . . .	203
<b>B</b>	<b>Wigner rotation</b>	<b>205</b>
B.1	Relativistic addition of velocities . . . . .	205
B.2	2 successive non-collinear Lorentz boosts . . . . .	207
B.3	Wigner rotation . . . . .	208
B.4	Generalization in Lorentz ( $SO^+(1,3)$ ) group . . . . .	209
<b>C</b>	<b>Non-depolarizing and depolarizing planar chirality</b>	<b>211</b>
<b>D</b>	<b>General multivariate linear regression</b>	<b>215</b>
D.1	General form . . . . .	215
D.2	Least square estimation . . . . .	216
D.3	Unbiased estimation of variance . . . . .	216
D.4	Test of significance . . . . .	218
D.4.1	Significance test of the regression relation . . . . .	218
D.4.2	Significance test of parameters . . . . .	219
D.5	Goodness-of-fit . . . . .	220
<b>E</b>	<b>Systematic error and accuracy</b>	<b>221</b>
	<b>Bibliography</b>	<b>223</b>

## List of Publications

### Journal publications

*Work covered in this thesis*

- Jérôme Gautier, Minghao Li, Cyriaque Genet, and Thomas W. Ebbesen  
**Cryptochiral anamorphous polymers for chiral Fabry-Pérot cavities,**  
*in preparation (2020)*
- Anoop Thomas, Thibault Chervy, Stefano Azzini, Minghao Li, Jino George, Cyriaque Genet, and Thomas W. Ebbesen  
**Mueller Polarimetry of Chiral Supramolecular Assembly,**  
J. Phys. Chem. C 2018, 122, 25, 14205-14212 (2018)

*Other publications*

- Samuel Albert, Minghao Li, Rémi Goerlich, Giovanni Manfredi, Paul-Antoine Hervieux, Cyriaque Genet  
**Probing discretization noise in the first principle of stochastic thermodynamics,**  
*in preparation (2020)*
- Minghao Li, Oussama Sentissi, Stefano Azzini, Gabriel Schnoering, and Cyriaque Genet  
**Weak Galilean invariance in Brownian colloidal systems,**  
*in preparation (2020)*
- Rémi Goerlich\*, Minghao Li\*, Samuel Albert, Giovanni Manfredi, Paul-Antoine Hervieux, Cyriaque Genet  
**Noise and ergodic properties of Brownian motion in an optical tweezer: looking at the crossover between Wiener and Ornstein-Uhlenbeck processes,**  
<https://arxiv.org/abs/2007.12246>, *submitted (2020)*
- Minghao Li, Oussama Sentissi, Stefano Azzini, Gabriel Schnoering, Antoine Canaguier-Durand, and Cyriaque Genet  
**Subfemtonewton force fields measured with ergodic Brownian ensembles,**  
Phys. Rev. A 100, 063816 (2019)

## Conference presentations

- Nanolight 2020, Benasque, March 9-14, 2020 (poster)  
**Deciphering the spontaneous emergence of chirality in self-assembling supramolecular aggregates using Mueller polarimetry**  
Minghao Li, Oussama Sentissi, Stefano Azzini, Gabriel Schnoering, Antoine Canaguier-Durand and Cyriaque Genet
- Nanolight 2020, Benasque, March 9-14, 2020 (Talk)  
**Mueller polarimetry and spontaneous symmetry breaking in complex systems**  
Minghao Li
- ISIS young scientist seminar, Strasbourg, December 5, 2019 (Talk)  
**Deciphering the spontaneous emergence of chirality in self-assembling supramolecular aggregates using Mueller polarimetry**  
Minghao Li
- Journée des doctorants, Strasbourg, November 25, 2018 (Talk)  
**Femto-Newton optical force profile reconstruction by Brownian motion**  
Minghao Li

# Chapter 1

## Introduction

### 1.1 Interaction between polarized light and matter

Polarization is known as a basic property of transverse waves specifying the orientation of the oscillation. In English, "polarization" is the namesake of "electric/magnetic polarization" necessary to describe the electrodynamic properties of matter. However in Chinese, "polarization" is a specific word signifying literally "biased oscillation", clearly referring to oscillations along a specific direction.

The history of polarization of light is rich, long, and progressive and involved throughout the 18th and 19th centuries a plethora of scientists. But a few landmarks can be given easily, following the interesting presentation of Ch. Brosseau in [1]. Early in 1669, Bartholinus discovered birefringence looking at the splitting of a light beam passing through a crystal of Iceland spar (i.e. calcite) into two beams of equal intensity. This effect was rapidly discussed by Huygens already in 1672 when he applied his spherical wavelet approach, even realizing that if a second, rotated crystal is used, the double refraction phenomenon can sometimes disappear [2].

Only later in 1808 was this question solved and explained by Malus who actually introduced the concept of polarization of light for the first time. The well-known Malus law for light passing through 2 polarizers was derived from experiments involving calcite. In 1817, while studying polarization effects on double-slit experiments, Fresnel and Arago came out with the transverse wave description of light and the interference properties between different polarization states quantified in the Fresnel-Arago laws. In this period, chiral issues were already present and recognized to be central in determining how matter interacts with polarized light. In 1811, Arago observed that sunlight can pass through a system with two orthogonal linear polarizers when a quartz crystal is inserted between them. This phenomenon referred as "optical rotation" by Biot in 1815 was explained, in 1824, by Fresnel. To do so, Fresnel introduced the concept of circular polarization states and noted that linearly polarized light can be decomposed into left- and right-handed circular polarizations associated each to different refraction index in the crystal [3].

In 1852, Stokes came up with the notion of partially polarized light and proposed a formalism, based on intensity measurements, capable of describing all kinds of polarization states of light, including pure, partial, and non polarized ones. The Stokes parameters were then formalized [4]. As stressed in [1], this work of Stokes received little attention but one agrees today that it inaugurated the modern description of polarization optics, to be fully formalized by Maxwell in his 1873 fundamental treatise of light.

From then on, polarization of light received a consistent theoretical framework that enabled Jones to unveil in 1941 the specific algebra associated with pure polarization states of light. In 1943, extending on the work of P. Soleillet and F. Perrin in the 1930's, Mueller proposed a fully general formalism that was based on the 1852 Stokes parameters and that allowed a full and exhausted description of the phenomenon of polarization.

This short history can not forget that it is Pasteur who first understood in 1848 that molecular chirality is responsible for the optical rotation effect described by Arago, Fresnel and Biot. Pasteur separated left- and right-handed tartrate crystallites under a microscope and dealing with such separated samples (we would now speak about enantio-pure samples) unveiled the relationship between optical rotation and molecular structures with no mirror symmetry and that appeared to mirror-images of one another. This lack of mirror symmetry pushed Lord Kelvin to call "chiral" any such objects [5]. It is interesting to note that the word "chiral" comes from "kheir" in Greek which means "hand". Interestingly, the translation in Chinese of "chirality" literally signifies also "property of hand".

Ever since then, chirality of matter has been studied using optics, developing apposite observables such as circular dichroism and optical rotatory dispersion. The importance of chirality of chemistry and therefore in pharmaceuticals pushed, and still does today, for the development of new technologies for measuring, always ever better, the chiral response of matter. Fundamentally, this is possible because of the remarkable fact that chiral matter is endowed with polarization-selective light-matter interaction modes where matter of a given chirality couples specifically with left- or right-circularly polarized light. This inherent property of chiral matter eventually leads to describe it as "optically active".

## 1.2 Motivations

Ever since the pioneering observation of spontaneous formation of left- and right-handed tartrate crystallites by Pasteur, chiral compounds have been intensively studied in physics, chemistry, and biology. From an energetic point of view, both left- and right-handed enantiomers of an asymmetric compound have equal probability of forming, resulting normally in racemic mixtures [6]. However, homochirality, where one enantiomer prevails over the other enantiomer, is observed in many living organisms and for this

stitching and unexplained reason remains, to date, a topic of intense activities combining many different disciplines [7–10]. Physically speaking, the emergence of one chiral enantiomer over the other is identified as a spontaneous mirror symmetry breaking event, which is also observed in the crystallization process of molecules such as NaClO [11, 12], in liquid crystals [13, 14], and in supramolecular self-assembled systems [15, 16].

The aim of the thesis is the study of such spontaneous mirror symmetry breaking phenomena. To do so, we decided to resort to the most appropriate optical tools for measuring the progressive emergence of chiroptical signals induced in the course of a supramolecular self-assembling process. From a molecular point of view, we have selected achiral amphiphilic carbocyanine dyes that can self-assembled in large, tubular, chiral J-aggregates. Optically, we chose Mueller polarimetry as the most appropriate methodology when aiming at probing the emergence of chirality.

These choices of a method and of a system connect our thesis to current research efforts that exploit supramolecular assemblies for the development of new optical devices, and/or elaborate new chiroptical spectroscopy and imaging tools that can be applied to a great variety of chiral systems, either molecular, biological or artificial.

With respect to this second aspect, Mueller polarimetry, among all existing polarization characterization methodologies, offers a unique capacity to decipher the dynamics of all types of polarization states of light. This has long been recognized and Mueller polarimetry is nowadays an essential tool largely exploited whenever polarization is relevant for investigating physical, chemical, and biological processes. This penetration of Mueller polarimetry in many fields of research has been accompanied by a vast body of theoretical work largely concerned in relating a Mueller matrix measurement to the standard chiroptical observables used in traditional chiroptical spectroscopy. This central question will be at the core of this thesis and we will explain how it is based on some specific and important theory papers in this field.

Once this relation is mastered, Mueller polarimetry offers many assets for analyzing and understanding the optical properties of complex chiral systems. For instance, Bart Kahr, Oriol Arteaga and colleagues have exploited Mueller polarimetry, both experimentally and theoretically, with great mastery and profusion [17]. For instance, they have exploited Mueller polarimetry imaging of vaterite helicoids [18]. Mueller imaging led them to measure differentiated circular retardances at different growth stages of the crystallization, as shown in Fig. 1.1. Such a work is emblematic of the contribution of Mueller polarimetry to chiral material science.



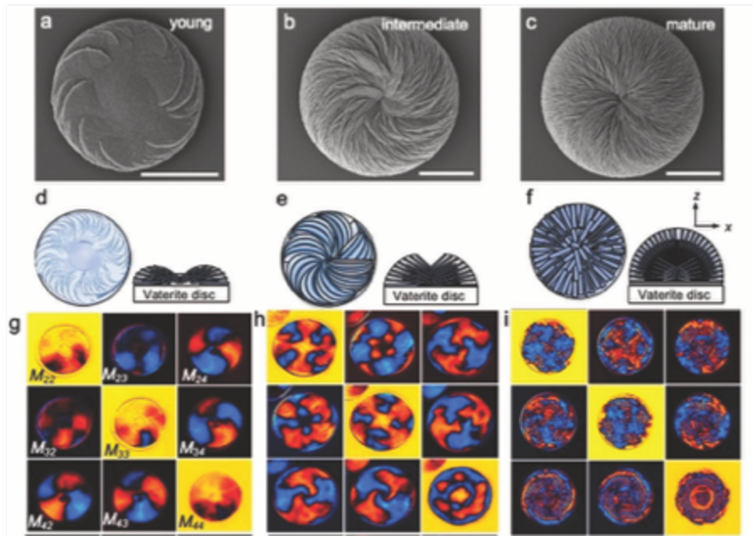


FIGURE 1.1: An example taken from the work of B. Kahr et al., where Mueller polarimetry imaging is used for characterizing precisely the chiroptical properties of vaterite chiral nanocrystals at different stages of their crystallization [18].

Mueller polarimetry has also been exploited in the field of nano-optics, where the variety of designed artificial metallic nanostructures have led to the generation and control of new types of optical modes and excitations. As often, the unique optical properties of such nanostructured optical systems are encoded in their polarization dynamics perfectly revealed and monitored using Mueller polarimetry. In this context for instance, recent studies done in the group of J. Bellessa in Lyon and in the group of A. Drezet in Grenoble give clear examples of the method. In particular, these authors emphasized the capacity of Mueller polarimetry to reveal how slight deviations in the lithography process of mirror-symmetrically designed nanostructures can actually lead to strong chiroptical effects, combining both bi- and three-dimensional chiral effects [19]. Along these lines and precisely for its sensitivity with respect to symmetry aspects, S. Fan and colleagues recently promoted the use of Poincaré sphere representation in the context of non-reciprocal metamaterials that obey time-reversal symmetry (see Fig. 1.2) [20]. As we will see in the thesis, Mueller polarimetry indeed is an interesting tool to use when exploring the connections between chirality, reciprocity and time-reversal symmetry.

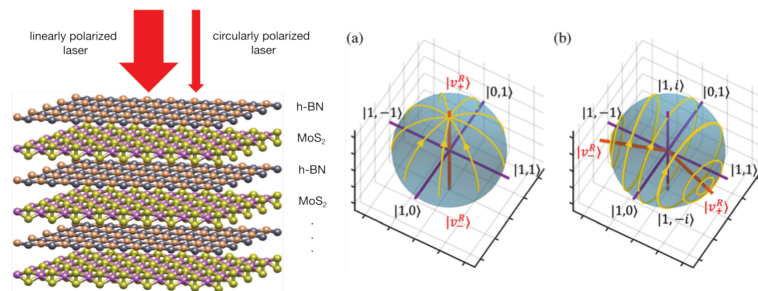


FIGURE 1.2: Proposed in [20], a metamaterial made of layered van der Waals heterostructure (Boron nitride intercalated with Molybdenum disulfide) can surprisingly yield a new type of optical response characterized as being nonreciprocal yet time-reversal symmetric. As shown in this work, a description in the Poincaré sphere is interesting for monitoring the polarization dynamics at play on such an optical system.

The notion of hierarchy will also play an important role in the thesis. It has been central in recent papers (Y. Battie in Metz, E. Pouget in Bordeaux, M. Pauly and G. Decher in Strasbourg for instance) involving chiral colloidal plasmonic nanoparticles. In a recent papers, these authors have used grazing incidence spraying techniques in order to hierarchically organize colloidal dispersions of chiral gold nanohelices -see Fig. 1.3. As clearly demonstrated using Mueller polarimetry, these organized colloids display collectively remarkable chiroptical properties [21].

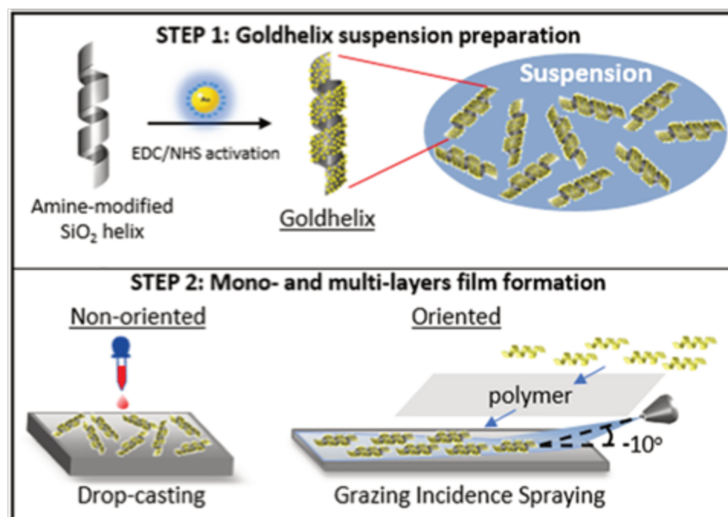


FIGURE 1.3: Nanoscaled gold helices synthesized in Bordeaux in the group of E. Pouget and R. Oda, are deposited on a substrate using grazing incidence spray deposition techniques developed in Strasbourg in the group of M. Pauly and G. Decher. This technique gives possibilities to orient, and organize (potentially layer by layer) such chiral colloidal ensembles so that they can display fascinating chiroptical signatures measured using an interesting polar-spectral Mueller polarimetry performed in the group of Y. Battie in Metz [21].

The possibility to actually create new optical functions using nanoscaled chiral assemblies is currently a strong drive in supramolecular chemistry. There, one major challenge is the capacity to control supramolecular self-assemblies in order to generate specific functions. This connection between supramolecular architectures and functions is particularly well explored in the context of optics with the target of using such supramolecular systems as genuine optical materials enabling new functions. In this context, helicene supramolecular films have been recognized as particularly promising. Verbiest et al. showed how the chirality of such systems can enhance non-linear optical properties when compared to the non-linear response of racemate helicene mixtures [22]. Recently, J. Crassous and colleagues in Rennes have developed helicene-based chiroptical switches where chemical functions are transferred into optical functionalities [23]. The possibility to control the dynamic equilibrium between bistable chiral forms of helicene using light, redox or pH triggers led to the demonstration of efficient optical switches, opening the way to many applications in the context of all-optical logic gates and memories-see fig. 1.4.

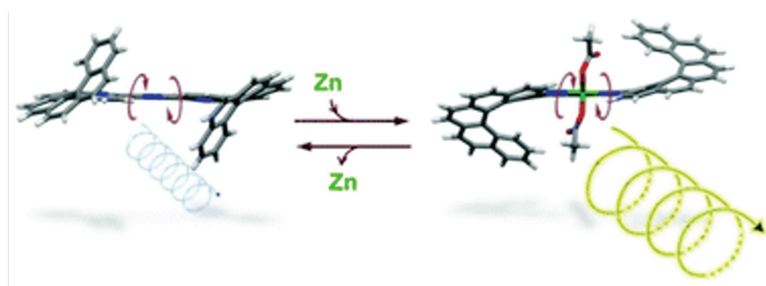


FIGURE 1.4: By modifying the conformation of a bis-helicenic terpyridine system using Zn binding mechanism, large changes in the chiroptical properties of the supramolecular system are induced. Zinc binding acting as an external trigger, such a chemical system can be used as an optical switch, working on chiral polarization degrees of freedom [24].

Such switches operate on both spectral and amplitude modulations of circularly polarized luminescence (CPL). CPL is highly interesting for probing the electronic structure of chiral molecules, but it is also particularly interesting in the context of spintronics, bio-imaging, asymmetric synthesis, etc. This explains why chemical sources of CPL have been searched for a long time. In a field essentially focused on lanthanide complexes that do show high CPL contrasts, Fuchter et al. realized that supramolecular assemblies can actually lead to large enhancement of CPL dissymmetries [25], reinvigorating a whole field aiming at exploiting chiral supramolecular assemblies for chiral light generation [26]. The last chapter of the thesis tries to insert itself within this line of research, promoting chiral supramolecular systems as new optical media, at the level of which chemical hierarchy is imprinted in hierarchical polarization signatures that can lead to topologically non-trivial and hence fascinating optical dynamics.

## 1.3 Outline

This thesis is divided in 3 main parts. Part 1, consisting of Chapters 2 and 3, reviews the theoretical framework of Mueller polarimetry. The second part given by Chapter 4 details our home-made Mueller polarimeter and the detection methods we have adopted in the thesis. The third part of the manuscript corresponds to Chapters 5 and 6 that gather our experimental results acquired on a chiral supramolecular self-assembling system in both absorption and emission polarimetry. More precisely:

**Chapter2** reminds the standard theoretical tools used for describing polarization states of light moving from Jones to Stokes-Mueller formalisms. We insist here on the importance of the physical realizability constraint put on a Mueller matrix and how, on the basis of this, chiroptical observables can be extracted from an experimental Mueller matrix.

**Chapter3** focuses on the algebraic structure of the Stokes-Mueller formalism. We explain why the group theory formulation is useful when analyzing Mueller matrix decomposition procedures and associated polarization dynamics. We show in particular how this formulation directly leads to an *ab initio* approach for designing optical media with specific polarization features.

**Chapter4** describes our Mueller polarimeter based on the broad-band dual rotating quarter-wave plate (QWP) polarimetric approach. We detail our calibration and noise estimation procedures, together with the methods we use for reference correction and data processing both for passive and active media. Finally, we describe different experimental configurations that can be used depending on samples' properties.

**Chapter5** gathers our experimental results where Mueller polarimetry is used for monitoring the emergence of chirality in the course of the self-assembly of chiral J-aggregates. We show how the hierarchy in the self-assembly is encoded in a hierarchical evolution of the polarimetric properties measured on this supramolecular system. We visualize the polarization dynamics in the Poincaré sphere and discuss how such a representation leads to new strategies for artificially building evolving systems mimicking complex polarization responses.

**Chapter6** specializes the discussion to the use of Mueller polarimetry for characterizing the polarization properties of molecular fluorescence. A careful comparison between the standard methods of fluorescence anisotropy and Mueller polarimetry in emission stresses the relevance and necessity of measuring a full Mueller matrix in the case of an emissive anisotropic medium. In particular, we illustrate how artifacts are induced by internal

filtering effects in a Circularly Polarized Luminescence experiment. Finally, we insist on the limitations of our method and face some remaining difficulties that must be overcome when aiming at generalizing our methodology to any type of emitting molecular systems.

**Chapter7** discusses some perspectives opened by the thesis.

## Chapter 2

# Polarization of light: the Stokes-Mueller formalism

This chapter presents the standard formalisms used for describing the polarisation of light, namely the Jones formalism [27, 28] for pure polarisation states of light and the Stokes-Mueller formalism [29] for all polarisation states including partially polarized light and depolarizing medium. For this thesis, the Stokes-Mueller formalism will play a key role considering that supramolecular media are generally depolarizing. Within the Stokes-Mueller formalism, we review first the physical realizability constraints put on Stokes vectors and Mueller matrices and then different decomposition methods for analyzing Mueller matrices. Finally, we show how polarimetric properties can be extracted directly from a Mueller matrix by relating Mueller to Jones matrices.

## 2.1 Polarization states of light

In this section, we briefly review the theoretical description of the state of polarization of the electromagnetic field following Maxwell's equations.

### 2.1.1 Light propagation and polarization

Maxwell's equations in a given medium are classically written as

$$\nabla \times \mathbf{E}(\mathbf{r}, t) = -\frac{\partial \mathbf{B}(\mathbf{r}, t)}{\partial t} \quad (2.1)$$

$$\nabla \times \mathbf{H}(\mathbf{r}, t) = \mathbf{J}(\mathbf{r}, t) + \frac{\partial \mathbf{D}(\mathbf{r}, t)}{\partial t} \quad (2.2)$$

$$\nabla \cdot \mathbf{D}(\mathbf{r}, t) = \rho(\mathbf{r}, t) \quad (2.3)$$

$$\nabla \cdot \mathbf{B}(\mathbf{r}, t) = 0 \quad (2.4)$$

where  $\mathbf{E}$  is the electric field,  $\mathbf{H}$  is the magnetic field strength,  $\mathbf{D}$  is the electric displacement,  $\mathbf{B}$  is the magnetic induction,  $\rho(\mathbf{r}, t)$  and  $\mathbf{J}(\mathbf{r}, t)$  are the charge and current densities.

These equations are solved together with the constitutive relations

$$\mathbf{D} = \varepsilon_0 \mathbf{E} + \mathbf{P} \quad (2.5)$$

$$\mathbf{B} = \mu_0 (\mathbf{H} + \mathbf{M}), \quad (2.6)$$

where  $\varepsilon_0$  is the dielectric constant in vacuum,  $\mathbf{P}$  is the electric polarization,  $\mu_0$  is the vacuum permeability and  $\mathbf{M}$  is the magnetic polarization. For the simple situation of a homogeneous linear isotropic medium,

$$\mathbf{P} = \varepsilon_0 \chi_e \mathbf{E} \quad (2.7)$$

$$\mathbf{M} = \chi_m \mathbf{H}, \quad (2.8)$$

where  $\chi_e$  and  $\chi_m$  are the electric and magnetic susceptibilities respectively. Therefore, the constitutive relations can be reduced to

$$\mathbf{D} = \varepsilon_0 (1 + \chi_e) \mathbf{E} = \varepsilon \mathbf{E} \quad (2.9)$$

$$\mathbf{B} = \mu_0 (1 + \chi_m) \mathbf{H} = \mu \mathbf{H}, \quad (2.10)$$

where  $\varepsilon$  and  $\mu$  are the electric and magnetic permeabilities respectively. Now, let us consider a source-free medium without any charge and current densities. In such medium:

$$\nabla \times \mathbf{E}(\mathbf{r}, t) = -\mu \frac{\partial \mathbf{H}(\mathbf{r}, t)}{\partial t} \quad (2.11)$$

$$\nabla \times \mathbf{H}(\mathbf{r}, t) = \varepsilon \frac{\partial \mathbf{E}(\mathbf{r}, t)}{\partial t} \quad (2.12)$$

$$\nabla \cdot \mathbf{D}(\mathbf{r}, t) = 0 \quad (2.13)$$

$$\nabla \cdot \mathbf{H}(\mathbf{r}, t) = 0. \quad (2.14)$$

By taking the curl on Eq.(2.11) and Eq.(2.12) and applying the identity  $\nabla \times \nabla \times = \nabla(\nabla) - \nabla^2$ , wave equations for electric field and magnetic field can be derived:

$$\nabla^2 \mathbf{E}(\mathbf{r}, t) - \frac{1}{u^2} \frac{\partial^2 \mathbf{E}(\mathbf{r}, t)}{\partial t^2} = 0 \quad (2.15)$$

$$\nabla^2 \mathbf{H}(\mathbf{r}, t) - \frac{1}{u^2} \frac{\partial^2 \mathbf{H}(\mathbf{r}, t)}{\partial t^2} = 0, \quad (2.16)$$

where  $u = (\varepsilon\mu)^{-1/2}$  is the phase velocity of the electromagnetic wave propagation in the medium.

We have discussed here the most simple case where the medium is linear and isotropic. But generally, an anisotropic linear medium described by the constitutive relations

$$\mathbf{D} = \varepsilon \mathbf{E} \quad (2.17)$$

$$\mathbf{B} = \mu \mathbf{H} \quad (2.18)$$

has its permeabilities  $\varepsilon$  and  $\mu$  represented by tensors. To be more general, in particular in relation with chiral media of the type discussed in this thesis, the constitutive relations have to be extended to a general bi-anisotropic case where the electric displacement and the magnetic induction depend both on the electric and magnetic fields.

$$\mathbf{D} = \varepsilon \mathbf{E} + \xi \mathbf{H} \quad (2.19)$$

$$\mathbf{B} = \zeta \mathbf{E} + \mu \mathbf{H}, \quad (2.20)$$

where the electric-magnetic coupling permeabilities  $\xi$  and  $\zeta$  are also tensors in general.

In order to introduce the concept of the polarization, we consider the plane wave monochromatic solutions of the wave equations. From Maxwell's equations, the electromagnetic field must be perpendicular to the direction of propagation yielding the transverse nature of electromagnetic wave. By fixing the  $z$  axis as the direction of propagation, the wave equation of the transverse electric field can be simplified to

$$u^2 \frac{\partial^2 \mathbf{E}(z, t)}{\partial z^2} - \frac{\partial^2 \mathbf{E}(z, t)}{\partial t^2} = 0. \quad (2.21)$$

The general solution of such a one dimensional wave equation is

$$\mathbf{E}(z, t) = \mathbf{F}(z - ut) + \mathbf{G}(z + ut), \quad (2.22)$$

where  $\mathbf{F}(z - ut)$  and  $\mathbf{G}(z + ut)$  are vectorial arbitrary function, and where  $z \pm ut$  reveal the propagating nature of the solution. This solution can be decomposed into monochromatic plan wave eigenmodes

$$\mathbf{E}(z, t) = \mathbf{F}(z - ut) + \mathbf{G}(z + ut) = \int_{-\infty}^{\infty} (s_+(\omega) e^{-i\omega(z+ut)/u} + s_-(\omega) e^{-i\omega(z-ut)/u}) d\omega, \quad (2.23)$$

written as:

$$\mathbf{E}(z, t) = \int_{-\infty}^{\infty} (s_+(\omega) e^{-i(kz+\omega t)} + s_-(\omega) e^{i(kz-\omega t)}) d\omega \quad (2.24)$$

by defining the wave number  $k = \omega/u$ . The monochromatic solution of the wave equation is thus given by

$$\mathbf{E}_\omega(z, t) = \mathbf{E}_+ e^{-i(kz+\omega t)} + \mathbf{E}_- e^{i(kz-\omega t)}, \quad (2.25)$$



supposing two wave that propagate in opposite directions. Along one chosen direction (for instance along the positive  $z$  axis), the electric field vector is expressed as

$$\mathbf{E}_\omega(z, t) = (E_{0x}e^{i\delta_x}\hat{\mathbf{x}} + E_{0y}e^{i\delta_y}\hat{\mathbf{y}})e^{i(kz-\omega t)}, \quad (2.26)$$

where  $E_{0x}$  and  $E_{0y}$  are the real amplitudes of the x and y components of the field vector with  $\delta_x$  and  $\delta_y$  the associated constant phase shifts. This description clearly reveals the concept of polarization as the oscillation of the field vector entirely determined in the xOy plane at all z-position. However, this description for polarization is not so convenient for field manipulations. We need to introduce a different formalism better suited for expressing the polarization. We will start with the Jones formalism.

### 2.1.2 Jones formalism

The Jones formalism is well adapted to describe a pure state of polarization involving the electric field oscillating only in xOy plane. In the Jones formalism, a state of polarization is described by a Jones vector written as:

$$\mathbf{E}_\omega(z, t) = \begin{pmatrix} E_{0x}e^{i\delta_x} \\ E_{0y}e^{i\delta_y} \end{pmatrix} e^{i(kz-\omega t)} = \begin{pmatrix} E_{0x}e^{i(-\omega t)} \\ E_{0y}e^{i(-\omega t+\delta)} \end{pmatrix} e^{i(kz+\delta_x)}, \quad (2.27)$$

where the position along the propagation and the common phase are extracted from the total vector, and where  $\delta = \delta_y - \delta_x$  represents the phase difference between the x and y components. Then expressing these components in a real form

$$E_x(t) = E_{0x} \cos(\omega t) \quad (2.28)$$

$$E_y(t) = E_{0y} \cos(\omega t + \delta) \quad (2.29)$$

will lead to the trace equation of the field vector in the xOy plane as

$$\frac{E_x^2}{E_{0x}^2} + \frac{E_y^2}{E_{0y}^2} - \frac{2E_xE_y}{E_{0x}E_{0y}} \cos \delta = \sin^2 \delta \quad (2.30)$$

that corresponds to an ellipse and that defines the "pure" nature of the polarization states.

<sup>1</sup> When  $\delta = 0$ , this equation, as it is well known, represents all linear polarizations. When  $\delta = \pm\pi/2$  and  $E_{0x} = E_{0y}$ , it represents right (+) or left (-) circular polarizations. For all other values for  $\delta$ ,  $E_{0x}$  and  $E_{0y}$ , it represents all elliptical polarizations.

---

<sup>1</sup>The notion of "purity" will be clarified below, in Eq. (2.54)

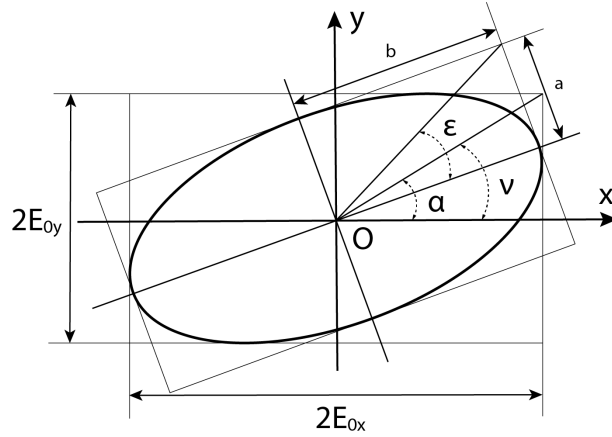


FIGURE 2.1: Geometric demonstration of a general pure state of polarization by the ellipse (as expressed in Eq. (2.30)) described by ellipse parameters where  $\alpha$  represents the azimuth angle,  $\varepsilon$  represents the ellipticity and  $\nu$  relates to the ratio between the x and y components of the electric field vector

Any ellipse can be described by 2 independent parameters, relating angles and phase differences as

$$\tan \nu = \frac{E_{0y}}{E_{0x}}, \quad (2.31)$$

$$\cos 2\nu = \cos 2\varepsilon \cos 2\alpha, \quad (2.32)$$

$$\sin 2\nu \cos \delta = \cos 2\varepsilon \sin 2\alpha. \quad (2.33)$$

Then, simplifying further the notations for polarization, we can extract from Eq. (2.27) a common part that leaves aside the information related to phase differences and amplitude ratio between x and y components as

$$\mathbf{E}_\omega(z, t) = e^{i(kz - \omega t + \delta_x)} \begin{pmatrix} E_{0x} \\ E_{0y} e^{i(\delta)} \end{pmatrix}. \quad (2.34)$$

Conventionally, the vector that we try to build must be normalized

$$\mathbf{E}_\omega(z, t) = E_0 e^{i(kz - \omega t + \delta_x)} \begin{pmatrix} v_x \\ v_y e^{i\delta} \end{pmatrix} \quad (2.35)$$

where real numbers  $v_x$  and  $v_y$  fulfill  $v_x^2 + v_y^2 = 1$ , thus making the total intensity  $I_0 = E_0^2$ . This way, the Jones vector  $\mathbf{V}$  is properly defined as:

$$\mathbf{V} = \begin{pmatrix} v_x \\ v_y e^{i\delta} \end{pmatrix} = \begin{pmatrix} V_x \\ V_y \end{pmatrix}. \quad (2.36)$$

With the polarization states represented by a Jones vector, and in the absence of depolarization (see below for this discussion), the interaction between a single light beam and the medium can be described as a linear transformation relating the Jones vectors associated with the incident and transmitted beams:

$$\begin{pmatrix} V_x^{out} \\ V_y^{out} \end{pmatrix} = \begin{pmatrix} J_{xx} & J_{xy} \\ J_{yx} & J_{yy} \end{pmatrix} \begin{pmatrix} V_x^{in} \\ V_y^{in} \end{pmatrix} \quad (2.37)$$

This  $2 \times 2$  matrix  $\mathbf{J}$  is called the Jones matrix. Matrix elements  $J_{ij}$  are complex numbers so that Jones matrices are parameterized by 8 independent real numbers. In the Jones formalism, because of the product recursion nature of Jones matrix definition, the Jones calculus is a multiplicative calculus. Thereby, the Jones matrix  $\mathbf{J}_{tot}$  of a medium corresponding to a stack of  $N$  multilayers can be expressed as the product of the Jones matrices  $\mathbf{J}_i$  of each layer

$$\mathbf{J}_{tot} = \mathbf{J}_N \mathbf{J}_{N-1} \dots \mathbf{J}_2 \mathbf{J}_1 = \prod_{i=N}^1 \mathbf{J}_i. \quad (2.38)$$

We should emphasize that the order of the product is determined strictly according to the stacking order since matrix products are generally not commutative.

Conventionally, Jones matrices are defined in the Cartesian coordinate system together with a transverse basis  $\hat{\mathbf{x}}$  and  $\hat{\mathbf{y}}$ . It is however simple to change basis which is often useful for simplifying problems according to their symmetry. For instance, when studying optical anisotropy problems, diagonalizable Jones matrices manifest their diagonal form in the eigenmode basis where it is easier to manipulate and analyze their properties. Other situations are important to describe: when the medium needs to be rotated or sample turn. In such case too, the resulting matrices can be obtained using a change of basis. The transform of Jones matrix simply writes as:

$$\mathbf{J}_t = \mathbf{P} \cdot \mathbf{J} \cdot \mathbf{P}^{-1} \quad (2.39)$$

where  $\mathbf{P}$  is an invertible matrix called the change-of-basis matrix. For example, if we want to study a rotation of the medium around the optical  $z$ -axis with an angle  $\theta$ , one has

$$\mathbf{P} = \mathbf{R}(\theta) = \begin{pmatrix} \cos \theta & \sin \theta \\ -\sin \theta & \cos \theta \end{pmatrix}. \quad (2.40)$$

If we are more interested in circular polarization properties such as circular birefringence and dichroism, it is easier to work in the basis of left and right circularly polarized light.

The matrix  $\mathbf{P}$  is set in this case as:

$$\mathbf{P} = \mathbf{U}_c = \begin{pmatrix} \mathbf{V}_l \\ \mathbf{V}_r \end{pmatrix} = \frac{1}{\sqrt{2}} \begin{pmatrix} 1 & -i \\ 1 & i \end{pmatrix}. \quad (2.41)$$

A flip of the medium with respect to the light propagation direction can also be applied to a Jones matrix. This way, an in-plane mirror inversion in the plane perpendicular to the optical axis and making an angle  $\theta/2$  with respect to the Ox direction can be written as

$$\mathbf{P} = \mathbf{\Pi}(\theta) = \begin{pmatrix} \cos \theta & \sin \theta \\ \sin \theta & -\cos \theta \end{pmatrix}. \quad (2.42)$$

To summarize, the Jones formalism is best applied in situations where light is fully polarized and where the symmetry of the medium is a key point of the problem. However experimentally, light beams are often partially polarized or even non-polarized. In such generic cases, another formalism is needed: the Stokes-Mueller formalism.

### 2.1.3 Stokes-Mueller formalism

In the Stokes-Mueller formalism, the states of polarization are described by the so called Stokes vectors built in the following way. We take the time averages of electric field quadratic forms as:

$$\begin{aligned} \langle E_i^2(t) \rangle &= \frac{1}{T} \int_0^T E_i^2(t) dt \\ \langle E_i(t) E_j(t) \rangle &= \frac{1}{T} \int_0^T E_i(t) E_j(t) dt, \end{aligned} \quad (2.43)$$

where the  $i, j$  correspond to the different components  $x, y$  and  $T$  is the oscillation period of the field. According to Eq.(2.28), (2.29) the time averages are given by

$$\begin{aligned} \langle E_i^2(t) \rangle &= \frac{1}{2} E_{0i}^2 \\ \langle E_i(t) E_j(t) \rangle &= \frac{1}{2} E_{0i} E_{0j} \cos \delta. \end{aligned} \quad (2.44)$$

With these time averages, Eq. (2.30) becomes:

$$E_{0y}^2 \langle E_x^2(t) \rangle + E_{0x}^2 \langle E_y^2(t) \rangle - 2E_{0x} E_{0y} \langle E_x(t) E_y(t) \rangle \cos \delta = E_{0x}^2 E_{0y}^2 \sin^2 \delta, \quad (2.45)$$

an expression rearranged by adding and subtracting  $E_{0x}^4 + E_{0y}^4$  as

$$\underbrace{(E_{0x}^2 + E_{0y}^2)^2}_{S_0^2} = \underbrace{(E_{0x}^2 - E_{0y}^2)^2}_{S_1^2} + \underbrace{(2E_{0x} E_{0y} \cos \delta)^2}_{S_2^2} + \underbrace{(2E_{0x} E_{0y} \sin \delta)^2}_{S_3^2} \quad (2.46)$$

With this, the 4 Stokes parameters  $S_i$  that construct the Stokes vector can be defined [30]:

$$\mathbf{S} = \begin{pmatrix} S_0 \\ S_1 \\ S_2 \\ S_3 \end{pmatrix} = \begin{pmatrix} I \\ Q \\ U \\ V \end{pmatrix} = \begin{pmatrix} E_{0x}^2 + E_{0y}^2 \\ E_{0x}^2 - E_{0y}^2 \\ 2E_{0x}E_{0y} \cos \delta \\ 2E_{0x}E_{0y} \sin \delta \end{pmatrix}. \quad (2.47)$$

This expression of Stokes vector is given in the basis of Cartesian coordinates. We can also express  $\mathbf{S}$  under the  $\pm 45^\circ$  orthonormal basis  $\hat{\mathbf{a}}$  and  $\hat{\mathbf{b}}$  and the basis of left and right circular polarization basis  $\hat{\mathbf{l}}$  and  $\hat{\mathbf{r}}$  as

$$\mathbf{S} = \begin{pmatrix} E_{0x}^2 + E_{0y}^2 \\ E_{0x}^2 - E_{0y}^2 \\ 2E_{0x}E_{0y} \cos \delta \\ 2E_{0x}E_{0y} \sin \delta \end{pmatrix} = \begin{pmatrix} E_{0a}^2 + E_{0b}^2 \\ -2E_{0a}E_{0b} \cos \delta' \\ E_{0a}^2 - E_{0b}^2 \\ -2E_{0a}E_{0b} \sin \delta' \end{pmatrix} = \begin{pmatrix} E_{0l}^2 + E_{0r}^2 \\ 2E_{0l}E_{0r} \cos \delta'' \\ 2E_{0l}E_{0r} \sin \delta'' \\ E_{0l}^2 - E_{0r}^2 \end{pmatrix}. \quad (2.48)$$

Since  $E_{0i}^2$  is the intensity measured along the corresponding polarization  $I_i$ , the Stokes vector can also be written as

$$\mathbf{S} = \begin{pmatrix} E_{0x}^2 + E_{0y}^2 \\ E_{0x}^2 - E_{0y}^2 \\ E_{0a}^2 - E_{0b}^2 \\ E_{0l}^2 - E_{0r}^2 \end{pmatrix} = \begin{pmatrix} I_{tot} \\ I_x - I_y \\ I_{45^\circ} - I_{-45^\circ} \\ I_l - I_r \end{pmatrix}, \quad (2.49)$$

which is a commonly used definition because it involves directly measurable quantities  $I_x$ ,  $I_y$ ,  $I_{45^\circ}$ ,  $I_{-45^\circ}$ ,  $I_l$  and  $I_r$  i.e. balanced intensities measured by an ideal polarizer oriented along the  $Ox$ ,  $Oy$  directions, the directions in  $45^\circ$  and  $-45^\circ$  with respect to  $Ox$  direction and by left and right circular polarizers, respectively. Therefore, the Stokes vector is related to measurable quantities, contrasting with the Jones vector, which parameters are defined in terms of electric field amplitudes that can not be measured directly. In this way, Stokes vector expresses all pure polarization states of light that fulfill the condition

$$I^2 = Q^2 + U^2 + V^2. \quad (2.50)$$

Since the Stokes vector is originally defined from average values, it can also be written more generally as a function of the averages taken over complex field amplitudes as

$$\mathbf{S} = \begin{pmatrix} \langle E_x E_x^* + E_y E_y^* \rangle \\ \langle E_x E_x^* - E_y E_y^* \rangle \\ \langle E_x E_y^* + E_y E_x^* \rangle \\ i \langle E_x E_y^* - E_y E_x^* \rangle \end{pmatrix}. \quad (2.51)$$

The averaging done here can be time average, spatial average or spectral average depending on the experimental situation.

Since partially polarized light can be viewed as an incoherent superposition of different pure states of polarization, it becomes possible to express the Stokes vector by simple intensities superposition without interference effects. The Stokes vector of a partially polarized light  $\mathbf{S}_{pp}$  can therefore be written as:

$$\mathbf{S}_{pp} = \sum_i \mathbf{S}_{cp}^i = \begin{pmatrix} \sum_i I_i \\ \sum_i Q_i \\ \sum_i U_i \\ \sum_i V_i \end{pmatrix} = \begin{pmatrix} I_{pp} \\ Q_{pp} \\ U_{pp} \\ V_{pp} \end{pmatrix}, \quad (2.52)$$

where  $\mathbf{S}_{cp}^i$  represents the different Stokes vectors of fully polarized light that fulfill the condition  $I_i^2 = Q_i^2 + U_i^2 + V_i^2$ . Considering a 3 dimensional vector  $\mathbf{a}_i = (Q_i, U_i, V_i)$  which norm is noted  $I_i$ , the Stokes vector of partially polarized light yields

$$I_{pp} > \sqrt{Q_{pp}^2 + U_{pp}^2 + V_{pp}^2} \quad (2.53)$$

because  $\sum_i \|\mathbf{a}_i\| > \|\sum_i \mathbf{a}_i\|$  for not all identical vectors  $\mathbf{a}_i$ . Combining with Eq.(2.50), we can define a parameter  $p$  for Stokes vector, that measures the degree of polarization:

$$p = \frac{\sqrt{Q^2 + U^2 + V^2}}{I} \quad (2.54)$$

which varies between 0 for totally unpolarized light and 1 for totally polarized light (pure state of polarization). The Stokes vector, after being normalized by its first element (corresponding to the total intensity), is a four dimensional vector that can be drawn in a 3-dimensional space limited by a sphere of radius 1, called the Poincaré Sphere [31]. In this sphere, the pure state of polarization are distributed on the surface of the sphere and the partially polarized states of light are distributed inside the sphere. We can show that the Stokes vector can also be expressed as a function of the azimuth angle  $\alpha$  and the ellipticity  $\varepsilon$  instead of the relative amplitudes of the x and y components and the phase difference  $\delta$ . In this representation, the normalized Stokes vector for a pure state of polarization can be written as

$$\mathbf{s} = \begin{pmatrix} 1 \\ S_1 \\ S_2 \\ S_3 \end{pmatrix} = \begin{pmatrix} 1 \\ \cos 2\varepsilon \cos 2\alpha \\ \cos 2\varepsilon \sin 2\alpha \\ \sin 2\varepsilon \end{pmatrix}. \quad (2.55)$$

This vector can be easily drawn in the Poincaré sphere as shown in Fig. 2.2. This

expression also allows us to identify how different polarization states are distributed in different zones of sphere. All linear polarization states are represented by points on the equator. The north and south poles represent the right and left circular polarization states and the points on north and south hemispheres correspond to right and left elliptical polarization states. Also we can see that 2 orthogonal polarization states are center symmetrically distributed in the space. The Poincaré sphere representation can thus be used as a very efficient visual representation of Stokes vectors which can greatly clarify and help visualizing polarization problems in particular when studying the evolution of the polarization states (polarization dynamics) in connection with specific polarimetric properties. This representation will be at the heart of Chapters 4 and 5.

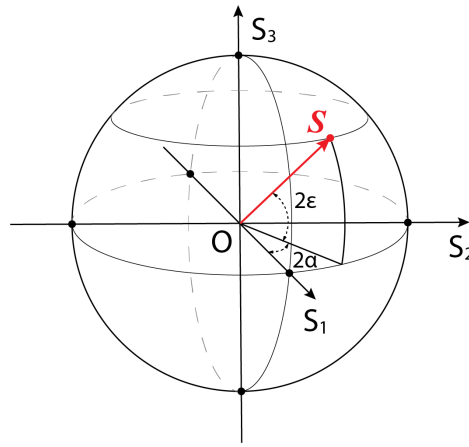


FIGURE 2.2: The Poincaré sphere represented in the Stokes vector  $(S_1, S_2, S_3)$  space. Any Stokes vector  $\mathbf{S}$  (marked with the red arrow) can be drawn in this space, defining each its own parameter of azimuth  $\alpha$  and ellipticity  $\varepsilon$ .

In the Stokes-Mueller formalism, the interaction with a medium can be described by a linear application on the Stoker vector realized by a  $4 \times 4$  real matrix called the Mueller matrix. Therefore, the Stokes vectors associated with the incident and transmitted light beams when interacting with the medium are related by the Mueller matrix as

$$\mathbf{S}_{out} = \mathbf{M}\mathbf{S}_{in}. \quad (2.56)$$

From this formula, we can see that the Mueller calculus in the Stokes-Mueller formalism is similar to Jones formalism and is a multiplicative calculus too. Therefore, the Mueller matrix for light interacting with several media successively can be expressed as:

$$\mathbf{S}_{out} = \mathbf{M}_N \mathbf{M}_{N-1} \dots \mathbf{M}_2 \mathbf{M}_1 \mathbf{S}_{in} = \prod_{i=N}^1 \mathbf{M}_i \mathbf{S}_{in}. \quad (2.57)$$

With the Stokes vectors drawn in the Poincaré sphere, the Mueller matrix can be represented as a transformation operating on the Stokes vectors in the sphere. We note here that the Mueller matrix is not defined in the real Cartesian coordinate of the electric field, implying that a transformation of the coordinates in the real space of interaction can not be applied directly in the space of the Stokes-Mueller formalism. This issue will be discussed in the next section by exploring the relation between the Jones formalism and the Stokes-Mueller formalism.

### 2.1.4 Relation between Jones and Stokes-Mueller formalisms

In the Jones formalism, the medium is described by a Jones matrix with 8 independent real parameters while in the Stokes-Mueller formalism, 16 independent real parameters are needed, corresponding to the fact that the Mueller matrix can describe more general media, including depolarizing ones. Because the Jones formalism can only describe pure states of polarization, the medium can only be non-depolarizing. In this case only, there is a relation between the non-depolarizing Mueller matrix (called Mueller-Jones matrix) and the Jones matrix.

To demonstrate this relation, we start from a vector called the coherence vector defined as:

$$\mathbf{C} = \begin{pmatrix} C_1 \\ C_2 \\ C_3 \\ C_4 \end{pmatrix} = \begin{pmatrix} \langle E_x E_x^* \rangle \\ \langle E_x E_y^* \rangle \\ \langle E_y E_x^* \rangle \\ \langle E_y E_y^* \rangle \end{pmatrix}. \quad (2.58)$$

From the Eq.(2.51), the Stokes vector is related to the coherence vector

$$\mathbf{S} = \mathbf{A} \mathbf{C} \quad (2.59)$$

through a change-of-basis matrix

$$\mathbf{A} = \begin{pmatrix} 1 & 0 & 0 & 1 \\ 1 & 0 & 0 & -1 \\ 0 & 1 & 1 & 0 \\ 0 & i & -i & 0 \end{pmatrix}. \quad (2.60)$$

This coherence vector  $\mathbf{C}$ , plays an important role in optics [32]. Having the Jones matrix, the incident and transmitted Jones vector of electric fields are related by :

$$E_i^{out} = \sum_k J_{ik} E_k^{in}, \quad (2.61)$$



so that the incident and transmitted coherence vectors are related as

$$\langle E_i^{out}(E_j^{out})^* \rangle = \left\langle \left( \sum_k J_{ik} E_k^{in} \right) \left( \sum_l J_{jl} E_l^{in} \right)^* \right\rangle. \quad (2.62)$$

For a Jones matrix associated with a homogeneous medium i.e.  $\langle \mathbf{J} \rangle = \mathbf{J}$ , one writes

$$\langle E_i E_j^* \rangle_{out} = \sum_{k,l} J_{ik} J_{jl}^* \langle E_k E_l^* \rangle_{in}, \quad (2.63)$$

showing the matrix that relates the incident and transmitted  $\mathbf{C}$  vectors

$$\mathbf{C}_{out} = \mathbf{F} \mathbf{C}_{in}, \quad (2.64)$$

with

$$\mathbf{F} = \begin{pmatrix} J_{xx} J_{xx}^* & J_{xx} J_{xy}^* & J_{xy} J_{xx}^* & J_{xy} J_{xy}^* \\ J_{xx} J_{yx}^* & J_{xx} J_{yy}^* & J_{xy} J_{yx}^* & J_{xy} J_{yy}^* \\ J_{yx} J_{xx}^* & J_{yx} J_{xy}^* & J_{yy} J_{xx}^* & J_{yy} J_{xy}^* \\ J_{yx} J_{yx}^* & J_{yx} J_{yy}^* & J_{yy} J_{yx}^* & J_{yy} J_{yy}^* \end{pmatrix} = \mathbf{J} \otimes \mathbf{J}^*, \quad (2.65)$$

where  $\otimes$  is the Kronecker product. From Eq.(2.59), the matrix  $\mathbf{F}$  and Mueller-Jones matrix  $\mathbf{M}_J$  are related through a simple change of basis according to

$$\mathbf{M}_J = \mathbf{A} \mathbf{F} \mathbf{A}^{-1} = \mathbf{A} (\mathbf{J} \otimes \mathbf{J}^*) \mathbf{A}^{-1}. \quad (2.66)$$

This relation reveals that the information related to the total absolute phase change is lost due to the product of complex conjugates of Jones matrix elements. Therefore, a Mueller-Jones matrix has only 7 independent parameters among its 16 initial matrix elements.

Once this relation established, we can derive the equations describing a change of basis from real Cartesian coordinates to the space of Mueller matrices. A change of basis in the real space in the  $xOy$  plane is given by a matrix of change-of-basis  $\mathbf{P}$ , with Eq.(2.39) transforming the Jones matrices. By using Eq.(2.66), we calculate the corresponding Mueller matrix  $\mathbf{M}_t$  from the Jones matrix  $\mathbf{J}_t$  in the new base as,

$$\mathbf{M}_t = \mathbf{A} (\mathbf{J}_t \otimes \mathbf{J}_t^*) \mathbf{A}^{-1} = \mathbf{A} [(\mathbf{P} \mathbf{J} \mathbf{P}^{-1}) \otimes (\mathbf{P} \mathbf{J} \mathbf{P}^{-1})^*] \mathbf{A}^{-1} \quad (2.67)$$

Using the property of the Kronecker product,  $(A \otimes B)(C \otimes D) = (AC) \otimes (BD)$ , we have,

$$\mathbf{M}_t = \mathbf{A} [(\mathbf{P} \otimes \mathbf{P}^*) (\mathbf{J} \otimes \mathbf{J}^*) (\mathbf{P}^{-1} \otimes (\mathbf{P}^{-1})^*)] \mathbf{A}^{-1}. \quad (2.68)$$

The Mueller matrix expressed in the original basis  $\mathbf{M} = \mathbf{A}(\mathbf{J} \otimes \mathbf{J}^*)\mathbf{A}^{-1}$  leads to the equation

$$\mathbf{M}_t = [\mathbf{A}(\mathbf{P} \otimes \mathbf{P}^*)\mathbf{A}^{-1}] [\mathbf{A}(\mathbf{J} \otimes \mathbf{J}^*)\mathbf{A}^{-1}] [\mathbf{A}(\mathbf{P}^{-1} \otimes (\mathbf{P}^{-1})^*)\mathbf{A}^{-1}] = \mathbf{P}_M \mathbf{M} \mathbf{P}_M^{-1} \quad (2.69)$$

defining thereby the change-of-basis Mueller matrix

$$\mathbf{P}_M = \mathbf{A}(\mathbf{P} \otimes \mathbf{P}^*)\mathbf{A}^{-1}, \quad (2.70)$$

determined from the coherence-to-Stokes vector transfer matrix  $\mathbf{A}$  and the change-of-basis matrix in Cartesian coordinates  $\mathbf{P}$ .

For instance, considering the most commonly used transform, namely a rotation, for which the transformation matrix  $\mathbf{P} = \mathbf{R}(\theta)$  is given by Eq.(2.40), the rotation writes for Mueller matrix as

$$\mathbf{R}_M(\theta) = \mathbf{A}(\mathbf{R}(\theta) \otimes \mathbf{R}(\theta))\mathbf{A}^{-1} = \begin{pmatrix} 1 & 0 & 0 & 0 \\ 0 & \cos 2\theta & \sin 2\theta & 0 \\ 0 & -\sin 2\theta & \cos 2\theta & 0 \\ 0 & 0 & 0 & 1 \end{pmatrix}. \quad (2.71)$$

This transform given by Eq.(2.69) will be very important in this work for obtaining the Mueller matrix of an optical component after being rotated, as discussed in chapter 3 and chapter 5.

## 2.2 Mueller matrix algebra

In this section, we discuss some well-known properties of Mueller matrices. We will first introduce the physical constraints that need to be put on Mueller matrices before showing how to extract from a Mueller matrix the optical properties of the medium it describes. It is true that Mueller matrices can be interpreted on a more phenomenological level by looking at the Stokes vectors or by using the Poincaré sphere for representing the polarization dynamics that one studies. But clear and precise decomposition methods are useful when the aim is to measure, through their extraction, well-defined optical properties. Basically, Mueller matrix decomposition can be classified into 2 types: sum decomposition and product decomposition methods that we explore here in detail.

### 2.2.1 Physical realizability of a Mueller matrix

Following the previous section, the Mueller matrix is a  $4 \times 4$  matrix that describes an optical medium from the view point of polarization under the framework of Stokes-Mueller formalism. In the Jones formalism, any 2 dimensional complex vector can be associated

to a Jones vector and any  $2 \times 2$  complex matrix can represent a Jones matrix without any constraint. However, not all  $4 \times 4$  matrices correspond to a physically realizable Mueller matrix and not all 4 dimensional vectors can yield a Stokes vector. As we stressed above, a physical Stokes vector must fulfill the condition that the degree of polarization  $p$  defined in Eq.(2.54) remains between 0 and 1. This implies that a Mueller matrix that relates incident to transmitted Stokes vectors must also fulfill associated constraints. These constraints ensure that the Stokes vector generated from the incident one after applying the Mueller matrix represented in the Poincaré sphere must also lie inside the Poincaré sphere. This can be expressed mathematically as follows. Writing the incident Stokes vector as a function of the ellipticity  $\varepsilon$  and the azimuth of the polarization  $\alpha$  shown in Eq.(2.55), gives for the transmitted Stokes vector after the application of the Mueller matrix:

$$\mathbf{S}_{out} = \begin{pmatrix} S_0 \\ S_1 \\ S_2 \\ S_3 \end{pmatrix} = \begin{pmatrix} m_{00} + m_{01} \cos 2\varepsilon_{in} \cos 2\alpha_{in} + m_{02} \cos 2\varepsilon_{in} \sin 2\alpha_{in} + m_{03} \sin 2\varepsilon_{in} \\ m_{10} + m_{11} \cos 2\varepsilon_{in} \cos 2\alpha_{in} + m_{12} \cos 2\varepsilon_{in} \sin 2\alpha_{in} + m_{13} \sin 2\varepsilon_{in} \\ m_{20} + m_{21} \cos 2\varepsilon_{in} \cos 2\alpha_{in} + m_{22} \cos 2\varepsilon_{in} \sin 2\alpha_{in} + m_{23} \sin 2\varepsilon_{in} \\ m_{30} + m_{31} \cos 2\varepsilon_{in} \cos 2\alpha_{in} + m_{32} \cos 2\varepsilon_{in} \sin 2\alpha_{in} + m_{33} \sin 2\varepsilon_{in} \end{pmatrix}, \quad (2.72)$$

enabling to express the transmitted Stokes vector as a function of the incident polarization ellipticity and azimuth. The condition for a physically realizable Mueller matrix can be described from Eq. (2.54) applied to  $\mathbf{S}_{out}$ :

$$p_{out}(\varepsilon_{in}, \alpha_{in}) = \frac{\sqrt{\sum_{j=1}^3 S_j(\varepsilon_{in}, \alpha_{in})^2}}{S_0(\varepsilon_{in}, \alpha_{in})} \leq 1 \quad (2.73)$$

for any values of  $\varepsilon_{in}$  and  $\alpha_{in}$ . If this condition is not satisfied, the Mueller matrix is said to be nonphysical. In other words, if the Mueller matrix applied to a Stokes vector gives a transmitted Stokes vector outside the Poincaré sphere, the Mueller matrix is then non physically realizable.

This is one first way for putting constraints on a Mueller matrix. Actually, the condition expressed in Eq.(2.73) is only a necessary condition for defining a physically realizable Mueller matrix. For a strictly sufficient and necessary condition of physical realizability for the Mueller matrix, one need to take one step further. This has been the topic for extensive discussions these last years. For instance, a study of the Mueller matrix for the depolarizing and non-depolarizing medium has led Fry and Kattawar [33] to propose as a condition for physical realizability the inequality

$$\text{Tr}(\mathbf{M}^T \mathbf{M}) = \sum_{i=0}^3 \sum_{j=0}^3 m_{ij}^2 \leq 4m_{00}^2 \quad (2.74)$$

where the equality is taken for a non-depolarizing medium. Another parameter allowing to measure directly on the Mueller matrix the depolarization properties has been first introduced by Gil and Bernabeu [34] as

$$P = \frac{\sqrt{\sum_{i=0}^3 \sum_{j=0}^3 m_{ij}^2 - m_{00}^2}}{\sqrt{3}m_{00}} \quad (2.75)$$

with the value varying from 0 to 1. If the medium under study is non-depolarizing,  $P = 1$  while if depolarizing,  $0 \leq P < 1$ . Therefore, we can formulate a necessary condition for physical realizability as  $0 \leq P \leq 1$ . But this still does not provide a sufficient and necessary condition. Many attempts have been made to explore the constraints for physical realizable Mueller matrix [35–38]. In this work, we will not introduce them all. We are simply interested in finding the physical realizable Mueller matrix that is as close as possible to experimental measurements. To find the constraints for the Mueller matrix most relevant to our case, we will follow an approach proposed and developed by Cloude [37]. Taking Eq.(2.62) for a general case, a depolarizing medium can be seen as composed by a probabilistic, linear, combination of different non-depolarizing media. This implies that averages must be taken over the second moments of the Jones matrices associated with each medium as:

$$\langle E_i E_j^* \rangle_{out} = \sum_{k,l} \langle J_{ik} J_{jl}^* \rangle \langle E_k E_l^* \rangle_{in}. \quad (2.76)$$

We thus get the expression of the corresponding general Mueller matrix from the averages of these Jones matrices

$$\mathbf{M} = \mathbf{A}(\langle \mathbf{J} \otimes \mathbf{J}^* \rangle) \mathbf{A}^{-1} \quad (2.77)$$

This means that all Mueller matrices can be expressed as a probabilistic, linear combination of second moments of Jones matrices. To implement this as a criteria of physical realizability, we follow Cloude and introduce a coherence matrix  $\mathbf{N}$  in order to decompose the Mueller matrix [37, 39]. To write this coherence matrix, one can define a Jones matrix vector as:

$$(\mathbf{J}^v)^T = (J_{xx}, J_{xy}, J_{yx}, J_{yy}), \quad (2.78)$$

from which the coherence matrix can be written as:

$$\mathbf{N} = \langle \mathbf{J}^v \otimes [(\mathbf{J}^v)^T]^* \rangle = \begin{pmatrix} \langle J_{xx} J_{xx}^* \rangle & \langle J_{xx} J_{xy}^* \rangle & \langle J_{xx} J_{yx}^* \rangle & \langle J_{xx} J_{yy}^* \rangle \\ \langle J_{xy} J_{xx}^* \rangle & \langle J_{xy} J_{xy}^* \rangle & \langle J_{xy} J_{yx}^* \rangle & \langle J_{xy} J_{yy}^* \rangle \\ \langle J_{yx} J_{xx}^* \rangle & \langle J_{yx} J_{xy}^* \rangle & \langle J_{yx} J_{yx}^* \rangle & \langle J_{yx} J_{yy}^* \rangle \\ \langle J_{yy} J_{xx}^* \rangle & \langle J_{yy} J_{xy}^* \rangle & \langle J_{yy} J_{yx}^* \rangle & \langle J_{yy} J_{yy}^* \rangle \end{pmatrix} \quad (2.79)$$

We can see that the matrix  $\mathbf{N}$  is a variance and covariance matrix. From Eq.(2.77), it can be written from a rearrangement of Mueller matrix elements as:

$$\mathbf{N} = \frac{1}{2} \sum_{i,j} m_{ij} \boldsymbol{\sigma}_i \otimes \boldsymbol{\sigma}_j^* \quad (2.80)$$

where  $\boldsymbol{\sigma}_i$  represents one of the Pauli matrices defined as

$$\boldsymbol{\sigma}_0 = \begin{pmatrix} 1 & 0 \\ 0 & 1 \end{pmatrix}, \boldsymbol{\sigma}_1 = \begin{pmatrix} 1 & 0 \\ 0 & -1 \end{pmatrix}, \boldsymbol{\sigma}_2 = \begin{pmatrix} 0 & 1 \\ 1 & 0 \end{pmatrix}, \boldsymbol{\sigma}_3 = \begin{pmatrix} 0 & -i \\ i & 0 \end{pmatrix}. \quad (2.81)$$

The explicit relation between the coherent matrix elements  $n_{ij}$  and Mueller matrix elements  $m_{ij}$  is listed here:

$$n_{00} = \frac{1}{2}(m_{00} + m_{11} + m_{01} + m_{10}) \quad (2.82)$$

$$n_{01} = \frac{1}{2}[m_{02} + m_{12} + i(m_{03} + m_{13})] \quad (2.83)$$

$$n_{02} = \frac{1}{2}[m_{20} + m_{21} - i(m_{30} + m_{31})] \quad (2.84)$$

$$n_{03} = \frac{1}{2}[m_{22} + m_{33} + i(m_{23} - m_{32})] \quad (2.85)$$

$$n_{10} = n_{01}^* \quad (2.86)$$

$$n_{11} = \frac{1}{2}(m_{00} - m_{11} - m_{01} + m_{10}) \quad (2.87)$$

$$n_{12} = \frac{1}{2}[m_{22} - m_{33} - i(m_{23} + m_{32})] \quad (2.88)$$

$$n_{13} = \frac{1}{2}[m_{20} - m_{21} - i(m_{30} - m_{31})] \quad (2.89)$$

$$n_{20} = n_{02}^* \quad (2.90)$$

$$n_{21} = n_{12}^* \quad (2.91)$$

$$n_{22} = \frac{1}{2}(m_{00} - m_{11} + m_{01} - m_{10}) \quad (2.92)$$

$$n_{23} = \frac{1}{2}[m_{02} - m_{12} + i(m_{03} - m_{13})] \quad (2.93)$$

$$n_{30} = n_{03}^* \quad (2.94)$$

$$n_{31} = n_{13}^* \quad (2.95)$$

$$n_{32} = n_{23}^* \quad (2.96)$$

$$n_{33} = \frac{1}{2}(m_{00} + m_{11} - m_{01} - m_{10}) \quad (2.97)$$

By this construction, the matrix  $\mathbf{N}$  is a Hermitian matrix, meaning that its eigenvalues are real. Since we know that the number of non-zero eigenvalues is equal to the rank of a matrix and that  $\text{rank}(\mathbf{A} \otimes \mathbf{B}) = \text{rank}\mathbf{A} \cdot \text{rank}\mathbf{B}$ , we have for a coherence matrix calculated from a Mueller-Jones matrix its final rank equal to 1 according to Eq. (2.79). Therefore, the number of its non-zero eigenvalue equals 1. Since that the eigenvalue of a matrix built by a Kronecker product of two rectangular matrices is the product of their non-zero singular values<sup>2</sup>, the eigenvalue of this coherence matrix built from a Mueller-Jones matrix must be positive since it results from the product of two singular values which are complex conjugates of each other.

A conclusion therefore is that a necessary and sufficient condition for a  $4 \times 4$  matrix to be a Mueller-Jones matrix states that its coherent matrix  $\mathbf{N}$  has only one positive non-zero eigenvalue. Since a general Mueller matrix is built from a probabilistic linear combination of Jones matrix elements as given by Eq.(2.77), the necessary and sufficient condition for a  $4 \times 4$  matrix to be a physically realizable Mueller matrix is that the coherence matrix  $\mathbf{N}$  calculated from this matrix is a positively defined Hermitian matrix i.e. that all its eigenvalues are non-negative with at least one of them positively defined.

Now that we have a criteria for the physical realizability of a Mueller matrix, it is important to stress that experimentally, a measured Mueller matrix might sometimes be non-physically realizable due to measurement errors or/and noise sources. Our objective is rather to find the closest physically realizable Mueller matrix using a filtering procedure that exploits the necessary and sufficient condition of the physical realizability detailed above. To do so, we first build the corresponding coherence matrix  $\mathbf{N}_{exp}$  from an experimental Mueller matrix  $\mathbf{M}_{exp}$ . This matrix  $\mathbf{N}_{exp}$  can be then diagonalized as

$$\mathbf{\Lambda} = \mathbf{U}^{-1}\mathbf{N}_{exp}\mathbf{U} = \begin{pmatrix} \lambda_1 & 0 & 0 & 0 \\ 0 & \lambda_2 & 0 & 0 \\ 0 & 0 & \lambda_3 & 0 \\ 0 & 0 & 0 & \lambda_4 \end{pmatrix} \quad (2.98)$$

with all eigenvalues  $\lambda_i$  in the diagonal. In order to perform the filtering procedure, all negative eigenvalues are removed. This gives a filtered diagonal matrix  $\mathbf{\Lambda}_0$  from which a filtered coherence matrix  $\mathbf{N}_0$  is obtained by simple inversion:

$$\mathbf{N}_0 = \mathbf{U}\mathbf{\Lambda}_0\mathbf{U}^{-1}. \quad (2.99)$$

Herein, the matrix  $\mathbf{N}_0$  is the coherence matrix of the physically realizable Mueller matrix closest to the experimentally measured Mueller matrix. The final physically realizable Mueller matrix  $\mathbf{M}_{pr}$  can be built from a coherence matrix  $\mathbf{N}_0$  by the relations listed

---

<sup>2</sup>A singular value can be considered as a generalized eigenvalue for non-square matrices.

below:

$$m_{10} = \frac{1}{2}(n_{00} + n_{11} - n_{22} - n_{33}) \quad (2.100)$$

$$m_{01} = m_{10} + n_{22} - n_{11} \quad (2.101)$$

$$m_{11} = n_{00} - n_{11} - m_{01} \quad (2.102)$$

$$m_{00} = 2n_{00} - m_{11} - m_{01} - m_{10} \quad (2.103)$$

$$m_{02} = \Re(n_{10} + n_{32}) \quad (2.104)$$

$$m_{12} = \Re(2n_{10}) - m_{02} \quad (2.105)$$

$$m_{20} = \Re(n_{20} + n_{31}) \quad (2.106)$$

$$m_{21} = \Re(2n_{20}) - m_{20} \quad (2.107)$$

$$m_{22} = \Re(n_{30} + n_{21}) \quad (2.108)$$

$$m_{33} = \Re(2n_{30}) - m_{22} \quad (2.109)$$

$$m_{03} = -\Im(n_{10} + n_{32}) \quad (2.110)$$

$$m_{13} = \Im(2n_{32}) + m_{03} \quad (2.111)$$

$$m_{30} = \Im(n_{20} + n_{31}) \quad (2.112)$$

$$m_{31} = \Im(2n_{20}) - m_{30} \quad (2.113)$$

$$m_{32} = \Im(n_{30} + n_{21}) \quad (2.114)$$

$$m_{23} = \Im(2n_{21}) - m_{32} \quad (2.115)$$

This is how the filtered experimental Mueller matrix is determined according to the procedure proposed by F. Boulvert et al. [40]. But this filtering process is only a tool that must be compared with experimental statistical errors that will be discussed in next chapter. In order to measure the degree of physical realizability, one important quantity is the norm of the non-physical part of Mueller matrix (noted as  $\mathbf{M}_{np}$ ) which can be calculated from the negative eigenvalues  $\lambda_-$  as [41]

$$\|\mathbf{M}_{np}\|_F = \|\mathbf{M}_{pr} - \mathbf{M}_{exp}\|_F = \sqrt{\sum \lambda_-^2} \quad (2.116)$$

where  $\sum \lambda_-^2$  is the square sum of all negative eigenvalues of the coherence matrix  $\mathbf{N}_{exp}$  given in Eq. (2.98). Since the difference between the experimental Mueller matrix and the filtered Mueller matrix is taken to be caused by the measurement noise, a difference measured to be much larger than the systematic error might be caused by some uncontrolled failure of the experiment procedure such as calibration issues or drifts of the sample

during the measurements. Interestingly therefore, the filtering procedure can be used as a way to confirm the validity and stability of a series of measurements.

### 2.2.2 Sum decomposition of a Mueller matrix

A second important point to address in the Mueller algebra is how physical, chiroptical, observables can be extracted from the decomposition of an experimental Mueller matrix generally measured as a depolarizing Mueller matrix. Previous important work [39, 42, 43] being carried out to this aim identifies two main methods, one based on a sum decomposition of the experimental Mueller matrix, the other on a product decomposition. We will here summarize both methodologies, starting with the sum decomposition.

The sum decomposition treats the experimental depolarizing Mueller matrix  $\mathbf{M}_{tot}^d$  as a sum of non-depolarizing Mueller matrices  $\mathbf{M}^{nd}$  with a resulting total Stokes vector associated with the transmitted beam written as

$$\mathbf{S}_{tot}^{out} = \mathbf{S}_1^{out} + \mathbf{S}_2^{out} \dots + \mathbf{S}_n^{out} = (\mathbf{M}_1^{nd} + \mathbf{M}_2^{nd} \dots + \mathbf{M}_n^{nd}) \mathbf{S}^{in} = \mathbf{M}_{tot}^d \mathbf{S}^{in} \quad (2.117)$$

This superposition leads to decomposing

$$\mathbf{M}_{tot}^d = \sum_{i=1}^n \mathbf{M}_i^{nd} \quad (2.118)$$

into  $n$   $\mathbf{M}_i^{nd}$  non-depolarizing Mueller matrices or Mueller-Jones matrices, hence considering the depolarizing Mueller matrix as an incoherent superposition of Mueller Jones matrices associated each with different portions of the sample probed by the incident beam that extends over all portions thus forming the total depolarizing Mueller matrix of the whole sample as schematized in Fig. 2.3. Because many samples are not fully homogeneous or because the optical path within the sample varies from region to region, this decomposition turns very useful when dealing with an experimental Mueller matrix. Typical situations are: a spatially inhomogeneous sample with relatively large domain such as molecular aggregates in solution or colloidal suspensions, samples with multiple-reflections such as a Fabry-Pérot cavity or thin cuvettes with short path length, etc. Measuring with a focused beam composed of different input angles will correspond to probing the sample with different optical lengths, making the total transmission be like an averaged measurement.

However in most of practical cases, what we need is not so much to know all the Mueller Jones matrices decomposed from a depolarizing Mueller matrix, but rather to extract the non-depolarizing polarimetric optical properties associated with the sample and characterizing its optical response. In this view, the aim of the sum decomposition



method is to extract the closest Mueller Jones matrix from the experimental depolarizing Mueller matrix.

To do so, the most commonly used method is known as the Cloude decomposition method [44]. This decomposition can be done via 2 routines based on 2 different reconstructed Hermitian matrices. These 2 routines give the same results but we will distinguish the procedures associated with these 2 routines. For both routines, any depolarizing Mueller matrix  $\mathbf{M}$  can be decomposed into the spectral weighted sum of four non-depolarizing Mueller matrix as

$$\mathbf{M} = \sum_{k=0}^3 \lambda_k \mathbf{M}_k \quad (2.119)$$

The routines are different in that they resort to different intermediate Hermitian matrices in order to construct the non-depolarizing Mueller matrix  $\mathbf{M}_k$ . The choice of the intermediate Hermitian matrix determines the whole procedure of the decomposition and should be made with great care.

The first routine involves a coherence matrix  $\mathbf{N}$  defined by Eq.(2.79). Once the matrix  $\mathbf{N}$  is built from the matrix  $\mathbf{M}$ , this matrix is decomposed according to the eigenvalues  $\lambda_k$  of  $\mathbf{N}$  and the non-depolarizing matrix  $\mathbf{M}_k$  is constructed from its coherence matrix  $\mathbf{N}_k$

$$\mathbf{N}_k = \mathbf{v}_k \mathbf{v}_k^\dagger \quad (2.120)$$

where  $\mathbf{v}_k$  is the eigenvector associated with the eigenvalue  $\lambda_k$  of the matrix  $\mathbf{N}$ . One can show that  $\mathbf{v}_k$  is the vector form of a Jones matrix  $\mathbf{J}_k^v$ , introduced above. We can then reconstruct the corresponding Jones matrix  $\mathbf{J}_k$  and the Mueller matrix can later be built according to Eq.(2.66).

The second routine uses a matrix  $\mathbf{T}$  called target coherency matrix introduced by Cloude [42]. Here, the eigenvalues  $\lambda_k$  involved in Eq.(2.119) are those of the matrix  $\mathbf{T}$  built from the experimental depolarizing Mueller matrix  $\mathbf{M}$  according to

$$\mathbf{T} = \frac{1}{4} \sum_{i,j} m_{ij} \mathbf{A} \sigma_i \otimes \sigma_j^* \mathbf{A}^\dagger \quad (2.121)$$

Therefore, the elements of  $\mathbf{T}$  matrix can be calculated one by one as follow:

$$t_{00} = \frac{1}{4}(m_{00} + m_{11} + m_{22} + m_{33}) \quad (2.122)$$

$$t_{01} = \frac{1}{4}[m_{01} + m_{10} + i(-m_{23} + m_{32})] \quad (2.123)$$

$$t_{02} = \frac{1}{4}[m_{02} + m_{20} + i(m_{13} + m_{31})] \quad (2.124)$$

$$t_{03} = \frac{1}{4}[m_{03} + m_{30} + i(m_{21} - m_{12})] \quad (2.125)$$

$$t_{10} = t_{01}^* \quad (2.126)$$

$$t_{11} = \frac{1}{4}(m_{00} + m_{11} - m_{22} - m_{33}) \quad (2.127)$$

$$t_{12} = \frac{1}{4}[m_{12} + m_{21} + i(m_{03} - m_{30})] \quad (2.128)$$

$$t_{13} = \frac{1}{4}[m_{13} + m_{31} - i(m_{02} - m_{20})] \quad (2.129)$$

$$t_{20} = t_{02}^* \quad (2.130)$$

$$t_{21} = t_{12}^* \quad (2.131)$$

$$t_{22} = \frac{1}{4}(m_{00} - m_{11} + m_{22} - m_{33}) \quad (2.132)$$

$$t_{23} = \frac{1}{4}[m_{23} + m_{32} + i(m_{01} - m_{10})] \quad (2.133)$$

$$t_{30} = t_{03}^* \quad (2.134)$$

$$t_{31} = t_{13}^* \quad (2.135)$$

$$t_{32} = t_{23}^* \quad (2.136)$$

$$t_{33} = \frac{1}{4}(m_{00} - m_{11} - m_{22} + m_{33}) \quad (2.137)$$

If we closely follow the method presented in [45], the decomposed non-depolarizing Mueller matrix  $\mathbf{M}_k$  can be built by the eigenvectors of the  $\mathbf{T}$  matrix each noted as  $\Psi_k$ . To do so, one first calculate the associated Jones matrix  $\mathbf{J}_k$  from the eigenvector elements

$$\mathbf{J}_k = \begin{pmatrix} \Psi_{k1} + \Psi_{k2} & \Psi_{k3} - i\Psi_{k4} \\ \Psi_{k3} + i\Psi_{k4} & \Psi_{k1} - \Psi_{k2} \end{pmatrix}, \quad (2.138)$$

where  $\Psi_{ki}$  represents the  $i$ th element of eigenvector  $\Psi_k$ , and then, using Eq.(2.66), build the corresponding Mueller matrices  $\mathbf{M}_k$ .

In both routines, extracting the non-depolarizing Mueller matrix from the experimental depolarizing Mueller matrix relies on the possibility to identify a dominating Mueller Jones matrix, in other words to have  $\lambda_0 \gg \lambda_1, \lambda_2, \lambda_3$  for the eigenvalues. In such a case,  $\lambda_0 \mathbf{M}_0$  can be taken as a good estimate for the non-depolarizing Mueller matrix that allows extracting the dominating polarization properties from a pure state point of view. However if the 4 eigenvalues are of a similar magnitude, the different decomposed non-depolarizing Mueller matrices do not physically represent the different parts of the sample. This rather means that the spatial inhomogeneity is too strong so that more precise characterizations of the sample are needed in order to study its sources of inhomogeneity in

details.

### 2.2.3 Product decomposition of a Mueller matrix

The second decomposition method is based on a product decomposition that decomposes the experimental Mueller matrix into a product of a series of elementary Mueller matrices, each corresponding to basic polarization elements: diattenuators, retarders and depolarizers, in such a way that

$$\mathbf{M} = \mathbf{M}_1 \mathbf{M}_2 \dots \mathbf{M}_n. \quad (2.139)$$

Clearly, the physical picture behind this type of decomposition is that the entire optical system is layered where each layer corresponds to an obvious property associated with an elementary polarization element. In this case, the beam passing through the entire system interacts sequentially with each of its layer. But of course, such a layered configuration is very rarely found in real systems and it turns out that in many situations, the product decomposition method does not lead to very precise determinations of the polarimetric properties of the medium. Specifically, we will give a comparison in chapter 3 between product decomposition and differential decomposition (to be introduced in 2.3.2) for a uniform medium. But despite the fact that we will not apply this type of decomposition in this thesis, it is a standard method that justifies that we briefly introduce its basic concepts. The most commonly used product decomposition methodology is the Lu-Chipman decomposition [43] where the elementary Mueller matrices are defined as diattenuator, retarder and depolarizer. The Lu-Chipman decomposition has been applied in recent experiments for instance in [46] in order to extract the polarimetric signature of biological tissue in biomedical imaging.

In order to define the diattenuator, which displays the absorption difference of light between 2 orthogonal polarization states, one must first define a parameter of diattenuation  $D$

$$D = \frac{I_{max} - I_{min}}{I_{max} + I_{min}}, \quad (2.140)$$

describing the difference between the maximum and minimum intensities transmitted through the diattenuator. From this parameter, a diattenuation vector can be defined by projecting diattenuation on different Stokes vector components as

$$\mathbf{D} = D \begin{pmatrix} d_1 \\ d_2 \\ d_3 \end{pmatrix} = \begin{pmatrix} D_{hv} \\ D_{\pm 45} \\ D_{lr} \end{pmatrix}, \quad (2.141)$$

with  $d_1^2 + d_2^2 + d_3^2 = 1$ . From the Mueller matrix point of view, we see that the intensity ratio  $\rho$  before and after the medium can be expressed as

$$\rho = \frac{S_0^{out}}{S_0^{in}} = \frac{m_{00}S_0^{in} + m_{01}S_1^{in} + m_{02}S_2^{in} + m_{03}S_3^{in}}{S_0^{in}} = m_{00} + \mathbf{m}_0 \cdot \hat{\mathbf{S}}_{in} \quad (2.142)$$

where  $\mathbf{m}_0$  is the vector of the first column of the Mueller matrix, excluding its first element  $\mathbf{m}_0 = (m_{01}, m_{02}, m_{03})$  and  $\hat{\mathbf{S}}_{in}$  is the normalized Stokes vector  $\hat{\mathbf{S}}_{in} = (s_1, s_2, s_3)$ . By using the property of the scalar product, the maximum and minimum of  $\rho$  are reached when  $\hat{\mathbf{S}}_{in}$  is collinear with the vector  $\mathbf{m}_0$  so that

$$\rho_{max} = m_{00} + \sqrt{m_{01}^2 + m_{02}^2 + m_{03}^2}, \quad (2.143)$$

$$\rho_{min} = m_{00} - \sqrt{m_{01}^2 + m_{02}^2 + m_{03}^2}. \quad (2.144)$$

The corresponding incident Stokes vectors for  $\rho_{max}$  and  $\rho_{min}$  are the polarization eigenstates of the diattenuator and write as:

$$\mathbf{S}_{max}^T = \left( 1, \frac{m_{01}}{\sqrt{m_{01}^2 + m_{02}^2 + m_{03}^2}}, \frac{m_{02}}{\sqrt{m_{01}^2 + m_{02}^2 + m_{03}^2}}, \frac{m_{03}}{\sqrt{m_{01}^2 + m_{02}^2 + m_{03}^2}} \right), \quad (2.145)$$

$$\mathbf{S}_{min}^T = \left( 1, -\frac{m_{01}}{\sqrt{m_{01}^2 + m_{02}^2 + m_{03}^2}}, -\frac{m_{02}}{\sqrt{m_{01}^2 + m_{02}^2 + m_{03}^2}}, -\frac{m_{03}}{\sqrt{m_{01}^2 + m_{02}^2 + m_{03}^2}} \right). \quad (2.146)$$

When therefore the diattenuation axis is set along the direction of the eigenstates, the first column of the Mueller matrix is related to the diattenuation vector

$$\mathbf{D} = \frac{1}{m_{00}} \begin{pmatrix} m_{01} \\ m_{02} \\ m_{03} \end{pmatrix}, \quad (2.147)$$

such that the matrix of diattenuator can be written in terms of the diattenuation vector as

$$\mathbf{M}_D = \begin{pmatrix} 1 & \mathbf{D}^T \\ \mathbf{D} & \mathbf{m}_d \end{pmatrix}, \quad (2.148)$$

with the diattenuator sub-matrix  $\mathbf{m}_d$  defined according to Lu and Chipman [43] as:

$$\mathbf{m}_d = \sqrt{1 - D^2} \mathbf{I}_3 + (1 - \sqrt{1 - D^2}) \mathbf{D} \mathbf{D}^T \quad (2.149)$$

Following the same path, we can also define the retarder matrix. A retarder describes a medium that induces a phase difference between 2 eigenstates of polarization. Just like

the diattenuation vector, we can define a vector of retardance  $\mathbf{R}$  as

$$\mathbf{R} = R \begin{pmatrix} r_1 \\ r_2 \\ r_3 \end{pmatrix} = \begin{pmatrix} R_{hv} \\ R_{\pm 45} \\ R_{lr} \end{pmatrix} \quad (2.150)$$

with  $r_1^2 + r_2^2 + r_3^2 = 1$  and  $R$  the total retardance between fast and slow axis. Retardance eigenstates correspond to polarization states along the fast and slow axis, and write

$$\mathbf{S}_f^T = (1, r_1, r_2, r_3), \quad (2.151)$$

$$\mathbf{S}_s^T = (1, -r_1, -r_2, -r_3). \quad (2.152)$$

At this stage, we use the property that a pure retarder corresponds to a rotation of a Stokes vector in the Poincaré sphere, a property that we will demonstrate in next chapter using the concepts of differential decomposition and group theory. The Mueller matrix of a pure retarder can then be written as

$$\mathbf{M}_R = \begin{pmatrix} 1 & \mathbf{0}^T \\ \mathbf{0} & \mathbf{m}_r \end{pmatrix}, \quad (2.153)$$

with the sub-matrix of retarder elements  $(\mathbf{m}_r)_{ij}$  defined according to [43] as

$$(\mathbf{m}_r)_{ij} = \delta_{ij} \cos R + r_i r_j (1 - \cos R) \sum_{k=1}^3 \varepsilon_{ijk} r_k \sin R \quad (2.154)$$

where  $\varepsilon$  is the the Levi-Civita permutation sign and  $\delta$  is the Kronecker symbol.

Finally, we define the Mueller matrix of a pure depolarizer  $\mathbf{M}_\Delta$  written directly as

$$\mathbf{M}_\Delta = \begin{pmatrix} 1 & \mathbf{0}^T \\ \mathbf{0} & \mathbf{m}_\delta \end{pmatrix} \quad (2.155)$$

where the sub-matrix  $\mathbf{m}_\delta$  is a symmetric matrix and with a choice of adequate orthonormal basis this matrix can be reduced into a diagonal form. So the diagonal form of Mueller matrix can be written as

$$\mathbf{M}_\Delta = \begin{pmatrix} 1 & 0 & 0 & 0 \\ 0 & a & 0 & 0 \\ 0 & 0 & b & 0 \\ 0 & 0 & 0 & c \end{pmatrix}, \quad (2.156)$$

with  $a, b$  and  $c$  corresponding to the degrees of depolarization along the different polarisation states. Since the form proposed in Eq.(2.155) does not include the polarizance that

a pure depolarizer may display as well, a more general form of a pure depolarizer writes according to Lu and Chipman [43],

$$\mathbf{M}_{\Delta} = \begin{pmatrix} 1 & \mathbf{0}^T \\ \mathbf{P}_{\Delta} & \mathbf{m}_{\delta} \end{pmatrix}, \quad (2.157)$$

where  $\mathbf{P}_{\Delta}$  called the polarizance vector gives the polarization states of an emergence beam that probes the system using totally unpolarized light.

Once we have the definition for the Mueller matrices for all the elementary polarization elements, the decomposition can be carried out following a certain choice of ordering of the different matrices modeling the sample. But since the actual ordering of the different polarization elements is unknown, and even does not exist, this approach becomes somehow arbitrary. Theoretically, the product of 3 elementary components yields 6 different ordering possibilities. Among these, some turn out to be not stable, meaning that they do not correspond to physically realizable elementary component Mueller matrix. The most widely used ordering was first introduced by Lu and Chipman [43] and defined as

$$\mathbf{M} = \mathbf{M}_{\Delta 1} \mathbf{M}_{R1} \mathbf{M}_{D1} \quad (2.158)$$

which has been tested as the most stable ordering choice, and has therefore been commonly used [46, 47]. It exists 2 other possible orderings that also give physically realizable Mueller matrices, namely

$$\mathbf{M} = \mathbf{M}_{R2} \mathbf{M}_{\Delta 2} \mathbf{M}_{D2}, \quad (2.159)$$

$$\mathbf{M} = \mathbf{M}_{\Delta 2} \mathbf{M}_{D2} \mathbf{M}_{R2}. \quad (2.160)$$

Common to these 3 ordering is the position of depolarizer matrix before the diattenuation matrix, giving the so-called forward decomposition. The other 3 orderings with the matrix of depolarizer after the matrix of diattenuation are called reverse decomposition. Morio and Goudail [48] showed that the reverse decomposition with the same definitions of the 3 elementary matrix does not always give physical realizable Mueller matrix in the presence of a significant level of depolarization. This issue has been later solved by Ossikovski [49] by modifying the depolarizer matrix to the form

$$\mathbf{M}_{\Delta'} = \begin{pmatrix} 1 & \mathbf{D}'^T \\ \mathbf{0} & \mathbf{m}_{\delta} \end{pmatrix}, \quad (2.161)$$

enabling more stable orderings of product decomposition, with the most commonly used being

$$\mathbf{M} = \mathbf{M}_{D4} \mathbf{M}_{R4} \mathbf{M}_{\Delta'}. \quad (2.162)$$

Apart from the forward and reverse decompositions, there is also another type of ordering which is the symmetric decomposition expressed as

$$\mathbf{M} = \mathbf{M}_D \mathbf{M}_R \mathbf{M}_\Delta \mathbf{M}'_R \mathbf{M}'_D, \quad (2.163)$$

with  $\mathbf{M}_\Delta$  the Mueller matrix of pure depolarizer with diagonal form detailed in Eq.(2.156). This form of decomposition is, within certain limitation, more accurate in many physical situations than the forward and reverse decompositions [49, 50].

## 2.2.4 Sum vs. Product decompositions

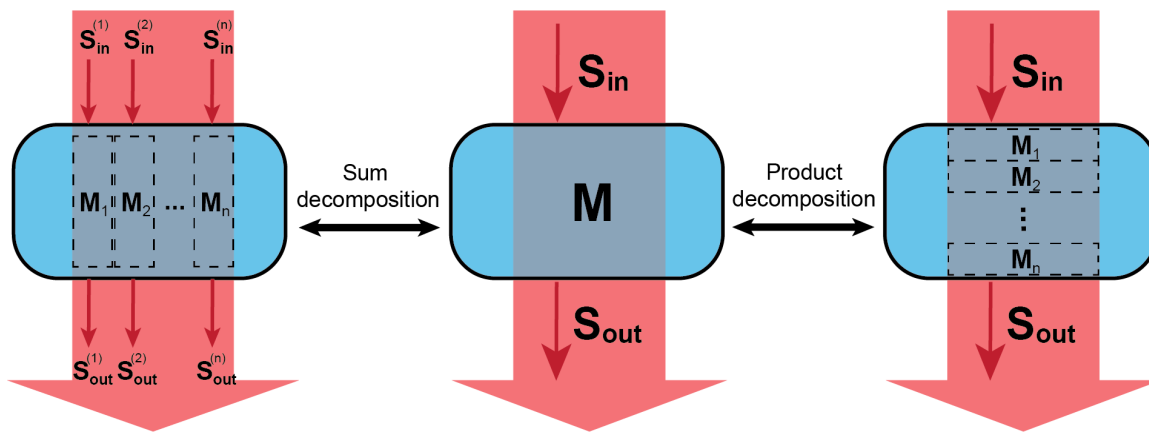


FIGURE 2.3: Schematized physical picture of the sum and product decomposition methods.

The main aim of these 2 decomposition methods is to extract the optical properties from an experimental depolarizing Mueller matrix. The sum decomposition decomposes the system into a parallel combination of 4 major arbitrary non-depolarizing parts given by Eq.(2.119). The product decomposition is to decompose the depolarizing Mueller matrix into a product of 3 basic polarization components, namely diattenuation, retardance and depolarization with 3 different types of ordering (forward, backward and symmetric decomposition). The physical picture of these 2 decomposition methods is shown in Fig. 2.3.

From a general perspective, the product decomposition does not always provide precise estimation of the optical properties of a given sample. Although we can use numerical iteration procedures in order to approach the actual value of the polarimetric properties for example the pseudo-polar decomposition proposed by O. Arteaga [51], product decomposition remains limited and one can miss some important optical features, for example Cotton effect signatures as discussed in [52].

If we compare the 2 methods of decomposition when dealing with depolarizing Mueller matrices, we see that none of them is exact due to depolarization and that both of them

have their limitations. It is thus difficult to identify a "best" method and one can only adapt the methods according to the specific situation, aiming at the best estimate of the polarimetric properties. According to their physical pictures associated with these 2 decomposition methods, sum decomposition is preferred when the depolarization is induced by a stochastic source all along the entire optical path and where one non-depolarizing Mueller matrix dominates, while product decomposition provides more accurate estimates when the sample under study has a clear layered structure with each layer presenting one of the 3 basic polarization components (retardance, diattenuation and depolarization).

In this thesis, we are dealing for most experiments with molecular systems in solution phase which are generally relatively homogeneous and only slightly depolarizing. We therefore prefer to use the sum decomposition in order to isolate the non-depolarizing Mueller matrix. This approach can give a good estimate for the averaged non-depolarizing Mueller matrix, leading to extract the polarimetric properties using differential decomposition which is exact for a non-depolarizing Mueller matrix associated with a homogeneous medium. This will be discussed in detail below.

## 2.3 Polarimetric properties of a transmissive medium

The methods discussed above are developed for a light beam transmitted through a medium. The transmissive polarimetric properties that can be extracted are generally related to ground state properties of the sample. We now describe a methodology that relies on the following work [42, 53] and that aims at accessing the basic polarimetric quantities. The methodology is based first on the sum decomposition of the experimental Mueller matrix and then on the differential decomposition.

### 2.3.1 Degree of polarization

For a depolarizing Mueller matrix, before its decomposition, the first parameter we can extract is the degree of polarization of the matrix. We recall the definition of the degree of polarization

$$P = \frac{\sqrt{\sum_{ij} m'_{ij}{}^2 - m'_{00}{}^2}}{\sqrt{3}m'_{00}}. \quad (2.164)$$

Here we note that conventionally, we normalize the Mueller matrix to  $m_{00}$  so that the normalized matrix  $\mathbf{M}$  relates to the original matrix  $\mathbf{M}'$  as

$$\mathbf{M} = \frac{1}{m_{00}}\mathbf{M}' = \begin{pmatrix} 1 & m'_{01}/m'_{00} & m'_{02}/m'_{00} & m'_{03}/m'_{00} \\ m'_{10}/m'_{00} & m'_{11}/m'_{00} & m'_{12}/m'_{00} & m'_{13}/m'_{00} \\ m'_{20}/m'_{00} & m'_{21}/m'_{00} & m'_{22}/m'_{00} & m'_{23}/m'_{00} \\ m'_{30}/m'_{00} & m'_{31}/m'_{00} & m'_{32}/m'_{00} & m'_{33}/m'_{00} \end{pmatrix}. \quad (2.165)$$



With this normalization, the degree of polarization can be written as

$$P = \frac{\sqrt{\sum_{ij} m_{ij}^2 - 1}}{\sqrt{3}} = \frac{\sqrt{\text{Tr}(\mathbf{M}\mathbf{M}^T) - 1}}{\sqrt{3}}. \quad (2.166)$$

The physical interpretation of the degree of polarization is a measure of the order vs. disorder of the sample. For a perfectly ordered system, meaning that the medium is homogeneous and its optical response even everywhere, the measured Mueller matrix must be purely non-depolarizing and the associated optical properties defined without uncertainty. For a depolarizing medium, we resort to a linear combination of different non-depolarizing media corresponding to the disorder or forming the inhomogeneity in the system, as we described above.

In this context, the notion of optical order and disorder can be related to the concept of entropy, where the degree of polarization becomes a measure of entropy of the system following an appropriate definition. A. Aiello and J. P. Woerdman [54] have discussed the relation between entropy and depolarization from the Mueller matrix point of view. Defining the entropy via a Mueller matrix proceeds from a sum decomposition since this decomposition describes how the depolarizing Mueller matrix is contributed from different non-depolarizing Mueller matrices giving a way to measure entropy. We remind the Shanon entropy formula

$$S = - \sum_i^N p_i \log_N p_i \quad (2.167)$$

where  $p_i$  is the probability of conformation  $i$  with normalization condition  $\sum_i p_i = 1$ . Analogically, the entropy can be calculated from the eigenvalues of any  $\mathbf{N}$  matrix as [55]:

$$S_M = - \sum_{i=0}^3 \frac{\lambda_i}{\sum_i \lambda_i} \log_4 \left( \frac{\lambda_i}{\sum_i \lambda_i} \right) \quad (2.168)$$

where  $\lambda_i$  is the eigenvector of  $\mathbf{N}$  shown in Eq.(2.119). One can easily verify that  $S_M = 0$  for a medium characterized by a non-depolarizing Mueller matrix ( $\lambda_0 \neq 0, \lambda_1 = \lambda_2 = \lambda_3 = 0$ ) and  $S_M = 1$  for a totally depolarizing medium ( $\lambda_0 = \lambda_1 = \lambda_2 = \lambda_3 \neq 0$ ).

### 2.3.2 Birefringence and dichroism extracted by differential decomposition

After having calculated the degree of polarization and extracted the information from the initial depolarizing Mueller matrix, a further step can be taken in extracting, from the non-depolarizing Mueller matrix estimated by the Cloude decomposition the other optical properties. In the context of this thesis, a homogeneous molecular system can be modeled

as a general bi-anisotropic medium. The basic optical properties associated with such a medium are: (i) birefringence that describes the real part of refraction index difference between 2 polarization eigenstates, and (ii) dichroism that describes the imaginary part of the same refraction index difference between the 2 polarization eigenstates.

Here we detail the exact method proposed by R. C. Jones in 1948 [56] capable of extracting such properties from a non-depolarizing Mueller matrix or a Mueller-Jones matrix. Following [56], we introduce the derivatives of the Jones and Mueller matrices along the propagation direction of the light beam, which are respectively defined as Jones N-matrix  $\mathbf{N}_J$  and Mueller N-matrix  $\mathbf{N}_M$ . Birefringence and dichroism are then defined as elementary actions performed by the differential Jones matrix on polarization, that is an electric field vector. The result of this action is then translated into Mueller Jones matrices.

By definition [56], if  $\mathbf{J}_z$  is a Jones matrix of an optical system up to a position  $z$  along the propagation direction, the differential Jones matrix at this position  $z$ , noted as  $\mathbf{N}_{J,z}$ , is defined as

$$\mathbf{N}_{J,z} \equiv \lim_{z' \rightarrow z} \frac{\mathbf{J}_{z,z'} - \mathbf{I}}{z' - z}. \quad (2.169)$$

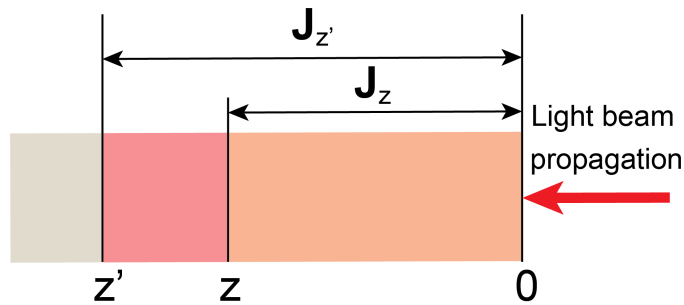


FIGURE 2.4: Schematic representation for deducing differential Jones matrix along the optical path.

According to Jones calculus, a Jones matrix defined over a length  $z'$  but evaluated at position  $z$  noted as  $\mathbf{J}_{z,z'}$  can be defined as

$$\mathbf{J}_{z,z'} = \mathbf{J}_{z'} \mathbf{J}_z^{-1}. \quad (2.170)$$

as illustrated in Fig. 2.4. Then, Eq.(2.169) becomes

$$\mathbf{N}_{J,z} \equiv \lim_{z' \rightarrow z} \frac{\mathbf{J}_{z'} - \mathbf{J}_z}{z' - z} \mathbf{J}_z^{-1}, \quad (2.171)$$

and we can use the notation of the derivative

$$\mathbf{N}_J \equiv \frac{d\mathbf{J}}{dz} \mathbf{J}^{-1} \quad (2.172)$$

to define the derivative of Jones matrix itself as

$$\frac{d\mathbf{J}}{dz} = \mathbf{N}_J \mathbf{J}. \quad (2.173)$$

With this relation, we can similarly define higher order derivatives of the Jones matrix as

$$\frac{d^k \mathbf{J}}{dz^k} = \mathbf{N}_J^k \cdot \mathbf{J}. \quad (2.174)$$

With these definitions, we can develop a Jones matrix  $\mathbf{J}$  at the vicinity of a matrix  $\mathbf{J}_0$  by a Taylor expansion of the matrix involving these derivatives as

$$\mathbf{J} = \mathbf{J}_0 + \sum_{k=1}^{\infty} \frac{1}{k!} \frac{d^k \mathbf{J}}{dz^k} (z - z_0)^k, \quad (2.175)$$

which, by substituting Eq.(2.174), gives

$$\mathbf{J} = \left( \mathbf{I} + \sum_{k=1}^{\infty} \frac{1}{k!} \mathbf{N}_J^k \cdot (z - z_0)^k \right) \mathbf{J}_0, \quad (2.176)$$

that can be noted symbolically as

$$\mathbf{J} = e^{\mathbf{N}_J(z-z_0)} \mathbf{J}_0. \quad (2.177)$$

By taking  $z_0 = 0$ , we have  $\mathbf{J}_0 = \mathbf{I}$ . The total Jones matrix  $\mathbf{J}$  then reads as

$$\mathbf{J} = \exp(\mathbf{N}_J z), \quad (2.178)$$

where it is important to note that the exponential function here is a matrix exponential that differs from a scalar exponential. Similarly, the differential Jones matrix  $\mathbf{N}_J$  can be inverted from a Jones matrix  $\mathbf{J}$  by taking the matrix logarithm as

$$\mathbf{N}_J = \frac{1}{z} \ln(\mathbf{J}). \quad (2.179)$$

With this notion of differential Jones matrices, it is possible to study an elementary action of the differential Jones matrices over the electric field vector, i.e. over polarization. Starting with the variation of the electric field  $\mathbf{E}$  during its transmission through a medium defined by a Jones matrix  $\mathbf{J}$ :

$$\frac{d\mathbf{E}(z, t)}{dz} = \frac{d}{dz} [\mathbf{J}\mathbf{E}(z = 0, t)] = \frac{d\mathbf{J}}{dz} \mathbf{E}(z = 0, t), \quad (2.180)$$

we obtain after substituting Eq.(2.173),

$$\frac{d\mathbf{E}(z,t)}{dz} = \mathbf{N}_J \mathbf{J} \mathbf{E}(z=0,t) = \mathbf{N}_J \mathbf{E}(z,t). \quad (2.181)$$

This equation shows that the differential Jones matrix generates an infinitesimal variation for the electric field vector. This gives us the possibility to define a series of elementary actions for the differential Jones matrix  $\mathbf{N}_J$  which possesses 8 degrees of freedom. According to R. C. Jones [56], any differential Jones matrix can be decomposed into a 8 dimensional  $2 \times 2$  elementary action matrix basis  $\{\mathbf{n}_i\}$  as

$$\mathbf{N}_J = \sum_{i=1}^8 \theta_i \mathbf{n}_i = \sum_{i=1}^8 \Theta_i \quad (2.182)$$

with the 8 independent parameters identified as the following polarimetric properties: linear birefringence ( $LB, LB'$ ) and dichroism ( $LD, LD'$ ) and circular birefringence ( $CB$ ) and dichroism ( $CD$ ), defined explicitly as:

$$LB = 2\pi(n_x - n_y)z/\lambda_0 \quad (2.183)$$

$$LD = 2\pi(\kappa_x - \kappa_y)z/\lambda_0 \quad (2.184)$$

$$LB' = 2\pi(n_{45^\circ} - n_{-45^\circ})z/\lambda_0 \quad (2.185)$$

$$LD' = 2\pi(\kappa_{45^\circ} - \kappa_{-45^\circ})z/\lambda_0 \quad (2.186)$$

$$CB = 2\pi(n_l - n_r)z/\lambda_0 \quad (2.187)$$

$$CD = 2\pi(\kappa_l - \kappa_r)z/\lambda_0 \quad (2.188)$$

together with other 2 parameters associated with the total phase difference  $\Phi$  and the intensity attenuation  $A$  defined as

$$\Phi = 2\pi n z / \lambda_0 \quad (2.189)$$

$$A = 2\pi \kappa z / \lambda_0, \quad (2.190)$$

where  $n$  represents the real part of the refraction index,  $\kappa$  represents the imaginary part of the refraction index,  $\lambda_0$  is the wavelength of the light in vacuum and  $z$  the optical thickness of the sample. In Eqs.(2.183) - (2.188) above, the  $l$  corresponds to a  $45^\circ$  rotation of the  $(x, y)$  Cartesian basis and  $(n_i, \kappa_i)$  corresponds to the refractive index (real, imaginary) measured with the chosen pure state  $i$  of polarization (linear  $x, y, \pm 45^\circ$  and circular left and right).

The 8 elementary actions for the differential Jones matrix derived from a total Jones matrix along an optical path  $l$  can thus be expressed explicitly as

$$\Theta_1 = -\frac{\Phi}{z} \begin{pmatrix} i & 0 \\ 0 & i \end{pmatrix} \quad (2.191)$$

$$\Theta_2 = -\frac{A}{z} \begin{pmatrix} 1 & 0 \\ 0 & 1 \end{pmatrix} \quad (2.192)$$

$$\Theta_3 = -\frac{CB}{2z} \begin{pmatrix} 0 & -1 \\ 1 & 0 \end{pmatrix} \quad (2.193)$$

$$\Theta_4 = -\frac{CD}{2z} \begin{pmatrix} 0 & i \\ -i & 0 \end{pmatrix} \quad (2.194)$$

$$\Theta_5 = -\frac{LB}{2z} \begin{pmatrix} i & 0 \\ 0 & -i \end{pmatrix} \quad (2.195)$$

$$\Theta_6 = -\frac{LD}{2z} \begin{pmatrix} 1 & 0 \\ 0 & -1 \end{pmatrix} \quad (2.196)$$

$$\Theta_7 = -\frac{LB'}{2z} \begin{pmatrix} 0 & i \\ i & 0 \end{pmatrix} \quad (2.197)$$

$$\Theta_8 = -\frac{LD'}{2z} \begin{pmatrix} 0 & 1 \\ 1 & 0 \end{pmatrix}. \quad (2.198)$$

With these definition, we can rearrange birefringence and dichroism terms as well as the real and imaginary parts of refraction index as

$$X = 2(\Phi - iA) \quad (2.199)$$

$$C = CB - iCD \quad (2.200)$$

$$L = LB - iLD \quad (2.201)$$

$$L' = LB' - iLD', \quad (2.202)$$

in order to express Jones  $\mathbf{N}_J$  matrix simply as

$$\mathbf{N}_J = -\frac{i}{2z} \begin{pmatrix} X + L & L' + iC \\ L' - iC & X - L \end{pmatrix}. \quad (2.203)$$

Using Eq.(2.178), the total Jones matrix can be inverted as a function of birefringence and dichroism as

$$\mathbf{J} = e^{-iX/2} \begin{pmatrix} \cos \frac{T}{2} - \frac{iL}{T} \sin \frac{T}{2} & \frac{C - iL'}{T} \sin \frac{T}{2} \\ -\frac{C + iL'}{T} \sin \frac{T}{2} & \cos \frac{T}{2} + \frac{iL}{T} \sin \frac{T}{2} \end{pmatrix} \quad (2.204)$$

with  $T = \sqrt{C^2 + L^2 + L'^2}$ .

With the same method, we can also build the Mueller-Jones matrix with the same parameters of birefringence and dichroism. We can define in the same way a differential Mueller matrix, Mueller N-matrix  $\mathbf{N}_M$ , since both the Jones calculus and Mueller calculus are multiplicative. Similarly thus, the definition of a derivative of the Mueller matrix as:

$$\mathbf{N}_{M,z} \equiv \lim_{z' \rightarrow z} \frac{\mathbf{M}_{z,z'} - \mathbf{I}}{z' - z} \quad (2.205)$$

leads to,

$$\mathbf{N}_M \equiv \frac{d\mathbf{M}}{dz} \cdot \mathbf{M}^{-1} \quad (2.206)$$

with the same properties as the  $\mathbf{N}_J$  matrix. To allow us to relate the Mueller-Jones matrix with the Jones matrix, taking Eq.(2.66),

$$\mathbf{N}_M = \frac{d\mathbf{M}}{dz} \mathbf{M}^{-1} = \frac{d}{dz} [\mathbf{A}(\mathbf{J} \otimes \mathbf{J}^*) \mathbf{A}^{-1}] \mathbf{M}^{-1} = \mathbf{A} \frac{d}{dz} (\mathbf{J} \otimes \mathbf{J}^*) \mathbf{A}^{-1} \mathbf{M}^{-1}. \quad (2.207)$$

Then using

$$\mathbf{M}^{-1} = \mathbf{A}(\mathbf{J}^{-1} \otimes (\mathbf{J}^{-1})^*) \mathbf{A}^{-1}, \quad (2.208)$$

we have

$$\mathbf{N}_M = \mathbf{A} \frac{d}{dz} (\mathbf{J} \otimes \mathbf{J}^*) (\mathbf{J}^{-1} \otimes (\mathbf{J}^{-1})^*) \mathbf{A}^{-1}. \quad (2.209)$$

Considering the Kronecker product is linear, we obtain

$$\mathbf{N}_M = \mathbf{A} \left[ \left( \frac{d\mathbf{J}}{dz} \otimes \mathbf{J}^* \right) + \left( \mathbf{J} \otimes \frac{d\mathbf{J}^*}{dz} \right) \right] [\mathbf{J}^{-1} \otimes (\mathbf{J}^{-1})^*] \mathbf{A}^{-1} \quad (2.210)$$

on which we apply the property of the mix product between the Kronecker product and the matrix product to get

$$\mathbf{N}_M = \mathbf{A} \left[ \frac{d\mathbf{J}}{dz} \mathbf{J}^{-1} \otimes \mathbf{J}^* (\mathbf{J}^*)^{-1} + \mathbf{J} \mathbf{J}^{-1} \otimes \frac{d\mathbf{J}^*}{dz} (\mathbf{J}^*)^{-1} \right] \mathbf{A}^{-1}. \quad (2.211)$$

Finally, by comparing with Eq.(2.173), we derive the relation between the differential Mueller-Jones matrix and the differential Jones matrix as:

$$\mathbf{N}_M = \mathbf{A} (\mathbf{N}_J \otimes \mathbf{I} + \mathbf{I} \otimes \mathbf{N}_J^*) \mathbf{A}^{-1}. \quad (2.212)$$

Combined with the explicit expression of the differential Jones matrix  $\mathbf{N}_J$  shown in Eq.(2.203), Eq.(2.212) leads to the explicit expression of differential Mueller Jones matrix as

$$\mathbf{N}_M = \frac{1}{z} \begin{pmatrix} A & -LD & -LD' & CD \\ -LD & A & CB & LB' \\ -LD' & -CB & A & -LB \\ CD & -LB' & LB & A \end{pmatrix} = \frac{1}{z} \mathbf{m}, \quad (2.213)$$

where  $z$  is the total optical path length in the medium. This new matrix  $\mathbf{m}$ , built explicitly on all the relevant optical observables of a polarimetry experiments, is an important result of the differential decomposition.

Similar to Eq.(2.178), the matrix built by the polarimetric properties  $\mathbf{m}$  also known as cumulative differential Mueller matrix can be obtained by the inversion of the Mueller-Jones matrix using the matrix logarithm

$$\mathbf{m} = z\mathbf{N}_M = \ln(\mathbf{M}), \quad (2.214)$$

and the Mueller matrix built as

$$\mathbf{M} = \exp(z\mathbf{N}_M) = \exp(\mathbf{m}) \quad (2.215)$$

Therefore, Eq.(2.214) and Eq.(2.213) based on the Cloude decomposition give a clear methodology for extracting the relevant polarimetric properties from the measurement of a depolarizing Mueller matrix. It has been used and exploited in many recent work, in particular by B. Kahr and O. Arteaga in the context of material science polarimetry (see Introduction).

In the absence of numerical tools for evaluating the matrix logarithm, there is also an analytical way to obtain these polarimetric properties by using the explicit relation between a Jones matrix and a Mueller-Jones matrix. This analytical approach was proposed in [52] and consists in expressing a Jones matrix with its 8 independent real parameters as

$$\mathbf{J} = e^{i\theta_{00}} \begin{pmatrix} r_{00} & r_{01}e^{i(\theta_{01}-\theta_{00})} \\ r_{10}e^{i(\theta_{10}-\theta_{00})} & r_{11}e^{i(\theta_{11}-\theta_{00})} \end{pmatrix}. \quad (2.216)$$

Knowing that the absolute phase will be eventually lost when converting  $\mathbf{J}$  into a Mueller matrix, there are in fact only 7 independent relations between the Jones matrix elements

and the Mueller-Jones matrix ones. These relations are:

$$r_{00} = [(m_{00} + m_{01} + m_{10} + m_{11})/2]^{1/2} \quad (2.217)$$

$$r_{01} = [(m_{00} - m_{01} + m_{10} - m_{11})/2]^{1/2} \quad (2.218)$$

$$r_{10} = [(m_{00} + m_{01} - m_{10} - m_{11})/2]^{1/2} \quad (2.219)$$

$$r_{11} = [(m_{00} - m_{01} - m_{10} + m_{11})/2]^{1/2} \quad (2.220)$$

$$e^{i(\theta_{01}-\theta_{00})} = \frac{m_{02} + m_{12} - i(m_{03} + m_{13})}{[(m_{00} + m_{10})^2 - (m_{10} + m_{11})^2]^{1/2}} \quad (2.221)$$

$$e^{i(\theta_{10}-\theta_{00})} = \frac{m_{20} + m_{21} + i(m_{30} + m_{31})}{[(m_{00} + m_{01})^2 - (m_{10} + m_{11})^2]^{1/2}} \quad (2.222)$$

$$e^{i(\theta_{11}-\theta_{00})} = \frac{m_{22} + m_{33} + i(m_{32} - m_{23})}{[(m_{00} + m_{11})^2 - (m_{10} + m_{01})^2]^{1/2}} \quad (2.223)$$

Then in order to obtain birefringence and dichroism quantities, we simply identify the terms in Eqs.(2.217)-(2.223) with the matrix elements presented in Eq.(2.204). Generally, since we normalize the Mueller matrix to  $m_{00}$ , we lose any information on the absolute total intensity ratio. This implies that the Jones matrix shown in Eq.(2.216) must be normalized by its own determinant in order to be consistent with the Jones matrix elements calculated from a normalized Mueller matrix. This identification and normalization yield

$$\begin{pmatrix} \cos \frac{T}{2} - \frac{iL}{T} \sin \frac{T}{2} & \frac{C - iL'}{T} \sin \frac{T}{2} \\ -\frac{C + iL'}{T} \sin \frac{T}{2} & \cos \frac{T}{2} + \frac{iL}{T} \sin \frac{T}{2} \end{pmatrix} = K \begin{pmatrix} r_{00} & r_{01}e^{i(\theta_{01}-\theta_{00})} \\ r_{10}e^{i(\theta_{10}-\theta_{00})} & r_{11}e^{i(\theta_{11}-\theta_{00})} \end{pmatrix} \quad (2.224)$$

with  $K = [r_{00}r_{11}e^{i(\theta_{11}-\theta_{00})} - r_{10}r_{01}e^{i(\theta_{10}-\theta_{00})}e^{i(\theta_{01}-\theta_{00})}]^{-1/2}$  coming from the determinant  $\det(\mathbf{J})$ . Since all the matrix elements for the right-hand side matrix have been calculated, one immediately obtains both real and imaginary parts of  $C$ ,  $L$  and  $L'$ , leading to determine birefringence and dichroism parameters.

## 2.4 Polarimetric properties of an emissive medium

Previous discussions have focused on analyzing the polarization properties of a passive medium through which light is transmitted. But if we look back at the definition of a Mueller matrix in the Stokes-Mueller formalism, the relation between the 2 Stokes vectors in the incident and transmission planes allows many other configurations. In this section, we will expand the application of the Mueller algebra to the case where the medium is photoactive, for instance composed of fluorescent molecules.



The method is straightforward. Similarly to the definition written in Eq.(2.56), we define a  $4 \times 4$  matrix  $\mathbf{M}_E$  that relates the polarization state of the pump at a pumping wavelength  $\lambda_p$  and the polarization state of the photoluminescence at an emission wavelength  $\lambda_{pl}$  as

$$\mathbf{S}_{out}(\lambda_{pl}) = \mathbf{M}_E(\lambda_{pl}, \lambda_p) \mathbf{S}_{in}(\lambda_p) \quad (2.225)$$

where usually  $\lambda_{pl} > \lambda_p$  due to the Stokes shift effect. The Mueller matrix of an emissive medium turns out to be in contrast with a matrix for transmissive medium, easier to interpret in terms of polarimetric elements. Let us write the explicit expression of the Mueller matrix that relates the 2 Stokes vectors (pump-emission):

$$\begin{pmatrix} S_0^e \\ S_1^e \\ S_2^e \\ S_3^e \end{pmatrix} = \begin{pmatrix} m_{00} & m_{01} & m_{02} & m_{03} \\ m_{10} & m_{11} & m_{12} & m_{13} \\ m_{20} & m_{21} & m_{22} & m_{23} \\ m_{30} & m_{31} & m_{32} & m_{33} \end{pmatrix} \begin{pmatrix} S_0^p \\ S_1^p \\ S_2^p \\ S_3^p \end{pmatrix} \quad (2.226)$$

where  $S_i^e$  is a Stokes parameter of light emission and  $S_i^p$  is one for the pumping light. Each matrix element represents a different contribution from a pump light polarization ( $S_1^p, S_2^p, S_3^p$ ) and intensity ( $S_0^p$ ) to the emission polarization ( $S_1^e, S_2^e, S_3^e$ ) and intensity ( $S_0^e$ ). Specifically speaking, for a normalized emission Mueller matrix, the first row describes the contrasts in light emission intensity depending on the different polarizations of the pump light, and is thus related to the fluorescence detected dichroism. The first column of the matrix represents the polarization of the emission when the pump is fully non-polarized, displaying the polarization properties of the fluorescence such as LPL (linearly polarized luminescence) and CPL (circularly polarized luminescence). The remaining elements correspond to conversions of polarization from the pumping light to the emission light. The diagonal elements describe how the active sample can maintain polarization state of light. This Mueller matrix methodology applied to active media will be exploited in the last chapter of the thesis.

## 2.5 Conclusion

This chapter has summarized some of the most commonly used theoretical tools applied in the context of polarimetry. The experimental conditions of this work have pushed us to focus our discussion on the Stokes-Mueller formalism. Specifically, we discussed an important point related to the conditions of physical realizability, giving the possibility to find the closest physical realizable Mueller matrix from an experimental unfiltered Mueller matrix. In agreement with our experiments that will involve molecular systems that are generally depolarizing due to unavoidable spatial inhomogeneities, we choose the method

---

of Cloude's sum decomposition in order to estimate the closest non-depolarizing Mueller matrix and exploit a differential decomposition in order to further extract the basic polarimetric properties of the medium such as birefringence and dichroism. This chapter lays the theoretical foundations for the experimental discussions and the data analysis involved in this thesis and presented in the next chapters.



## Chapter 3

# Group-like algebraic structure of the Stokes-Mueller formalism

In this chapter, we focus on the algebraic structure of Stokes-Mueller formalism within the frame work of group-like structure. Starting from the normal form of the Mueller matrix based on the representation of the Stokes vectors in a Minkowski space, we review the algebraic structure of different sub-ensembles of physical Mueller matrices. Specifically for non-singular Mueller matrices, we define a Lie algebra which is shown to be useful in the context of Mueller matrix decomposition analysis, polarization trajectory maps in the Poincaré sphere and the *ab initio* construction of media with specific properties.

### 3.1 Normal form for Mueller matrices

As we discussed in the previous chapter, there are several constraints for a 4 dimensional vector to be a Stokes vector and for a  $4 \times 4$  matrix to be a physically realizable Mueller matrix. But, there is another way to express the Stokes-Mueller formalism starting from the space in which live the Stokes vectors [38]. In this approach, all Stokes vectors are defined in the 3+1 dimensional Minkowski space  $\mathcal{M}_{3,1}$  with the Minkowski metric

$$\mathbf{G} = \begin{pmatrix} 1 & 0 & 0 & 0 \\ 0 & -1 & 0 & 0 \\ 0 & 0 & -1 & 0 \\ 0 & 0 & 0 & -1 \end{pmatrix}. \quad (3.1)$$

According to the conditions for Stokes vectors -see in Chapter 2 Eq. (2.50) for fully polarized light and Eq. (2.53) for partially polarized light-, we get the Minkowski four-vector formulation of the Stokes vectors by writing these two conditions into a single quadratic form as

$$\mathbf{S}^T \mathbf{G} \mathbf{S} \geq 0, S_0 \geq 0 \quad (3.2)$$

with  $S_0$  being an intensity. Within the framework of Minkowski four-vectors, this condition implies that a Stokes vector can be only time-like or light-like<sup>1</sup>, which lives inside the positive side of solid light cone in  $\mathcal{M}_{3,1}$ . Thus, for a Mueller matrix that transforms a Stokes vector to another Stokes vector, the constraint for any physical realizable Mueller matrix  $\mathbf{M}$  writes in the context of Minkowski space as [38]:

- $m_{00} > 0$ ,
- the eigenvalues of the matrix  $\mathbf{GM}^T\mathbf{GM}$  are all real and there exists a time-like eigenvector for the largest eigenvalue;

and specifically, a non-singular Mueller matrix must fulfill

- $m_{00} > 0$ ,
- there exists a proper orthochronous Lorentz transformation [57, 58]  $\mathbf{\Lambda} \in \mathcal{L}_+^\uparrow$ <sup>2</sup> such that  $\mathbf{G}\mathbf{\Lambda}^T\mathbf{M}^T\mathbf{G}\mathbf{\Lambda} = \mathbf{diag}(D_0, D_1, D_2, D_3)$ , with  $D_0 \geq D_i > 0$  ( $i = 1, 2, 3$ )

These conditions are called "Stokes realizability" which only maintain the physical realizability of the incident and emergent Stokes vectors. Compared to the condition of physical realizability proposed by Cloude using eigenvalue study of coherency matrix, Stokes realizability is less general: Cloude's realizability implies indeed Stokes realizability according to Ossikovski [59]. But regardless the limitations of these constraints (which we will discuss in detail later), the study of the group generator of the Mueller formalism algebra is based on the Minkowski space representation of Stokes vector and the general constraint of physical realizability will be applied later on the parameters of each generator.

## 3.2 Group-like algebraic structures

Before discussing the details of the algebraic structure of Mueller matrices, we review some basic definitions of group-like algebraic structure taken as the premises for our discussions below. An algebraic structure is one, or several, closed set  $\mathcal{G}$  of operations such as group-like ones and ring-like ones. We here concentrate on the group-like structure which by definition consists of one binary operation. Within this framework, we mainly focus on the matrix Lie group, Lie monoid and monoid which involve only matrix products within an ensemble of matrices.

First of all, an ensemble  $\mathcal{G}$  has a structure of a group if and only if it obeys the following properties:

---

<sup>1</sup>As in special relativity, a four-vector  $v = (x_0, x_1, x_2, x_3)$  is called time-like when  $x_0^2 > x_1^2 + x_2^2 + x_3^2$ , light-like when  $x_0^2 = x_1^2 + x_2^2 + x_3^2$  and space-like when  $x_0^2 < x_1^2 + x_2^2 + x_3^2$ .

<sup>2</sup>The concept of proper and orthochronous for Lorentz transformation stems from in special relativity. Proper states from the determinant of the transformation matrix  $\mathbf{\Lambda}$  equal to 1 ( $\det(\mathbf{\Lambda}) = +1$ ) and orthochronous states are those with the element  $\Lambda_{11} \geq 1$ .

- 1) A binary operation  $\mathcal{G} \times \mathcal{G} \rightarrow \mathcal{G}$  called product and noted as  $(g, h) \mapsto gh$  with an associative law, namely that for any  $g, h, k \in \mathcal{G}$ ,  $(gh)k = g(hk)$ ;
- 2) A specific element  $e \in \mathcal{G}$  called identity such that for any  $g \in \mathcal{G}$ ,  $eg = ge = g$ ;
- 3) An unitary operation  $\mathcal{G} \rightarrow \mathcal{G}$  called inversion noted as  $g \mapsto g^{-1}$  such that for any  $g \in \mathcal{G}$ ,  $g^{-1}g = gg^{-1} = e$ .

Therefore, in order to verify whether an ensemble can form the structure of a group, these items one by one have to be validated: closure with respect to product operation fulfilling the associative laws, existence of an identity element and closure with respect to inversion. More specifically, we are here interested in the matrix group which consist of square matrices combined with the matrix product and matrix inversion. Conventionally, the matrix group consisting of all  $n$ -dimensional invertible square matrix in the field  $\mathbb{F}$  is noted as  $\text{GL}(n, \mathbb{F})$ .

A Lie group is a group which elements are represented by continuous operations. As such, each elements can be described and analyzed differentially. This local description associates finite group generators to specific finite parameters: for instance, elementary rotations associated to infinitesimal angles. This local version is known as the Lie algebra which is the key for studying the structure of the Lie group. One can verify that  $\text{GL}(n, \mathbb{C})$  is a Lie group together with any of its closed subgroups that also forms a Lie group.

The Lie algebra  $\mathfrak{g}$  of a Lie group  $\mathcal{G}$ , is defined as the tangent space of  $\mathcal{G}$  at its identity element  $e$  noted as  $T_e\mathcal{G}$ . In general, the tangent space at  $e$  can be given as

$$T_e\mathcal{G} = \{\dot{g}(\mathbf{0}) : g : (-\varepsilon, \varepsilon) \rightarrow \mathcal{G} \text{ is a smooth curve with } g(\mathbf{0}) = e\} = \mathfrak{g} \quad (3.3)$$

Explicitly, we can simplify the definition of the tangent space of a subgroup  $G$  of  $\text{GL}(n, \mathbb{F})$  to a single real parameter  $\Delta t$  as

$$T_eG = \left\{ X \left| X = \dot{g}(0) = \lim_{\Delta t \rightarrow 0} \frac{g(\Delta t) - e}{\Delta t}, g(\Delta t) \in \text{GL}(n, \mathbb{F}), \Delta t \in \mathbb{R} \right. \right\} \quad (3.4)$$

In order to explore the relation between Lie algebra and Lie group, within the subgroup  $G$ , we can define its tangent space at any element  $g$  noted as  $T_gG$  with the single real parameter  $t$  by

$$T_gG = \left\{ Y \left| Y = \dot{g}(t) = \lim_{\Delta t \rightarrow 0} \frac{g(t + \Delta t) - g(t)}{\Delta t}, (g(t), g(t + \Delta t)) \in \text{GL}(n, \mathbb{F}), t, \Delta t \in \mathbb{R} \right. \right\} \quad (3.5)$$

Therefore, we can define a differential equation as:

$$Y = \dot{g}(t) = Xg(t) \quad (3.6)$$

by using  $g(t + \Delta t) = g(t)g(\Delta t)$ . The solution of this equation is known as

$$g(t) = \exp(tX), \quad (3.7)$$

where  $\exp(\cdot)$  represents the matrix exponential. The general mapping between a matrix Lie algebra  $gl(n, \mathbb{F})$  and a Lie group  $GL(n, \mathbb{F})$  is therefore the exponential mapping by:

$$\exp : gl(n, \mathbb{F}) \rightarrow GL(n, \mathbb{F}) \quad (3.8)$$

Finally, the Lie algebra  $\mathfrak{g}$  of a matrix subgroup  $G$  in  $GL(n, \mathbb{F})$  can be also characterized as

$$\mathfrak{g} = \{A \in gl(n, \mathbb{F}) : \forall t \in \mathbb{R}, \exp(tA) \in G\} \quad (3.9)$$

This definition can be generalized to a multiple parameter matrix group defined by a  $n$ -dimensional vector  $\mathbf{t}$  with a set of matrix basis  $\mathbf{A}$ . If the elements of a Lie algebra  $\mathfrak{g}$  itself form the smallest sub-algebra containing all elements of  $\mathfrak{g}$ , this set of elements is called generator of the group.

Actually, the Lie algebra  $\mathfrak{g}$  also has an algebraic structure but different from the group. To explore the closed binary operation of the Lie algebra, we defined first the adjoint action as

$$\text{Ad}_A B = ABA^{-1}. \quad (3.10)$$

One can easily show that the elements in a group is closed with respect to this adjoint action because it only consists of matrix product and inversion operation. Starting from the adjoint in the matrix Lie group, one has:

$$\text{Ad}_x y = xyx^{-1}, x, y \in GL(n, \mathbb{F}) : x = \exp(tX), y = \exp(tY) : X, Y \in gl(n, \mathbb{F}). \quad (3.11)$$

Then, we can take the derivative on  $y$  at  $t = 0$  in order to get the adjoint on the corresponding Lie algebra  $Y$

$$\text{Ad}_x Y = xYx^{-1} \quad (3.12)$$

which is also closed in the Lie group  $GL(n, \mathbb{F})$ . Finally, by taking the derivative on  $x$ , we have

$$d_x[\text{Ad}_x Y] = [X \exp(tX) Y (\exp(tX))^{-1} - \exp(tX) Y X \exp(-tX)]_{t=0} = XY - YX = [X, Y] \quad (3.13)$$

Thereby, we get the closed operation in the Lie algebra  $gl(n, \mathbb{F})$ , as

$$[, ] : \mathfrak{g} \times \mathfrak{g} \rightarrow \mathfrak{g} \quad (3.14)$$

For the matrix Lie group, this operation corresponds to taking the matrix commutator. Generalized to all Lie groups, this operation is called a Lie bracket and represents a binary operation fulfilling the bilinearity, alternativity, the Jacobi identity and anticommutativity. So in order to verify that a set  $\mathfrak{g}$  of matrix basis form a Lie algebra, we verify for any  $X, Y \in \mathfrak{g}$ , that they remain closed with respect to the Lie bracket, namely that

$$[X, Y] := XY - YX \in \mathfrak{g}. \quad (3.15)$$

If in addition this set is the smallest set, it forms the set of generators of the group.

The next algebraic structures important for us are the semigroup and the monoid. The only difference for a semigroup with respect to the group is that in a semigroup, the identity element and inversion operation are not included in the structure. A monoid is then the associated structure including the identity element outside the semigroup. In other words, every group is a monoid, and all invertible elements in a monoid can form a group with their inversion. As long as the elements in the monoid  $\mathcal{M}(n, \mathbb{F})$  are invertible, and thus differentiable, we can define the tangent space at its identity  $T_e\mathcal{M}$  and if the elements of  $T_e\mathcal{M}$  have a Lie algebra structure, we called it a monoid of a Lie type or Lie monoid. Therefore, Lie monoids can be always constructed on finite Lie groups.

### 3.3 $SO^+(1,3)$ Lie groups for non-singular non-depolarizing Mueller matrices

In this section, we will focus on the algebraic structure of non-singular, non-depolarizing Mueller matrices starting from their symmetry properties. After verifying the group structure of this matrix ensemble, we study the Lie algebra of the group related to the differential decomposition important for extracting polarimetric properties. Then, we perform an eigenstate analysis in order to characterize the medium described by this type of Mueller matrix. Finally, we compare the product decomposition approach with the differential decomposition for this type of matrix and identify for each decomposition methods corresponding sample configurations.

#### 3.3.1 Description of the $SO^+(1,3)$ group

In order to describe the ensemble of non-singular, non-depolarizing Mueller matrices, we try to start with the Stokes realizability constraint formulated in the Minkowski space in Eq.(3.2). For a non-depolarizing medium, one criterion is that a fully polarized incident light should emerge through the medium fully polarized too. This can be simply written



as:

$$\mathbf{S}_{in}^T \mathbf{G} \mathbf{S}_{in} = \mathbf{S}_{out}^T \mathbf{G} \mathbf{S}_{out} = 0 \quad (3.16)$$

Thus by applying  $\mathbf{S}_{out} = \mathbf{M} \mathbf{S}_{in}$ , we get

$$\mathbf{S}_{in}^T \mathbf{G} \mathbf{S}_{in} = \mathbf{S}_{in}^T \mathbf{M}^T \mathbf{G} \mathbf{M} \mathbf{S}_{in}, \quad (3.17)$$

leading to:

$$\mathbf{G} = \mathbf{M}^T \mathbf{G} \mathbf{M}. \quad (3.18)$$

Since  $\mathbf{M}$  is also non-singular,  $\det(\mathbf{M}) \neq 0$  and  $\mathbf{M}$  is therefore invertible. Thus, a non-singular non-depolarizing Mueller matrix in the Minkowski space fulfills G-orthogonality written as:

$$\mathbf{M}^{-1} = \mathbf{G} \mathbf{M}^T \mathbf{G}. \quad (3.19)$$

We can then verify that the ensemble of Mueller matrices possessing G-orthogonality forms a group according to the definition given above. As these matrices are non-depolarizing, their product will also be non-depolarizing, satisfying the closure with respect to the matrix product. The identity element in this ensemble is the propagation in vacuum free space represented by a  $4 \times 4$  identity matrix  $\mathbf{I}_4$ . Finally, since all matrices in this ensemble are non-singular, they are also all invertible and one can easily verify that their inversion also fulfills Eq. (3.19) using the commutative law of transpose and inversion operations. We thus verify that all Mueller matrices that fulfill Eq. (3.19) representing a non-depolarizing medium form a group, more precisely a subgroup of  $GL(4, \mathbb{R})$ .

In the framework of the Minkowski space, Eq.(3.19) preserves the invariance of quadratic forms  $\mathbf{S}^T \mathbf{G} \mathbf{S}$ , with the same mathematical formulation as the Lorentz transformation described by the well known  $SO(1,3)$  group (Lorentz group). In the case of Mueller matrices, their real character imposing  $m_{00} > 0$ , leads to the restricted Lorentz subgroup  $SO^+(1,3)$  which only describes the proper orthochronous Lorentz transformation. The group formed by non-singular non-depolarizing Mueller matrices can therefore be identified with  $SO^+(1,3)$ , facilitating many analysis related to the properties of Mueller matrices treated in analogy with Lorentz transformation analysis.

### 3.3.2 The $\mathfrak{so}^+(1,3)$ Lie algebra

As we explained above, it is always convenient to characterize a Lie group by its Lie algebra. Since Lie group and Lie algebra are related by the exponential mapping of Eq.(3.8), we can try to analyze the symmetry of the Lie algebra by applying the exponential mapping to Eq.(3.19) which defines the group. Thus, according to the analysis of differential decomposition that we detailed in the previous chapter -see Eq.(2.214)-, we

have

$$\exp(-\mathbf{m}) = \mathbf{G} \exp(\mathbf{m}^T) \mathbf{G} = \exp(\mathbf{G} \mathbf{m}^T \mathbf{G}), \quad (3.20)$$

hence

$$-\mathbf{m} = \mathbf{G} \mathbf{m}^T \mathbf{G}. \quad (3.21)$$

The infinitesimal matrix associated with a non-depolarizing Mueller matrix has therefore a  $\mathbf{G}$ -antisymmetry. This is exactly the same symmetry as the matrix shown in Eq.(2.213). With this symmetry, the matrix group can be determined only by 6 independent real parameters implying that the Lie algebra has only 6 elements corresponding to the generators of the group. The generators of  $\mathfrak{so}^+(1,3)$  and the corresponding parameters can be classified into 2 sets depending on the kind of geometric transformations they generate, namely the set of generators for a rotation  $\{\mathbf{\Gamma}_1, \mathbf{\Gamma}_2, \mathbf{\Gamma}_3\}$  associated with a parameter vector  $\boldsymbol{\theta}$  and the set of generators for a Lorentz boost which represents a single Lorentz transformation  $\{\mathbf{K}_1, \mathbf{K}_2, \mathbf{K}_3\}$  associated with a parameter vector  $\boldsymbol{\zeta}$ . The geometric operations of a rotation and a boost on the surface of a sphere are shown on Fig.3.1.

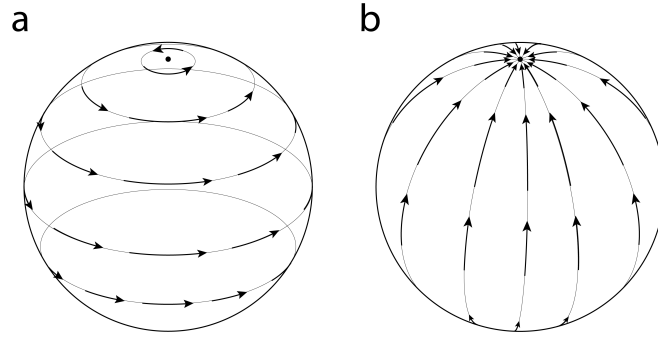


FIGURE 3.1: (a) represents a rotation on the surface of the sphere and (b) represents the motion associated with a boost on the surface of the sphere.

The set of the 6 generators is defined explicitly as:

$$\mathbf{\Gamma}_1 = \begin{pmatrix} 0 & 0 & 0 & 0 \\ 0 & 0 & 0 & 0 \\ 0 & 0 & 0 & -1 \\ 0 & 0 & 1 & 0 \end{pmatrix}, \mathbf{\Gamma}_2 = \begin{pmatrix} 0 & 0 & 0 & 0 \\ 0 & 0 & 0 & 1 \\ 0 & 0 & 0 & 0 \\ 0 & -1 & 0 & 0 \end{pmatrix}, \mathbf{\Gamma}_3 = \begin{pmatrix} 0 & 0 & 0 & 0 \\ 0 & 0 & -1 & 0 \\ 0 & 1 & 0 & 0 \\ 0 & 0 & 0 & 0 \end{pmatrix} \quad (3.22)$$

$$\mathbf{K}_1 = \begin{pmatrix} 0 & 1 & 0 & 0 \\ 1 & 0 & 0 & 0 \\ 0 & 0 & 0 & 0 \\ 0 & 0 & 0 & 0 \end{pmatrix}, \mathbf{K}_2 = \begin{pmatrix} 0 & 0 & 1 & 0 \\ 0 & 0 & 0 & 0 \\ 1 & 0 & 0 & 0 \\ 0 & 0 & 0 & 0 \end{pmatrix}, \mathbf{K}_3 = \begin{pmatrix} 0 & 0 & 0 & 1 \\ 0 & 0 & 0 & 0 \\ 0 & 0 & 0 & 0 \\ 1 & 0 & 0 & 0 \end{pmatrix} \quad (3.23)$$

The structure of the Lie algebra can easily be seen by defining the scalar product between a parameter and the corresponding generator into a dot product form as

$$\boldsymbol{\zeta} \cdot \mathbf{K} = \zeta_1 \mathbf{K}_1 + \zeta_2 \mathbf{K}_2 + \zeta_3 \mathbf{K}_3 \quad (3.24)$$

$$\boldsymbol{\theta} \cdot \boldsymbol{\Gamma} = \theta_1 \boldsymbol{\Gamma}_1 + \theta_2 \boldsymbol{\Gamma}_2 + \theta_3 \boldsymbol{\Gamma}_3, \quad (3.25)$$

and through the commutation relations

$$[\mathbf{K}_i, \mathbf{K}_j] = -\varepsilon_{ijk} \boldsymbol{\Gamma}_k, \quad (3.26)$$

$$[\boldsymbol{\Gamma}_i, \boldsymbol{\Gamma}_j] = \varepsilon_{ijk} \mathbf{K}_k, \quad (3.27)$$

and

$$[\boldsymbol{\Gamma}_i, \mathbf{K}_j] = \varepsilon_{ijk} \mathbf{K}_k, \quad (3.28)$$

where  $\varepsilon_{ijk}$  is the symbol of Levi-Civita. The closure with respect to the commutation rules can be easily verified, thus showing the Lie algebra structure. The interpretation of these matrix generators is clear:  $\mathbf{K}_1$  represents the elementary action associated with a boost along the  $x$  direction and  $\boldsymbol{\Gamma}_1$  represents the elementary action associated with a rotation around the  $x$  axis. Once we get the explicit expression of all the matrix generators of the group, we can derive the expressions for any finite transformation matrix. The elementary transformations  $-\boldsymbol{\zeta} \cdot \mathbf{K}$  and  $\boldsymbol{\theta} \cdot \boldsymbol{\Gamma}$  can be written in the matrix form as:

$$-\boldsymbol{\zeta} \cdot \mathbf{K} = - \begin{pmatrix} 0 & \zeta_1 & \zeta_2 & \zeta_3 \\ \zeta_1 & 0 & 0 & 0 \\ \zeta_2 & 0 & 0 & 0 \\ \zeta_3 & 0 & 0 & 0 \end{pmatrix} = -\zeta \begin{pmatrix} 0 & n_x & n_y & n_z \\ n_x & 0 & 0 & 0 \\ n_y & 0 & 0 & 0 \\ n_z & 0 & 0 & 0 \end{pmatrix} = -\zeta \mathbf{n} \cdot \mathbf{K}, \quad (3.29)$$

$$\boldsymbol{\theta} \cdot \boldsymbol{\Gamma} = \begin{pmatrix} 0 & 0 & 0 & 0 \\ 0 & 0 & -\theta_3 & \theta_2 \\ 0 & \theta_3 & 0 & -\theta_1 \\ 0 & -\theta_2 & \theta_1 & 0 \end{pmatrix} = \theta \begin{pmatrix} 0 & 0 & 0 & 0 \\ 0 & 0 & -e_z & e_y \\ 0 & e_z & 0 & -e_x \\ 0 & -e_y & e_x & 0 \end{pmatrix} = \theta \mathbf{e} \cdot \boldsymbol{\Gamma}, \quad (3.30)$$

where  $\mathbf{n}$  and  $\mathbf{e}$  are the unitary vector along the center direction of the boost and the rotation axis respectively, with  $n_x^2 + n_y^2 + n_z^2 = 1$  and  $e_x^2 + e_y^2 + e_z^2 = 1$  and where the scalars  $\theta$  and  $\zeta$  represent the strength of the transformation. Coming back to the Lie group  $\text{SO}^+(1, 3)$  through its Lie algebra  $\mathfrak{so}^+(1, 3)$  according to the definition given in Eq.(3.9), we can write the matrices of a boost  $\mathbf{B}(\boldsymbol{\zeta})$ , a rotation  $\mathbf{R}(\boldsymbol{\theta})$  and a general Lorentz boost  $\boldsymbol{\Lambda}(\boldsymbol{\zeta}, \boldsymbol{\theta})$  that combines at the same time a boost and rotation, using matrix exponentials

as:

$$\mathbf{B}(\boldsymbol{\zeta}) = e^{-\boldsymbol{\zeta} \cdot \mathbf{K}} = e^{-\boldsymbol{\zeta} \mathbf{n} \cdot \mathbf{K}} = \sum_{n=0}^{\infty} (-\boldsymbol{\zeta})^n \frac{1}{n!} (\mathbf{n} \cdot \mathbf{K})^n, \quad (3.31)$$

$$\mathbf{R}(\boldsymbol{\theta}) = e^{\boldsymbol{\theta} \cdot \boldsymbol{\Gamma}} = e^{\boldsymbol{\theta} \mathbf{e} \cdot \boldsymbol{\Gamma}} = \sum_{n=0}^{\infty} (\boldsymbol{\theta})^n \frac{1}{n!} (\mathbf{e} \cdot \boldsymbol{\Gamma})^n, \quad (3.32)$$

$$\boldsymbol{\Lambda}(\boldsymbol{\zeta}, \boldsymbol{\theta}) = e^{-\boldsymbol{\zeta} \cdot \mathbf{K} + \boldsymbol{\theta} \cdot \boldsymbol{\Gamma}}. \quad (3.33)$$

Here we need to emphasize that since generally the boost  $\mathbf{B}(\boldsymbol{\zeta})$  and the rotation  $\mathbf{R}(\boldsymbol{\theta})$  do not commute,

$$\boldsymbol{\Lambda}(\boldsymbol{\zeta}, \boldsymbol{\theta}) = e^{-\boldsymbol{\zeta} \cdot \mathbf{K} + \boldsymbol{\theta} \cdot \boldsymbol{\Gamma}} \neq e^{-\boldsymbol{\zeta} \cdot \mathbf{K}} e^{\boldsymbol{\theta} \cdot \boldsymbol{\Gamma}} = \mathbf{B}(\boldsymbol{\zeta}) \mathbf{R}(\boldsymbol{\theta}). \quad (3.34)$$

However any general Lorentz boost can be decomposed into either 2 successive proper Lorentz boosts or into a single Lorentz boost followed by a rotation or a rotation followed by a boost with the appropriate parameters fixed according to a Wigner rotation [60]<sup>3</sup> as

$$\boldsymbol{\Lambda}(\boldsymbol{\zeta}_0, \boldsymbol{\theta}_0) = \mathbf{B}(\boldsymbol{\zeta}_1) \mathbf{B}(\boldsymbol{\zeta}_2) = \mathbf{R}(\boldsymbol{\alpha}) \mathbf{B}(\boldsymbol{\zeta}') = \mathbf{B}(\boldsymbol{\zeta}'') \mathbf{R}(\boldsymbol{\alpha}). \quad (3.35)$$

Another consequence of this decomposition is that 2 single boosts can always be related to each other through a rotational change of basis with:

$$\mathbf{B}(\boldsymbol{\zeta}'') = \mathbf{R}(\boldsymbol{\alpha}) \mathbf{B}(\boldsymbol{\zeta}') \mathbf{R}^{-1}(\boldsymbol{\alpha}). \quad (3.36)$$

Then, going back to the analogue group of Mueller matrices, the logarithm of a non-singular, non-depolarizing Mueller matrix  $\mathbf{m}$  can also be written according to Eq.(2.213) as

$$\mathbf{m} = -\mathbf{d} \cdot \mathbf{K} + \mathbf{b} \cdot \boldsymbol{\Gamma}, \quad (3.37)$$

where the parameter vectors  $\mathbf{b}$  and  $\mathbf{d}$ , which can be named as the birefringence vector and the dichroism vector, are defined by the following:

$$\mathbf{b} = (b_1, b_2, b_3)^T = (LB, LB', -CB)^T = \theta_B \hat{\mathbf{b}} \quad (3.38)$$

$$\mathbf{d} = (d_1, d_2, d_3)^T = (LD, LD', -CD)^T = \zeta_D \hat{\mathbf{d}} \quad (3.39)$$

with  $\hat{\mathbf{b}}$  and  $\hat{\mathbf{d}}$  being the birefringence and dichroism unitary vectors and  $\mathbf{K}$  and  $\boldsymbol{\Gamma}$  are defined in Eq.(3.23) and Eq.(3.22). Taking the notations for the Lorentz group, the non

---

<sup>3</sup>In special relativity, the successive composition of two non-collinear Lorentz boots results in a Lorentz transformation that is not a pure boost but a composition of a boost and a rotation. This rotation is called Thomas rotation, Thomas-Wigner rotation or Wigner rotation.

singular Mueller matrix describing a non-depolarizing medium can be written as

$$\mathbf{M} = \mathbf{\Lambda}(\mathbf{d}, \mathbf{b}) = e^{-\mathbf{d} \cdot \mathbf{K} + \mathbf{b} \cdot \mathbf{\Gamma}} = \exp \begin{pmatrix} 0 & -d_1 & -d_2 & -d_3 \\ -d_1 & 0 & -b_3 & b_2 \\ -d_2 & b_3 & 0 & -b_1 \\ -d_3 & -b_2 & b_1 & 0 \end{pmatrix} \quad (3.40)$$

This closes the full description of the non-singular, non-depolarizing subgroup of Mueller matrices, with a physical interpretation of the Lie algebra parameters in terms of birefringence and dichroism.

### 3.3.3 Eigenstate analysis

Within the  $\text{SO}^+(1, 3)$  description of the ensemble of Mueller matrices and the Lorentz transformation analogy, we can perform an analysis of the eigenvectors of non-singular, non-depolarizing Mueller matrices that mainly describe a non-depolarizing, bi-anisotropic medium. The eigenvectors of a Mueller matrix are of great interest: first, because they represent the eigenstates of polarization of the medium thereby characterizing it, second since the eigenstates can be presented in a polarization space i.e. Poincaré sphere, the eigenvectors leads to an easy study of the symmetry of the medium as well as to how transformation operations act on the Mueller matrix. As we show below, this gives way to constructing optical media with specifically chosen symmetries. To do so, we first deduce the relation between the eigenvector and the conformation of the matrix.

From the characteristic equation

$$\mathbf{M}\mathbf{S} = \lambda\mathbf{S}, \quad (3.41)$$

an eigenvector is a state of polarization which remain unchanged through the medium. Since we always normalize the Stokes vector and the Mueller matrix, the eigenvalue is not particularly significant but its sign must be strictly positive. To find the eigenvector of such a Mueller matrix, we can start with the exponential form of the matrix, an efficient approach considering that generally, the Mueller matrix has a complicated form from which it is difficult to extract the eigenvectors.

Starting from the matrix  $\mathbf{m}$  defined in Chapter 1, Eq. (2.215) is interesting because  $\mathbf{m}$  has a clearer form enabling to find its eigenvectors more easily. But we should first establish the relation between the eigenvector of the matrix  $\mathbf{m}$  and those of the matrix  $\mathbf{M}$ . Taking the characteristic equation of the matrix  $\mathbf{m}$

$$\mathbf{m}\mathbf{v} = \lambda\mathbf{v} \quad (3.42)$$

where  $\lambda$  and  $\mathbf{v}$  are respectively the eigenvalue and eigenvector of the matrix  $\mathbf{m}$ , we know that for an exponent of a matrix, one has

$$\mathbf{m}^n \mathbf{v} = \mathbf{m}^{n-1} \mathbf{m} \mathbf{v} = \lambda \mathbf{m}^{n-1} \mathbf{v}, \quad (3.43)$$

that is by induction:

$$\mathbf{m}^n \mathbf{v} = \lambda^n \mathbf{v}, \quad (3.44)$$

leading to define the eigenvector and eigenvalue of  $\mathbf{m}^n$  respectively as  $\mathbf{v}$  and  $\lambda^n$ . Applying the matrix  $\mathbf{M}$  on the eigenvectors of the matrix  $\mathbf{m}$  gives

$$\mathbf{M} \mathbf{v} = e^{\mathbf{m}} \mathbf{v} = \sum_{n=0}^{\infty} \frac{1}{n!} \mathbf{m}^n \mathbf{v} = \sum_{n=0}^{\infty} \frac{1}{n!} \lambda^n \mathbf{v} = e^{\lambda} \mathbf{v} \quad (3.45)$$

with  $\mathbf{v}$  the eigenvector of the matrix  $\mathbf{M}$  associated with the eigenvalue  $e^{\lambda}$ . This implies that for studying the eigenvectors of the  $\mathbf{M}$ , we can directly study the eigenvectors of the matrix  $\mathbf{m}$ .

From this point, we want to prove the existence of eigenvectors corresponding to physical realizable Stokes vectors associated with real positive eigenvalues and then study their distributions for various types of Mueller matrices within the  $SO^+(1,3)$  group. We first look at the most simple cases. If the matrix is purely birefringent, that is:

$$\mathbf{M}_{br} = \mathbf{R}(\boldsymbol{\alpha}), \quad (3.46)$$

an eigenvector is obviously along the axis of rotation for  $\mathbf{R}(\boldsymbol{\alpha})$ . We can thus find 2 normalized vectors orthogonal to each other as the eigenvector, which are physically realizable, non depolarizing Stokes vectors, namely  $\mathbf{v} = (1, \pm \boldsymbol{\alpha})^T$ .

Then for a dichroic medium represented by a boost matrix, we start with a boost along  $Ox$  direction

$$\mathbf{K}_1 = \begin{pmatrix} 0 & 1 & 0 & 0 \\ 1 & 0 & 0 & 0 \\ 0 & 0 & 0 & 0 \\ 0 & 0 & 0 & 0 \end{pmatrix}. \quad (3.47)$$

The eigenvectors of this matrix with real eigenvalues are

$$\mathbf{v} = \begin{pmatrix} 1 \\ \pm 1 \\ 0 \\ 0 \end{pmatrix}, \quad (3.48)$$

and can represent 2 non-depolarizing physical realizable Stokes vectors which are orthogonal. We can extend this particular case to a boost along any direction. This boost can be obtained by a rotation transformation of the boost along the  $Ox$  direction according to Eq.(3.36) as:

$$\mathbf{M}_{dc} = \mathbf{B}(\mathbf{u}) = \mathbf{R}(\boldsymbol{\theta})\mathbf{B}(u_x)\mathbf{R}(-\boldsymbol{\theta}). \quad (3.49)$$

We then left-multiply the rotation matrix  $\mathbf{R}(\boldsymbol{\theta})$  to the characteristic equation of  $\mathbf{B}(u_x)$

$$\mathbf{R}(\boldsymbol{\theta})\mathbf{B}(u_x)\mathbf{v} = \lambda\mathbf{R}(\boldsymbol{\theta})\mathbf{v}. \quad (3.50)$$

If we define a vector  $\mathbf{v}' = \mathbf{R}(\boldsymbol{\theta})\mathbf{v}$ , we have

$$\mathbf{R}(\boldsymbol{\theta})\mathbf{B}(u_x)\mathbf{R}(-\boldsymbol{\theta})\mathbf{v}' = \mathbf{B}(\mathbf{u})\mathbf{v}' = \lambda\mathbf{v}', \quad (3.51)$$

giving the eigenvector of  $\mathbf{B}(\mathbf{u})$  as  $\mathbf{v}'$  obtained by just a rotation of the eigenvector  $\mathbf{v}$  of  $\mathbf{B}(u_x)$ . This vector thus keeps the same degree of polarization as  $\mathbf{v}$ , therefore being a non-depolarizing Stokes vector too. Since a rotation of the vector is applied the same way to all the eigenvectors, it does not change the orthogonality between 2 Stokes eigenvectors.

For the special case where the medium presents both birefringence and dichroism, with birefringence and dichroism vectors collinear  $\hat{\mathbf{d}} = \hat{\mathbf{b}}$ , the matrices  $\mathbf{B}(\mathbf{d})$  (or  $-\mathbf{d} \cdot \mathbf{K}$ ) and  $\mathbf{R}(\mathbf{b})$  (or  $\mathbf{b} \cdot \mathbf{\Gamma}$ ) have the same set of eigenvectors. Therefore, the total matrix calculated from the infinitesimal matrix  $-\mathbf{d} \cdot \mathbf{K} + \mathbf{b} \cdot \mathbf{\Gamma}$  has the same set of eigenvectors as both  $\mathbf{B}(\mathbf{d})$  and  $\mathbf{R}(\mathbf{b})$  which are also orthogonal and non-depolarizing.

Finally, we can extend this to the general case of a bi-anisotropic Mueller matrix with both birefringence and dichroism vectors  $\mathbf{b}$  and  $\mathbf{d}$  not necessarily collinear. In this case, the Mueller matrix can be represented as a general Lorentz boost involving both rotation and a boost noted as  $\mathbf{M}_{bd} = \mathbf{\Lambda}(\mathbf{u}, \boldsymbol{\theta})$ . This matrix can always be decomposed into a product between a rotation matrix and a boost matrix with appropriate parameters

$$\mathbf{\Lambda}(\mathbf{u}, \boldsymbol{\theta}) = \mathbf{R}(\boldsymbol{\theta}')\mathbf{B}(\mathbf{u}'). \quad (3.52)$$

Starting again from the characteristic equation of a boost matrix  $\mathbf{B}(\mathbf{u})$

$$\mathbf{B}(\mathbf{w})\mathbf{v} = \lambda\mathbf{v}, \quad (3.53)$$

we can left-multiply the equation by a boost matrix  $\mathbf{B}(\mathbf{w}')$

$$\mathbf{B}(\mathbf{w}')\mathbf{B}(\mathbf{w})\mathbf{v} = \lambda\mathbf{B}(\mathbf{w}')\mathbf{v}, \quad (3.54)$$

and define in the same way  $\mathbf{v}' = \mathbf{B}(\mathbf{w}')\mathbf{v}$ , thereby yielding

$$\mathbf{B}(\mathbf{w}')\mathbf{B}(\mathbf{w})\mathbf{B}(-\mathbf{w}')\mathbf{v}' = \lambda\mathbf{v}'. \quad (3.55)$$

Because two successive single Lorentz transformations are not equivalent to a single Lorentz transformation with the relativistic sum of the velocities of the two successive transformations but rather to a rotation followed by a Lorentz boost (or a Lorentz boost followed by a rotation) with appropriate parameters determined by Wigner rotation [60], the product of 2 boost matrices can be always decomposed by a rotation and a boost (as Eq.(3.35)), such that

$$\mathbf{R}(\boldsymbol{\alpha}')\mathbf{B}(\mathbf{w}'')\mathbf{B}(-\mathbf{w}')\mathbf{v}' = \mathbf{R}(\boldsymbol{\alpha}')\mathbf{R}(\boldsymbol{\alpha}'')\mathbf{B}(\mathbf{w}''')\mathbf{v}' = \lambda\mathbf{v}'. \quad (3.56)$$

If we assign  $\mathbf{R}(\boldsymbol{\alpha}')\mathbf{R}(\boldsymbol{\alpha}'') = \mathbf{R}(\boldsymbol{\theta}')$  and  $\mathbf{B}(\mathbf{w}''') = \mathbf{B}(\mathbf{u}')$ , we then obtain

$$\mathbf{R}(\boldsymbol{\theta}')\mathbf{B}(\mathbf{u}')\mathbf{v}' = \boldsymbol{\Lambda}(\mathbf{u}, \boldsymbol{\theta})\mathbf{v}' = \lambda\mathbf{v}', \quad (3.57)$$

implying that the eigenvector  $\mathbf{v}' = \mathbf{B}(\mathbf{w}')\mathbf{v}$  of a general Lorentz boost that represents a general bi-anisotropic medium is obtained by a Lorentz boost transformation on the eigenvector of a boost matrix. We know that a pure Lorentz boost transformation preserves the degree of polarization. Therefore, a general bi-anisotropic medium will also have 2 non-depolarizing Stokes eigenvectors. However, unlike the case of a rotation transformation, the 2 Stokes eigenvectors obtained from a Lorentz transformation do not always preserve the orthogonality, implying therefore that the 2 eigenstates of polarization are not strictly orthogonal. An example will be given in Chapter 5 with the Mueller matrix measured for chiral tubular J-aggregates.

To summarize, the Mueller Jones matrix of a bi-anisotropic medium always has 2 non depolarizing Stokes eigenvectors with positive eigenvalues. These 2 eigenvectors of the Mueller matrix thus represent the eigenstates of the medium and characterize its anisotropy. For instance, a purely birefringent or purely dichroic medium always has 2 orthogonal states of polarization, defined along the birefringence vector and dichroism vector according to Eq.(3.38) and Eq.(3.39), namely  $S_{br} = (1, \pm\hat{\mathbf{b}})^T$  for birefringence and  $S_{dc} = (1, \pm\hat{\mathbf{d}})^T$  for dichroism. A special case is when the medium is both birefringent and dichroic at the same time. If the vectors  $\hat{\mathbf{b}}$  and  $\hat{\mathbf{d}}$  are collinear, the 2 eigenstates of polarization are also orthogonal. But if in the general case vectors  $\hat{\mathbf{b}}$  and  $\hat{\mathbf{d}}$  are not collinear, the 2 eigenstates are not orthogonal. This discussion will be helpful when studying the symmetry of Mueller matrices.



### 3.3.4 Product decomposition and differential decomposition

Another aspect of the analogy based on the Lorentz group is related to the product decomposition of a non-singular, non-depolarizing Mueller matrix. Such a decomposition can be compared with the decomposition of a Lorentz transformation. As we mentioned in the previous section, using Wigner rotations and the connectivity of the  $SO^+(1, 3)$  group, any matrix of a general Lorentz boost  $\Lambda(\mathbf{u}, \boldsymbol{\theta})$  can be decomposed in 3 ways as:

$$\Lambda(\mathbf{u}, \boldsymbol{\theta}) = \mathbf{B}(\mathbf{v}_1)\mathbf{B}(\mathbf{v}_2) = \mathbf{B}(\mathbf{v}')\mathbf{R}(\boldsymbol{\alpha}) = \mathbf{R}(\boldsymbol{\alpha})\mathbf{B}(\mathbf{v}''). \quad (3.58)$$

The parameters can be analytically inverted from the decomposed matrix elements according to the relations of Wigner rotation [60]. For the case of a non-singular, non-depolarizing Mueller matrix, we can also use these relations to perform our product decomposition. A normalized Mueller matrix with both birefringence and dichroism  $\Lambda(\mathbf{d}, \mathbf{b})$  defined in Eq.(3.40), can be written into a block matrix form as

$$\mathbf{M} = \Lambda(\mathbf{d}, \mathbf{b}) = \begin{pmatrix} 1 & -\mathbf{a}^T \\ -\mathbf{c} & \mathbf{m}_3 \end{pmatrix}, \quad (3.59)$$

with  $\mathbf{a}$  and  $\mathbf{c}$  3-dimensional vectors and  $\mathbf{m}_3$  a  $3 \times 3$  square matrix. This matrix can be decomposed similarly into the product of a birefringent matrix  $\mathbf{M}_R$  and a dichroic matrix  $\mathbf{M}_D$  as

$$\mathbf{M} = \mathbf{M}_{R1}\mathbf{M}_{D1} \quad (3.60)$$

or

$$\mathbf{M} = \mathbf{M}_{D2}\mathbf{M}_{R2}. \quad (3.61)$$

The case of the product of 2 dichroic media represented by Lorentz boosts is less interesting for Mueller matrix decomposition analysis and it is actually not easy to calculate the parameters of the 2 boosts by knowing only the final matrix. We will therefore leave aside the relatively poor configuration of 2 dichroic layer stacking. For the 2 cases discussed above, according to the principle of Wigner rotation [60],  $\mathbf{M}_{D1}$  and  $\mathbf{M}_{D2}$  matrix can be uniquely determined from the block matrix elements as

$$\mathbf{M}_{D1} = \exp [-(\tanh^{-1} \mathbf{a}) \cdot \mathbf{K}] \quad (3.62)$$

$$\mathbf{M}_{D2} = \exp [-(\tanh^{-1} \mathbf{c}) \cdot \mathbf{K}]. \quad (3.63)$$

Once we get the  $\mathbf{M}_D$  matrix, the matrix associated with the birefringent part can be easily calculated by simply inverting  $\mathbf{M}_D$  on the matrix to be decomposed. This decomposition method gives the same result as the product decomposition introduced in previous chapter. However, it is important to note that from the product decomposition, the dichroism

estimated from either  $\tanh^{-1} \mathbf{a}$  or  $\tanh^{-1} \mathbf{c}$  is not necessarily the same as the dichroism defined by the  $\mathbf{d}$  vector from the exponential decomposition. Therefore, in order to get the best estimate of polarimetric properties, it is clear that the method of decomposition should be carefully chosen according to the actual sample. The exponential decomposition gives a more accurate estimation for globally homogeneous bulky type samples while the product decomposition is well adapted to layered samples with each layer characterized by a specific polarimetric response (birefringence or dichroism), as we mentioned in the previous chapter.

## 3.4 Lie Monoid for all non-singular Mueller matrices

Once characterized the first subgroup of all non-singular non-depolarizing matrices, we will expand the description towards the whole ensemble of Mueller matrix. So the next hierarchy of the group-like algebraic structure will now include all non-singular Mueller matrices including depolarizing Mueller matrices. In this section, we will start from one source of depolarization: spatial inhomogeneities. This will allow us to study the symmetry property of the depolarizing part of a Mueller matrix using the Lie algebra. Then, we will present the basis set of the depolarizing part of the Mueller matrix together with the parameters associated with each basis. This will eventually yield a complete interpretation of all matrix elements derived from the exponential decomposition.

### 3.4.1 Non-singular depolarizing Mueller matrices

In order to deduce the Mueller matrix signatures of depolarization, we first model the origin of depolarization as stemming from spatial inhomogeneities. Let us start with a probing light beam of finite cross-section taken smaller than the typical dimension of the sample's inhomogeneities. In this situation, the probing area within the beam cross-section can be considered as homogeneous, and thus can be described using a succession of non-depolarizing Mueller matrices as shown in Fig.3.2(a). In this picture, the total Mueller matrix can be written as the product of the corresponding sequence of "elementary" non-depolarizing Mueller matrices  $\mathbf{M}_{nd}^{(i)}$  as

$$\mathbf{M} = \prod_{i=1}^N \mathbf{M}_{nd}^{(i)}. \quad (3.64)$$

As we discussed above, non-singular non-depolarizing Mueller matrices form a Lie group, so that the product of such matrices will also lie in this non-depolarizing group. So basically, a small enough diameter probing beam can not see any effect of depolarization with a resulting Mueller matrix that remains non-depolarizing.

In contrast, when the beam cross-section increases, the medium can be no longer considered as homogeneous, a situation illustrated in Fig.3.2.(b) where each sub-layer of  $\Delta z$  can not even be considered as a homogeneous non-depolarizing medium. Therefore, the total effective Mueller matrix is the product of a sequence of "elementary" depolarizing Mueller matrices  $\mathbf{M}_d^{(i)}$  that writes as:

$$\mathbf{M} = \prod_{i=1}^N \mathbf{M}_d^{(i)}. \quad (3.65)$$

There, the question is how to express this depolarizing Mueller matrix and see whether the product of such Mueller matrices forms a closed structure. In order to answer this question, we start by looking at the depolarizing Mueller matrix of a thin layer of thickness  $\Delta z$  noted  $\mathbf{M}_d^{(i)}$ . Through this layer, we can divide the incident beam described by  $\mathbf{S}_{in}$  along its cross section into  $N$  identical small portion  $\mathbf{S}_{in}^{(i)}$  so that for each sub-beam, the medium can be considered as homogeneous and hence described by a non-depolarizing Mueller matrix  $\mathbf{M}_{nd,q}$ . The beam polarization  $\mathbf{S}_{out}$  transmitted through these  $N$  layer portions can be calculated as

$$\mathbf{S}_{out}^{(i)} = \sum_{q=1}^N \mathbf{S}_{out,q}^{(i)} = \sum_{q=1}^N \mathbf{M}_{nd,q}^{(i)} \mathbf{S}_{in,q}^{(i)} = \left( \frac{1}{N} \sum_{q=1}^N \mathbf{M}_{nd,q}^{(i)} \right) \mathbf{S}_{in}^{(i)}, \quad (3.66)$$

leading to model the depolarizing Mueller matrix  $\mathbf{M}_d^{(i)}$  of a thin layer of inhomogeneous medium along the probing beam cross section in following way:

$$\mathbf{M}_d^{(i)} = \frac{1}{N} \sum_{q=1}^N \mathbf{M}_{nd,q}^{(i)}, \quad (3.67)$$

schematized in Fig.3.2(c).

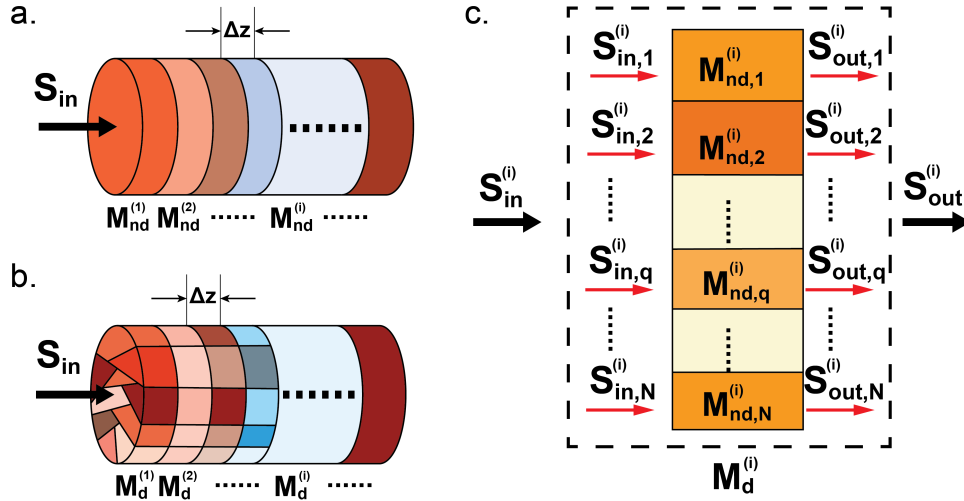


FIGURE 3.2: (a) shows the situation of a small probe beam diameter, where the inhomogeneity developed along the optical axis of the medium can be divided into a sequence of non-depolarizing sub-media with a thickness of  $\Delta z$ . Therefore, the resulting Mueller matrix will be a product of non-depolarizing Mueller matrices. (b) shows the situation of a larger beam diameter where the inhomogeneity develops also transversely. Therefore, each divided segment of thickness  $\Delta z$  can no longer be considered as non-depolarizing. (c) shows the modeling for the inhomogeneity along the cross section of a light beam illuminating an inhomogeneous medium. The incident beam can be separated into many small portions interacting with a small part of the sample's cross section which can be considered as homogeneous and thus non-depolarizing.

In order to compute the general expression of a depolarizing Mueller matrix where depolarization stems from spatial inhomogeneities, we simplify our notation to one thin layer of thickness  $\Delta z$ . The expression for the depolarizing Mueller matrix  $\mathbf{M}_d$  becomes

$$\mathbf{M}_d = \frac{1}{N} \sum_{q=1}^N \mathbf{M}_q = \frac{1}{N} \sum_{q=1}^N \exp(\mathbf{m}_q) \quad (3.68)$$

with

$$\mathbf{m}_q = -\mathbf{d}_q \cdot \mathbf{K} + \mathbf{b}_q \cdot \mathbf{\Gamma} \quad (3.69)$$

for the non-depolarizing elementary term, as determined in the previous section. The matrix  $\mathbf{m}_q$  within the light beam cross section can always be written as a sum of the averaged non-depolarizing matrix  $\mathbf{m}_{nd}$  and a residual part  $\Delta\mathbf{m}_q$

$$\exp(\mathbf{m}_q) = \exp(\mathbf{m}_{nd} + \Delta\mathbf{m}_q), \quad (3.70)$$

with

$$\mathbf{m}_{nd} = \langle \mathbf{m}_q \rangle \text{ and } \langle \Delta\mathbf{m}_q \rangle = \mathbf{0} \quad (3.71)$$

where  $\langle \cdot \rangle = \frac{1}{N} \sum \cdot$  corresponds to an ensemble average over  $q$ . According to the Lie product formula, also known as the Lie-Trotter-Kato formula between 2 linear operators  $A$  and  $B$  that do not necessarily commute, the relation

$$\exp(A + B) = \lim_{n \rightarrow \infty} \left[ \exp\left(\frac{A}{n}\right) \exp\left(\frac{B}{n}\right) \right]^n \quad (3.72)$$

can be extended to infinitesimal operators with

$$\exp[t(A + B)] = \exp(tA) \exp(tB) + O(t^2) \quad (3.73)$$

where  $O(t^2)$  converges to 0 very fast with  $t^2$ . Then according to Eq.(2.214), the  $\mathbf{m}_q$  matrix can also be written as a single scalar parameter corresponding to the thickness times the matrix  $\mathbf{N}_{M,q}$  per unit length. With the parameter  $z$  in Eq.(2.214) a thickness  $\Delta z$  of the depolarizing medium, Eq.(3.70) can be decomposed as

$$\exp(\mathbf{m}_{nd} + \Delta \mathbf{m}_q) = \exp[\Delta z(\mathbf{N}_{M,nd} + \Delta \mathbf{N}_{M,q})] = \exp(\Delta z \mathbf{N}_{M,nd}) \exp(\Delta z \Delta \mathbf{N}_{M,q}) + O(\Delta z^2). \quad (3.74)$$

By substituting in to Eq.(3.68), one gets

$$\mathbf{M}_d = \frac{1}{N} \sum_{q=1}^N \left[ \exp(\Delta z \mathbf{N}_{M,nd}) \exp(\Delta z \Delta \mathbf{N}_{M,q}) + O(\Delta z^2) \right]. \quad (3.75)$$

Since  $\Delta z$  is generally small, we perform a Taylor expansion of the matrix exponential on the second term  $\exp(\Delta z \Delta \mathbf{N}_{M,q})$  that leads to

$$\mathbf{M}_d = \frac{1}{N} \sum_{q=1}^N \left[ \exp(\Delta z \mathbf{N}_{M,nd}) \left( \mathbf{I} + \Delta z \Delta \mathbf{N}_{M,q} + \frac{1}{2} \Delta z^2 \Delta \mathbf{N}_{M,q}^2 \right) + O(\Delta z^2) \right]. \quad (3.76)$$

Then by applying the conditions in Eq.(3.71) and defining the ensemble average over  $q$ , we have

$$\begin{aligned} \mathbf{M}_d &= \exp(\Delta z \mathbf{N}_{M,nd}) \left( \mathbf{I} + \Delta z \langle \Delta \mathbf{N}_{M,q} \rangle + \frac{1}{2} \Delta z^2 \langle \Delta \mathbf{N}_{M,q}^2 \rangle \right) + O(\Delta z^2) \\ &= \exp(\Delta z \mathbf{N}_{M,nd}) \left( \mathbf{I} + \mathbf{0} + \frac{1}{2} \Delta z^2 \langle \Delta \mathbf{N}_{M,q}^2 \rangle \right) + O(\Delta z^2) \\ &= \exp(\Delta z \mathbf{N}_{M,nd}) \exp\left(\frac{1}{2} \Delta z^2 \langle \Delta \mathbf{N}_{M,q}^2 \rangle\right) + O(\Delta z^2). \end{aligned} \quad (3.77)$$

By using again the Lie-Trotter-Kato product formula, the final depolarizing Mueller matrix is expressed as:

$$\mathbf{M}_d = \exp \left( \Delta z \mathbf{N}_{M,nd} + \frac{1}{2} \Delta z^2 \langle \Delta \mathbf{N}_{M,q}^2 \rangle \right) = \exp(\mathbf{m}_{nd} + \mathbf{m}_d) \quad (3.78)$$

where  $\mathbf{m}_{nd}$  is the non-depolarizing part which can be related to the by  $\text{SO}^+(1,3)$  group and  $\mathbf{m}_d$  is the depolarizing part which can be calculated as

$$\mathbf{m}_d = \frac{1}{2} \Delta z^2 \langle \Delta \mathbf{N}_{M,q}^2 \rangle = \frac{1}{2} \langle \Delta \mathbf{m}_q^2 \rangle. \quad (3.79)$$

Once we know how to calculate  $\mathbf{m}_d$ , we can explore the explicit expression of the depolarizing part of the differential matrix, an important expression for discussing the algebraic structure.

First of all,  $\Delta \mathbf{m}_q$  can be written according to the  $\text{SO}^+(1,3)$  Lie algebra as:

$$\Delta \mathbf{m}_q = -\Delta \mathbf{d}_q \cdot \mathbf{K} + \Delta \mathbf{b}_q \cdot \mathbf{\Gamma} = \sum_{i=1}^3 -\Delta d_{qi} \mathbf{K}_i + \Delta b_{qi} \mathbf{\Gamma}_i, \quad (3.80)$$

so that the square of this matrix can be expressed by the anti-commutators of the generators  $\mathbf{K}, \mathbf{\Gamma}$  as

$$\begin{aligned} \Delta \mathbf{m}_q^2 &= \left( \sum_{i=1}^3 -\Delta d_{qi} \mathbf{K}_i + \Delta b_{qi} \mathbf{\Gamma}_i \right)^2 \\ &= \sum_{i=1}^3 \Delta d_i^2 \mathbf{K}_i^2 + \sum_{i=1}^3 \Delta b_i^2 \mathbf{\Gamma}_i^2 + \frac{1}{2} \sum_{i \neq j} \left( \Delta d_i \Delta d_j \{ \mathbf{K}_i, \mathbf{K}_j \} + \Delta b_i \Delta b_j \{ \mathbf{\Gamma}_i, \mathbf{\Gamma}_j \} \right) \\ &\quad - \sum_{i=1}^3 \sum_{j=1}^3 \Delta d_i \Delta b_j \{ \mathbf{K}_i, \mathbf{\Gamma}_j \}, \end{aligned} \quad (3.81)$$

It is from this expression that we generate the new basis matrices out of the generators of  $\text{SO}^+(1,3)$ . In order to calculate this expression, one needs only the anti-commutators between  $\mathbf{K}$  and  $\mathbf{\Gamma}$  which generate a new set of basis as listed here:

$$\{ \mathbf{\Gamma}_i, \mathbf{\Gamma}_j \} = \varepsilon_{ijk}^2 \mathbf{\Omega}_k + 2\delta_{ij} \mathbf{\Delta}_i \quad (3.82)$$

$$\{ \mathbf{K}_i, \mathbf{K}_j \} = \varepsilon_{ijk}^2 \mathbf{\Omega}_k + 2\delta_{ij} (\mathbf{I} + \mathbf{\Delta}_i) \quad (3.83)$$

$$\{ \mathbf{\Gamma}_i, \mathbf{K}_j \} = \varepsilon_{ijk}^2 \mathbf{Q}_k = -\{ \mathbf{K}_i, \mathbf{\Gamma}_j \} \quad (3.84)$$

with 3 new basis sets defined explicitly as:

$$\mathbf{\Omega}_1 = \begin{pmatrix} 0 & 0 & 0 & 0 \\ 0 & 0 & 0 & 0 \\ 0 & 0 & 0 & 1 \\ 0 & 0 & 1 & 0 \end{pmatrix}, \mathbf{\Omega}_2 = \begin{pmatrix} 0 & 0 & 0 & 0 \\ 0 & 0 & 0 & 1 \\ 0 & 0 & 0 & 0 \\ 0 & 1 & 0 & 0 \end{pmatrix}, \mathbf{\Omega}_3 = \begin{pmatrix} 0 & 0 & 0 & 0 \\ 0 & 0 & 1 & 0 \\ 0 & 1 & 0 & 0 \\ 0 & 0 & 0 & 0 \end{pmatrix} \quad (3.85)$$

$$\mathbf{Q}_1 = \begin{pmatrix} 0 & 1 & 0 & 0 \\ -1 & 0 & 0 & 0 \\ 0 & 0 & 0 & 0 \\ 0 & 0 & 0 & 0 \end{pmatrix}, \mathbf{Q}_2 = \begin{pmatrix} 0 & 0 & -1 & 0 \\ 0 & 0 & 0 & 0 \\ 1 & 0 & 0 & 0 \\ 0 & 0 & 0 & 0 \end{pmatrix}, \mathbf{Q}_3 = \begin{pmatrix} 0 & 0 & 0 & 1 \\ 0 & 0 & 0 & 0 \\ 0 & 0 & 0 & 0 \\ -1 & 0 & 0 & 0 \end{pmatrix} \quad (3.86)$$

$$\mathbf{\Delta}_1 = \mathbf{diag}(0, 0, -1, -1), \mathbf{\Delta}_2 = \mathbf{diag}(0, -1, 0, -1), \mathbf{\Delta}_3 = \mathbf{diag}(0, -1, -1, 0). \quad (3.87)$$

Together with the identity matrix  $\mathbf{I}$ , the depolarizing differential matrix is therefore generated by 10 generators. By taking the average of Eq.(3.81), the depolarizing differential Mueller matrix can be written in a scalar product form as

$$\mathbf{m}_d = \frac{1}{2} \langle \Delta \mathbf{m}_q^2 \rangle = -\mathbf{q} \cdot \mathbf{Q} + \boldsymbol{\eta} \cdot \boldsymbol{\Omega} + \mu_0 \mathbf{I} + \boldsymbol{\mu} \cdot \boldsymbol{\Delta} \quad (3.88)$$

with the parameter vectors for each basis expressed explicitly as

$$\mathbf{q} = \begin{pmatrix} q_1 \\ q_2 \\ q_3 \end{pmatrix} = \frac{1}{2} \begin{pmatrix} \langle \Delta d_2 \Delta b_3 \rangle - \langle \Delta d_3 \Delta b_2 \rangle \\ \langle \Delta d_1 \Delta b_3 \rangle - \langle \Delta d_3 \Delta b_1 \rangle \\ \langle \Delta d_1 \Delta b_2 \rangle - \langle \Delta d_2 \Delta b_1 \rangle \end{pmatrix}, \quad (3.89)$$

$$\boldsymbol{\eta} = \begin{pmatrix} \eta_1 \\ \eta_2 \\ \eta_3 \end{pmatrix} = \frac{1}{2} \begin{pmatrix} \langle \Delta d_2 \Delta d_3 \rangle + \langle \Delta b_2 \Delta b_3 \rangle \\ \langle \Delta d_1 \Delta d_3 \rangle + \langle \Delta b_1 \Delta b_3 \rangle \\ \langle \Delta d_1 \Delta d_2 \rangle + \langle \Delta b_1 \Delta b_2 \rangle \end{pmatrix}, \quad (3.90)$$

$$\boldsymbol{\mu} = \begin{pmatrix} \mu_1 \\ \mu_2 \\ \mu_3 \end{pmatrix} = \frac{1}{2} \begin{pmatrix} \langle \Delta b_1^2 \rangle + \langle \Delta d_1^2 \rangle \\ \langle \Delta b_2^2 \rangle + \langle \Delta d_2^2 \rangle \\ \langle \Delta b_3^2 \rangle + \langle \Delta d_3^2 \rangle \end{pmatrix}, \quad (3.91)$$

$$\mu_0 = \frac{1}{2} \left( \langle \Delta d_1^2 \rangle + \langle \Delta d_2^2 \rangle + \langle \Delta d_3^2 \rangle \right) \quad (3.92)$$

This leads to the explicit expression of the depolarizing part of the logarithm of a general non-singular Mueller matrix  $\mathbf{M}_d$  that writes as:

$$\mathbf{m}_d = \ln(\mathbf{M}_d) - \mathbf{m}_{nd} = \frac{1}{2} \times \begin{pmatrix} \langle \Delta d_1^2 + \Delta d_2^2 + \Delta d_3^2 \rangle & -\langle \Delta d_2 \Delta b_3 - \Delta d_3 \Delta b_2 \rangle & \langle \Delta d_1 \Delta b_3 - \Delta d_3 \Delta b_1 \rangle & -\langle \Delta d_1 \Delta b_2 - \Delta d_2 \Delta b_1 \rangle \\ \langle \Delta d_2 \Delta b_3 - \Delta d_3 \Delta b_2 \rangle & \langle \Delta d_1^2 - \Delta b_2^2 - \Delta b_3^2 \rangle & \langle \Delta d_1 \Delta d_2 + \Delta b_1 \Delta b_2 \rangle & \langle \Delta d_1 \Delta d_3 + \Delta b_1 \Delta b_3 \rangle \\ -\langle \Delta d_1 \Delta b_3 - \Delta d_3 \Delta b_1 \rangle & \langle \Delta d_1 \Delta d_2 + \Delta b_1 \Delta b_2 \rangle & \langle -\Delta b_1^2 + \Delta d_2^2 - \Delta b_3^2 \rangle & \langle \Delta d_2 \Delta d_3 + \Delta b_2 \Delta b_3 \rangle \\ \langle \Delta d_1 \Delta b_2 - \Delta d_2 \Delta b_1 \rangle & \langle \Delta d_1 \Delta d_3 + \Delta b_1 \Delta b_3 \rangle & \langle \Delta d_2 \Delta d_3 + \Delta b_2 \Delta b_3 \rangle & \langle -\Delta b_1^2 - \Delta b_2^2 + \Delta d_3^2 \rangle \end{pmatrix} \quad (3.93)$$

revealing the meaning of each element. Our approach turns out to give similar conclusion than those presented in [61, 62] although with different methods. Basically, this depolarizing matrix  $\mathbf{m}_d$  is a matrix of variance and covariance among the non-depolarizing polarimetric properties (birefringence and dichroism). This expression is also general in the sense that it can describe the impact of inhomogeneity stemming from either stochasticity of a disordered system or a deterministic arrangement in space. Because the demonstration of this expression imposes that the medium must be considered as uniform along the light propagation within a thickness of  $\Delta z$ , this interpretation for the matrix elements is valid in the case of thin enough samples, homogeneous along the optical path. If strong inhomogeneities along the light propagation direction are found, the total matrix then results from the cumulative product of a sequence of such "elementary" depolarizing Mueller matrix as in Eq.(3.65) which gives no-longer the same interpretation as Eq.(3.93) according to the Baker-Campbell-Hausdorff formula.

### 3.4.2 Algebraic structure for all non-singular Mueller matrices

In this section, we are going to look at the properties of the ensemble of all non-singular Mueller matrices including depolarizing and non-depolarizing parts. Starting from the  $\text{SO}^+(1,3)$  group that includes all non-singular, non-depolarizing Mueller matrices, we will include all non-singular but depolarizing Mueller matrices. With the help of the analysis given in the previous section, we already have the generators associated with the depolarizing part of the logarithm of a non-singular Mueller matrix, as written in Eq.(3.88). To verify first if the basis matrices in Eq.(3.85), (3.86) and (3.87) together with the identity matrix give already the generators of a Lie algebra, it is enough to check the closure with respect to commutation. One can easily show that the commutator within this basis set is not closed, for instance the commutator between  $\mathbf{\Omega}$  and  $\mathbf{Q}$  gives  $\mathbf{K}$  and  $\mathbf{\Gamma}$ . This implies that the basis sets of vectors  $\{\mathbf{Q}, \mathbf{\Omega}, \mathbf{\Delta}, \mathbf{I}\}$  can not form a Lie algebra and that, therefore, the pure non-singular depolarizing Mueller matrix can not give a well defined group-like algebraic structure. But since some of their commutation



relations map to the basis set of  $\{\mathbf{K}, \mathbf{\Gamma}\}$ , it is possible to expand the basis set associated with all non-singular Mueller matrix including both depolarizing and non-depolarizing. One can verify indeed that the generator set  $\{\mathbf{K}, \mathbf{\Gamma}, \mathbf{Q}, \mathbf{\Omega}, \mathbf{\Delta}, \mathbf{I}\}$  associated with a total of 16 basis matrices is closed with respect to the commutation. Hence, this means that any non-singular Mueller matrix can be decomposed into this set of 16 basis matrices and that the non-singular Mueller matrix ensemble is closed under the matrix product, one of the condition needed to form a group-like algebraic structure for a matrix ensemble.

We then need to determine which kind of algebraic structure this new ensemble forms. Because we included the non-depolarizing Mueller matrices that form a  $\text{SO}^+(1, 3)$  group, the identity matrix belongs to our new ensemble. Therefore, this ensemble forms at least a monoid of a Lie type (rather than a semigroup according to the definition). Finally, in order to see if it forms a group, we should check whether the inversion of each matrix also belongs to this ensemble. Since we already know that the non-depolarizing Mueller matrices form a Lie group included in this ensemble, all the non-depolarizing Mueller matrices have an inverted matrix belonging to this ensemble. We now need to check whether the inversion of a pure depolarizing matrix can also be included in this ensemble, meaning that the inversion of the depolarizing Mueller matrix is also physically realizable. This would imply that the whole ensemble can be considered as a group. If not, it forms only a monoid. In order to study the physical realizability of the inverted matrix, we can start with the symmetry of the pure depolarizing matrix. According to the results shown in Eq.(3.93), the depolarizing matrix can be written using the elements of the parameter vectors as

$$\mathbf{m}_d = \begin{pmatrix} \mu_0 & -q_1 & q_2 & -q_3 \\ q_1 & \mu_0 - \mu_2 - \mu_3 & \eta_3 & \eta_2 \\ -q_2 & \eta_3 & \mu_0 - \mu_1 - \mu_3 & \eta_1 \\ q_3 & \eta_2 & \eta_1 & \mu_0 - \mu_1 - \mu_2 \end{pmatrix}. \quad (3.94)$$

A matrix written in this form has a G-symmetry in the framework of the Minkowski space which is expressed as

$$\mathbf{G}\mathbf{m}_d^T\mathbf{G} = \mathbf{m}_d. \quad (3.95)$$

Thus, a pure depolarizing Mueller matrix written as

$$\mathbf{M}_{pd} = \exp(\mathbf{m}_d) \quad (3.96)$$

possesses the same symmetry through the property of the matrix exponential

$$\mathbf{G}\mathbf{M}_{pd}^T\mathbf{G} = \mathbf{M}_{pd}. \quad (3.97)$$

We then rewrite for a G-symmetric matrix the necessary and sufficient condition for

Stokes realizability cited in the first section [38, 59]. For a G-symmetric Mueller matrix, the necessary and sufficient condition for it to be Stokes' realizable is that there exist a Lorentz transformation  $\Lambda \in \mathcal{L}_+^\uparrow$  such that the Mueller matrix can be written as

$$\mathbf{M}_{pd}^2 = \Lambda \cdot \text{diag}(D_0, D_1, D_2, D_3) \cdot \Lambda^{-1}, \quad (3.98)$$

with  $D_0 \geq D_i > 0$  [38]. This condition is more direct for the  $\mathbf{m}_d$  matrix with

$$\mathbf{m}_d = \frac{1}{2} \Lambda \cdot \text{diag}(D'_0, D'_1, D'_2, D'_3) \cdot \Lambda^{-1}, \quad (3.99)$$

where  $D'_i = \ln D_i$  and  $D'_0 \geq D'_i \in \mathbb{R}$ . If we therefore take the inversion of  $\mathbf{M}_{pd}$ , the corresponding differential matrix is  $-\mathbf{m}_p$ . We immediately see that a matrix written as  $\exp(-\mathbf{m}_p)$  will be no longer a physical realizable Mueller matrix because the condition for  $-D'_0$  to be the maximum is violated. Even if we switch the order of diagonal elements to make the correct form for the diagonal matrix, we will also switch the lines and columns of the  $\Lambda$  matrix which is no longer corresponds to a Lorentz transformation in  $\mathcal{L}_+^\uparrow$ . In all case, the inversion of  $\mathbf{M}_{pd}$  can not be a physical realizable matrix. The inversion of a depolarizing Mueller matrix is therefore not included in the ensemble, and the closure under the matrix inversion can not be ensured to all elements in the ensemble of all non-singular Mueller matrix. This makes this ensemble to be a monoid of a Lie type (known as a Lie monoid).

The Lie algebra of this monoid is the combination of the  $\mathfrak{so}^+(1, 3)$  algebra with the 10 other generators  $\{\mathbf{Q}, \mathbf{\Omega}, \mathbf{\Delta}, \mathbf{I}\}$  defined above. The general non-singular Mueller matrix  $\mathbf{M}_{ns}$  can be thus written like

$$\mathbf{M}_{ns} = \exp(\mathbf{m}) = \exp(-\mathbf{d} \cdot \mathbf{K} + \mathbf{b} \cdot \mathbf{\Gamma} - \mathbf{q} \cdot \mathbf{Q} + \boldsymbol{\eta} \cdot \mathbf{\Omega} + \mu_0 \mathbf{I} + \boldsymbol{\mu} \cdot \mathbf{\Delta}), \quad (3.100)$$

with constraints on the real parameter vectors  $\mathbf{q}$ ,  $\boldsymbol{\eta}$  and  $\boldsymbol{\mu}$  and no constraint on  $\mathbf{d}$ ,  $\mathbf{b}$  and  $\mu_0$  to be physically realizable. Here we note that the reason why  $\mu_0$  is generally not constrained comes from the fact that we normalize the final Mueller matrix to  $m_{00}$ .

Note that the basis set can also be represented in the complex plane  $\mathbb{C}$  in such a way that the 15 basis set rearranged as  $\{\mathbf{K}, i\mathbf{\Gamma}, i\mathbf{Q}, \mathbf{\Omega}, \mathbf{\Delta}'\}$  with  $\mathbf{\Delta}'$  defined as

$$\mathbf{\Delta}'_k = \mathbf{I} + \sum_{i=1}^3 \varepsilon_{ik}^2 \mathbf{\Delta}_i, \quad (3.101)$$

form one Lie algebra of the SU(4) group of the Hermitian type. Therefore, the ensemble for the non-singular Mueller matrices can be considered as a sub-monoid of the SU(4) group.

### 3.4.3 constraints for constructing physically realizable non-singular Mueller matrices

We have discussed in section 3.1 the conditions for the physical realizability introduced by Cloude [37, 39]. However, physical realizability can also be discussed from a different view point. As well discussed by R. Sridhar *et.al.* [38], the aforementioned Stokes' realizability only maintains the endomorphism of Stokes vector space by the Mueller matrix application. In this sense, it can be referred as a weak realizability. The Cloude's realizability, i.e. the physical realizability criterion that we discussed in the previous chapter, imposes that any Mueller matrix results from a non-coherent sum of non-depolarizing media. Thus, all non-depolarizing Mueller matrices are Cloude's realizable. This sets a relation between these two types of realizability with Cloude's realizability implying Stokes' realizability. But if we consider the most general situation described by a Mueller matrix, Stokes' realizability remains necessary while Cloude's realizability can be sometimes violated. This is the case in reflection and emission measurement configurations for example, where the Mueller matrix of a mirror written as  $\mathbf{diag}(1, 1, -1, -1)$  is not Cloude's realizable but Stokes' realizable.

At the same time, a non-singular Mueller matrix can be analyzed by its local Mueller matrix along an optical path  $\Delta z$  as

$$\mathbf{M}_{\Delta z} = \exp(\Delta z \mathbf{N}_M), \quad (3.102)$$

from which the global Mueller matrix is defined as

$$\mathbf{M} = \exp(z \mathbf{N}_M) = \exp(\mathbf{m}). \quad (3.103)$$

The realizability for this local matrix  $\mathbf{M}_{\Delta z}$  is stronger than that of the global Mueller matrix  $\mathbf{M}$ . This reads :Cloude's (or Stokes') local realizability  $\Rightarrow$  Cloude's (or Stokes') global realizability [59]. This conclusion has been at the core of a recent work by Ossikovski and Devlaminck [59] discussing different types of physical realizability. Moreover, in order to be locally physically realizable for any  $\Delta z$ , the constraint should be discussed for the infinitesimal matrix  $\mathbf{N}_M$  (or  $\mathbf{m}$ ). This allows deducing the global realizability for any optical path starting from a given physically realizable differential Mueller matrix.

We now look closely into the constraints put on the parameters associated with the group generators in order to generate physical realizability for a non-singular Mueller matrix in the sense of Stokes' and Cloude's. In general, according to the Lie algebra of the corresponding monoid, a differential decomposition of a Mueller matrix allows

parametrizing the elementary matrix  $\mathbf{m}$  following Eq.(3.100):

$$\mathbf{m} = \mathbf{m}_d + \mathbf{m}_{nd} = \begin{pmatrix} \mu_0 & -d_1 - q_1 & -d_2 + q_2 & -d_3 - q_3 \\ -d_1 + q_1 & \mu_0 - p_1 & -b_1 + \eta_3 & b_2 + \eta_2 \\ -d_2 - q_2 & b_1 + \eta_3 & \mu_0 - p_2 & -b_3 + \eta_1 \\ -d_3 + q_3 & -b_2 + \eta_2 & b_3 + \eta_1 & \mu_0 - p_3 \end{pmatrix} \quad (3.104)$$

with  $p_1 = (\mu_2 + \mu_3)$ ,  $p_2 = (\mu_1 + \mu_3)$  and  $p_3 = (\mu_1 + \mu_2)$ . This parametrization of the cumulative differential Mueller matrix  $\mathbf{m}$  is also used in many other works [63–65] for analyzing  $\mathbf{m}$ . This matrix can be decomposed into a depolarizing part  $\mathbf{m}_{nd}$  which is G-antisymmetric and a non-depolarizing part  $\mathbf{m}_d$  which is G-symmetric, as discussed above. If we want  $\mathbf{m}$  to be (Stokes' or Cloude's) physically realizable, we must have both  $\mathbf{m}_{nd}$  and  $\mathbf{m}_d$  (Stokes' or Cloude's) physically realizable according to the relation between the Lie algebra and the monoid.

For  $\mathbf{m}_{nd}$ , since all physically realizable non-depolarizing matrices form a Lie group, all the matrices generated by the Lie algebra  $\mathfrak{so}(1,3)$  are both Stokes' and Cloude's realizable, according to the definition. This means that no constraint is imposed on  $d_i$  and  $b_i$ . As for the depolarizing part  $\mathbf{m}_d$ , the Stokes' realizability, which is a weak physical realizability, is given directly by Eq.(3.99) with  $D'_0$  the largest among the diagonal elements. This generation method maps an unbounded field  $\mathbb{R}^{10}$  to a bounded (constrained) field of parameters  $q_i, \eta_i, \mu_i$  and  $\mu_0$ . Then, as for the Cloude's realizability, since it means that a depolarizing Mueller matrix originates from an incoherent sum of non-depolarizing Mueller matrix, a matrix  $\mathbf{m}_d$  written in the form of Eq.(3.93) is Cloude's realizable. And, since Cloude's realizability imposes Stokes realizability, a Cloude's realizable matrix  $\mathbf{m}_d$  can also be written in the form of Eq.(3.99) with  $D'_0$  the maximum diagonal element. Based on the latter, a Lorentz transformation  $\mathbf{\Lambda} \in \mathcal{L}_+^\uparrow$  can be also considered as a non-depolarizing Mueller matrix which is Cloude's realizable. If a totally pure depolarizing matrix  $\mathbf{m}_d$  has to be Cloude's realizable, it imposes according to Eq.(3.99) that the diagonal matrix  $\mathbf{diag}(D'_0, D'_1, D'_2, D'_3)$  must be Cloude's realizable itself. Therefore, the depolarizing diagonal matrix  $\mathbf{diag}(D'_0, D'_1, D'_2, D'_3)$  can be written in the form of Eq(3.93). This gives an extra constraint on the diagonal elements in order for them to be Cloude's realizable, namely that  $\Delta b_i^2$  and  $\Delta d_i^2$  have to be non-negative, which gives  $\mu_1, \mu_2, \mu_3 \geq 0$ . It thus leads to the following constraint on the parameters  $p_1, p_2$  and  $p_3$ :

$$p_2 + p_3 \geq p_1 \geq |p_2 - p_3|, \quad p_1, p_2, p_3 \geq 0. \quad (3.105)$$

To summarize,  $\mathbf{m}_d$  is Cloude's realizable if and only if there exist a Lorentz transformation  $\mathbf{\Lambda} \in \mathcal{L}_+^\uparrow$  with which the matrix  $\mathbf{m}_d$  can be written as

$$\mathbf{m}_d = \frac{1}{2} \mathbf{\Lambda} \cdot \mathbf{diag}(\mu_0, \mu_0 - p_1, \mu_0 - p_2, \mu_0 - p_3) \cdot \mathbf{\Lambda}^{-1}, \quad (3.106)$$

with  $p_2 + p_3 \geq p_1 \geq |p_2 - p_3|$  and  $p_1, p_2, p_3 \geq 0$ , and  $\mu_0 \in \mathbb{R}$ . Since  $\mu_0$  corresponds to a prefactor for an identity matrix which contributes only as a prefactor on the final Mueller matrix  $\mathbf{M}$ , there is no constraint on this parameter.

### 3.4.4 Eigenstates analysis for non-singular Mueller matrices

As for the eigenstates of a non-singular Mueller matrix, we shall discuss different situations starting from a non-depolarizing Mueller matrix. Since a matrix and its matrix exponential have the same set of eigenvectors, we will again look at the differential Mueller matrix  $\mathbf{N}_M$  or  $\mathbf{m}$ . As we discussed in the previous section, the non-singular, non-depolarizing Mueller matrix  $\mathbf{m}_{nd}$  has always 2 eigenvectors in the form of non-depolarizing Stokes vectors.

We consider then the case of a pure depolarizing Mueller matrix  $\mathbf{m}_d$ . Since it can always be written as Eq.(3.99), this equation actually corresponds to the diagonalisation process with  $\mathbf{\Lambda}$  built on column eigenvectors and the diagonal matrix gathering the corresponding eigenvalues. According to the property of a  $\mathbf{\Lambda}$  matrix in the  $\text{SO}^+(1,3)$  group, we can only find one column corresponding to a Stokes vector fulfilling Eq.(3.2), that is the first column corresponding to the first eigenvalue  $D'_0$ . One conclusion therefore is that we can get for the eigenstate of pure depolarizing medium always one Stokes vector (not necessarily non-depolarizing) eigenstate corresponding to the largest eigenvalue, This result has been already discussed by Ossikovski and used as a criterion for Stokes realizability [63].

Next, we consider the eigenstates of a general non-singular Mueller matrix  $\mathbf{M}_{ns} = \exp(\mathbf{m}_{nd} + \mathbf{m}_d)$ . Such a matrix  $\mathbf{M}_{ns}$  can be always written as:

$$\mathbf{M}_{ns} = \mathbf{\Lambda} \mathbf{M}_{pd} \mathbf{\Lambda}' \quad (3.107)$$

according to [38], with  $\mathbf{M}_{pd}$  a pure depolarizing Mueller matrix and  $\mathbf{\Lambda}$  and  $\mathbf{\Lambda}'$  two different Lorentz transformations in  $\mathcal{L}_+^\uparrow$ . According to Stokes realizability [59],  $\mathbf{M}_{pd}$  always has one Stokes-type eigenvector noted as  $\mathbf{v}_d$  and we can always find 2 different Lorentz transformations  $\mathbf{\Lambda}$  and  $\mathbf{\Lambda}'$  for one vector  $\mathbf{v}'_d$  such that

$$\mathbf{\Lambda} \mathbf{v}_d = \mathbf{\Lambda}'^{-1} \mathbf{v}'_d = \mathbf{v}'_d. \quad (3.108)$$

Starting from the characteristic equation of  $\mathbf{M}_{pd}$ :

$$\mathbf{M}_{pd}\mathbf{v}_d = \lambda_d\mathbf{v}_d, \quad (3.109)$$

and substituting  $\mathbf{v}_d$  by  $\mathbf{v}'_d$ , we are led to

$$\mathbf{M}_{pd}\mathbf{\Lambda}'\mathbf{v}'_d = \lambda_d\mathbf{\Lambda}^{-1}\mathbf{v}'_d, \quad (3.110)$$

and thus

$$\mathbf{\Lambda}\mathbf{M}_{pd}\mathbf{\Lambda}' \cdot \mathbf{v}'_d = \mathbf{M}_{ns}\mathbf{v}'_d = \lambda_d\mathbf{v}_d. \quad (3.111)$$

We conclude that for a general non-singular Mueller matrix, one Stokes eigenvector can be specified for a depolarizing medium and two for a non-depolarizing medium.

### 3.5 Monoid for the ensemble of all physical Mueller matrices

The ensemble of all physical Mueller matrices, based on what we have discussed before, has here to be complemented with all singular Mueller matrices characterized by  $\det(\mathbf{M}) = 0$ . A horizontal polarizer characterized by

$$\mathbf{M}_{LP} = \frac{1}{2} \begin{pmatrix} 1 & 1 & 0 & 0 \\ 1 & 1 & 0 & 0 \\ 0 & 0 & 0 & 0 \\ 0 & 0 & 0 & 0 \end{pmatrix} \quad (3.112)$$

for instance, with  $\det(\mathbf{M}_{LP}) = 0$ , corresponds to such a singular Mueller matrix. For this ensemble of all physically realizable Mueller matrices, we can verify the closure with respect to the matrix product because the matrix product only implies successive stacks of different physically realizable media. The product therefore of a physically realizable Mueller matrix will remain physically realizable. This imposes the closure with respect to the matrix product. With the identity within the ensemble, but not all elements being invertible, the ensemble has a monoid structure. Singular Mueller matrices included, we can not define a Lie algebra for the whole ensemble. Hence, the ensemble of all physically realizable Mueller matrices forms a matrix monoid with the sub-group-like algebraic structure shown in Fig. 3.3.

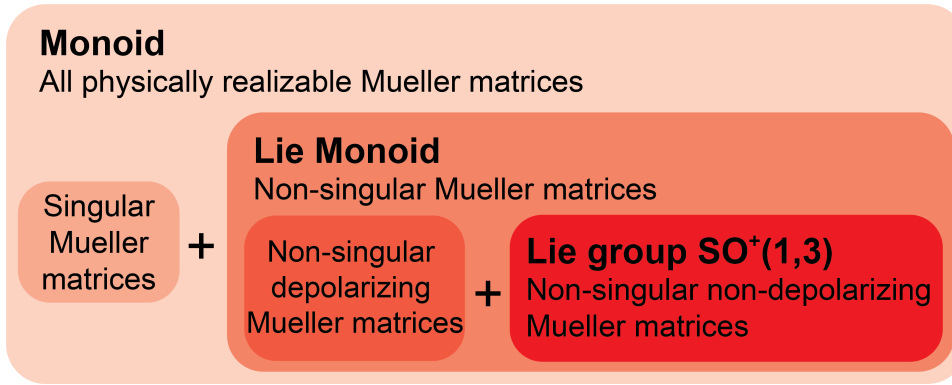


FIGURE 3.3: The sub-group-like algebraic structure for the Stokes-Mueller formalism

To summarize: non-singular, non-depolarizing Mueller matrices form a Lie group which is the same as the restricted Lorentz group noted as  $SO^+(1,3)$ . All matrices in this group can be generated by the Lie algebra  $\mathfrak{so}(1,3)$  with 6 real parameters with no constraint that correspond physically to birefringence and dichroism. All non-singular, non-depolarizing Mueller matrices have 2 light-like eigenvectors serving as the eigenstates of polarization of the medium. Then, by expanding this group to non-singular, depolarizing Mueller matrices, all non-singular Mueller matrices form a monoid of a Lie type where a Lie algebra is defined. This Lie algebra includes  $\mathfrak{so}(1,3)$  and other 10 matrix basis sets that contribute to the depolarizing part of the Mueller matrices with 10 other parameters related to the variance and covariance of non-depolarizing polarimetric properties defined in an inhomogeneous medium. Since all basis can form a Lie algebra of the  $SU(4)$  group, this Lie monoid can be considered as a sub-monoid of  $SU(4)$ . Due to depolarization, all non-singular Mueller matrices have at least one Stokes eigenvector corresponding to the largest eigenvalue. Finally, by including all singular Mueller matrices, we obtain the whole ensemble of physically realizable Mueller matrices which forms a monoid.

### 3.6 Applications

The analysis of the algebraic structure associated with all physical realizable Mueller matrices facilitates many problems involving optical polarization within the framework of the Stokes-Mueller formalism. In this section, we are going to illustrate with some specifically chosen problems how group theory can become efficient in polarization optics. We start by discussing how the differential decomposition analysis of a Mueller matrix can be used for extracting polarimetric observables. Then, with the help of the Lie algebra, we study the polarization dynamics (evolution of polarization states) in the Poincaré sphere. Exploiting the properties of Mueller matrix eigenvectors in the Stokes vector space, we explore the connection between the symmetries of a medium and the symmetries of the

Stokes eigenvectors, i.e. the eigenstates of polarization of the chosen medium. Finally, we show how the algebraic structure formalism combined with the symmetry analysis can provide an efficient path for constructing a medium with predefined specific symmetries.

### 3.6.1 Mueller matrix analysis by differential decomposition

The first application where the algebraic structure of the Stokes-Mueller formalism is helpful is for the differential decomposition of a Mueller matrix. This is one among many methods that enables to analyze and extract the polarimetric properties of a Mueller matrix. As introduced in the previous chapter in detail, the differential Mueller matrix  $\mathbf{N}_M$  can be defined similarly as the differential Jones matrix first introduced by R. Clark Jones [56], which was later, for the first time, adapted to the Mueller formalism by Azzam [66]. However, differential decomposition can not be applied to any non-singular Mueller matrix. It is only valid when the optical properties of the sample are uniformly or continuously distributed along the direction of light propagation or when only an averaged polarimetric property along the optical path is interested. Under these conditions, differential decomposition approach is reliable and it has been used in different groups recently [63–65].

The basic form of a general differential Mueller matrix is parameterized in Eq.(3.104) as proposed by others [63–65]. The explicit form of the differential Mueller matrix  $\mathbf{N}_M$  for the non-depolarizing part of a Mueller matrix is deduced from the Jones differential matrix  $\mathbf{N}_J$  in Eq.(2.213) as a function of non-depolarizing polarimetric properties, i.e. arbitrary birefringences and dichroisms. Then the explicit form of the depolarizing part of Mueller matrix due to spatial inhomogeneities is deduced from Eq.(3.93) as a function of variances and covariances involving non-depolarizing polarimetric properties (i.e. birefringences and dichroisms).

### 3.6.2 Stokes vector Poincaré sphere trajectory analysis

Another problem that can be explored using the group theory formalism applied to Mueller matrices is the interpretation of polarization dynamics represented in the Poincaré sphere. This approach can be applied in the context of polarization state control by optical systems [67, 68], geometric (Pancharatnam-Berry) phase effects and analysis [69, 70] and coherent input engineering [71], for instance. For such topics, a clear knowledge of the polarization path, which is the trajectory of the Stokes vectors inside the Poincaré sphere, is a key to understanding the specific dynamics of the properties under study within the framework of Stokes-Mueller formalism.



Generally, the evolution of a Stokes vector  $\mathbf{S}(z)$  when passing through a medium can be written as

$$\frac{d\mathbf{S}(z)}{dz} = \lim_{z' \rightarrow z} \frac{\mathbf{S}(z') - \mathbf{S}(z)}{z' - z} = \lim_{z' \rightarrow z} \frac{\mathbf{M}_{z,z'}\mathbf{S}(z) - \mathbf{S}(z)}{z' - z} = \lim_{z' \rightarrow z} \frac{\mathbf{M}_{z,z'} - \mathbf{I}}{z' - z} \cdot \mathbf{S}(z), \quad (3.113)$$

which by substituting the limit with  $\mathbf{N}_M$  according to Eq.(2.205), leads to the dynamic equation for a Stokes vector,

$$\frac{d\mathbf{S}(z)}{dz} = \mathbf{N}_{M,z}\mathbf{S}(z). \quad (3.114)$$

There is no explicit analytical solution for this dynamic equation for any  $\mathbf{N}_{M,z}$  in general. But for one given  $\mathbf{N}_{M,z}$  that evolves with the light propagation direction  $z$ , we can solve numerically the trajectory of  $\mathbf{S}(z)$ . For a constant  $\mathbf{N}_{M,z}$  with  $z$ , the solution can even be explicitly written as

$$\mathbf{S}(z) = \exp(z\mathbf{N}_M)\mathbf{S}(0) = \mathbf{M}\mathbf{S}(0), \quad (3.115)$$

implying that the medium described by  $\mathbf{M}$  is homogeneous. According to the definition of the Lie algebra, this  $z\mathbf{N}_{M,z}$  matrix can be constructed directly by the linear combination of group generators using polarimetric properties as the parameters of the linear combination, as discussed in previous sections. Since each group generator discussed above corresponds to specific geometric operation, the resulting trajectory in the Poincaré sphere of  $\mathbf{S}(z)$  for a medium which is homogeneous along  $z$  is simply drawn from the trace of each corresponding geometric operations.

Specifically, for a non-depolarizing medium represented by a Mueller matrix in the  $\text{SO}^+(1,3)$  group, according to the group structure, the geometric operations are single rotation generated by  $\mathbf{\Gamma}_i$ , a boost generated by  $\mathbf{K}_i$  and a general Lorentz boost combining at the same time a rotation and a boost. This is the most applied case, of course usually discussed in polarimetric applications.

However, the Stokes vector trajectory through a depolarizing medium is more subtle to discuss and must be based on the geometric interpretation of depolarizing Mueller matrices from their associated Lie algebra as presented in sections 4.4.2 and 4.4.3 above. We remind the structure given in Eq.(3.104) of the cumulative differential matrix for a general depolarizing medium. In order to study the geometric interpretation of each term,

we can decompose the matrix  $\mathbf{m}$  according to independent geometric operations as

$$\begin{aligned}
\mathbf{m} &= \begin{pmatrix} \mu_0 & -d_1 - q_1 & -d_2 + q_2 & -d_3 - q_3 \\ -d_1 + q_1 & \mu_0 - p_1 & -b_3 + \eta_3 & b_2 + \eta_2 \\ -d_2 - q_2 & b_3 + \eta_3 & \mu_0 - p_2 & -b_1 + \eta_1 \\ -d_3 + q_3 & -b_2 + \eta_2 & b_1 + \eta_1 & \mu_0 - p_3 \end{pmatrix} \\
&= \begin{pmatrix} 0 & -d_1 - q_1 & -d_2 + q_2 & -d_3 - q_3 \\ -d_1 - q_1 & 0 & -b_3 + \eta_3 & b_2 + \eta_2 \\ -d_2 + q_2 & b_3 - \eta_3 & 0 & -b_1 + \eta_1 \\ -d_3 - q_3 & -b_2 - \eta_2 & b_1 - \eta_1 & 0 \end{pmatrix} + \begin{pmatrix} 0 & 0 & 0 & 0 \\ 2q_1 & 0 & 0 & 0 \\ -2q_2 & 0 & 0 & 0 \\ 2q_3 & 0 & 0 & 0 \end{pmatrix} \\
&\quad + \begin{pmatrix} 0 & 0 & 0 & 0 \\ 0 & 0 & 0 & 0 \\ 0 & 2\eta_3 & 0 & 0 \\ 0 & 2\eta_2 & 2\eta_1 & 0 \end{pmatrix} + \begin{pmatrix} 0 & 0 & 0 & 0 \\ 0 & -p_1 & 0 & 0 \\ 0 & 0 & -p_2 & 0 \\ 0 & 0 & 0 & -p_3 \end{pmatrix} + \begin{pmatrix} \mu_0 & 0 & 0 & 0 \\ 0 & \mu_0 & 0 & 0 \\ 0 & 0 & \mu_0 & 0 \\ 0 & 0 & 0 & \mu_0 \end{pmatrix} \quad (3.116)
\end{aligned}$$

where the first term can be expressed as the operations generated by  $\mathfrak{so}(1,3)$  as explained in Eq.(3.40), the second corresponds to a translation, the third to a shearing transformation and the fourth term represents a scaling followed by the identity matrix. So the matrix  $\mathbf{m}$  can be reduced to

$$\mathbf{m} = - \begin{pmatrix} d_1 + q_1 \\ d_2 - q_2 \\ d_3 + q_3 \end{pmatrix} \cdot \mathbf{K} + \begin{pmatrix} b_1 - \eta_1 \\ b_2 + \eta_2 \\ b_3 - \eta_3 \end{pmatrix} \cdot \mathbf{\Gamma} + 2 \begin{pmatrix} q_1 \\ -q_2 \\ q_3 \end{pmatrix} \cdot \mathbf{P} + 2 \begin{pmatrix} \eta_1 \\ \eta_2 \\ \eta_3 \end{pmatrix} \cdot \mathbf{\Psi} + \mathbf{diag} \begin{pmatrix} \mu_0 \\ \mu_0 - p_1 \\ \mu_0 - p_2 \\ \mu_0 - p_3 \end{pmatrix} \quad (3.117)$$

with group generators  $\mathbf{K}$ ,  $\mathbf{\Gamma}$  defined as Eq.(3.23) and Eq.(3.22), the basis  $\mathbf{P}$  defined as

$$\mathbf{P}_1 = \begin{pmatrix} 0 & 0 & 0 & 0 \\ 1 & 0 & 0 & 0 \\ 0 & 0 & 0 & 0 \\ 0 & 0 & 0 & 0 \end{pmatrix}, \mathbf{P}_2 = \begin{pmatrix} 0 & 0 & 0 & 0 \\ 0 & 0 & 0 & 0 \\ 1 & 0 & 0 & 0 \\ 0 & 0 & 0 & 0 \end{pmatrix}, \mathbf{P}_3 = \begin{pmatrix} 0 & 0 & 0 & 0 \\ 0 & 0 & 0 & 0 \\ 0 & 0 & 0 & 0 \\ 1 & 0 & 0 & 0 \end{pmatrix} \quad (3.118)$$

generating the translation in the 3 dimensional space, the basis  $\mathbf{\Psi}$  defined as

$$\mathbf{\Psi}_1 = \begin{pmatrix} 0 & 0 & 0 & 0 \\ 0 & 0 & 0 & 0 \\ 0 & 0 & 0 & 0 \\ 0 & 0 & 1 & 0 \end{pmatrix}, \mathbf{\Psi}_2 = \begin{pmatrix} 0 & 0 & 0 & 0 \\ 0 & 0 & 0 & 0 \\ 0 & 0 & 0 & 0 \\ 0 & 1 & 0 & 0 \end{pmatrix}, \mathbf{\Psi}_3 = \begin{pmatrix} 0 & 0 & 0 & 0 \\ 0 & 0 & 0 & 0 \\ 0 & 1 & 0 & 0 \\ 0 & 0 & 0 & 0 \end{pmatrix} \quad (3.119)$$

where  $\mathbf{\Psi}_1$  represents the shearing motion of the  $xOz$  plane along the  $Oz$  direction,  $\mathbf{\Psi}_2$

represents the shearing motion of the  $yOz$  plane along the  $Oz$  direction and  $\Psi_3$  represents the shearing motion of the  $yOz$  plane along the  $Oy$  direction, and the last term corresponds to the scaling operation. Here these basis sets also form a closed ensemble with respect to the commutator and thus form the set of a Lie algebra. We note here that the generators of translation  $\mathbf{P}$  are different from those of the Poincaré group.

Finally for singular Mueller matrices, since no Lie algebra can be defined for them, the geometric operations are often projective. For instance, a polarizer in the Poincaré sphere corresponds to a projection operation on the polarizer state.

It is only after such a geometric interpretation of the different types of homogeneous Mueller matrices that the Stokes vector trajectories can be constructed and analyzed properly. However for a medium consisting of a stacking of different homogeneous layers, the trajectory should be analyzed layer by layer but not from the total matrix. More precisely, the total trajectory should not be calculated from the total matrix  $\mathbf{M}_{all} = \prod_i \mathbf{M}_i$  but instead, it should be calculated from each homogenous layers successively. Eventually, this does not change the final resulting Stokes vector, however calculating the trajectory from the total matrix will lead to a path that does not correspond to the real polarization dynamics of light transmitted through the staked medium. Therefore, a stacking of several optical systems will give rise to a polyline on the sphere. Interestingly, if the final state of polarization coincides with the initial state of polarization, this polyline will also form a closed polygon giving rise to a geometric phase induced between the incident and the transmitted light at this state of polarization. This geometric phase  $\Phi_g$  is directly related to the solid angle of the polygon area  $\Omega$  measured on the Poincaré sphere as

$$\Phi_g = -\frac{1}{2}\Omega, \quad (3.120)$$

shown in Fig.3.4. Calculating this solid angle for an arbitrary polygon with all vertices connected by a great arc<sup>4</sup> has been discussed in detail in the very recent work of J. C. Gutierrez-Vega [72].

---

<sup>4</sup>A great arc is the shortest line on a sphere connecting 2 points on it.

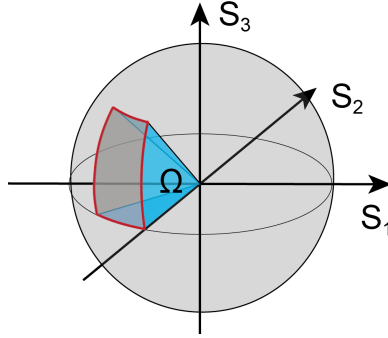


FIGURE 3.4: A closed path on the Poincaré sphere inducing a geometric phase related to the solid angle  $\Omega$ .

Since in many polarization dynamics, 2 successive vertices are not necessarily connected by a great arc, a given trajectory must be divided in this case into the infinitesimal segments and then sum them up all to get the final solid angle. In practice, a close trajectory for polarization state in the Poincaré sphere is not easy to achieve naturally, as we will see using a molecular system. This requires most of the time to engineer the trajectory by different layers whose polarimetric response are tailored to the problem.

### 3.6.3 Studying the symmetries of a medium by an eigenstate analysis of its Mueller matrix

The importance of symmetries in the context of polarimetry is obvious. Symmetries play key roles for instance in the context of chiral optics. Here we discuss how group theory and eigenstate analysis of a Mueller matrix allow to study efficiently the connection between symmetries and polarimetric properties. This can be understood since the characteristic polarimetric properties of an optical medium can be represented by the eigenstates of polarization. This implies that the Stokes eigenvectors under symmetry operations are directly related to the symmetries of the medium. Specifically, a symmetry transformation  $\mathbf{P}_t$  applied on the Mueller matrix representing the medium is written as

$$\mathbf{M}_t = \mathbf{P}_t \mathbf{M}_0 \mathbf{P}_t^{-1}, \quad (3.121)$$

with  $\mathbf{M}_t$  the resulting Mueller matrix that is to be compared with the initial matrix  $\mathbf{M}_0$  in order to reveal some symmetry invariance. From the eigenvector point of view, the eigenvector corresponding to  $\mathbf{M}_t$  is related to the initial eigenvector  $\mathbf{v}_0$  of the matrix  $\mathbf{M}_0$  by  $\mathbf{P}_t$  as

$$\mathbf{v}_t = \mathbf{P}_t \mathbf{v}_0. \quad (3.122)$$

Therefore, by comparing the conformation<sup>5</sup> of the final set of eigenvectors with the initial set of eigenvectors, we can equally access the symmetry of the medium.

As we discussed in the previous section, a Mueller matrix is not defined in the Cartesian space while a Jones matrix is. This implies that any Cartesian space geometric transformation should be translated in the space of Mueller matrix following Eq.(2.70). With these premises, we can look into specific symmetries using the eigenstates of the medium described within a set of coordinates in Cartesian space as described in Fig 3.5.

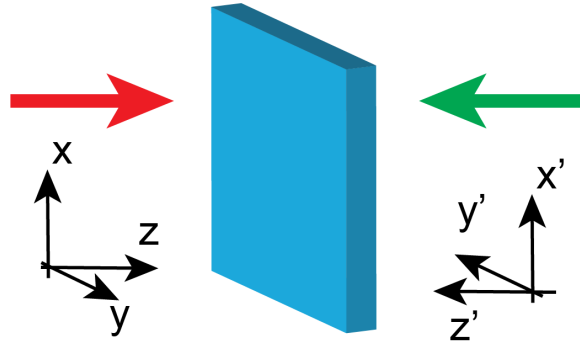


FIGURE 3.5: The coordinate setting for a medium in Cartesian space with the red and green arrows indicating the forward and backward propagation directions with respect to one chosen side of the sample.

### Rotation symmetries

Let us look first into rotation symmetries. As we are in the framework of paraxial approximation, we consider here only a rotation around the optical axis  $Oz$  (in-plane rotation) represented by a 2D matrix in a Cartesian space  $(x, y, z)$  :

$$\mathbf{R}(\theta) = \begin{pmatrix} \cos \theta & \sin \theta \\ -\sin \theta & \cos \theta \end{pmatrix}, \quad (3.123)$$

where  $\theta$  is the angle of rotation. The corresponding transformation matrix in the Mueller matrix space has been deduced in chapter 2 in Eq.(2.71). In the Poincaré sphere, the rotation in Eq.(3.123) is transformed into a rotation around the  $OS_3$  axis of the Poincaré sphere. This then immediately implies that a medium that possesses Mueller matrix eigenvectors only along the  $S_3$  component in the Poincaré sphere has rotational symmetry along the optical axis. Therefore, using the results given above for a non-depolarizing medium where there are 2 non-depolarizing Stokes eigenvectors, the eigenvectors  $\mathbf{v}$  must

<sup>5</sup>We use here the word "conformation" since we look at the spatial distribution in Poincaré sphere and the relative position of the eigenvectors, making an analogy with molecular conformation.

have the structure

$$\mathbf{v} = \begin{pmatrix} 1 \\ 0 \\ 0 \\ \pm 1 \end{pmatrix}, \quad (3.124)$$

shown in Fig 3.6 (a). As all eigenvectors are orthogonal to each other, the birefringence vector  $\mathbf{b}$  and dichroism vector  $\mathbf{d}$  are collinear and with an  $S_3$  component only for a bi-isotropic medium that has CD and CB as discussed in 3.3.3. The corresponding accumulated differential Mueller matrix  $\mathbf{m}$  can be written as

$$\mathbf{m} = \begin{pmatrix} 0 & 0 & 0 & -d_3 \\ 0 & 0 & -b_3 & 0 \\ 0 & b_3 & 0 & 0 \\ -d_3 & 0 & 0 & 0 \end{pmatrix} = -d_3 \mathbf{K}_3 + b_3 \mathbf{\Gamma}_3. \quad (3.125)$$

A depolarizing medium, in contrast, has only one Stokes eigenvector as discussed in section 3.4.4., and the eigenvector must be right on the  $OS_3$  axis. Also we note that any eigenvector will preserve its  $S_3$  component by any in-plane rotation operation, revealing the nature of optical chirality as an invariance with respect to in-plane rotations in other words conservation of handedness with respect to the in-plane rotations.

### In-plane mirror symmetries

The second operation we look at is the in-plane mirror symmetry associated with the 2D operation described in the Cartesian space as:

$$\mathbf{\Pi}_\theta = \begin{pmatrix} \cos \theta & \sin \theta \\ \sin \theta & -\cos \theta \end{pmatrix}. \quad (3.126)$$

By definition, this matrix represents a mirror reflection with an in-plane symmetry axis perpendicular to the optical axis making an angle  $\theta$  with the  $Ox$  direction. Using Eq.(2.70), this transformation can be expressed for a Mueller matrix as

$$\mathbf{\Pi}_{\theta,M} = \begin{pmatrix} 1 & 0 & 0 & 0 \\ 0 & \cos 2\theta & \sin 2\theta & 0 \\ 0 & \sin 2\theta & -\cos 2\theta & 0 \\ 0 & 0 & 0 & -1 \end{pmatrix}, \quad (3.127)$$

which represents 2 successive operations in the Poincaré sphere: a reflection with respect to a plane perpendicular to the  $S_1OS_2$  plane making an angle  $2\theta$  with the  $OS_1$  axis, and a second reflection with respect to the  $S_1OS_2$  plane. Therefore, a medium that has an

in-plane mirror symmetry is invariant through the operation given by Eq.(3.127). For a non-depolarizing medium, the corresponding pair of eigenvectors must write as

$$\mathbf{v}_+ = \begin{pmatrix} 1 \\ a_1 \\ a_2 \\ 0 \end{pmatrix}, \mathbf{v}_- = \begin{pmatrix} 1 \\ -a_1 \\ -a_2 \\ 0 \end{pmatrix}, \quad (3.128)$$

with  $a_1^2 + a_2^2 = 1$  and a spatial configuration shown in Fig 3.6 (b). This shows that the medium possess a birefringence vector  $\mathbf{b}$  and a dichroism vector  $\mathbf{d}$  collinear but here without any  $S_3$  component. The corresponding accumulated differential Mueller matrix writes as:

$$\mathbf{m} = \begin{pmatrix} 0 & -d_1 & -d_2 & 0 \\ -d_1 & 0 & 0 & b_2 \\ -d_2 & 0 & 0 & -b_1 \\ 0 & -b_2 & b_1 & 0 \end{pmatrix} = -d_1 \mathbf{K}_1 - d_2 \mathbf{K}_2 + b_1 \mathbf{\Gamma}_1 + b_2 \mathbf{\Gamma}_2 \quad (3.129)$$

with  $b_1/b_2 = d_1/d_2$ . As for a depolarizing medium, it is sufficient that the only one Stokes eigenvector has no  $S_3$  component.

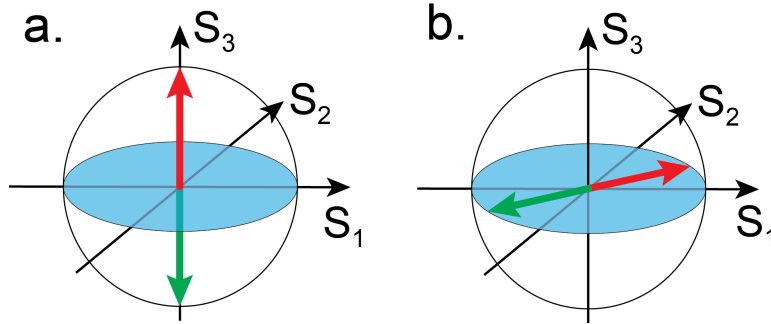


FIGURE 3.6: (a) shows the Poincaré spatial conformation of the eigenstates for a medium with rotational symmetry. (b) shows the conformation of eigenstates for a medium that displays in-plane mirror symmetry.

### Reciprocity and flip operation

The next symmetry property investigated is reciprocity. In optics, reciprocity connects, by equating their results, the two opposite probing directions of light passing through a linear, passive medium. The Lorentz principle of reciprocity [lorentz1896] has been discussed in details within the framework of Jones matrices in [73]. Following [73], the reciprocal Jones matrix for the light propagating backwards  $\mathbf{J}_{rec}$  is related to

the matrix associated with a forward propagation of light  $\mathbf{J}$  as

$$\mathbf{J}_{rec.} = \mathbf{J}^T, \quad (3.130)$$

where  $\cdot^T$  is a matrix transpose operation. This relation can be translated in the Stokes-Mueller formalism using Eq.(2.66), which yields

$$\mathbf{M}_{rec.} = \mathbf{M}_{J^T} = \mathbf{U}\mathbf{M}_J^T\mathbf{U}^{-1}, \quad (3.131)$$

where  $\mathbf{U}$  is defined as

$$\mathbf{U} = \begin{pmatrix} 1 & 0 & 0 & 0 \\ 0 & 1 & 0 & 0 \\ 0 & 0 & 1 & 0 \\ 0 & 0 & 0 & -1 \end{pmatrix}. \quad (3.132)$$

As discussed in [73], reciprocity can be described in an operational way using a flip operation. In the Mueller matrix context, we can also define the sample flip operation. Based on the reciprocal matrix, the matrix of the sample flipping is just a change of basis determined by an in-plane reflection in a symmetry plane parallel to the  $Ox$  direction ( $\theta = 0$ ). With this in-plane reflection, the reciprocal Jones matrix of the sample immediately gives the Jones matrix of the flipped medium

$$\mathbf{J}_{flip} = \mathbf{\Pi}_0\mathbf{J}_{rec.}\mathbf{\Pi}_0^{-1}. \quad (3.133)$$

If the medium is reciprocal, one can then simply write:

$$\mathbf{J}_{flip} = \mathbf{\Pi}_0\mathbf{J}^T\mathbf{\Pi}_0^{-1}. \quad (3.134)$$

These relations can be directly translated into a relation for the Mueller matrix, that writes as:

$$\mathbf{M}_{flip} = \mathbf{\Pi}_{0,M}\mathbf{M}^{rec.}\mathbf{\Pi}_{0,M}^{-1} = \mathbf{\Pi}_{0,M}\mathbf{U}\mathbf{M}^T\mathbf{U}^{-1}\mathbf{\Pi}_{0,M}^{-1} = \mathbf{O}\mathbf{M}^T\mathbf{O}^{-1}, \quad (3.135)$$

with  $\mathbf{O}$  defined as

$$\mathbf{O} = \begin{pmatrix} 1 & 0 & 0 & 0 \\ 0 & 1 & 0 & 0 \\ 0 & 0 & -1 & 0 \\ 0 & 0 & 0 & 1 \end{pmatrix}. \quad (3.136)$$

This result is consistent with what A. Schönhofer found in [74]. Therefore by verifying the relation between the matrix of a sample turn, given by Eq.(3.135) and the original matrix, we have here a direct way to test the reciprocity of a medium.



But the  $\mathbf{M}_{flip}$  can not be deduced directly from an arbitrary Mueller matrix  $\mathbf{M}$ , since a Mueller matrix is a phenomenological observable and its elements do not constrain all information related to a possible source of non-reciprocity, such as magnetic coupling for instance. Hence, reciprocity can not be seen directly from the symmetry of a Mueller matrix. Despite this, we can still derive the constraints on a Mueller matrix for a non-magnetic medium looking at the symmetry signatures of different polarimetric properties. Indeed, for a non-magnetic medium homogeneous along the light propagation direction, the differential Mueller matrix  $\mathbf{N}_M$  can be divided into 2 parts: a bi-dimensional structured part describing only the planar properties of the medium and a three-dimensional structured part which contains all 3D properties in particular all dispersive properties along the light propagation direction such as handedness. The flip operation for the 2D part  $\mathbf{N}_{2D}$  can be considered as a  $180^\circ$  rotation around the  $Ox$  direction, and thus equivalent to an in-plane reflection via  $\mathbf{\Pi}_{0,M}$ . The flip operation for the 3D part  $\mathbf{N}_{3D}$  in contrast remains neutral since the 3D structured properties of the medium are invariant under any rotation transformation. This explains that the flip differential matrix can be constructed as a simple superposition

$$\mathbf{N}_{M,flip} = \mathbf{\Pi}_{0,M}\mathbf{N}_{2D}\mathbf{\Pi}_{0,M}^{-1} + \mathbf{N}_{3D}. \quad (3.137)$$

Because we only discuss homogeneous media, this relation is also valid for the cumulative differential Mueller matrix  $\mathbf{m}$ , thus having

$$\mathbf{m}_{flip} = \mathbf{\Pi}_{0,M}\mathbf{m}_{2D}\mathbf{\Pi}_{0,M}^{-1} + \mathbf{m}_{3D}. \quad (3.138)$$

Therefore, using Eq.(3.135), the reciprocity constraint for a Mueller matrix reads for both 2D and 3D parts like:

$$\mathbf{m}_{2D} = \mathbf{U}\mathbf{m}_{2D}^T\mathbf{U}^{-1}, \quad (3.139)$$

$$\mathbf{m}_{3D} = \mathbf{O}\mathbf{m}_{3D}^T\mathbf{O}^{-1}. \quad (3.140)$$

We know that the optical properties associated with the 2D part are  $LD, LD', LB$  and  $LB'$  and that the properties associated with the 3D part are  $CD$  and  $CB$ . We can thus verify that a non-magnetic medium described by a non-singular, non-depolarizing Mueller matrix written as Eq.(3.40) satisfy the reciprocity conditions in Eq. (3.139) Eq. (3.140). Moreover, since the reciprocity constraints listed above do not apply to the diagonal elements of Mueller matrix, these elements, basically, can take any values within the conditions of physical realizability. The flip operation too described in Eq.(3.138) for a non-depolarizing matrix is nothing but taking the additive inverse of  $LB'$  and  $LD'$  or of the parameter  $b_2$  and  $d_2$ . This allows us to verify that the depolarization due to the distribution of spatial inhomogeneities coming from non-depolarizing elements described

by Eq.(3.93) also fulfills the constraint of reciprocity written in Eq.(3.135).

To sum up, reciprocity can not be directly viewed from the symmetries of the Mueller matrix. The rigorous way is only to measure experimentally the original and flipped Mueller matrix and estimate their relation expected to be fixed by Eq.(3.135). But with the additional information on the polarimetric properties that excludes any magnetic coupling, we can verify that the standard form of a Mueller matrix is generally reciprocal. Based on reciprocity, we can define directly the flip operation by Eq.(3.135) for a sample turn from the original Mueller matrix. Finally, from the point of view of the eigenstates of a reciprocal medium, the flip operation described by Eq.(3.135) consists of 2 operations made on the eigenvector(s): the transpose of the matrix and a change of basis that inverts  $S_2$  components in the Poincaré sphere. Since a matrix and its transpose have the same set of eigenvalues and the eigenvectors corresponding to different eigenvalues from the matrix and its transpose are mutually orthogonal, reading

$$\mathbf{v}_{\lambda_i, \mathbf{M}} \perp \mathbf{v}_{\lambda_j, \mathbf{M}^T}, \quad i \neq j, \quad (3.141)$$

a transpose operation geometrically transforms one eigenvector into a vector which is orthogonal to the other eigenvectors of the original matrix. For the case of a non-depolarizing Mueller matrix, one eigenstate of the transpose will become orthogonal to the other eigenstate of the original Mueller matrix. For a depolarizing Mueller matrix, the transpose operation just turns the only Stokes eigenvector orthogonal to its state. In order to perform the flip operation after the transpose operation, it is sufficient to perform a reflection with respect to the  $S_1OS_3$  plane. Therefore, we can see that a reciprocal medium which is invariant with respect to the flip operation is essentially a medium with 2 orthogonal eigenstates on the  $S_1OS_3$  plane in the Poincaré sphere.

### Time reversal and energy conservation

The next symmetry investigated is the time reversal symmetry. Different from reciprocity, time reversal symmetry is analyzed by reversing time-flow direction and motion. Within the Jones formalism, the matrix corresponding to a time reversal writes simply as [73]

$$\mathbf{J}_{inv.} = \mathbf{J}^{-1,*} \quad (3.142)$$

where \* stands for complex conjugate. By the inversion defined in Eq.(2.66), time reversal reads within Stokes-Mueller formalism as

$$\mathbf{M}_{inv.} = \mathbf{U}\mathbf{M}^{-1}\mathbf{U}^{-1}. \quad (3.143)$$

This relation shows that, if  $\mathbf{M}_{inv.}$  is physically realizable, the process analyzed via the Mueller matrix approach is time reversible. From group theory, we can immediately see that a process characterized by a depolarizing Mueller matrix is not time reversible since a depolarizing Mueller matrix only forms a monoid where the inverse matrix is not a physically realizable Mueller matrix. This implies in this case that the time reversal process can not be optically realized. For these reasons, a Mueller matrix characterizing a time reversible process should be non-singular and non-depolarizing.

Another symmetry closely related to time reversal symmetry is the conservation of energy. This conservation law simply means that the energy of the incident light equals the energy of the transmitted light which can be expressed within the Jones formalism as

$$\mathbf{E}_{in}^\dagger \mathbf{E}_{in} = \mathbf{E}_{out}^\dagger \mathbf{E}_{out} = \mathbf{E}_{in}^\dagger (\mathbf{J}^\dagger \mathbf{J}) \mathbf{E}_{in}. \quad (3.144)$$

This implies

$$\mathbf{J}^\dagger = \mathbf{J}^{-1} \quad (3.145)$$

or

$$\mathbf{J}^T = \mathbf{J}^{-1,*}. \quad (3.146)$$

By definition of the reciprocal matrix and the time reversal matrix, the energy conservation reads also as

$$\mathbf{J}_{rec.} = \mathbf{J}_{inv.} \quad (3.147)$$

In other words, energy conservation imposes the equality between the reciprocal matrix and the time reversal matrix. In the Stokes-Mueller formalism, the matrix characterizing an energy conservation process therefore writes like

$$\mathbf{M}^{-1} = \mathbf{M}^T \quad (3.148)$$

which, for the accumulated differential matrix, gives

$$-\mathbf{m} = \mathbf{m}^T. \quad (3.149)$$

This imposes the matrix to have the following structure:

$$\mathbf{m} = \begin{pmatrix} 0 & 0 & 0 & 0 \\ 0 & 0 & -b_3 & b_2 \\ 0 & b_3 & 0 & -b_1 \\ 0 & -b_2 & b_1 & 0 \end{pmatrix} = b_1 \mathbf{\Gamma}_1 + b_2 \mathbf{\Gamma}_2 + b_3 \mathbf{\Gamma}_3 \quad (3.150)$$

which contains only birefringence. We therefore conclude that a medium inducing an

optically energy conserving process must be a non-depolarizing birefringent medium, a result physically expected.

### Optical chirality: optical activity and planar chirality

With the symmetry operations discussed previously, we can now look at chiral properties of the medium within the paraxial limit. Chirality, related to the observable of optical activity corresponds, according to the definition of Lord Kelvin [5], to a medium that does not have in-plane mirror symmetry. This can be simply formulated as [73]:

$$\forall \theta, [\mathbf{M}, \mathbf{\Pi}_{\theta, M}] \neq 0. \quad (3.151)$$

Beyond the discussion made in [73], this operation can be taken as a criterion for optical chirality, looking at the conformation of Mueller matrix eigenstates. Basically, any medium that does not have eigenvectors written like Eq.(3.128) presents a sort of optical chirality. For such a medium that does not have in-plane mirror symmetry, and therefore identified as chiral, we can define its enantiomer characterized by the cumulative differential Mueller matrix as

$$\mathbf{m}_{en.,\theta} = \mathbf{\Pi}_{\theta, M} \mathbf{m} \mathbf{\Pi}_{\theta, M}^{-1}, \quad (3.152)$$

with the corresponding set of eigenvector

$$\mathbf{v}_{en.,\pm} = \mathbf{\Pi}_{\theta, M} \mathbf{v}_{\pm}. \quad (3.153)$$

This however does not close the discussion. Optical chirality can manifest itself through different features. We first introduce the well-known concept of optical activity. Optical activity, phenomenologically speaking, corresponds to any polarimetric quantity that displays rotatory powers, basically CD and CB signals. This generally originates from a helicoidal structure in the medium such as the case of sugar molecules studied by Arago and Pasteur [75, 76]. Formally, from the symmetry property of a helix, optical activity can be formulated within Jones formalism as the possibility to write, for one given orientation  $\theta$  [73] :

$$\mathbf{J}_{flip} = \mathbf{\Pi}_0 \mathbf{J}^T \mathbf{\Pi}_0^{-1} = \mathbf{R}(\theta) \mathbf{J} \mathbf{R}(\theta)^{-1}. \quad (3.154)$$

The corresponding relation within Stokes-Mueller formalism is

$$\exists \theta, \mathbf{M}_{flip} = \mathbf{O} \mathbf{M}^T \mathbf{O}^{-1} = \mathbf{R}_M(\theta) \mathbf{M} \mathbf{R}_M(\theta)^{-1}. \quad (3.155)$$

From the eigenstates point of view, this relation characterizing optical activity can be translated in the following way: the conformation of eigenvector after a flip operation can

always be obtained by a rotation of this set of eigenvectors. It so, the medium, displays pure optical activity. With this constraint combined with the definition of optical chirality given by Eq.(3.151), the medium must be non-depolarizing and its eigenvectors can be only written as

$$\mathbf{v}_+ = \begin{pmatrix} 1 \\ a_1 \\ a_2 \\ a_3 \end{pmatrix}, \mathbf{v}_- = \begin{pmatrix} 1 \\ a'_1 \\ a'_2 \\ -a_3 \end{pmatrix}. \quad (3.156)$$

This leads to 3 typical conformations as shown in Fig. 3.7 (a)-(c), namely, one with no linear polarimetric properties ( $a_1 = a_2 = a'_1 = a'_2 = 0$ ) shown in Fig. 3.7 (a) for a bi-isotropic medium, one with no  $S_3$  component ( $a_3 = 0$ ) shown in Fig. 3.7 (b), and one with all non-zero components shown in Fig. 3.7 (c). The corresponding cumulative differential Mueller matrix in such cases writes as:

$$\mathbf{m}_{O.A.} = \begin{pmatrix} 0 & -d_1 & -d_2 & -d_3 \\ -d_1 & 0 & -b_3 & b_2 \\ -d_2 & b_3 & 0 & -b_1 \\ -d_3 & -b_2 & b_1 & 0 \end{pmatrix} = -d_1\mathbf{K}_1 - d_2\mathbf{K}_2 - d_3\mathbf{K}_3 + b_1\mathbf{\Gamma}_1 + b_2\mathbf{\Gamma}_2 + b_3\mathbf{\Gamma}_3, \quad (3.157)$$

with  $d_1/d_2 = b_1/b_2$  indicating the  $S_1OS_2$  plane projection of the collinear birefringence  $\mathbf{b}$  and dichroism  $\mathbf{d}$  vectors, and  $d_3$  and  $b_3$  not both zero.

As discussed recently in particular in the field of surface plasmon and metamaterial optics [77], another type of chirality can be discussed in optics when involving planar configurations: the so called planar chirality or 2D chirality. This chirality does not have any in-plane mirror symmetry obviously but has neither, in its most general form, any 3D space rotation invariance, considering that it is associated with planar structures. According to the discussion on reciprocity in Eq.(3.138), the flip operation for such 2D structures can be also written directly as the change of basis by  $\mathbf{\Pi}_0$ . Another condition thus for 2D chirality within Jones formalism is written as [73] :

$$\mathbf{J}_{flip} = \mathbf{\Pi}_0\mathbf{J}^T\mathbf{\Pi}_0^{-1} = \mathbf{\Pi}_0\mathbf{J}\mathbf{\Pi}_0^{-1}, \text{ i.e. } \mathbf{J}^T = \mathbf{J}. \quad (3.158)$$

Combined with the condition of optical chirality given in Eq.(3.151), the full description of a cumulative differential Mueller matrix characterizing a 2D chiral system is

$$\mathbf{m} \neq \mathbf{\Pi}_{\theta,M}\mathbf{m}\mathbf{\Pi}_{\theta,M}^{-1} \quad (3.159)$$

with

$$\mathbf{m}^T = \mathbf{U}\mathbf{m}\mathbf{U}^{-1}. \quad (3.160)$$

In order to fulfill these conditions,  $\mathbf{m}$  can be generally written as

$$\mathbf{m}_{P.C.} = \begin{pmatrix} 0 & -d_1 & -d_2 & -q_3 \\ -d_1 & -p_1 & \eta_3 & b_2 \\ -d_2 & \eta_3 & -p_2 & -b_1 \\ q_3 & -b_2 & b_1 & -p_3 \end{pmatrix} = -d_1 \mathbf{K}_1 - d_2 \mathbf{K}_2 - q_3 \mathbf{Q}_3 + b_1 \mathbf{\Gamma}_1 + b_2 \mathbf{\Gamma}_2 + \eta_3 \mathbf{\Omega}_3 + \boldsymbol{\mu} \cdot \boldsymbol{\Delta} \quad (3.161)$$

with an additional condition that if  $q_3, \eta_3 = 0$ , then  $d_1/d_2 \neq b_1/b_2$ . We can see that a medium displaying 2D chirality is not necessarily non-depolarizing but it can be also depolarizing when  $q_3, \eta_3 \neq 0$ , which means that 2D chiral systems can be either time-reversal or non time-reversal, in agreement with what has been discussed in the context of surface plasmon optics [73, 78, 79]. In the special case where there is no depolarization ( $q_3, \eta_3 = 0$ ), the 2 eigenvectors can be simply written as

$$\mathbf{v}_+ = \begin{pmatrix} 1 \\ a_1 \\ a_2 \\ a_3 \end{pmatrix}, \mathbf{v}_- = \begin{pmatrix} 1 \\ -a_1 \\ -a_2 \\ a_3 \end{pmatrix}, \quad (3.162)$$

with  $a_1^2 + a_2^2 + a_3^2 = 1$ . The space conformation of these eigenvectors is shown in Fig. 3.7 (d). This conformation comes from the non-collinearity between the birefringence and the dichroism vectors, contrasting with a trivial anisotropic medium with mirror symmetry.

Finally, the generalization towards an optical chiral Mueller matrix is done by combining optical activity and a planar chirality, writing the matrix as a sum of  $\mathbf{m}_{O.A.}$  and  $\mathbf{m}_{P.C.}$  with a conformation of eigenvectors shown in Fig. 3.7 (e).

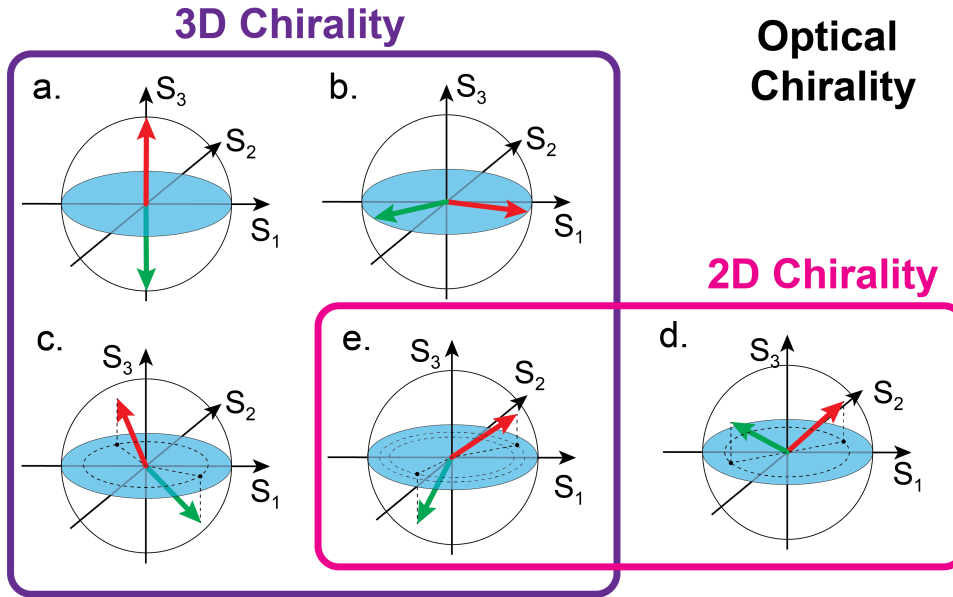


FIGURE 3.7: Different conformations for the eigenstates of an optically chiral medium. (a)-(c) show the typical conformations of a medium with pure optical activity expressed as Eq.(3.156). (d) shows the conformation of a medium presenting only 2D (planar) chirality expressed as Eq.(3.162). (e) shows the most general case with both optical activity and 2D chirality.

## Summary

Finally, we summarize the symmetry analysis of Mueller matrix in a synthetic way. First, for non-depolarizing Mueller matrices, we give in Table. 3.1 a list of media of different symmetries, with their symmetry features indicated, their typical cumulative Mueller matrix  $\mathbf{m}$  with letters representing independent parameters, the form of their total Mueller matrix  $\mathbf{M}$  and the corresponding conformation of eigenvectors.

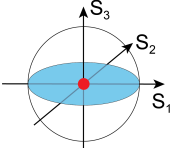
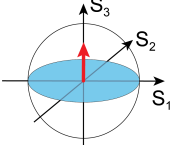
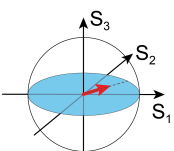
TABLE 3.1: Symmetry analysis for non-depolarizing Mueller matrices.

Type	Symmetry	$\mathbf{m}$	$\mathbf{M}$	Eigenvectors	Eigenvector conformation
Chiral isotropic	Rotation symmetry	$\begin{pmatrix} 0 & 0 & 0 & b \\ 0 & 0 & a & 0 \\ 0 & -a & 0 & 0 \\ b & 0 & 0 & 0 \end{pmatrix}$	$\begin{pmatrix} A_0 & 0 & 0 & D \\ 0 & A_1 & C & 0 \\ 0 & -C & A_2 & 0 \\ D & 0 & 0 & A_3 \end{pmatrix}$	$\begin{pmatrix} 1 \\ 0 \\ 0 \\ \pm 1 \end{pmatrix}$	
Non-chiral anisotropic	Mirror symmetry	$\begin{pmatrix} 0 & a & ka & 0 \\ a & 0 & 0 & kb \\ ka & 0 & 0 & -b \\ 0 & -kb & b & 0 \end{pmatrix}$	$\begin{pmatrix} A_0 & B & C & 0 \\ B & A_1 & D & E \\ C & D & A_2 & -F \\ 0 & -E & F & A_3 \end{pmatrix}$	$\begin{pmatrix} 1 \\ \pm a_0 \\ \pm ka_0 \\ 0 \end{pmatrix}$	
2D chiral anisotropic	Planar chirality	$\begin{pmatrix} 0 & a & k_1a & 0 \\ a & 0 & 0 & k_2b \\ k_1a & 0 & 0 & -b \\ 0 & -k_2b & b & 0 \end{pmatrix}$	$\begin{pmatrix} A_0 & B & C & G \\ B & A_1 & D & E \\ C & D & A_2 & -F \\ -G & -E & F & A_3 \end{pmatrix}$	$\begin{pmatrix} 1 \\ \pm a_1 \\ \pm a_2 \\ a_3 \end{pmatrix}$	
3D chiral anisotropic	3D chirality	$\begin{pmatrix} 0 & a & ka & d \\ a & 0 & c & kb \\ ka & -c & 0 & -b \\ d & -kb & b & 0 \end{pmatrix}$	$\begin{pmatrix} A_0 & B_1 & C_1 & G \\ B_2 & A_1 & D_2 & E_1 \\ C_2 & D_1 & A_2 & -F_1 \\ G & -E_2 & F_2 & A_3 \end{pmatrix}$	$\begin{pmatrix} 1 \\ a_1 \\ a_2 \\ a_3 \end{pmatrix}, \begin{pmatrix} 1 \\ a'_1 \\ a'_2 \\ -a_3 \end{pmatrix}$	
General bi-anisotropic	No symmetry	$\begin{pmatrix} 0 & a & k_1a & d \\ a & 0 & c & k_2b \\ k_1a & -c & 0 & -b \\ d & -k_2b & b & 0 \end{pmatrix}$	$\begin{pmatrix} A_0 & B_1 & C_1 & G_1 \\ B_2 & A_1 & D_2 & E_1 \\ C_2 & D_1 & A_2 & -F_1 \\ G_2 & -E_2 & F_2 & A_3 \end{pmatrix}$	$\begin{pmatrix} 1 \\ a_1 \\ a_2 \\ a_3 \end{pmatrix}, \begin{pmatrix} 1 \\ a'_1 \\ a'_2 \\ a'_3 \end{pmatrix}$	

Then, we look at purely depolarizing Mueller matrices. Since depolarizing Mueller matrices only have one depolarizing Stokes eigenvector, their symmetry properties are not easy to determine by resorting only to eigenstates analysis. As many source of depolarization are related to random inhomogeneities, corresponding Mueller matrices are not deterministic, and thus do not always have a well defined symmetry. However, for the case of deterministic inhomogeneity, their symmetry can be engineered by manipulating their elements, in order to reach specific forms associated with specific symmetries. Here we list 3 typical symmetries in Table. 3.2.



TABLE 3.2: Symmetry analysis for depolarizing Mueller matrices

Type	Symmetry	$\mathbf{m}$	$\mathbf{M}$	Eigenvectors	Eigenvector conformation
Depolarizing isotropic	Rotation symmetry mirror symmetry	$\begin{pmatrix} 0 & 0 & 0 & 0 \\ 0 & a & 0 & 0 \\ 0 & 0 & a & 0 \\ 0 & 0 & 0 & b \end{pmatrix}$	$\begin{pmatrix} A_0 & 0 & 0 & 0 \\ 0 & A_1 & B & 0 \\ 0 & B & A_1 & 0 \\ 0 & 0 & 0 & A_3 \end{pmatrix}$	$\begin{pmatrix} 1 \\ 0 \\ 0 \\ 0 \end{pmatrix}$	
Depolarizing 2D chiral	Planar chirality	$\begin{pmatrix} 0 & 0 & 0 & -a \\ 0 & -c & b & 0 \\ 0 & b & -d & 0 \\ a & 0 & 0 & -(c+d) \end{pmatrix}$	$\begin{pmatrix} A_0 & 0 & 0 & B \\ 0 & A_1 & C & 0 \\ 0 & C & A_2 & 0 \\ -B & 0 & 0 & A_3 \end{pmatrix}$	$\begin{pmatrix} 1 \\ 0 \\ 0 \\ k \end{pmatrix}$	
General bi-anisotropic	Mirror symmetry	$\begin{pmatrix} 0 & -b & -kb & 0 \\ b & a & 0 & -kd \\ kb & 0 & a & d \\ 0 & -kd & d & c \end{pmatrix}$	$\begin{pmatrix} A_0 & B & D & 0 \\ B & A_1 & C & E \\ D & C & A_2 & F \\ 0 & E & F & A_3 \end{pmatrix}$	$\begin{pmatrix} 1 \\ a_1 \\ a_2 \\ 0 \end{pmatrix}$	

### 3.6.4 Path for designing media with specific symmetries

Elaborating further on the notion of constraint discussed above, we discuss here how different symmetries can lead to design a medium itself. Concretely speaking, for a non-depolarizing medium, its symmetries can be not only given by the symmetries of its Mueller matrix, but can also be visualized directly from the conformation of two eigenvectors. For a depolarizing medium however, the symmetry constraint can not be completely embodied by the eigenstate approach because it has only one Stokes eigenvector. Here, the symmetry constraint appears directly on the matrix elements themselves. With these premises, we can draw a path for designing a non-depolarizing medium with specific symmetries exploiting both eigenvector conformations and Mueller matrix symmetries, and for a depolarizing medium, exploiting only Mueller matrix symmetries.

Our method basically resorts to the matrix product which corresponds to the physical picture of successive stacking. Starting from the most simple case, i.e. only one layer of homogeneous medium, the symmetry is indicated directly by the matrix elements, considering that we can address specific elements of the matrix with certain symmetries according to their physical interpretation. For a non-depolarizing medium, this is trivial. However for a depolarizing medium, one design is useful in the context of 2D chirality characterized by Eq.(3.161) summarized in Table. 3.2. According to the symmetry of the matrix given in Eq.(3.161), in order to construct a 2D Mueller matrix, we need to "switch on" the term  $q_3$  only and no other depolarizing terms. According to Eq.(3.93), it is possible to engineer only the linear spatial inhomogeneity terms in order to achieve

2D chirality by setting  $\Delta d_3 = 0$  and arranging the angle of each single linear structure inducing the inhomogeneity with a non zero correlation such that:

$$\langle \Delta d_1 \Delta b_2 - \Delta d_2 \Delta b_1 \rangle \neq 0 \quad (3.163)$$

A typical example is to arrange an elementary 2D chiral structure in an inhomogeneous way. This can be understood as follows by taking an L shaped structure which is planar chiral. A simple way to fulfill the condition of Eq.(3.163) is to take a inhomogeneous distribution of non-depolarizing 2D chiral structure modeled by a Mueller matrix with misalignment between linear birefringence and dichroism vector ( $b_1/b_2 \neq d_1/d_2$ ) as shown in Fig. 3.9 (a). When this structure is collectively arranged with identical orientations, it naturally forms a non-depolarizing 2D structure shown in Fig. 3.9 (b) where no local inhomogeneity is involved. When each structure is arranged with different orientations (Fig. 3.9 (c)), a depolarizing 2D medium is constructed. The advantage of this kind of depolarizing 2D chiral structure is that it gives a Mueller matrix without any linear feature as shown in Table. 3.2.

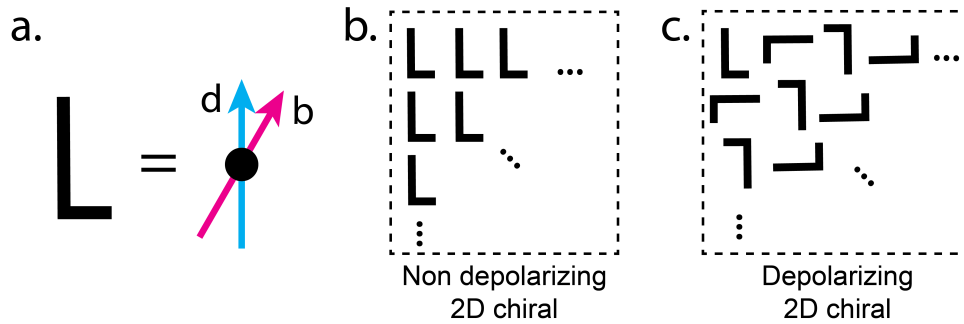


FIGURE 3.8: (a) shows the basic model of an elementary 2D chiral structure. (b) and (c) present the configurations that generate non-depolarizing and depolarizing 2D chiral structures.

f Then, if we have 2 layer-stacking where the total matrix is the product of the 2 associated homogeneous Mueller matrices, the symmetry can also be evaluated on the resulting matrix. Since a product of matrix exponentials writes as

$$\exp(\mathbf{m}_{tot}) = \exp(\mathbf{m}_A) \exp(\mathbf{m}_B), \quad (3.164)$$

the Baker-Campbell-Hausdorff relation leads to

$$\mathbf{m}_{tot} = \mathbf{m}_A + \mathbf{m}_B + \frac{1}{2}[\mathbf{m}_A, \mathbf{m}_B] + \frac{1}{12}[\mathbf{m}_A, [\mathbf{m}_A, \mathbf{m}_B]] + \frac{1}{12}[\mathbf{m}_B, [\mathbf{m}_B, \mathbf{m}_A]] + \dots \quad (3.165)$$

We also know that the cumulative differential matrix can be decomposed in a general way into the group generators as Eq.(3.100). From the known commutation relations between

these generators, we can generate specific elements of  $\mathbf{m}_{tot}$  from 2 individual homogeneous medium characterized by  $\mathbf{m}_A$  and  $\mathbf{m}_B$ . For example, using this method, the construction of a medium with a global optical activity, should, according to Eq.(3.157) display at least one generator among  $\mathbf{K}_3$  and  $\mathbf{\Gamma}_3$ . According to the commutation relations, a total matrix with  $\mathbf{K}_3$  or  $\mathbf{\Gamma}_3$  can be built from 2 linear media decomposed as

$$\mathbf{m}_A = -d_{A1}\mathbf{K}_1 - d_{A2}\mathbf{K}_2 + b_{A1}\mathbf{\Gamma}_1 + b_{A2}\mathbf{\Gamma}_2, \quad (3.166)$$

$$\mathbf{m}_B = -d_{B1}\mathbf{K}_1 - d_{B2}\mathbf{K}_2 + b_{B1}\mathbf{\Gamma}_1 + b_{B2}\mathbf{\Gamma}_2, \quad (3.167)$$

with  $k_1 = d_{A1}/d_{A2} = b_{A1}/b_{A2}$ ,  $k_2 = d_{B1}/d_{B2} = b_{B1}/b_{B2}$  and  $k_1 \neq k_2$ . Actually, this example reveals that the origin of optical activity in both microscopic and macroscopic scales, stems from a misalignment of elementary linear structures successively distributed along the light propagation direction, as shown in Fig 3.9 (a). Moreover one can prove that the optically active enantiomer can be obtained by simply switching the order between  $A$  and  $B$ .

Finally, we look into the situation corresponding to 3 and more than 3 layer stackings. In this case, only looking at the total matrix resulting from a cumulative matrix product will not be easy. Therefore, we introduce a method for constructing a medium through a manipulation of its eigenvectors (thus applicable to non-depolarizing Mueller matrices). In this context of non-depolarizing matrices, we can exploit the structure of the  $SO^+(1,3)$  group. The principle of this method is the following. Since a non-depolarizing Mueller matrix has always 2 non-depolarizing Stokes eigenvectors which can reveal the symmetry of the medium, manipulating the conformation of the eigenvectors is simply equivalent to applying a change of basis as described in Eq.(3.121) that only consists of a matrix product. In order to make the transformation realizable with Mueller matrices, the type of transformation is limited within the  $SO^+(1,3)$  group. Hence, if we target a Mueller matrix with a specific symmetry  $\mathbf{M}_f$  characterized by a certain conformation of eigenvectors, we can always find a Mueller matrix that serves as a transformation matrix within  $SO^+(1,3)$   $\mathbf{M}_{tr.}$  and an initial matrix  $\mathbf{M}_i$  from which the targeting matrix can be constructed by the product:

$$\mathbf{M}_f = \mathbf{M}_{tr.}\mathbf{M}_i\mathbf{M}_{tr.}^{-1}. \quad (3.168)$$

This construction corresponds to a physical picture of successive stacking of 3 layers characterized by  $\mathbf{M}_{tr.}$ ,  $\mathbf{M}_i$  and  $\mathbf{M}_{tr.}^{-1}$  respectively, where  $\mathbf{M}_{tr.}$  is chosen according to the targeted relation between the eigenvectors of  $\mathbf{M}_i$  and  $\mathbf{M}_f$ .

We present here some examples of our method. First let us start from a simple case for constructing a pure bi-isotropic medium represented by the eigenvectors shown in Fig. 3.6 (a). Since its eigenstates are orthogonal, this medium can be simply obtained by a  $90^\circ$  rotation of a linear anisotropic medium with eigenvectors shown in Fig. 3.6 (b)

which can be realized by a linear birefringent medium (e.g. a quarter-wave-plate) with the appropriate azimuth of the fast axis. If the Mueller matrix of the initial linear medium  $\mathbf{M}_L$  is written as

$$\mathbf{M}_L = \exp(-d\mathbf{K}_1 - dk\mathbf{K}_2 + b\mathbf{\Gamma}_1 + bk\mathbf{\Gamma}_2) \quad (3.169)$$

with  $b, d$  and  $k$  arbitrary real numbers, the appropriate matrix on which to apply the rotation can be therefore written as

$$\mathbf{M}_{tr.} = \exp(-b'k\mathbf{\Gamma}_1 + b'\mathbf{\Gamma}_2) \quad (3.170)$$

with  $b'$  and  $k$  arbitrary real numbers so that the angle of fast axis is in  $45^\circ$  with respect to the polarization axis of  $\mathbf{M}_L$ . Finally the Mueller matrix of the total bi-isotropic medium  $\mathbf{M}_{B.I.}$  can be constructed as

$$\mathbf{M}_{B.I.} = \exp(-b'k\mathbf{\Gamma}_1 + b'\mathbf{\Gamma}_2) \cdot \exp(-d\mathbf{K}_1 - dk\mathbf{K}_2 + b\mathbf{\Gamma}_1 + bk\mathbf{\Gamma}_2) \cdot \exp(b'k\mathbf{\Gamma}_1 - b'\mathbf{\Gamma}_2) \quad (3.171)$$

The physical picture of such a system is a linear anisotropic medium sandwiched between 2 quarter-wave plates with the polarization axis of the linear anisotropy arranged successively with an angular increment of  $45^\circ$  as shown in Fig 3.9 (b).

A second example is to construct a non-depolarizing (time reversal) 2D chiral system which has the eigenvector conformation shown in Fig. 3.7 (d). Looking closely at it, this conformation can be obtained generally by applying a Lorentz boost along the  $OS_3$  direction and an in-plane rotation expressed as

$$\mathbf{M}_{tr.} = \mathbf{\Lambda}(\zeta_3, \theta_3) = \exp(-d_3\mathbf{K} + b_3\mathbf{\Gamma}). \quad (3.172)$$

Starting from a trivial linear anisotropic medium characterized by  $\mathbf{M}_L$ , with eigenvectors shown in Fig. 3.6 (b), the Mueller matrix of a planar chiral system  $\mathbf{M}_{P.C}$  can be constructed as

$$\mathbf{M}_{P.C} = \mathbf{M}_{tr.}\mathbf{M}_L\mathbf{M}_{tr.}^{-1} = \exp(-d_3\mathbf{K} + b_3\mathbf{\Gamma}) \cdot \mathbf{M}_L \cdot \exp(d_3\mathbf{K} - b_3\mathbf{\Gamma}). \quad (3.173)$$

Since the matrix  $\mathbf{M}_{tr.}$  stands for a bi-isotropic medium and  $\mathbf{M}_{tr.}^{-1}$  stands for its enantiomer, the physical image of this kind of 2D chiral system is a linear anisotropic medium sandwiched between 2 bi-isotropic media having opposite handedness, as shown in Fig 3.9 (c). Moreover, if we look into this path construction, we can split the optical response of this chiral system into 2 parts with opposite handedness as

$$\mathbf{M}_{P.C} = [\exp(-d_3\mathbf{K} + b_3\mathbf{\Gamma}) \cdot \mathbf{M}_L^{1/2}] [\mathbf{M}_L^{1/2} \cdot \exp(d_3\mathbf{K} - b_3\mathbf{\Gamma})] = \mathbf{M}_{LH}\mathbf{M}_{RH} \quad (3.174)$$

One can then show that the left handed and right handed parts can be actually decomposed as a function of  $\mathbf{m}_A$  and  $\mathbf{m}_B$  defined in Eq.(3.166) and Eq.(3.167) as

$$\mathbf{M}_{LH} = \exp(\mathbf{m}_A) \exp(\mathbf{m}_B), \quad \mathbf{M}_{RH} = \exp(\mathbf{m}_B) \exp(\mathbf{m}_A) \quad (3.175)$$

with the physical picture shown in Fig 3.9 (d). Thereby, we get another, even more trivial, way to construct a 2D chiral medium by purely linear anisotropic systems.

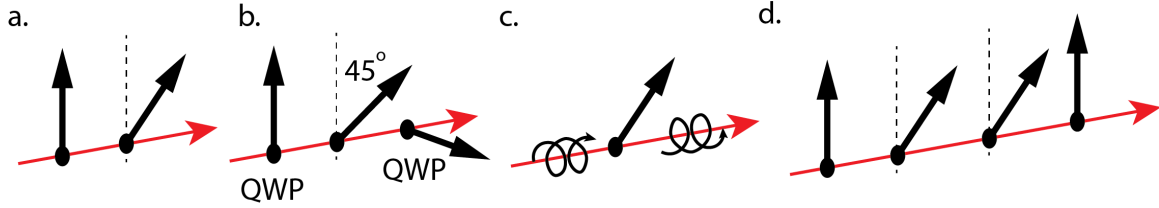


FIGURE 3.9: (a)-(d) display the physical picture associated with different examples of medium constructions with specific symmetries, where the red arrow indicates the direction of propagation, the black arrows give the direction of the polarization axis. The helix represents a 3D helix, either right or left handed.

This method based on the eigenvector analysis and symmetry study of the Mueller matrix is general and clearly opens new possibilities for the conception of heterostructures, metasurfaces and optical systems for designed polarization manipulations and tailored new polarization dynamics. For instance, the method can be inspired by, and operational in the context of recent studies that explore from a bottom-up perspectives the connections between structured systems and chirality [21, 80].

### 3.7 Conclusion

This chapter starts from the normal form of a Mueller matrix as a physical constraint put on Mueller matrices formulated in the Minkowski space where all Stokes vectors can be represented. By exploiting the group-like algebraic structure of the Stokes-Mueller formalism, we identify 2 main substructures out of the ensemble of all physically realizable Mueller matrices:  $SO^+(1, 3)$  Lie group for all non-singular, non-depolarizing Mueller matrices and a Lie monoid for all non-singular Mueller matrices. With this analysis, we perform an eigenstate analysis for Mueller matrices that relates directly the symmetry of conformation of Mueller matrix eigenvectors in the Poincaré sphere to the symmetry properties of the medium characterized by this Mueller matrix. We give some applications based on these concepts such as differential decomposition and polarization dynamics analysis. This leads us to propose an original method for constructing optical media with specific symmetries and corresponding specific polarization features.

## Chapter 4

# Mueller polarimetry

In this chapter, we investigate the experimental realization of Mueller matrix polarimetry based on a dual rotating quarter-wave plate (QWP) polarimetry [81] in a broad-band detection scheme. We introduce in details our calibration procedure to get the basic parameters of the 2 QWPs under the homogeneous elliptical birefringence model. Then, the quality of our measurements has been evaluated by the basic test of hypothesis and through a statistical noise analysis.

We also introduce the standard procedure for performing the experiment including a reference correction method and data processing, distinguishing between passive and active media. We finally propose possible measuring configurations offered by our setup, depending on the sample properties that we are interested in.

### 4.1 Introduction of Mueller polarimetry

Polarimetry (also known as ellipsometry) is a well known and established experimental tool to characterize the polarization optical properties of samples such as crystals, multilayer thin films, molecular solutions [82], meta-materials and nano-structures [83, 84]. This tool aims at measuring the Jones matrix or Mueller matrix of the medium from which the polarimetric properties are extracted by numerical data processing. The method implemented for a Mueller matrix is called Mueller polarimetry (or Mueller ellipsometry).

From the mathematical description of a Mueller matrix, we can see that Mueller polarimetry needs to determine all 16 matrix elements. Since a direct measurable quantity can only be an intensity corresponding to first element of the Stokes vector, we need to vary the intensities that correspond to different incident polarization states and analyze the emergent polarization states in order to determine all the 16 different unknown matrix elements. To this aim, a general Mueller polarimetry is built in 5 parts: a light source, an optical system for polarization state generation (PSG), the sample to be characterized, an optical system for polarization state analysis (PSA) and finally a detector. This sequence is described in Fig. 4.1.

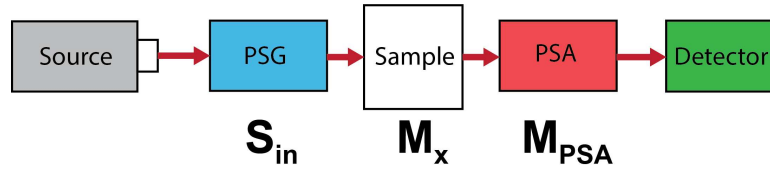


FIGURE 4.1: The general structure of Mueller polarimetry with the input polarization states Stokes vector after the PSG (polarization state generator) noted as  $\mathbf{S}_{in}$ , the Mueller matrix of the unknown sample noted as  $\mathbf{M}_x$  and the Mueller matrix of the ensemble of the PSA (polarization state analyzer) noted as  $\mathbf{M}_{PSA}$ .

The light coming from the light source passes through the PSG and gives a known polarization state corresponding to the input Stokes vector  $\mathbf{S}_{in}$ . The light then will go through the sample characterized by a Mueller matrix  $\mathbf{M}_x$  that we aim to measure with the PSA described by its own known Mueller matrix  $\mathbf{M}_{PSA}$ . The output final Stokes vector for the polarization state  $\mathbf{S}_d$  can be written as

$$\mathbf{S}_d = \mathbf{M}_{PSA} \mathbf{M}_x \mathbf{S}_{in} \quad (4.1)$$

where the measurable first element of  $\mathbf{S}_d$  corresponds to the detected intensity. As  $\mathbf{S}_{in}$  and  $\mathbf{M}_{PSA}$  are known and vary according to the experimental settings, the first element of  $\mathbf{S}_d$  can be written as a function of the vector and matrix elements of  $\mathbf{S}_{in}$  and  $\mathbf{M}_{PSA}$  with the matrix elements of  $\mathbf{M}_x$  as parameter. The principle of the measurement thus becomes a multi-variable linear regression problem.

Basically, there are mainly 2 different approaches for the measurement. A first approach is to vary the parameters of PSG and PSA with different frequencies, and to perform a Fourier transform of the measured intensity signal. The Mueller matrix elements that correspond to the amplitudes of different combinations of frequencies then can be solved from a linear equation system [85, 86]. The variation of the PSG and PSA can be realized by rotating the polarization optical component or by oscillating the retardance of a photoelastic modulator. The Mueller matrix therefore can be obtained in a single measurement, keeping in mind however that each measurement can be only done at one wavelength.

The second approach is to preset a certain number  $N$  of different combinations of the PSG and PSA parameters. Measurements are performed for each combination of a given PSA and PSG and then the system switches to the next combination [81, 86, 87]. Following this approach allows one to obtain a Mueller matrix after  $N$  individual measurements. More time consuming than the first one, this approach is suitable for measurements coupled to slow but broad-band detectors such as imaging camera or a CCD-based spectrometer.

In this thesis, where we aim for broadband Mueller matrices and imaging measurements, we will design our Mueller polarimetry based on the second approach, using 2 QWPs as discussed in the next section.

## 4.2 Dual rotating QWP broad-band Mueller polarimetry

As just mentioned, in order to meet our measurement needs, our Mueller polarimetry is realized using 2 rotating QWPs coupled with a CCD based spectrometer, i.e. so-called dual rotating QWP broad-band Mueller polarimetry. In the following sections, the details of the optical setup and the standard procedure for basic calibration are presented. We will also discuss the evaluation of the accuracy related to the calibration, including noise. Finally, we describe the standard reference correction procedure and our method for processing of measurement data.

### 4.2.1 Optical setup

In this section, we detail the optical features of our dual rotating QWP Mueller polarimetry and the associated measurement protocol. The core part of the dual rotating QWP Mueller polarimetry is shown in Fig.4.2. As seen, the polarization state generator and the polarization state analyzer are both composed of fixed linear polarizers (LP) whose the optical axis are set to be orthogonal with each other and rotating QWPs. The rotation of the QWP in the PSG, leads to explore all the states of polarization along a meridian in the Poincaré sphere which includes all types of polarization states. The combination of a rotating QWP together with the linear polarizer in the PSA can analyze all types of polarizations too.

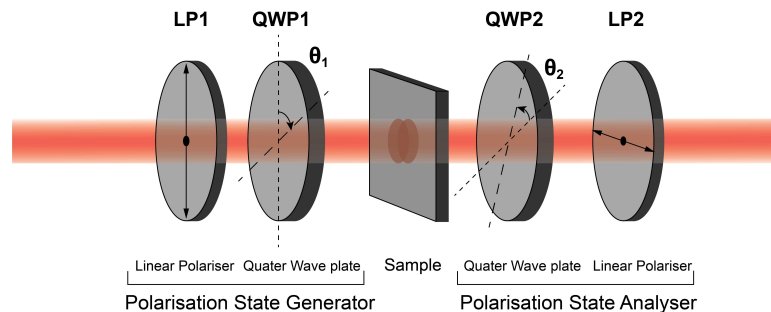


FIGURE 4.2: The core feature of a general dual rotating QWP Mueller polarimetry with the PSG composed by a fixed vertical polarizer and a rotating QWP, the PSA composed by another rotating QWP and a fixed horizontal linear polarizer.



To be explicit, at each combination of the two QWPs, the intensity finally measured  $I_{out} = S_{out}^0$  can be related to the incident polarization state  $\mathbf{g}$  prepared by PSG, the Mueller matrix of the sample  $\mathbf{M}_x$  and the first row vector of the Mueller matrix of the PSA  $\mathbf{a}$  according to:

$$I_{out} = \mathbf{a} \cdot \mathbf{M}_x \cdot \mathbf{g} = \begin{pmatrix} a_{00} & a_{01} & a_{02} & a_{03} \end{pmatrix} \cdot \begin{pmatrix} m_{00} & \cdots & m_{03} \\ \vdots & \ddots & \vdots \\ m_{30} & \cdots & m_{33} \end{pmatrix} \cdot \begin{pmatrix} g_0 \\ g_1 \\ g_2 \\ g_3 \end{pmatrix} \quad (4.2)$$

with  $g_j$  and  $a_{0i}$  depending on the angles of the QWP in PSG and PSA  $\theta_1, \theta_2$ . If we perform multiple acquisitions with different angle combinations  $\{\theta_1, \theta_2\}_k$  for any time  $k$

$$I_{out}^{(k)} = \sum_{i=0}^3 \sum_{j=0}^3 a_{0i}^{(k)} g_j^{(k)} m_{ij}, \quad (4.3)$$

a linear equation system with 16 unknown variable  $m_{ij}$  can be built. We can arrange the Mueller matrix elements into a 16 dimensional column vector  $\mathbf{x}_m$ . The matrix associated with this linear equation system consists of the  $a_{0i}^{(k)} g_j^{(k)}$  noted as  $\mathbf{A}_m$ , and the intensities measured in each acquisition can be arranged also into a column vector  $\mathbf{I}_m$  with the dimension of the total number of single acquisition  $N$ . The problem to solve in order to obtain the Mueller matrix of the sample then becomes:

$$\mathbf{I}_m = \mathbf{A}_m \cdot \mathbf{x}_m. \quad (4.4)$$

We can impose conditions on the number of single acquisition. In order to have unique solution (precise or least squared), we impose that the rank of matrix  $\mathbf{A}_m$  should be larger than 16. Therefore, the number of single acquisition should be at least 16. But this can not ensure this matrix to be of rank 16 due to some combinations of angle that can reduce the rank of the matrix. To really ensure a unique solution while reducing the random error, we rather overdetermine the linear equation system therefore, from which a unique least squared solution is obtained. So the determination of the Mueller matrix elements in reality can be also considered as a problem of multiple linear regression with

$$\mathbf{I}_m = f(\mathbf{A}_i) = m_{00}\mathbf{A}_1 + m_{01}\mathbf{A}_2 + \dots + m_{33}\mathbf{A}_{16} + \boldsymbol{\rho}, \quad (4.5)$$

where  $\mathbf{A}_i$  is the  $i^{th}$  column vector of the matrix  $\mathbf{A}_m$  and  $\boldsymbol{\rho}$  is a random error vector with its elements  $\rho_k$  fulfilling  $\langle \rho_k \rangle = 0$  and  $\sigma^2(\rho_k) = \sigma_r^2$ . Using the principle of least square,

the most probable solution for the Mueller matrix elements can be obtained so that

$$\boldsymbol{\rho}^T \boldsymbol{\rho} = (\mathbf{I}_m - \mathbf{A}_m \cdot \mathbf{x}_m)^T \cdot (\mathbf{I}_m - \mathbf{A}_m \cdot \mathbf{x}_m) \quad (4.6)$$

takes a minimum value. Note that the systematic error estimation is based on this equation shown in Appendix E. Therefore, by imposing

$$d[(\mathbf{I}_m - \mathbf{A}_m \cdot \mathbf{x}_m)^T \cdot (\mathbf{I}_m - \mathbf{A}_m \cdot \mathbf{x}_m)] = -d(\mathbf{I}_m^T \cdot \mathbf{A}_m \cdot \mathbf{x}_m) - d(\mathbf{x}_m^T \cdot \mathbf{A}_m^T \mathbf{I}_m) + d(\mathbf{x}_m^T \cdot \mathbf{A}_m^T \cdot \mathbf{A}_m \cdot \mathbf{x}_m) = 0 \quad (4.7)$$

that is:

$$(\mathbf{x}_m^T \cdot \mathbf{A}_m^T \cdot \mathbf{A}_m - \mathbf{I}_m^T \cdot \mathbf{A}_m) \cdot d\mathbf{x}_m + d\mathbf{x}_m^T \cdot (\mathbf{A}_m^T \cdot \mathbf{A}_m \cdot \mathbf{x}_m - \mathbf{A}_m^T \mathbf{I}_m) = 0 \quad (4.8)$$

the column vector of the Mueller matrix elements can only write as

$$\mathbf{x}_m = (\mathbf{A}_m^T \cdot \mathbf{A}_m)^{-1} \mathbf{A}_m^T \cdot \mathbf{I}_m \quad (4.9)$$

This is the important formula that we use for data processing in order to obtain our experimental Mueller matrix.

In our experiments, where we aim to study broad-band optical responses, intensities correspond to spectra acquired by a CCD camera coupled with a monochromator. From Eq.(4.9), we can see that in order to get a measurement of the Mueller matrix as accurate as possible, each element of vector  $\mathbf{I}_m$  should be strictly proportional to the intensity. This thereby requires a strict linearity for the detector for all wavelengths and all intensities below the saturation level of the CCD.

We use a protocol using in total 64 different angle combinations  $\{\theta_1, \theta_2\}$ . Starting from the initial position of the 2 QWPs with the wavelength-averaged fast axis aligned with vertical linear polarizer, the first QWP rotates 7 times with each step of  $22.5^\circ$  and for each position of the QWP in the PSG, the QWP in the PSA rotates 7 times with a step of  $22.5^\circ$  then back to its initial position. The time taken for this whole procedure for 64 acquisitions in total depends largely on the acquisition time of each spectrum. Typically, for a single spectrum acquisition time of 1s, the total process takes ca. 1.5 min. We synchronize the motorized rotators that control the 2 QWPs with the spectra acquisition of the spectrometer. The protocol for one complete Mueller matrix measurement is presented as the diagram in Fig.4.3.

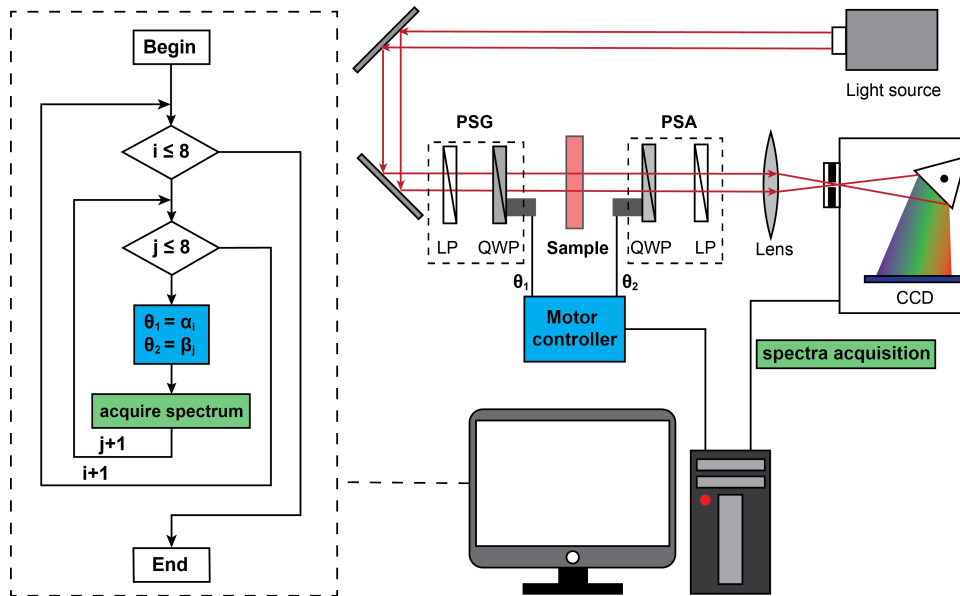


FIGURE 4.3: The 2 QWPs in PSA and PSG are controlled by a motorized rotator connected to the computer. Achromatic lenses are used to get a focused beam at the entrance of the monochromator. The monochromator coupled with the CCD is also connected to the computer. The measurement protocol shown in the diagram on the left is synchronized through the computer by a home-made Python script. The position of the first QWP takes 8 values noted as  $\alpha_i$  with  $i \in [1, 8]$  while the position of the second QWP takes also 8 values noted as  $\beta_j$  with  $j \in [1, 8]$ . All different combinations of  $\theta_1$  and  $\theta_2$  are implemented according to this diagram.

The light source can be switched to different sources from a broad band white light to a monochromatic source using a home-made plug-and-play switchable optical mount. White sources available for this experiment are a UV-Vis-NIR deuterium-tungsten halogen source from Ocean Optics (DH-2000) and a tungsten halogen source from Ocean Optics (HL-2000LL). The monochromatic light source is a wavelength tunable Supercontinuum white light laser with a filter allowing tuning the output wavelength from 405nm to 890nm (NKT photonics). With different fiber adapters at the input of the setup, these different light sources can be used according to the experimental needs. The setup is mainly working in the visible range and we want to work in a range as broad as possible. In order to do so, all main optics such as mirrors and lenses are chosen as achromatic in the visible range.

For polarization optics, the polarizer used in this experiment are of 2 different types which depend on the application. The first type is a nanoparticle linear film polarizer from Thorlabs (LPVISC100-MP2) which bandwidth extends from 510 nm to 800 nm. The second type of polarizer is a Glan-Taylor prism polariser from Thorlabs, relatively more broad-band (350nm to 2300nm) and uniform in the extinction ratio ( $10^5 : 1$ ). Note that however, the Glan-Taylor polarizer strictly works at normal incidence for the light, so that it is not suitable for measurements done in the imaging Fourier space, discussed

in detail in the following section. QWPs are achromatic zero order QWPs made from quartz-MgF<sub>2</sub> from Thorlabs. The mixture quartz-MgF<sub>2</sub> is used in order to minimize the wavelength dependence of the retardance which has a relatively flat response that we are going to probe in detail in the calibration procedure.

The motorized rotator is a rotation mount step motor (8MPR16-1) with the precision of  $5 \times 10^5$  degree from Standa, computer controlled. The spectrometer we use is a 300mm focal length monochromator (HRS300) with the possibility to select optical gratings coupled to a CCD camera (PIXIS1024) from Princeton Instrument. Finally, a Python script has been designed to synchronize the controller and the spectrometer with the logic shown in Fig.4.3.

## 4.2.2 Calibration procedure

Before performing the measurement, a precise calibration must be properly done. From the measurement method, the polarizer in PSA should be placed perfectly orthogonal to the vertical polarizer in PSG which is the reference for the whole system. According to Eq. (4.9), in order to get the measured Mueller matrix, an appropriate Mueller matrix model for the QWP should be chosen with the parameters of this Mueller matrix precisely determined. In this section, we introduce our standard calibration procedures which include mainly the calibration of the polarizer and of the QWPs.

### Calibration of the horizontal linear polarizer

The calibration of the linear polarizer in PSA aims at finding as precisely as possible, the orthogonal position with respect to the vertical polarizer in PSG. By assuming that the axis of polarization for the polarizer has barely no wavelength dependance, the calibration can be based on the extinction Malus' law for 2 polarizers. According to the Malus' law for an ideal polarizer, the transmitted intensity can be written as a function of the angle between the axis of 2 polarizers as [88]

$$I_T(\theta) = I_0 \cos^2 \theta. \quad (4.10)$$

In reality however, there is no such perfect polarizer, and the Malus' law for a real polarizer rather writes

$$I_T(\theta) = I_0 \frac{1 + d^2}{1 + d} \cos^2 \theta + I_0 \frac{1 - d^2}{1 + d} \sin^2 \theta \quad (4.11)$$

with  $d$  is the ratio of the extinction defined as

$$d = \frac{I_{max} - I_{min}}{I_{max} + I_{min}}. \quad (4.12)$$

According to this law, the position of the polarizer can be determined by finding the minimum of the transmission intensity by rotating the polarizer. However to precisely determine this position, we chose first to reduce the interval of the angle step by step down to the level of  $\pm 0.4^\circ$ . We can then expand Eq.(4.11) around the minima ( $\theta = (2n+1)\pi/2$ ) of the total transmitted intensity, giving

$$I_T(\theta) = \frac{1}{1+d} + \frac{d^2}{1+d} \cos 2\theta = (1-d) + \frac{d^2}{1+d} 2\theta^2. \quad (4.13)$$

The intensity variation at the vicinity of the minima can therefore be modeled by a parabolic function of the angle. Once we thus reduce the interval of the minima, we can rotate the polarizer with an increment as small as possible through the whole angular interval with an acquisition of the spectra at each step. We can then plot the total intensity by integrating the spectra as a function of angle and by fitting these points with a parabolic equation, and the best estimate of the cross polarization position with respect to the first polarizer can be eventually obtained.

One example we obtained in our experiment for our Glan-Taylor polarizer is shown in Fig. (4.4).

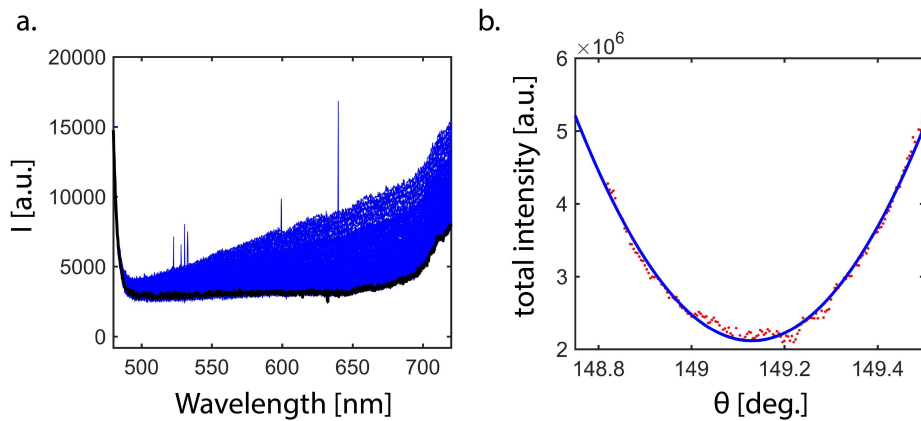


FIGURE 4.4: (a) shows all spectra acquired at the vicinity of the Malus extinction point. The integrated total intensity is plotted as a function of the azimuth of the polarizer  $\theta$  with the parabolic fitting shown in (b). The spectrum closest to the azimuth at the minimum from the fit is marked in black in (a) showing the validity of the fit and the calibration method.

### Calibration of the QWPs

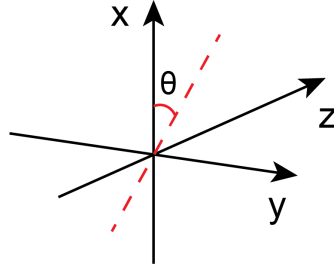


FIGURE 4.5: Coordinate setting for the orientation of the fast axis with the  $z$  axis corresponding to the light propagation direction

After calibrating the horizontal polarizer, we can start to calibrate each one of the two QWPs. Before that, we first chose a Mueller matrix that describes the QWP. The most simple one is the Mueller matrix of an ideal linear retarder  $\mathbf{M}_r$  with an azimuth  $\theta$  indicating the orientation of the fast axis with respect to the vertical Cartesian axis ( $x$ ) of the laboratory frame as shown in Fig. 4.5 and  $\delta$  the phase difference between two eigenstates of the retarder as :

$$\mathbf{M}_r = \begin{pmatrix} 1 & 0 & 0 & 0 \\ 0 & \cos^2 2\theta + \sin^2 2\theta \cos \delta & \sin 2\theta \cos 2\theta (1 - \cos \delta) & \sin 2\theta \sin \delta \\ 0 & \sin 2\theta \cos 2\theta (1 - \cos \delta) & \sin^2 2\theta + \cos^2 2\theta \cos \delta & -\cos 2\theta \sin \delta \\ 0 & -\sin 2\theta \sin \delta & \cos 2\theta \sin \delta & \cos \delta \end{pmatrix}. \quad (4.14)$$

However, we realized that this model is not working properly with our measurement protocol. While doing an empty sample experiment, it did not provide any result close enough to the expected identity matrix. We will use another model for describing the real linear retarder. The most general model to describe a real linear retarder is the homogeneous dichroic elliptic birefringent (HDEB) medium which takes into account all possible physical effect in a retarder type wave plate as discussed in [89, 90]. The parameters we need are the ellipticity and azimuth of the eigenstate of polarization, the extinction ratio and retardance between the 2 eigenstates. Generally, this matrix is however a little bit too complicated for the case of a QWP. B. Boulbry [91] in fact has shown that this model can be simplified to a homogeneous elliptic birefringent model (HEB) as most of the wave-plates yield no dichroism. The Mueller matrix of a HEB medium  $\mathbf{M}_{HEB}$  can thus be written as

$$\mathbf{M}_{HEB} = \begin{pmatrix} 1 & 0 & 0 & 0 \\ 0 & d^2 - e^2 - f^2 + g^2 & 2(de + fg) & 2(df - eg) \\ 0 & 2(de - fg) & -d^2 + e^2 - f^2 + g^2 & 2(e f + dg) \\ 0 & 2(df + eg) & 2(e f - dg) & -d^2 - e^2 + f^2 + g^2 \end{pmatrix} \quad (4.15)$$

with

$$\begin{aligned}
 d &= \cos 2\varepsilon \cos 2\theta \sin \frac{\delta}{2} \\
 e &= \cos 2\varepsilon \sin 2\theta \sin \frac{\delta}{2} \\
 f &= \sin 2\varepsilon \sin \frac{\delta}{2} \\
 g &= \cos \frac{\delta}{2}
 \end{aligned} \tag{4.16}$$

where  $\theta$  and  $\varepsilon$  are the azimuth and the ellipticity of the polarization eigenstates of the medium with  $\delta$  the retardance between the 2 eigenstates of polarization.

Within this description, the parameters are wavelength dependent and must therefore be calibrated for each wavelength individually, in contrast with the case of the polarizer. First we calibrate the fast axis for each wavelength, corresponding to the parameter azimuth for the HEB model. To do so, by rotating the QWP placed between the 2 calibrated orthogonal polarizers, we can find a range of positions where the total transmitted intensity is minimum. By reducing this range to an extent where the transmission intensity for any wavelength go through a minimum sequentially, we can start acquiring the spectra in this range of angle (ca.  $\pm 0.7^\circ$ ) with a tiny step (ca.  $0.004^\circ$ ) of the motorized rotator. After such an acquisition, the series of spectra are analyzed wavelength after wavelength. The intensity for each wavelength is plotted as a function of angle and modeled by a parabolic function, yielding the angle positions for each minimum as the position of the fast axis at each wavelength. In this way, we obtain the fast axis position as a function of wavelength  $\theta(\lambda)$ . Since  $\theta(\lambda)$  shows an oscillating feature, we chose a wavelength-averaged position that corresponds to the mean position of the fast axis  $\bar{\theta}$  in order to fix the initial position of the QWP. The difference between this mean position and the exact position of the fast axis at each wavelength  $\Delta\theta(\lambda) = \theta(\lambda) - \bar{\theta}$  is saved to retrieve the exact azimuth for each wavelength. An example of such a difference  $\Delta\theta$  determined from this calibration procedure is shown in Fig.4.6.

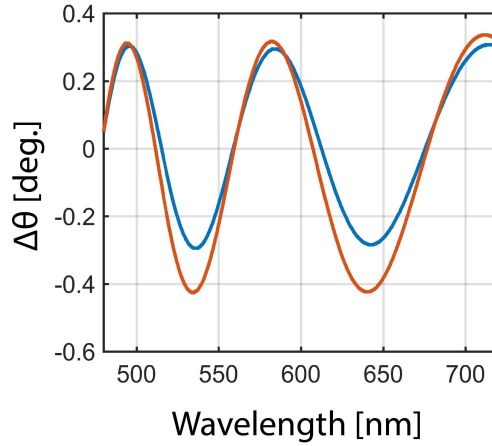


FIGURE 4.6: The fast axis position measured from a mean fast axis position for the QWP in PSG and PSA  $\Delta\theta_1$  (blue line) and  $\Delta\theta_2$  (red line) is plotted as a function of wavelength.

The fast axis calibration of the two QWPs therefore corresponds to the determination of the mean fast axis position for the QWPs in PSG and PSA  $\bar{\theta}_1$  and  $\bar{\theta}_2$  and the wavelength dependence compensation vector for the exact fast axis at each wavelength  $\Delta\theta_1(\lambda)$  and  $\Delta\theta_2(\lambda)$ .

We can then start to calibrating the other parameters within the HEB model, i.e. the wavelength dependence of ellipticity  $\varepsilon(\lambda)$  and retardance  $\delta(\lambda)$ . To do so, we go through the standard Mueller matrix measurement procedure described in Fig.4.3 but with nothing between the PSG and PSA (empty setup). Since the polarization state of the light can not be modified when propagating through air only (optically close to vacuum conditions), the measured Mueller matrix is expected to be a four-by-four identity matrix  $\mathbf{I}_4$ . We now use a minimization method to fit the actually measured Mueller matrix to an identity matrix by adjusting the parameters of ellipticity  $\varepsilon(\lambda)$  and retardance  $\delta(\lambda)$  for the 2 QWPs at each wavelength.

Explicitly, according to Eq.(4.9), the Mueller matrix elements  $\mathbf{x}_m$  at a given wavelength  $\lambda$  obtained using certain parameters of ellipticity  $\varepsilon_1(\lambda)$ ,  $\varepsilon_2(\lambda)$  and retardance  $\delta_1(\lambda)$ ,  $\delta_2(\lambda)$  can be written as

$$\mathbf{x}_m(\lambda; \varepsilon_1(\lambda), \varepsilon_2(\lambda), \delta_1(\lambda), \delta_2(\lambda)) = [(\mathbf{A}_m^T \cdot \mathbf{A}_m)^{-1} \mathbf{A}_m^T] (\lambda; \varepsilon_1(\lambda), \varepsilon_2(\lambda), \delta_1(\lambda), \delta_2(\lambda)) \cdot \mathbf{I}_m. \quad (4.17)$$

In order to get the best estimated parameter of the ellipticity and retardance, we try to minimize, by adjusting  $\{\varepsilon_1(\lambda), \varepsilon_2(\lambda), \delta_1(\lambda), \delta_2(\lambda)\}$  for each wavelength, the Frobenius norm  $\|\cdot\|_F$  [40]

$$\|\mathbf{x}_m(\lambda; \varepsilon_1(\lambda), \varepsilon_2(\lambda), \delta_1(\lambda), \delta_2(\lambda)) - \mathbf{I}_4^v\|_F \quad (4.18)$$

between the column vector  $\mathbf{x}_M$  of Mueller matrix elements and  $\mathbf{I}_4^v$  that stands for the line vector constructed by stacking a four-by-four identity matrix. To do so, we use the



Matlab<sup>TM</sup> routine "fitmincon" and Fig. 4.7 shows the results obtained for one estimation for the retardance and ellipticity of the 2 QWPs. These results show that the ellipticity is indeed a very small corrective parameter and that the retardance is in a good agreement with the data provided by the manufacturer [92].

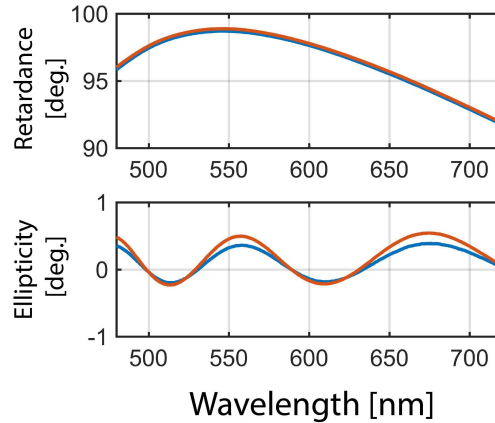


FIGURE 4.7: Wavelength dependences of the retardance  $\delta(\lambda)$  and the ellipticity  $\varepsilon(\lambda)$  determined from our calibration for each of the QWP in PSG (blue lines) and PSA (red lines).

Additionally, we can see that the retardance and the ellipticity of these two QWPs are slightly different. This reveals that there are unavoidable slight differences in angle between the light beam and the normal direction of the QWPs, implied from the shift observed in the retardance. These results thus show that an *in situ* calibration is indispensable in order to get accurate measurements beyond what is merely given by the manufacturer.

### Calibration accuracy

Once done the calibration of the linear polarizers and the two QWPs, the parameters that need to be kept throughout the experiments are the angle positions of the linear polarizers and the mean fast axis angle positions of each of the two QWPs. The vectors that save the information of the wavelength dependences of the exact fast axis position  $\{\Delta\theta_1(\lambda), \Delta\theta_2(\lambda)\}$ , of the ellipticity and of the retardance of two QWPs  $\{\varepsilon_1(\lambda), \varepsilon_2(\lambda), \delta_1(\lambda), \delta_2(\lambda)\}$  can then be built.

From these results, we can see the experimentally determined Mueller matrix of an empty setup shown in Fig.4.8. Noted as  $\mathbf{M}_{empty}$ , the matrix falls very closely to the expected four dimensional identity matrix. However to further evaluate the validity of the HEB model for QWPs and the accuracy of the measurement quantitatively, we perform a series of statistical test of hypothesis on the calibration parameters, describing its fitting quality (detailed in Appendix D). As we mentioned above in Eq.(4.5), the solving

procedure for the Mueller matrix elements from a series of intensity measurements under different PSA and PSG configurations is a problem of multiple variable linear regression.

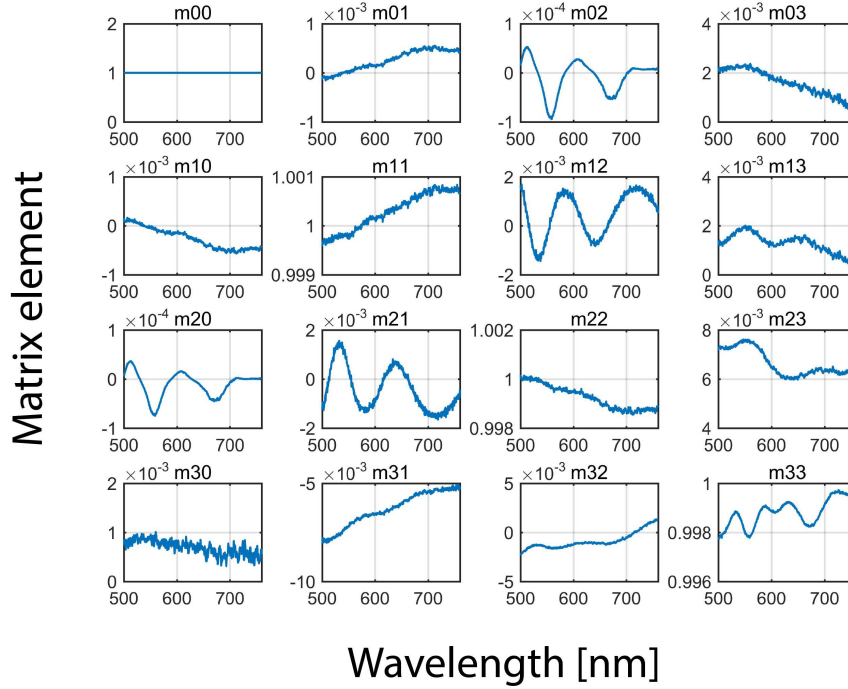


FIGURE 4.8: A typical Mueller matrix of an empty setup measurement  $\mathbf{M}_{empty}$  using the HEB model.

The first test needed is a significance test of linearity between  $\mathbf{I}_m$  and  $\mathbf{A}_m$  (see Eq.(4.5)), which indicates the existence of matrix elements that relate the incident Stokes vector to the final intensity. We can set the statistical hypothesis

$$\mathbf{H}_0 : m_{00} = m_{01} = \dots = m_{33} = 0$$

$$\mathbf{H}_1 : m_{00}, m_{01}, \dots, m_{33} \text{ are not all zero}$$

Thus parameter for the test of hypothesis is  $F$  defined

$$F = \frac{SSR/16}{SST/(64 - 16)} = \frac{[\sum_{i=1}^{64} (I_i - \bar{I}_i)^2] / 16}{(\sum_{i=1}^{64} \rho_i^2) / (64 - 16)} \quad (4.19)$$

where  $SSR$  stands for the residual sum of square,  $SST$  stands for the total sum of square,  $I_i$  is the matrix element of vector  $\mathbf{I}_m$  and  $\rho_i$  is the element of the residue vector  $\boldsymbol{\rho}$ . The criterion to tell whether  $H_0$  is valid is to investigate  $F \sim F_c(16, 48)$  where  $F_c(\nu_1, \nu_2)$  is a F-distribution with the degree of freedom  $\nu_1$  and  $\nu_2$  with a given level of confidence  $c$ . In another word, if  $F < F_c(16, 48)$  within a given level of confidence  $c$ , the hypothesis  $\mathbf{H}_0$  is accepted indicating that there is no linear correlation between the 2 sets of variables. If not, then  $\mathbf{H}_1$  is accepted. By applying this test to the Mueller measurement of an empty

setup with the calibrated parameters, we get the parameter  $F$  for each wavelength  $F(\lambda)$  which are at ca.  $10^4$ , corresponds to an almost absolute acceptance of  $\mathbf{H}_1$ . The validity of the existence of the Mueller matrix under the HEB model and the measurement protocol are thus very well confirmed.

We will then test the significance of linearity for each matrix element. Although we have verified the linearity of the model, the significance of linearity on each element is not the same test. The linear significance of some of the elements is not obvious and they can thus be considered as 0 within a chosen level of confidence. We can apply a test of hypothesis for each matrix elements  $m_{ij}$  as

$$\begin{aligned} \mathbf{H}_0^{ij} &: m_{ij} = 0 \\ \mathbf{H}_1^{ij} &: m_{ij} \neq 0 \end{aligned}$$

where the parameter of this test is

$$\tau = \frac{m_{ij}}{s_r \sqrt{q_{4i+j+1}}} \quad (4.20)$$

associated with a t-istribution  $t_c(\nu)$  under a confidence level  $c$  and of a degree of freedom  $\nu$ , with  $s_r$  the sample variance of the residue calculated as

$$s_r = \frac{1}{64 - 16} \sum_{i=i}^{64} \rho_i^2 \quad (4.21)$$

and  $q_{4i+j+1}$  the  $(4i + j + 1)$ th element of the vector  $\mathbf{q}$  obtained by extracting the diagonal elements of the matrix  $(\mathbf{A}_m^T \mathbf{A}_m)^{-1}$ . The acceptance of  $\mathbf{H}_0^{ij}$  is valid only when the parameter  $\tau < t_c(64 - 16)$  at a confidence level  $c$ . If not, it is  $\mathbf{H}_1^{ij}$  that must be accepted. We can then calculate the two side CDF(cumulative distribution function) probability from the t-distribution for each matrix elements for every wavelength in Fig.4.9. By setting a confidence level with certain cumulative probability from the CDF of t-distribution, we can select within all elements those that we accept as  $\mathbf{H}_0^{ij}$  or  $\mathbf{H}_1^{ij}$ .

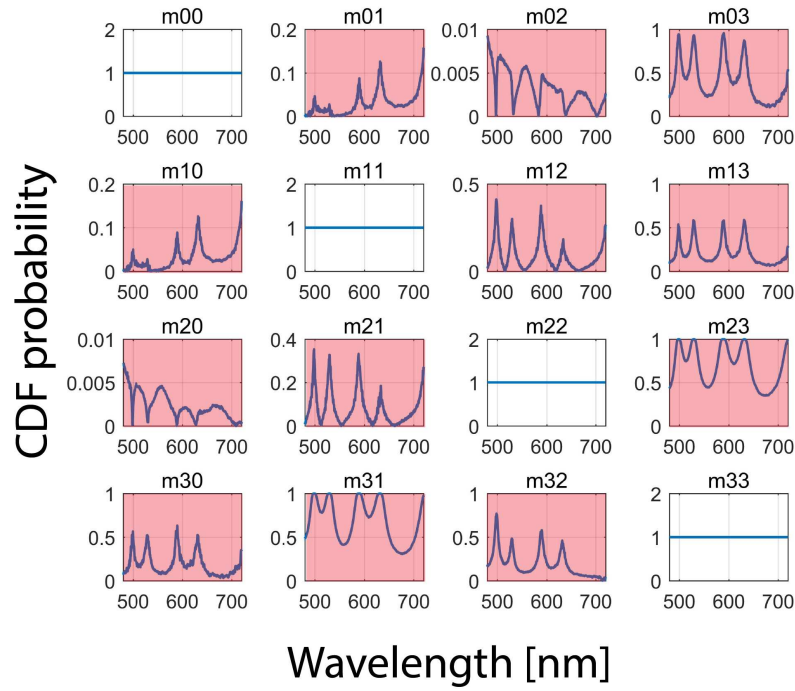


FIGURE 4.9: The CDF probability calculated from the  $\tau$  value within t-distribution for each matrix elements to show the significance of linearity for the acceptance of hypothesis  $\mathbf{H}_0^{ij}$  or  $\mathbf{H}_1^{ij}$ . The red colored elements show an acceptance of  $\mathbf{H}_0^{ij}$  at a confidence level of 99.7% which means that these elements can safely be assumed to be 0. The other elements have a value of CDF extremely close to 1 (within more than  $5\sigma$ ) implying that these elements can not be neglected. This analysis confirms the diagonal shape of the measured Mueller matrix of the empty setup.

The elements that we accept as  $\mathbf{H}_1$  can be considered as non-zero values and those accepted as  $\mathbf{H}_0$  can be set to zero values (i.e. the residual we measure are not significant). From this figure, the diagonal shape of the measured Mueller matrix of the empty setup is validated and is consistent with the expected identity matrix.

We can then evaluate the global validity of the calibration measurement using the R-square factor [93] called coefficient of determination and calculated as

$$R^2 = 1 - \frac{SSR}{SST}. \quad (4.22)$$

This factor is plotted as a function of wavelength in Fig. 4.10 and reveals the global accuracy of our estimation.

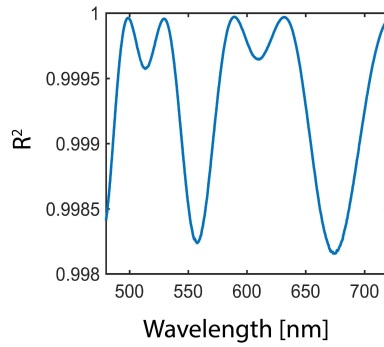


FIGURE 4.10: The  $R^2$  factor of our measurement procedure is plotted as a function of wavelength, showing an excellent goodness-of-fit.

From the plot of  $R^2$  we can see that the goodness-of-fit is excellent as the value at all wavelength remains very close to 1.

In addition to validating the model of HEB in the determination of the Mueller matrix elements, we can also evaluate the similarity between the experimentally measured Mueller matrix and the identity matrices, which can be quantified by the similarity factor of two matrix. There are many normalized parameters that can estimate the similarity between two matrices. We choose here 2 simple factors that are widely used. The first one is the correlation between two matrices  $\mathbf{A}$ ,  $\mathbf{B}$  which can be computed as

$$Cor(\mathbf{A}, \mathbf{B}) = \frac{\sum_{i,j} (A_{ij} - \overline{A_{ij}})(B_{ij} - \overline{B_{ij}})}{\sqrt{\left[\sum_{i,j} (A_{ij} - \overline{A_{ij}})^2\right] \left[\sum_{i,j} (B_{ij} - \overline{B_{ij}})^2\right]}}. \quad (4.23)$$

This parameter can take values between 0 and 1, the two matrices becoming more similar as the parameter  $Cor(\mathbf{A}, \mathbf{B})$  approaches 1. The second parameter that measures the matrix similarity is the generalized angle between two matrices  $\mathbf{A}$  and  $\mathbf{B}$  calculated as

$$Ang(\mathbf{A}, \mathbf{B}) = \frac{\sum_{i,j} A_{ij} B_{ij}}{\|\mathbf{A}\|_F \|\mathbf{B}\|_F}, \quad (4.24)$$

This parameter can take values between -1 and 1 and the two matrices are getting more similar as the parameter  $Ang(\mathbf{A}, \mathbf{B})$  gets close to 1. These two parameters calculated for the Mueller matrix of our empty setup shown in Fig.4.8 and the identity matrix are displayed in Fig.4.11. They reveal a high similarity that confirms that the accuracy of the calibration by HEB model is excellent. Finally, we also note that the generalized distance between the empty Mueller matrix from the calibration measurement and the ideal identity matrix

$$r_\delta = \|\mathbf{M}_\delta\|_F = \|\mathbf{M}_{empty} - \mathbf{I}_4\|_F \quad (4.25)$$

can help to quantify the accuracy of the calibration. This assessment is not shown here.

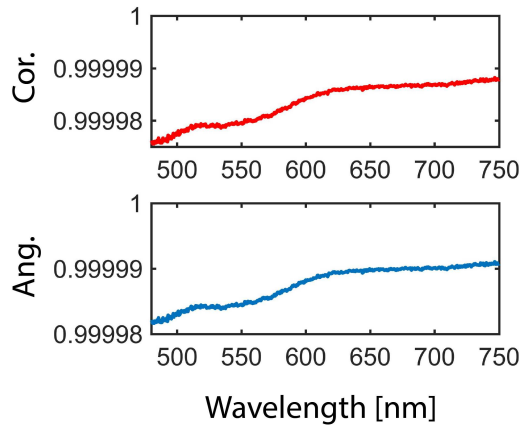


FIGURE 4.11: Matrix similarity factor between the Mueller matrix of an empty setup shown on Fig.4.8 and the identity matrix using correlation of 2 matrices (red line Eq.(4.23)) and the generalized angle between 2 matrices (blue line Eq.(4.24)).

### 4.2.3 Noise contributions and error estimation

In Mueller polarimetry, noise contributions come from different sources: fluctuations of the laser/illumination source intensity, fluctuations in the angle positioning of the motor, electronic noise sources associated with the detection line, and all other uncontrolled environmental fluctuations. These sources of noise cause fluctuations in all intensity measurements that propagate into every measured Mueller matrix elements. Generally, it is difficult to characterize each noise individually and it is also complicated to propagate each of their contribution into each Mueller matrix elements. Nevertheless, the statistical error can be estimated from an ensemble of measurements of Mueller matrix elements using appropriate statistical methods. Statistically, this error can be estimated through the variance of the system necessarily induced by these multiple noise sources. We can then estimate from an ensemble of single Mueller matrix measurements of the empty setup this population variance  $\sigma^2(m_{ij})$  through the sample variance  $s^2(m_{ij})$  built with each matrix element. The sample variance of any Mueller matrix element that gives an unbiased estimation of the population variance is calculated as

$$s^2(m_{ij}) = \frac{1}{N-1} \sum_{n=1}^N \left( m_{ij}^{(n)} - \langle m_{ij}^{(n)} \rangle \right)^2 \quad (4.26)$$

with  $N$  the total number of single measurements. If this number is sufficiently large, the estimation of the variance can be well approached to the population variance  $\sigma^2(m_{ij})$ .

This estimation transforms, through the algorithm used for solving the Mueller matrix elements, the fluctuations on the spectral intensities due to the multiple noise sources with the integration time into fluctuations on each Mueller matrix elements. It can thus provide

a measure of the resolution limit of the whole optical polarimetry setup. We set, as a minimal detection threshold, a level of confidence above which a measured signal can be identified as statistically distinguishable from the noise. This limit is therefore related to the choice of the level of confidence and the value of the standard deviation  $\sigma$ . For example, normally, we set the confidence interval to  $3\times\sigma$  corresponding to 99.7% level of confidence. Therefore, the  $3\times\sigma$  confidence interval gives a good reference for the limit of the resolution of our setup. Any signal below this limit is considered to be zero. We show here an example for the resolution limit in each matrix elements derived from 30 single measurements composing the matrix  $\mathbf{M}_\sigma$  shown below in Fig. 4.12.

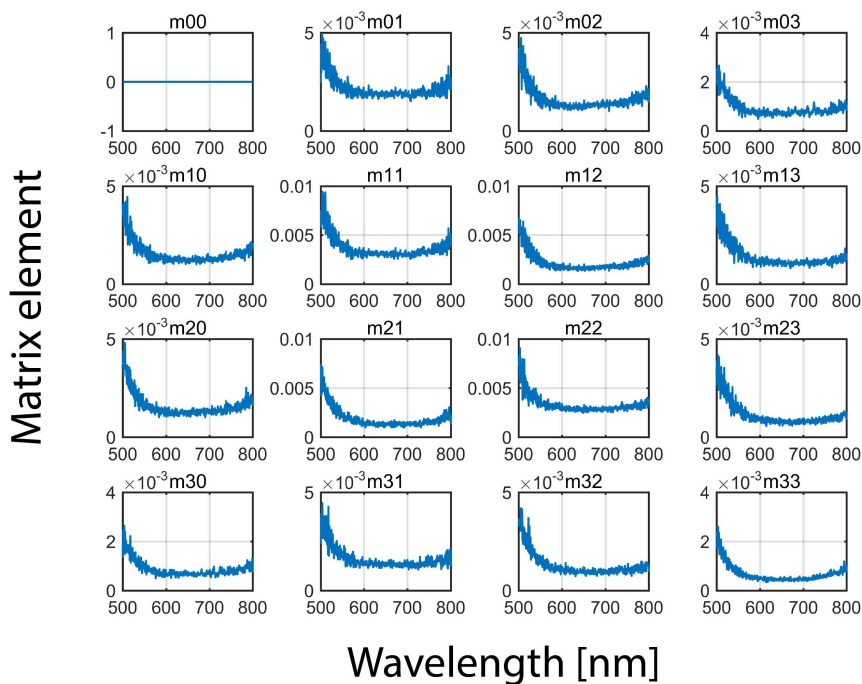


FIGURE 4.12: The  $3\times\sigma$  Mueller matrix.

As seen from the wavelength-dependent evolution of the signal for the  $\mathbf{M}_\sigma$  matrix elements, the noise limit is almost flat from 550 nm to 800 nm. This is essentially because the main spectral contribution of the light source covers this bandwidth. The resolution is therefore limited only by the noise of the light detector. Below 550 nm and above 800 nm, where the intensity from the source has decreased sensibly, the light intensity fluctuations strongly limit the resolution, as clearly observed.

The measurements we perform in practice for any sample are always coming from an average of at least 3 successive measurements, from which a matrix of sample standard deviation  $\mathbf{M}_s$  can be also obtained. Comparing this matrix  $\mathbf{M}_s$  with the matrix  $\mathbf{M}_\sigma$  determined for an empty setup measurement, allows us to quantify the quality of every measurement. If the matrix  $\mathbf{M}_s$  is of the same order of magnitude of  $\mathbf{M}_\sigma$  at a given

wavelength, the measurement can be considered as valid. However, if  $\mathbf{M}_s$  turns out to be much larger than  $\mathbf{M}_\sigma$  at certain wavelengths, this means that the sample at this wavelength is not stable enough, injecting in the measurement more fluctuations than the normal statistical error level.

#### 4.2.4 Reference correction

When aiming at measuring the Mueller matrix of a given sample, it is crucial to measure the contribution to the polarimetry signal of the cell enclosing the sample or the substrate on which it is deposited. Thanks to the multiplicative nature of Stokes-Mueller calculus, this reference correction can be performed by applying simple matrix product rules related to the multilayer configuration described below. Taking a sample in a liquid phase as an example, the full matrix measured from the Mueller polarimetry  $\mathbf{M}_{tot}$  is a product of the Mueller matrix of the front side of the cuvette  $\mathbf{M}_{front}$ , the actual sample solution  $\mathbf{M}_x$  and the back side of the cuvette  $\mathbf{M}_{back}$  as illustrated in Fig. 4.13. In order to get the Mueller matrix of the sample, the one we are really interested in, i.e.  $\mathbf{M}_x$ , we write

$$\mathbf{M}_x = \mathbf{M}_{front}^{-1} \mathbf{M}_{tot} \mathbf{M}_{back}^{-1}. \quad (4.27)$$

It clearly appears that in order to get  $\mathbf{M}_{back}$ , a measurement of the Mueller matrix of the empty cuvette must be performed, as shown in Fig. 4.13. Considering that the materials making the front and back sides of the cuvette are the same, the Mueller matrix of front side and back side are equal which we note as  $\mathbf{M}_w$ . Therefore, the "blank" reference measurement writes as:

$$\mathbf{M}_{ref} = \mathbf{M}_{front} \mathbf{I}_4 \mathbf{M}_{back} = \mathbf{M}_w^2 \quad (4.28)$$

This yields the real Mueller matrix of the sample, obtained from the reference measurement with

$$\mathbf{M}_x = \mathbf{M}_w^{-1} \mathbf{M}_{tot} \mathbf{M}_w^{-1} = \mathbf{M}_{ref}^{-1/2} \mathbf{M}_{tot} \mathbf{M}_{ref}^{-1/2} \quad (4.29)$$



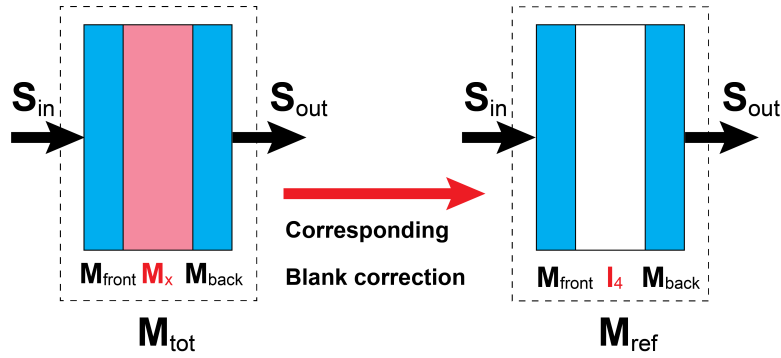


FIGURE 4.13: A real measurement of the Mueller matrix of a sample in liquid phase contained in a cuvette (left) must be corrected by the "blank" reference measurement show on the right side

This case serves as an example for most of the situation met usually. But the reference correction can be different depending on the experimental configuration. For instance, a transmission Mueller matrix measurement of a sample deposited on the surface of a substrate requires a reference correction of the substrate which corresponds to only one side of the configuration analyzed (sample + substrate). The real Mueller matrix of such a configuration is therefore obtained as:

$$\mathbf{M}_x = \mathbf{M}_{ref}^{-1} \mathbf{M}_{tot}, \quad (4.30)$$

or

$$\mathbf{M}_x = \mathbf{M}_{tot} \mathbf{M}_{ref}^{-1} \quad (4.31)$$

depending on the ordering of the substrate and the sample with respect to the light propagation direction. The correction algorithm is thus different from the one of a sample inside a cuvette. Additionally, for a cuvette which is not symmetric, the decomposition of the Mueller matrix of the blank measurement is not based on a square root of the Mueller matrix of the reference as discussed in Eq. (4.29), but rather obtained from a biased root of  $n$  as.

$$\mathbf{M}_x = \mathbf{M}_{ref}^{-q} \mathbf{M}_{tot} \mathbf{M}_{ref}^{-(1-q)} \quad (4.32)$$

with  $q$  the ratio between the thickness of the front face and the total thickness of the cuvette wall.

Our discussion so far is only based on a transmission measurement configuration. But for other configurations, such as the configuration for emission discussed below, the reference correction algorithm is different. While the front face is only involved in the Mueller matrix at pumping wavelength, the back face of the cuvette is only involved in the Mueller matrix at the emission wavelength. The Mueller matrix measuring the photoluminescence of a sample  $\mathbf{M}_x(\lambda_p, \lambda_{pl})$  relates the Stokes vector at the pumping wavelength  $\lambda_p$  and at

the emission wavelength  $\lambda_{pl}$ . Such a configuration can be corrected by a transmission Mueller matrix of the reference  $\mathbf{M}_{ref}$  as

$$\mathbf{M}_x(\lambda_p, \lambda_{pl}) = \mathbf{M}_{ref}^{-q}(\lambda_p) \mathbf{M}_{tot}(\lambda_p, \lambda_{pl}) \mathbf{M}_{ref}^{-(1-q)}(\lambda_{pl}) \quad (4.33)$$

There are of course many other types of configurations that can be described. But to summarize, an accurate reference correction measurement and the associated algorithm should always be performed based on the ordering of the multilayer structure of the sample within a specific configuration. In principle, every optical elements between PSG and PSA should be taken into account for the correction algorithm. This is extremely important: a measurement done without a reference correction will lead to artifacts on the optical properties of the sample extracted from the non-corrected Mueller matrix.

### 4.3 Data processing: passive vs. emissive samples

Following this discussion, one expects data processing to be dependent on the specific experimental configuration. Two important configurations must be discussed here, depending on whether our sample is passive or active. For passive samples, the light is only transmitted through the medium, and we only consider polarimetry as modifications of light polarization states at each wavelength before and after the sample, while an active sample generates light with its new polarization. In this case, data will be processed from the input polarization state at the excitation wavelength to the output polarization states at the emission wavelength.

#### 4.3.1 Passive sample

For a passive sample, the Mueller matrix we measured is defined for each wavelength independently from the other wavelengths. We only consider the Mueller matrix associated with light polarization change before and after the sample.

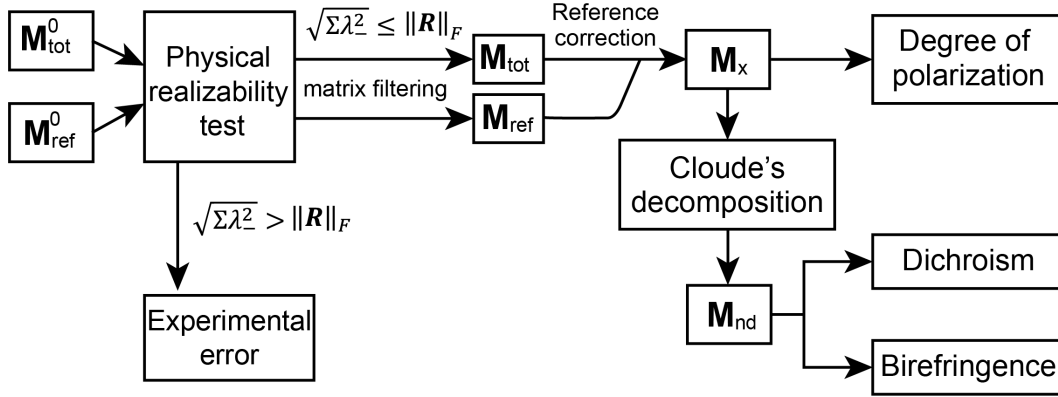


FIGURE 4.14: Data processing procedure for a passive sample

The acquisition sequence is shown on Fig.4.3 and the original Mueller matrix  $\mathbf{M}_{tot}^0$  is obtained using Eq. (4.9) under the HEB model description of the PSG and PSA QWPs. For each measurement, the Mueller matrix of the corresponding reference correction  $\mathbf{M}_{ref}^0$  is recorded for each sample. For all the Mueller matrices measured from the primitive experiment, a physical realizability test and filtering process must be performed as discussed in chapter 2. While performing the physical realizability test, a criteria is imposed to show if the measurement is valid. What needs to be compared is the norm of non-physically realizable part of Mueller matrix  $\|\mathbf{M}_-\|_F$  to the norm of intrinsic error as  $\|\mathbf{R}\|_F$  [40]. One can show that  $\|\mathbf{M}_-\|_F$  defined as the difference between the original Mueller matrix  $\mathbf{M}_{tot}^0$  and the closest physically realizable Mueller matrix  $\mathbf{M}_{tot}$  can be easily calculated from the square sum of all negative eigenvalues of the corresponding coherence matrix  $\mathbf{N}$  according to Eq. (2.116) as

$$\|\mathbf{M}_-\|_F = \|\mathbf{M}_{tot}^0 - \mathbf{M}_{tot}\|_F = \sqrt{\sum \lambda_-^2}. \quad (4.34)$$

This intrinsic error  $\|\mathbf{R}\|_F$  is evaluated as the largest value between the accuracy factor  $r_\delta$  defined in Eq. (4.25) and the limit of resolution calculated from the standard deviation matrix  $\mathbf{M}_\sigma$ . The factor  $\|\mathbf{R}\|_F$  is therefore chosen as

$$\|\mathbf{R}\|_F = \max\{r_\delta, \|\mathbf{M}_\sigma\|_F\}. \quad (4.35)$$

Hence, if the deviation between the original matrix  $\mathbf{M}_{tot}^0$  and a physical realizable matrix  $\mathbf{M}_{tot}$  is larger than the intrinsic error, i.e. if  $\sqrt{\sum \lambda_-^2} > \|\mathbf{R}\|_F$ , the measurement must be considered as non-valid. Often, drifting effects (on the calibrated states or on the sample itself through the measurement duration) can be responsible for such "non-physical" results. In such a case, the calibration must be verified by performing a blank measurement and the sample stability must be checked. If in contrast, the deviation remains within the intrinsic error, i.e. if  $\sqrt{\sum \lambda_-^2} \leq \|\mathbf{R}\|_F$ , we can perform a matrix filtering process with the method we introduced in section 2.2.1 to get the closest physical

realizable Mueller matrix for both the sample and the reference measurements noted as  $\mathbf{M}_{tot}$  and  $\mathbf{M}_{ref}$ . Then, depending on the sample configuration, a reference correction is included in order to get the Mueller matrix associated with the actual sample  $\mathbf{M}_x$ . Once  $\mathbf{M}_x$  is obtained, the first parameter that can be extracted is the degree of polarization. To extract all other polarimetric parameters, we first perform a Cloude's decomposition presented in section 2.2.2 that yields a non-depolarizing Mueller matrix. Then, by taking the matrix logarithm as discussed in section 2.3.2, the birefringence and dichroism terms can be obtained explicitly. The whole procedure is schematized in Fig.4.14.

### 4.3.2 Active sample

As for active samples, the data processing is slightly different. Since the reference correction measurement in this case also deals with a passive medium (cell or substrate), a physical realizability test must be performed on  $\mathbf{M}_{ref}^0$  to get  $\mathbf{M}_{ref}$ . However, for the measurement of an active sample Mueller matrix  $\mathbf{M}_{tot}^0$ , the physical realizability test is fragile because in general, a Mueller matrix relating excitation and emission polarization states is not always Cloude's realizable according to the discussion of Chapter 3. Compared to the noise estimation made on a passive medium measurements, the resolution for an active sample is much poorer since the emission intensity itself displays much more fluctuations than a probing light source. Therefore, the physical realizability test cannot provide a truly valid criteria for  $\mathbf{M}_{tot}^0$ . This leads us to move directly to the matrix filtering process in order to get the best estimate of a physical realizable Mueller matrix  $\mathbf{M}_{tot}$ . Then, we perform the reference correction determined from the sample configuration and get an estimate for the real sample  $\mathbf{M}_x$ . From this matrix, we can characterize the properties of the emission process by first visualizing through a Poincaré sphere representation to see the states of polarization associated with the emission and the pumping light propagation as discussed in Chapter 6. Then, from the matrix elements, we can get the parameters such as fluorescence detected dichroism (FDD), polarization of emission (PPL) including CPL (circularly polarized luminescence), LPL (linearly polarized luminescence) and maintain of polarization (MoP) as described in Chapter 2.

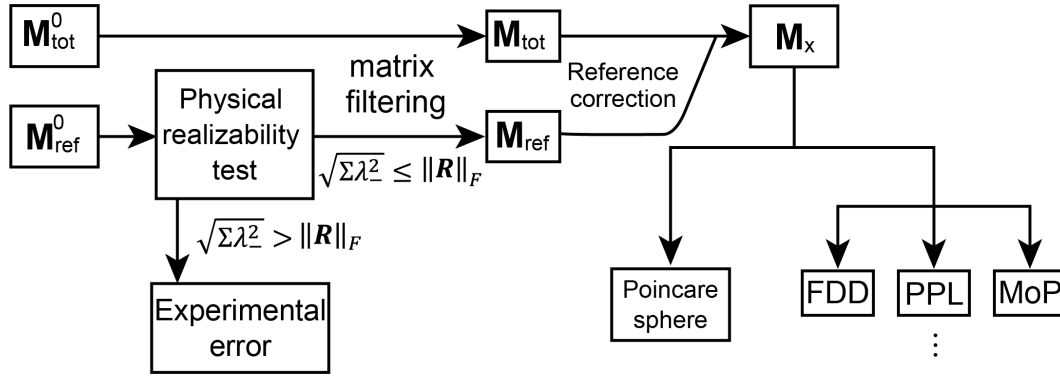


FIGURE 4.15: The data processing procedure for an active medium

## 4.4 Measurement configurations

Within the framework of dual rotating Mueller polarimetry and using the calibration presented in the previous sections, the Mueller matrix can be measured in many different configurations according to different optical paths available (transmission and/or reflection), different interactions analyzed (passive sample and/or active sample), different types of acquisition chosen (spectral and imaging) and different types of imaging space selected (real spaces and/or Fourier spaces). Our setup offers a great flexibility and we now describe the different configurations that we implemented in this thesis.

### 4.4.1 Transmission configuration

The most simple and basic configuration is when the Mueller matrix is measured in transmission, the same configuration that was used for the basic calibration of the polarimetric properties of a transmissive medium. In this transmission configuration, the PSG and PSA are aligned along the same optical path with the sample in between. The configuration is shown in the Fig.4.3 and the experimental implementation of this configuration is presented in Fig. 4.16.

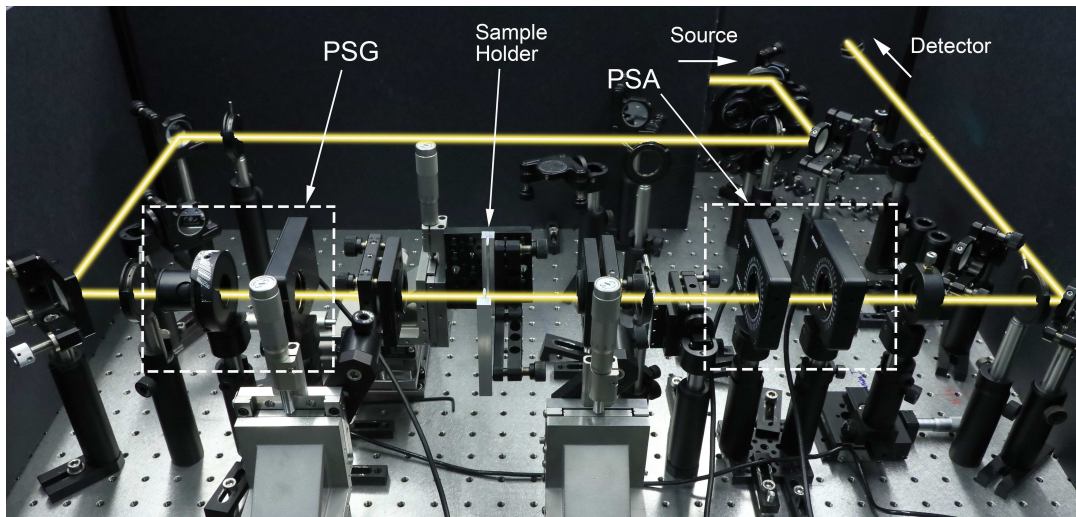


FIGURE 4.16: Photograph of the experimental implementation of a transmission Mueller matrix configuration following the optical path from the source to the detector.

The optical path is designed taking into consideration all type of configurations. Also this configuration can be used for microscope objectives with xyz-translation stage and adjusted in infinity conjugation to maintain the same optical path for the calibration and the measurement as shown in Fig. 4.17.

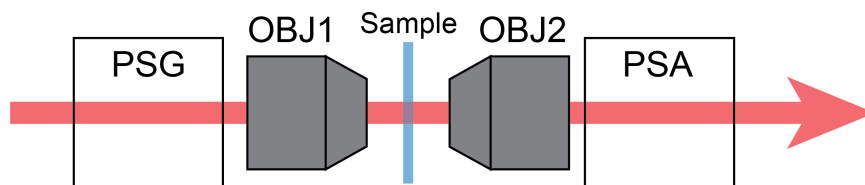


FIGURE 4.17: The transmission configuration with the Objectives.

#### 4.4.2 Reflection configuration

Our setup is also designed to be able to measure normal reflection Mueller matrices for non- or barely transmissive samples or highly reflective samples. The basic setup for measuring a Mueller matrix in reflection is shown in Fig. 4.18 below.

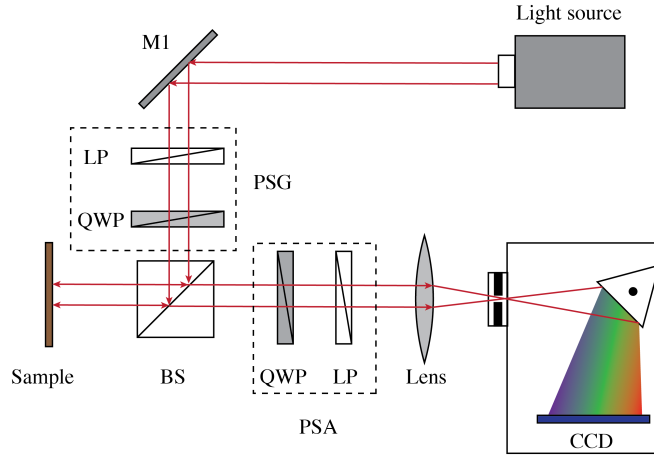


FIGURE 4.18: The optical setup for measuring a reflection Mueller matrix where BS is a neutral non-polarizing beam splitter.

In this configuration, the Mueller matrix combines one reflection by a beam-splitter (BS), one reflection by the sample and the transmission through the BS. As we mentioned in the previous section for the reference correction, all optical elements between PSG and PSA should be taken into account in order to get the real Mueller matrix of the sample. Therefore, the direct measurement matrix  $\mathbf{M}_0$  is the product of all these elements:

$$\mathbf{M}_0 = \mathbf{M}_{BSr} \mathbf{M}_R \mathbf{M}_{BS t} \quad (4.36)$$

where  $\mathbf{M}_{BSr}$  is the matrix of the  $90^\circ$  reflection by the BS,  $\mathbf{M}_{BS t}$  is the matrix of transmission through the BS and  $\mathbf{M}_R$  is the matrix describing the reflection by the sample. This reflection matrix of the sample is thus obtained as

$$\mathbf{M}_R = \mathbf{M}_{BSr}^{-1} \mathbf{M}_0 \mathbf{M}_{BS t}^{-1}. \quad (4.37)$$

In order to get the reflection Mueller matrix of the sample from such a setup, the matrices  $\mathbf{M}_{BSr}$  and  $\mathbf{M}_{BS t}$  must be determined. This constitutes an additional step in the calibration procedure for the reflection Mueller matrix measurement. Once the PSG and PSA are calibrated for the simple transmission configuration, this calibration is then used to measure these 2 matrices using the configuration sketched in Fig. 4.19.

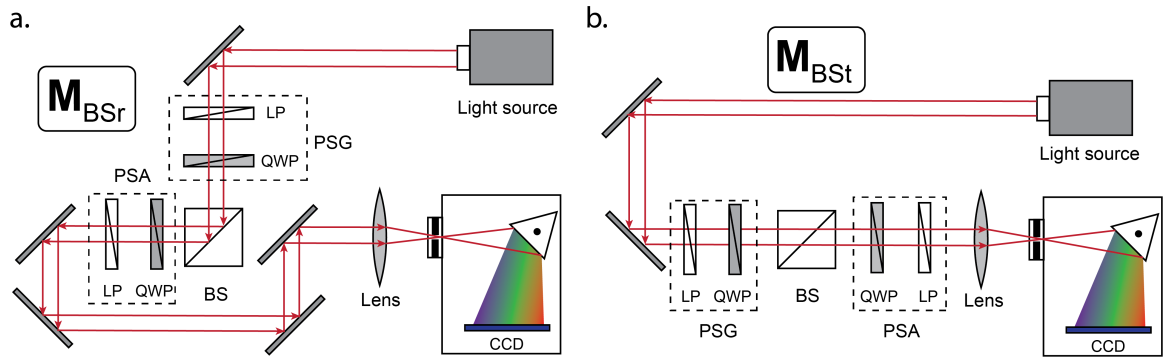


FIGURE 4.19: (a) displays the configuration for measuring the matrix  $\mathbf{M}_{BSr}$  which describes the reflection by the BS using the same source and detector; (b) displays the configuration for measuring the matrix  $\mathbf{M}_{BSt}$  which corresponds to the transmission through the BS.

Finally, a photograph of the reflection measurement configuration actually implemented in our setup is shown in Fig.4.20.

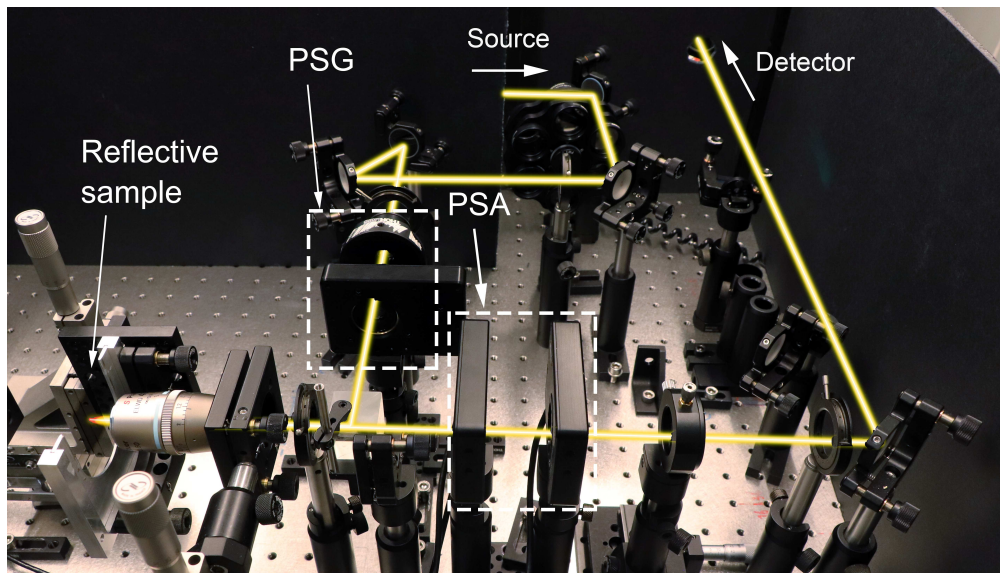


FIGURE 4.20: Photograph of the experimental implementation of the reflection measurement configuration. The light path from the source to the detector is high-lighted in yellow.

### 4.4.3 Emission

As mentioned in our chapter 2, our Mueller polarimetry setup also allows us to measure the Mueller matrix associated with the light emitted from an emissive sample, relating the polarization states of the pump and of the photoluminescence (PL). Contrasting with all configurations involved for passive samples, the light source is, for an emission measurement, filtered to be practically monochromatic (instead of being a broad-band white



source). Different options are available such as a white laser coupled to a filter (monochromator) with a minimum bandwidth of 10nm (SUPERK FIANIUM supercontinuum laser from NKT Photonics), a filtered Tungsten Halogen white light or an He-Ne laser when the specific 632 nm wavelength is needed. Also for the acquisition of the emission signal, we need to filter out the excitation light before entering into the detector. For most of the samples with a Stokes shift between absorption and emission (see Chapter 6), a long pass filter is used while for the anti-Stokes emission sample, a short pass filter is used instead.

When measuring emission signals, objectives are always necessary in order to focus the excitation light within certain limited region with an intensity high enough to generate the PL. Another objective collects this emission within its N.A. Since the PL is generally not directional. Therefore, an objective with a relatively large numerical aperture, collecting more PL signal, is useful. Also, the front focal point of the collection objective must be put within the sample. Moreover, for a sample with a thickness larger than the depth of field of the objective of collection, measuring the emission must be further corrected for the scattering of the excitation and for the emission within the sample itself, as we will discuss in the practical situations explored in chapter 6.

For emission too, measurements can be performed in the transmission or/and reflection configuration according to the property of the sample and the experimental conditions. A photograph of the emission setup operated in transmission is shown in Fig. 4.21.

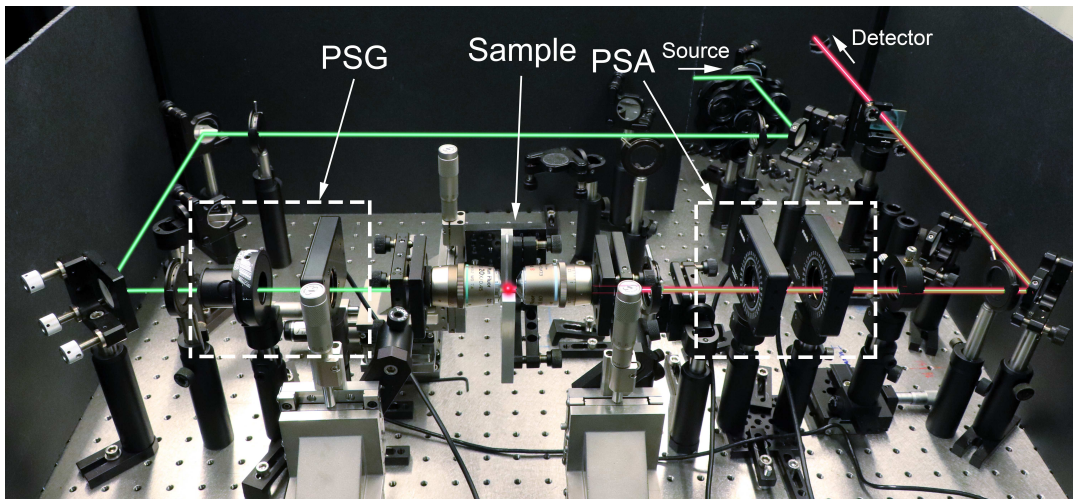


FIGURE 4.21: Photograph of the experimental implementation of the emission Mueller matrix measurement in transmission. The excitation light is indicated by the green beam and the emission light (PL) by the red beam. The filter cuts away the green excitation so that only red emission light can be measured by the detector.

#### 4.4.4 Real and Fourier spaces imaging

The configurations we presented above all correspond to spectral measurements. Since our detector is a CCD coupled to a monochromator, it is also possible to measure the Mueller matrix in an imaging mode by replacing the optical grating by a mirror in the monochromator. Mueller polarimetry for imaging has been introduced for the first time by Chipman *et. al.* [94] and has been extensively implemented recently in many group [46, 95]. According to Eq.(4.9), the Mueller matrix can be obtained from an image by taking  $\mathbf{I}_m$  as the intensity at a given pixel  $\{x, y\}$  noted as  $\mathbf{I}_m(x, y)$ . This leads to an imaging Mueller matrix  $\mathbf{M}(x, y)$  defined for any given pixel  $\{x, y\}$  of a CCD chip. Measuring the Mueller matrix in this imaging mode can be done in two imaging spaces: the real space (RS) and the Fourier space (FS) that provides angularly resolved measurements as explained in the transmission configuration by the 2 diagrams shown in Fig.4.22 and Fig.4.23. Note that it is also possible, following the methodology presented above, to work in imaging reflection mode.

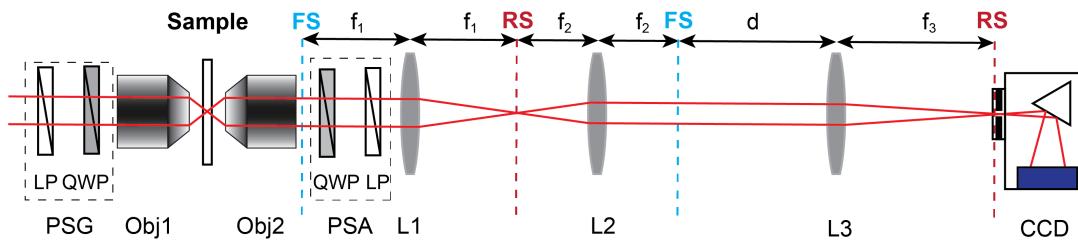


FIGURE 4.22: This diagram shows the real space imaging setup together with the polarimetry elements with the planes corresponding to the FS and the RS indicated. Microscope objectives (Obj1,2) are drawn, together with all lenses  $L_i$  of focal length  $f_i$ .

As sketched in Fig.4.22, for real space imaging, a first FS is generated at the back focal plane of the collection objective Obj2. By placing the lens  $L1$  at a distance equal to its focal length  $f_1$ , a RS is generated at the distance of  $f_1$  behind  $L1$  where we can perform real space filtering if necessary. Then by placing a second lens  $L2$  at  $f_2$  from this RS, a second Fourier space is generated where we can perform Fourier space filtering. Finally by bringing a third lens  $L3$  at the distance of  $f_3$  from the entry plane of the spectrometer, the real space becomes conjugated to the detector and thereby directly imaged.

For Fourier space imaging, a fourth lens noted as the Fourier transform lens (LF) is inserted between the second Fourier space plane and  $L3$  at a distance equal to its focal lens  $f_0$  from this second FS. The Fourier space image can then be sent to the spectrometer, and imaged.

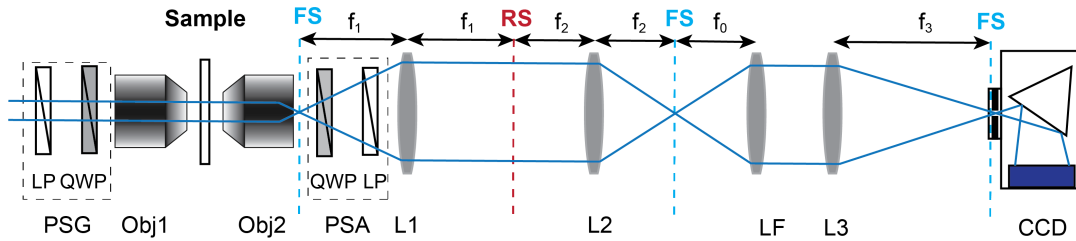


FIGURE 4.23: This diagram shows the Fourier space imaging setup together with the polarimetry elements with the planes corresponding to the FS and RS indicated. Microscope objectives (Obj1,2) are drawn, together with all lenses  $L_i$  of focal length  $f_i$  and the Fourier lens noted as LF with a focal length of  $f_0$ .

Finally, these FS and RS imaging configurations can be combined with spectral measurements, giving the capacity to perform spectral Mueller matrix imaging analysis, in both real space and Fourier space.

## 4.5 Conclusion

This chapter, has described our main experimental setup, namely the broad-band Mueller polarimetry based on the dual rotating QWP principle. With the help of HEB modeling of QWPs and our protocol for the calibration, the setup shows a good accuracy in performing Mueller matrix measurements. According to the statistical noise analysis, we quantified the resolution level of our setup for a given source and detection method. Then, we propose a standard procedure for data processing for both active and passive sample together with the reference correction method. Finally, within the feature of our optical realization of the setup, we introduce all types of possible configurations of measurement namely the transmission, reflection and emission measurements for spectral analysis and/or imaging in both real and Fourier spaces.

## Chapter 5

# Mueller polarimetry of chiral supramolecular assemblies

In this chapter, we apply the toolbox of Mueller polarimetry in the context of spontaneous mirror symmetry breaking and the emergence of chirality. In order to study these questions, chiral supramolecular self-assembly systems provide a perfect playground. Supramolecular organizations of achiral molecules are known to undergo spontaneous mirror symmetry breaking. Monitoring on such organizations the emergence of chiral macroscopic structures with enantiomeric excess using Mueller polarimetry leads to show that the hierarchy at play in the self-assembly can be encoded in a hierarchical evolution of the polarimetric properties revealed by the evolution of polarization states. As discussed here, these polarization dynamics can be visualized in the Poincaré sphere. This representation leads to new strategies for artificially building evolving systems that can mimic very complex polarization responses.

The chosen system for this study is the self-assembly of an achiral amphiphilic cyanine molecule, denoted C8O3, which forms chiral J-aggregates through a spontaneous mirror symmetry breaking. We will study each step of the self-assembly using Mueller polarimetry. As we will show, Mueller polarimetry will help in determining the intermediate conformations involved through the aggregation process. For instance, we will be able to relate the initial mirror symmetry breaking event to a drive stemming from hydrophobic forces in the earliest stage of the self-assembly. When chiral excitons are then formed in tubular J-aggregates via a secondary nucleation event, the amplification of the chiral signal is observed culminating in the final stage of the assembly, in exciton coupling signatures associated with the bundling of the tubular aggregates [].

The aim of this chapter is to show that complex polarization dynamics can be induced by supramolecular systems following their molecular hierarchies. In other words, we would like to contribute to the promotion of complex molecular systems as materials enabling to observe, generate and even mimic rich optical complexities [22, 23].

## 5.1 From achiral amphiphilic monomers to chiral aggregates

Spontaneous mirror symmetry breaking always comes with an enantiomeric excess that shows chirality. Optical characterization therefore becomes an efficient tool to study this problem. Two of the mostly simple methods are polarization rotatory power measurement and CD measurement. However, as the structure of the sample under study becomes more complex, a complete polarimetric characterization is required. One key value of Mueller polarimetry is to provide artifact-free characterizations of chiroptical properties, in particular for circular dichroism (CD). Chiroptical CD characterization is classically based on measuring differential absorption of left and right circularly polarized light through the sample but the determination of CD can be limited by the presence of linear dichroism (LD) and linear birefringence (LB) that arise from some preferred orientation induced within the sample (for instance in the case of supramolecular assemblies: macroscopic molecular building blocks). With such a classic CD characterization, systems with LD and LB will display artifact CD responses. This problem is well known and will be discussed in detail below from the point of view of the Mueller matrix [51, 96, 97]. This point of view turns relevant too with respect to other artifacts induced by some uncontrolled polarimetric optical responses stemming from the cuvette or fluidic cell containing the sample. With the correction procedures available within Mueller polarimetry that we discussed in chapter 4, such artifacts can be correctly removed. Therefore, the Mueller polarimetry can provide an isolated and complete polarimetric characterization of a chiral system and as such is a perfect tool for analyzing chiral supramolecular assemblies.

Despite its assets, and that it has been well developed and exploited in nano-optics [98–100], Mueller polarimetry is seldom applied in the field of molecular chirality, except for important efforts made to explain the chirality and asymmetric features of crystals in particular in the group of B. Kahr [101–104]. This manuscript aims at applying Mueller polarimetry and showing its relevance as a new approach for monitoring the formation of supramolecular self-assemblies.

One molecular process particularly appropriate for the study of the emergence of chirality, and thus of spontaneous mirror symmetry breaking, is the J-aggregation that an achiral amphiphilic carbocyanine dye can incur in specific conditions. The family of this monomer molecule is noted as **CmRn** with the chemical structure shown in Fig. 5.1 a. [105, 106]. In this family, not every **CmRn** variant can form chiral aggregates. To have this, we choose specifically the achiral monomer C8O3 which is known to form a tubular chiral J-aggregate with the aggregation process shown in Fig. 5.1 b [106, 107].

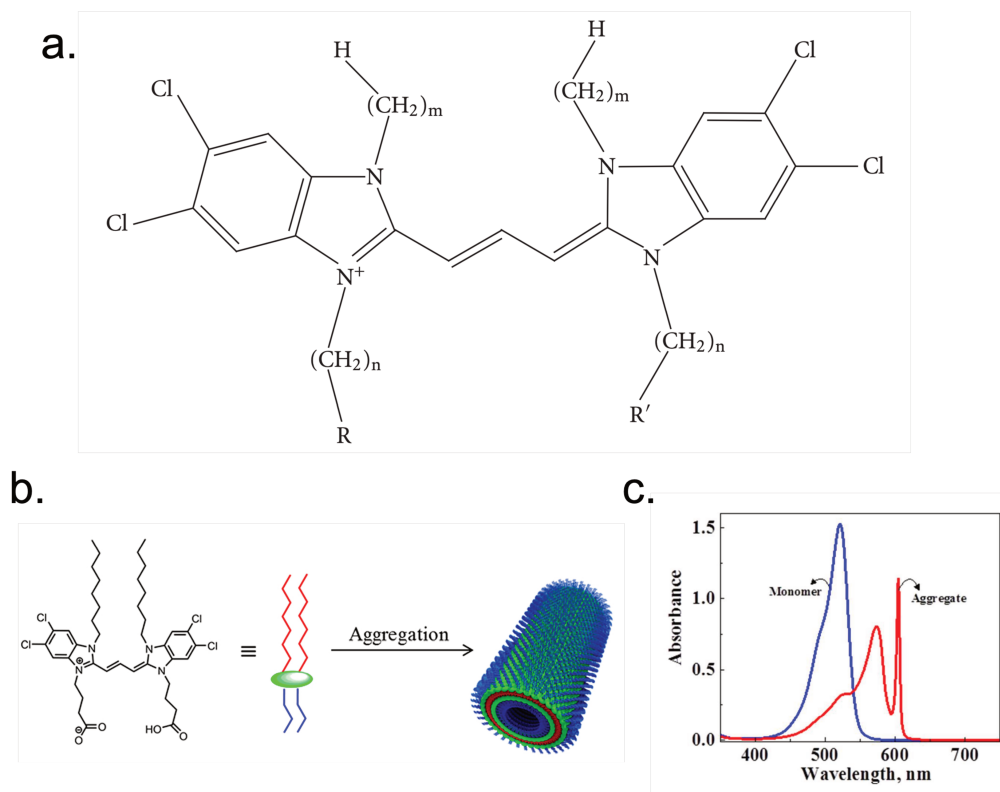


FIGURE 5.1: (a) shows the chemical variant of CmRn, where  $m$  and  $n$  indicate the length of the alkyl chains at the 1, 1'- and 3, 3'- positions, respectively. R is an abbreviation corresponding to the ionic groups for example O stands for the group  $-\text{COO}^-$ , (b) shows the J-aggregate formation of C8O3 monomer. (c) shows the evolution of the absorption spectra going from the monomeric phase (blue line) to the J-aggregated one (red line).

This molecule exists as monomeric phase in ethanol with an absorption peaked at  $\lambda_{max} = 523$  nm shown in Fig. 5.1 c. In such a monomeric phase, C8O3 does not show any interesting features revealed by Mueller polarimetry as expected from an achiral molecule. It is known that chiral J-aggregates of C8O3 can be obtained via an alcoholic route [107], by the addition of aqueous NaOH to the dye in ethanol. In our experiments, by varying the volume ratio (v/v) between aqueous NaOH (0.02 M) and C8O3 (0.3 mM) solution in ethanol, different stages of hierarchical assembly could be reached, and subsequently relaxed for 2 h to reach thermodynamic equilibrium. The formation of the J-aggregates is characterized by absorption bands at 573 and 605 nm observed in Fig. 5.1 c. These bands correspond to transverse and longitudinal excitons (see Fig. 5.3), respectively, and indicate the tubular structure of the C8O3 J-aggregates in solution. The aggregate solutions were then probed using our broadband transmission Mueller polarimetric methodology through a 1-mm path length cuvette, as schematized in Fig. 4.17.

## 5.2 Hierarchical aggregation analyzed by Mueller polarimetry

Such a supramolecular self-assembly system will allow us to approach the fundamental questions related to spontaneous mirror symmetry breaking and the progressive emergence of chirality through a self assembling process. The emergence of spontaneous optical activity in C8O3 J-aggregates, first observed by De Rossi et al.,[107] opens up questions on the role of the achiral monomer in the induction, transfer, and amplification of chirality. Although the structural aspects related to the alkyl-chain length and functional groups of the cyanine monomer are well studied [105, 108], the primary nucleation process and the role of monomer assemblies in defining the chiroptical features are not known. By systematically controlling the assembly of C8O3 and monitoring the assembly using Mueller polarimetry, not only can we get a complete artifact-free polarimetric characterization of the chiral supramolecular assembly, but also speculate on the intermediate conformation from which, through detailed processes, emerge chirality. As discussed below, we can also, based on these analysis, present all the polarization properties of each measured stages of the assembly in a Poincaré sphere and show the polarization dynamics at play when light passes through this evolving supramolecular system.

## 5.2.1 Mueller polarimetry measurements

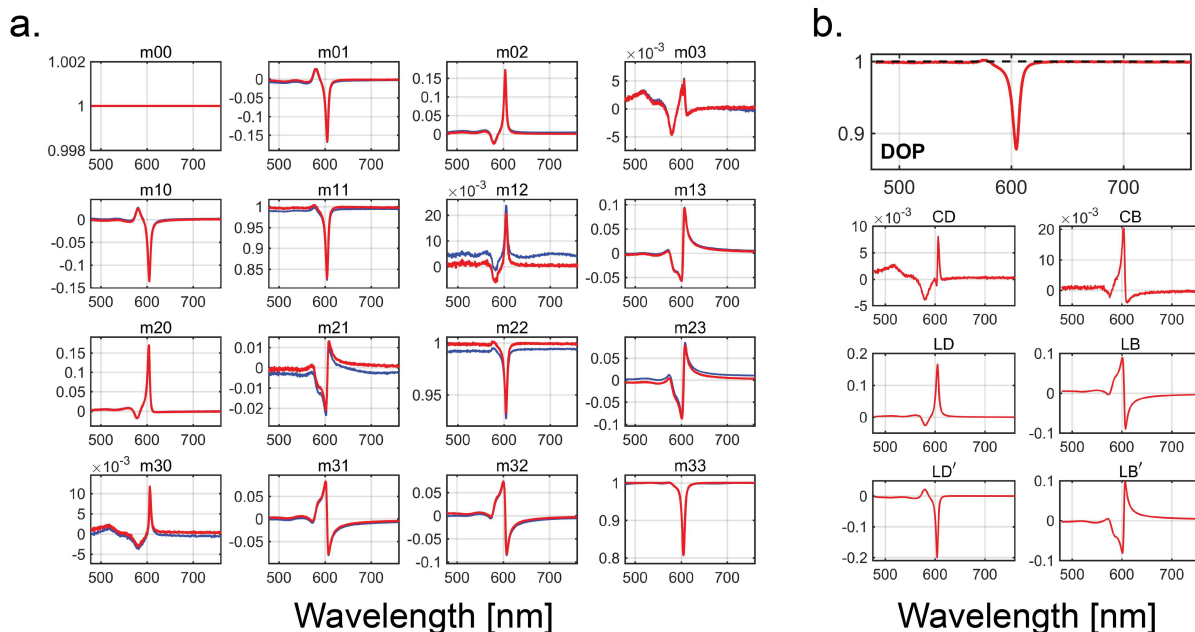


FIGURE 5.2: (a) displays a normalized transmission Mueller matrix of a solution of C8O3 J-aggregates formed by the addition of aqueous NaOH (0.02M) to the dye (0.3mM) in ethanol with a ratio of 3:1. The total matrix is presented as blue lines while the matrix corrected for the optical response of the cuvette is displayed by the red curve. (b) shows the corresponding polarimetric properties extracted from the matrix shown in (a) namely dichroisms (CD, LD, LD'), birefringences (CB, LB, LB') and the degree of polarization (DOP).

First, we would like to show an experimentally determined normalized  $4 \times 4$  Mueller matrix of C8O3 J-aggregate that we use for extracting the polarimetric properties, as well as the importance of a reference correction described in Chapter 4 that consists in "subtracting" the optical response of the fluidic cell enclosing the C8O3 solution. One example, formed by the addition of aqueous NaOH to the dye in ethanol in a 3:1 ratio (v/v), is presented in Fig. 5.2(a) from which we extract the essential polarimetric properties, namely, the degree of polarization, birefringences and dichroisms shown in Fig. 5.2(b). The direct measurement of the total matrix noted as  $\mathbf{M}_{tot}$  is represented by the blue curve in Fig. 5.2(a) as the Mueller matrix of the real sample  $\mathbf{M}_x$  is displayed by the red curve in Fig. 5.2(a). We can clearly see how the matrix elements after the reference correction display signals without offset. The polarimetric properties are extracted from this corrected matrix which therefore focuses solely on the optical signatures of the molecular system.

With this example, we can open the discussion on the advantage and necessity of using Mueller polarimetry in order to characterize any kind of chiral supramolecular sample.



The key parameter related to chirality is of course the circular dichroism (CD). Conventionally, the CD is defined by the difference between the absorbance of left and right handed circularly polarized light as

$$\Delta A = A_L - A_R. \quad (5.1)$$

It can be also expressed according to the Beer-Lambert law as

$$\Delta A = (\varepsilon_l - \varepsilon_r)cl, \quad (5.2)$$

where  $c$  is the concentration of the chiral solution,  $l$  stands for the length of the optical path (typically the fluidic cell thickness) and  $\varepsilon_l$  and  $\varepsilon_r$  represent respectively the molar extinction ratio of left and right handed circularly polarized light.

Hence, starting from these definitions, the most simple and classic method to measure the CD is by looking directly at the absorbance difference of left and right circularly polarized light beams. By the definition of Eq.(5.1), we can get the classically estimated phenomenological CD noted as  $CD_{ph}$ . However this measured signal is not necessarily proportional to the genuine CD, defined in Eq.(2.188), and here noted as  $CD_g$ . This problem can be easily solved with the Mueller formalism. The phenomenological CD can be expressed as function of the Mueller matrix elements as

$$CD_{ph} = \Delta A = \log_{10} \left( \frac{1 + m_{03}}{1 - m_{03}} \right). \quad (5.3)$$

Meanwhile, the genuine CD is written according to the differential decomposition of a Mueller matrix as

$$CD_g = \frac{1}{2} \left( [\ln(\mathbf{M})]_{03} + [\ln(\mathbf{M})]_{30} \right). \quad (5.4)$$

Generally, Eq.(5.3) and Eq.(5.4) do not yield the same results, since the phenomenological CD depends only on the  $m_{03}$  term while the genuine CD has contributions from many different elements of the Mueller matrix through the matrix logarithm. But despite that the classical method will not always give the genuine CD, most of the cases encountered when dealing with small molecule solutions show that  $CD_{ph}$  closely follows the tendency of a genuine CD. We will now show in what circumstances is the classical method limited by the principle of differential decomposition of a Mueller matrix.

First of all, the genuine CD is written in the cumulative differential matrix  $\mathbf{m}$  defined in Eq.(2.213), knowing that the total Mueller matrix can be written by  $\mathbf{m}$  as a matrix exponential, which can be then developed as

$$\mathbf{M} = \exp(\mathbf{m}) = \sum_{n=0}^{\infty} \frac{1}{n!} \mathbf{m}^n = \mathbf{I} + \mathbf{m} + \frac{1}{2} \mathbf{m}^2 + \dots \quad (5.5)$$

The phenomenological CD depends only on the  $m_{03}$  element of the total Mueller matrix  $\mathbf{M}$ , which can be written from Eq. (5.5) as a second order of development in  $\mathbf{m}$  as

$$m_{03} = CD_g + \frac{1}{2}(LD' \cdot LB - LD \cdot LB'). \quad (5.6)$$

This expression is important for discussing the limits of a classical CD measurement. The  $CD_{ph}$  determined uniquely by  $m_{03}$  in general depends not only on the  $CD$  but also the contribution from linear birefringence and linear dichroism. Therefore, for a sample where linear birefringence and linear dichroism can be neglected, the classical  $CD_{ph}$  measurement can give a good estimate of the genuine  $CD_g$ . In the simple case of bi-isotropic molecules in a homogeneous environment,  $CD_g$  can be safely estimated by the classical method. Generally small molecules that do not form any macro-structures do not present any determined linear birefringence and dichroism. Another case where we can neglect the last term of Eq.(5.6) is when the molecules are contained inside a thin cuvette with a very short optical path  $l$ . Knowing that  $CD_g$  in Eq.(5.6) is of the order  $l$  and that the product of the polarimetric quantities (the second term in Eq. (5.6)) is of the order of  $l^2$ , this second term corresponding to the linear properties can be neglected with respect to the first order  $CD_g$  even if the sample itself displays the linear birefringences and dichroisms. In such a situation, the total Mueller matrix can be safely approximated as

$$\mathbf{M} \simeq \mathbf{I} + \mathbf{m}, \quad (5.7)$$

where the polarimetric properties are directly estimated from the off diagonal elements of the Mueller matrix  $\mathbf{M}$  avoiding the differential decomposition procedure presented in chapter 2.

However in our experiments, the CD signals that we are searching for are in general weak with respect to linear birefringence and dichroism signatures. This comes from the fact that our system evolves towards the formation of tubular macrostructures, as shown in Fig. 5.2(b). With such a systems, the CD analysis should be as most rigorous as possible. In particular when intending to observe the emergence of chirality, measuring an artifact-free CD signal is critical. According to Eq.(5.6), the phenomenological CD signal will be affected when the linear structure has significant component along  $0^\circ/90^\circ$  and  $\pm 45^\circ$  basis such that LD and LD' (LB and LB') are almost of the same order of magnitude. Since linear dichroism and birefringence depend on both the size and orientation of the tubular macrostructures which are randomly determined, the measured  $m_{03}$  can give sometimes almost the same tendency as the genuine CD, whereas some other times  $m_{03}$  gives a different CD estimate compared to the genuine CD, as precisely seen in Fig. 5.2. This is where Mueller polarimetry must be implemented, enabling us to evaluate rigorously artifact-free CD signatures in the presence of large linear dichroism stemming

from oriented long aggregates. With this capacity to measure real chiroptical features, experiments were carried out aiming at identifying primary chiral nucleation event, chiral transfer and amplification processes in C8O3 J-aggregates by controlling methodically the stages of the self-organization evolution.

## 5.2.2 Experimental results

Mueller polarimetry combined with basic absorbance measurements gives a complete image of the different stages of the aggregation process. The discussion will be unfolded according to different observables. Combined with an absorbance analysis for the different stages of aggregation, the emergence of chirality and the evolution of chiroptical properties can be analyzed using CD observables. LD can be used as an observable for measuring the orientation of the tubular structure. Finally, the degree of the polarization extracted from the measured Mueller matrix reveals the ordering of the sample which can also serve as a complementary information related to aggregate conformations.

### Emergence and evolution of chirality

First, in order to determine the various stages of the hierarchical assembly of C8O3, the aggregation processes were first characterized by observing the evolution of the J-aggregate transitions in the visible absorption spectrum upon addition of varying amounts of NaOH solution (details are given in the caption of Fig. 5.4). We then recorded the associated Mueller matrices. Based on this analysis, different stages were identified whereby:

1. C8O3 exists as isolated monomers,
2. J-aggregation process commences,
3. tubular assemblies develop and grow,
4. self-assembly process is nearly complete,
5. self-assembled tubular structures come close to each other and eventually bundle.

By maintaining a ratio of 1:2 (v/v) between C8O3 in ethanol and NaOH in water (0.02 M), the monomeric stage 1 was achieved (Fig. 5.4(A)). The commencement of J-aggregation in stage 2 (referred to as primary chiral nucleation below) was marked by the appearance of a very low intense J-band at 608 nm and a shoulder at 570 nm (Fig. 5.4(B)). The growth of the J-aggregates was marked by the presence of pronounced transverse ( $\lambda_{max} = 572$  nm) and longitudinal ( $\lambda_{max} = 606$  nm) J-band transitions with a concomitant decrease in the monomer absorption band. These features correspond to stages 3 and 4 (Fig. 5.4(C-D)) when a ratio of 1:2.5 (v/v) and 1:3 (v/v) was preserved, respectively,

between C8O3 in ethanol and NaOH in water. A nearly complete transformation from monomer to J-aggregates was observed at stage 5 upon further increasing the C8O3-to-NaOH ratio, as clearly seen from the reduction of the monomer absorption band at 523 nm (Fig. 5.4(E)). Interestingly, the longitudinal J-band transition showed a blue shift ( $\lambda_{max} = 604$  nm) with a reduced amplitude as compared to stage 4. Concomitantly, a red shift was observed for the transverse J-band ( $\lambda_{max} = 576$  nm) with an increased intensity (Fig. 5.4(B)), suggesting a bundling interaction between the tubular assemblies that enhances the delocalization of transverse excitons. Having optimized stable conditions for the different stages of the hierarchical assembly, the response of these excitons toward the incident polarization states of light was then studied using Mueller polarimetry.

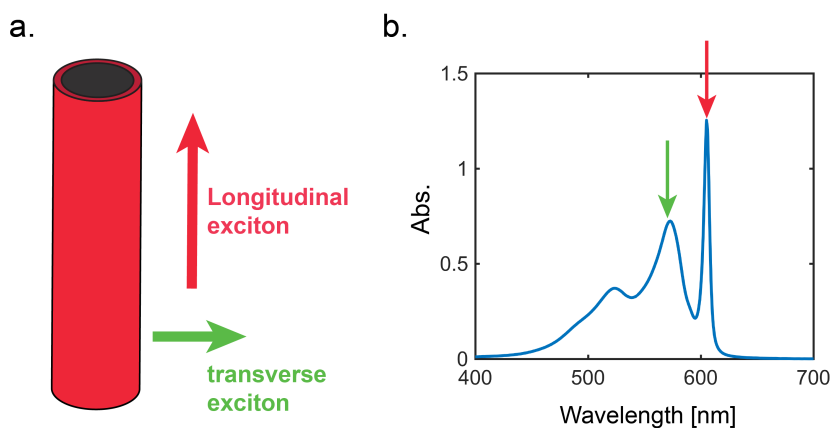


FIGURE 5.3: (a) schematics of a tubular J-aggregate where the effective dipole orientation of the transverse (green) and longitudinal (red) excitons are indicated. (b) J-aggregate absorption spectrum showing that the main peaks are respectively associated to one exciton type (longitudinal and transverse).

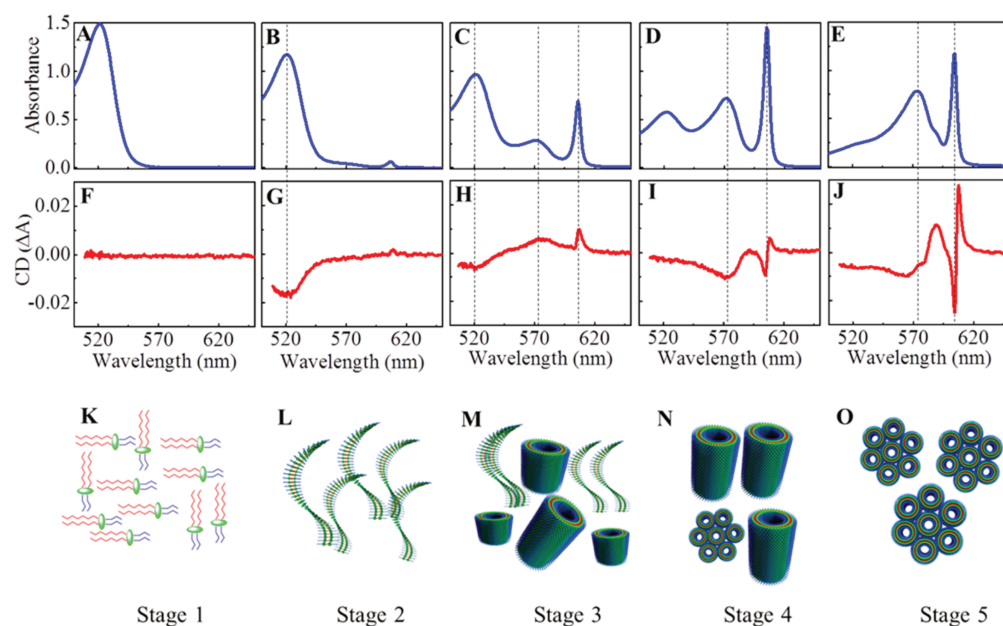


FIGURE 5.4: (A-E) Absorption spectra of C8O3 at different stages of J-aggregation obtained by maintaining a ratio (v/v) of (A) 1:2, (B) 1:2.2, (C) 1:2.5, (D) 1:3, and (E) 1:4 between C8O3 (0.3 mM) in ethanol and aqueous NaOH (0.02 M). Panels (F-J) show the corresponding CD spectra for each stage estimated from Mueller polarimetric analysis. The dotted line is a guide to the eye connecting the absorption and CD peaks. (K-O) Schematic representation of the molecular ordering at various stages of assembly, (K) isolated C8O3 monomers, (L) symmetry-broken C8O3 assembly indicating the primary nucleation process, (M) formation of chiral C8O3 J-aggregate, (N) growth of tubular assemblies, and (O) bundling of cylindrical C8O3 aggregates resulting in exciton coupling

The chiral signatures revealed by CD signals determined from Mueller analysis at each stage of the self-assembly are presented in Fig. 5.4(F-J). No noticeable CD signatures were observed in stage 1 shown in Fig. 5.4(F), as expected when starting with achiral monomers. But very interestingly, a negative Cotton type CD was observed predominantly at the monomer absorption band ( $\lambda_{max} = 523$  nm) in stage 2 shown in Fig. 5.4(G). Since the isolated monomers are achiral, the observed CD shows that already in stage 2 the symmetry breaking is nucleated in the earliest steps of aggregation. The aggregation in cyanine molecules is generally understood to be induced by the dispersion forces arising from the high polarizability of the  $\pi$ -electrons of the polymethine chains. However, such a  $\pi$ -stacking process would result in molecular exciton coupling and therefore in J-band transitions. Since the visible spectroscopic features are primarily monomer-like in stage 2, the assembly of amphiphilic C8O3 monomers inducing the primary chiral nucleation event must be driven by attractive forces of hydrophobic nature. From the reported crystal structure of the C8O3 molecule, it is known that the position and orientation of carboxy groups, favorable for both inter- and intra-molecular hydrogen bondings, are

mainly responsible for the twisted molecular structure leading to chiroptical properties [109]. Thus, the chirality spawned at stage 2 essentially implies that the primary chiral nucleation process is governed by hydrophobic interactions of the alkyl chains that bring the C8O3 molecules in a favorable geometry to have hydrogen bonding of the carboxy groups and generate the optical twist as shown schematically in Fig. 5.4(L). Since a chiral nucleation induced under a thermodynamic equilibrium process would result in a racemic mixture [110], the enantiomeric excess observed in stage 2 must therefore be driven by a kinetically controlled or trapped assembly process. From the analysis of the sign of the CD spectra for 10 different experiments, we found that there is a 9:1 bias toward negative Cotton type CD in contrast to an expected racemic 1:1 distribution from a statistical check. Although its origin is still unknown, this kind of non-statistical symmetry breaking has been reported by Lehn and co-workers in the case of foldamer-based supramolecular aggregates [111].

The symmetry broken assembly of stage 2 then transfers its chirality to the cylindrical J-aggregates in stage 3, marked by the appearance of two positive Cotton-type CD peaks at 573 nm and 606 nm corresponding to the two J-aggregate exciton transitions shown in Fig. 5.4(H). Interestingly, the reversal in the handedness of the J-band in stage 3 points to a secondary nucleation process taking place during the formation of cylindrical J-aggregates. The  $\pi$ -stacking of the chiral assemblies of stage 2 induces the growth of tubular structures of C8O3 shown in Fig. 5.4(M) that can either take the same or opposite handedness of the initial assembly during the secondary chiral nucleation. Since the coupling between chiral excitons is likely to show bisignate CD as predicted by the Nakanishi model [112, 113], a Cotton-type CD at stage 3 indicates that the chiral J-aggregates as well as the ordered monomer assemblies are isolated from each other as shown in Fig. 5.4(M). An amplification of the chirality is observed in stage 4, with a bisignate CD at the longitudinal exciton band of the J-aggregate (Fig. 5.4(I)); moreover, the negative Cotton type CD at 523 nm has become negligible at this stage, demonstrating that chiral assemblies governed by the hydrophobic interaction have all given way to  $\pi$ -stacked tubular assemblies as shown in Fig. 5.4(N). An even more pronounced chiral amplification is seen at stage 5 with bisignated CD for both J-aggregate exciton transitions as shown in Fig. 5.4(J). The exciton coupled bisignated CD signal is a manifestation of the bundling of the cylindrical aggregates as shown in Fig. 5.4(O). This is in good agreement with the visible spectroscopic features observed at this stage and described above.

### Analyzing signatures of linear dichroism (LD)

Apart from the CD, signatures of linear dichroism (LD) can also be extracted from the Mueller matrix at different stages of the aggregation. The formation of anisotropic, but oriented, macroscopic structures can be probed from the linear dichroism horizontal

projection (LD) and the linear dichroism 45° projection (LD') spectra of the medium [114, 115]. Linear dichroism results from differential absorption of light linearly polarized parallel or perpendicular to the orientation of the molecular axis, whose sign and magnitude are depending on the averaged orientation of the sample inside the probing volume during the measuring time. LD and LD' signals therefore depend on a choice of a coordinate system and enable to follow the formation and the growth of C8O3 J-aggregates at each stage of the self-assembly through the evolution of their total linear dichroic features.

From the Stokes space symmetry, a rotation transformation with respect to the optical axis of an angle  $\theta$  is written as in Eq. (2.71). According to the principle of differential decomposition by a matrix exponential, the linear dichroism of one Mueller matrix in two coordinate systems  $S1$  and  $S2$  related by a rotation can be written as

$$LD_{S2} = LD_{S1} \cos 2\theta + LD'_{S1} \sin 2\theta \quad (5.8)$$

$$LD'_{S2} = -LD_{S1} \sin 2\theta + LD'_{S1} \cos 2\theta. \quad (5.9)$$

If we set  $S2$  as the coordinate system of the proper frame of the macrostructure with  $x$  axis aligned along the averaged linear dichroism signal, in such a coordinate system,  $LD'_{S2} = 0$ . We can therefore determine explicitly the mean orientation angle with respect to the  $x$  axis of the laboratory frame as

$$\theta = \frac{1}{2} \tan^{-1} \frac{LD'_{S1}}{LD_{S1}}, \quad (5.10)$$

and the total linear dichroism as

$$LD_{tot} = \sqrt{LD_{S1}^2 + LD'_{S1}^2}. \quad (5.11)$$

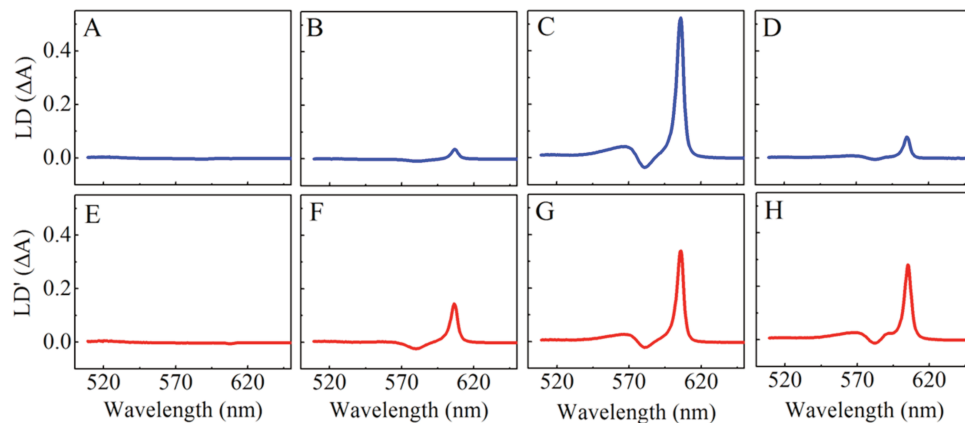


FIGURE 5.5: LD (A-D) and LD' (E-H) spectra of C8O3 assemblies estimated from Mueller polarimetric analysis at stage 2 (A, E), stage 3 (B,F), stage 4 (C,G), and stage 5 (D,H) of the self-assembly.

With these relations, we can take a close look at the experimental data allowing us to follow the formation and the growth of C8O3 J-aggregates at each stage of the self-assembly by considering their total linear dichroic features. No LD signal was observed as expected for the monomeric stage 1 since no macroscopic structure is formed. The symmetry-broken assemblies of stage 2 did not show significant LD nor LD' as shown in Fig 5.5(A),(E), indicating no specific orientations of the transitions dipoles (i.e., no macroscopic tubular structure of the J-aggregate is formed). Interestingly, the formation of tubular aggregates in stage 3 is marked by the appearance of positive LD and LD' peaks at the longitudinal exciton band and a bisignated signal at the transverse exciton band shown in Fig 5.5(B),(F). The intense and positive LD of the J-band transition at 606 nm points to the fact that the transition dipole moment is polarized parallel to the orientation of the cylindrical structures, whereas the less intense and bisignated signal at the transverse exciton wavelength shows that its transition dipole moment is perpendicular to the alignment of the tube. A significant enhancement in the amplitude of the LD and LD' shown in Fig 5.5(C),(G) is observed at stage 4, particularly for the longitudinal J-aggregate transition ( $\lambda_{max} = 606$  nm), indicating the growth of aggregates into long tubular structures. A reduction in the total LD (resulting from LD and LD') in stage 5 Fig 5.5(D),(H) might come from the fact that the tubular aggregates are no longer growing but the concentration of aggregates decreases as more NaOH solution is added or even from a possible case where the aggregates are starting to break into smaller pieces. Since these tubular structures diffuse within the sample solution, we can see by looking at many different measurements that the orientations revealed by the ratio between LD and LD' signals are not deterministically determined but rather randomly distributed among the various and different samples studied.



## Analyzing the degree of polarization

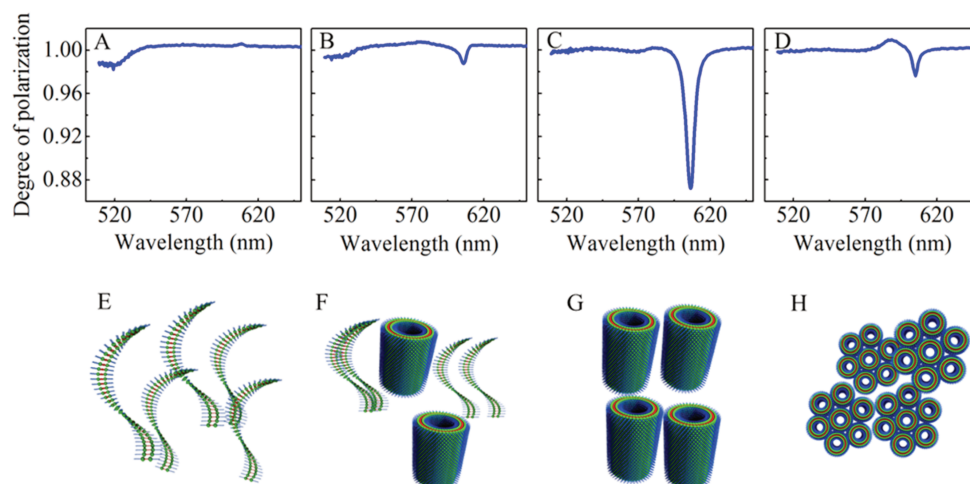


FIGURE 5.6: (A-D) Degree of polarization estimated from the Mueller polarimetric analysis at stage 2 (A), stage 3 (B), stage 4 (C), and stage 5 (D) of the C8O3 self-assembly. (E-H) Schematic illustration of the structural assemblies corresponding to stages 2 to 5, traced from depolarization studies.

Another quantity that can be analyzed using our Mueller polarimetry is the degree of polarization  $P$  extracted from the experimental Mueller matrix. This observable  $P$  can be evaluated following Eq.(2.164). This quantity is a particular intensity in the context of molecular self-organization processes considering the broadband relation between molecular macroscopic disorder and the degree of polarization of a light beam that has interacted with the molecular systems under study. As discussed before, for a fully non-depolarizing medium,  $P$  will be 1, and for a totally depolarizing medium,  $P$  will be 0. Since the level of depolarization depends on the oscillator strength, electronic couplings, size, and geometry of the sample [116, 117], a detailed analysis of the evolution of  $P$  could predict how the level of order evolves during the C8O3 aggregate formation in solution. Note that working with a collimated light beam, our experiments are not sensitive to depolarization due to scattering effects.

Similar to the LD measurements, the depolarization by isolated C8O3 molecules in stage 1 was found to be negligible. The chiral assembly of stage 2 showed noticeable depolarization only at the monomer absorption region as displayed in Fig. 5.6(A), further indicating the absence of any higher-order organization of molecules responsible for the primary chiral nucleation process. The formation of tubular J-aggregates in stage 3 resulted in the depolarization at 606 nm as shown in Fig. 5.6(B) that corresponds to the interaction of the longitudinal excitons with the polarized light. Similar to LD and LD' analysis, depolarization is also peaked at stage 4 and more interestingly is only detected

at the longitudinal J-band transition region. This large enhancement of depolarization is a result of the disorder developed by the formation of highly oriented anisotropic tubular aggregates, as shown schematically in Fig. 5.6(G). In contrast, at stage 5 of the hierarchical assembly, the breaking and bundling of the tubular aggregates enhances the overall order as the bundling forces several single tubular structures to align along one same orientation, thereby reducing the degree of depolarization as shown in Fig. 5.6(D). Thus, the formation of bundled assemblies as displayed in Fig. 5.6(H) not only induces the coupling of chiral excitons but also develops overall order and stability of the system.

### 5.3 Poincaré sphere representation

In this section, the evolution of the polarization states of light measured during the supramolecular self-assembly are represented in the Poincaré sphere and visualized in relation with the measured chiroptical observables.

We apply here the methods described in chapter 3 to our molecular C8O3 system. The dynamics imprinted on the polarization by the supramolecular evolution leads to landscapes when imaged in the Poincaré sphere. We explore and draw the Stokes vector trajectories in 4 different parameter spaces:

- 1) Wavelength-dependent evolutions of the Stokes eigenvectors at the different stages of the self-assembly.
- 2) Stokes vector trajectories describing the polarization dynamics of a light passing through a homogeneous medium at a given wavelength starting from a given initial polarization state.
- 3) Polarization dynamics of a light beam transmitted through a (reconstructed) system evolving throughout the self-assembly process along the light propagation direction (optical axis).
- 4) Reconstructed trajectories of output Stokes vector passing through homogeneous medium that evolve along the aggregation process at a given wavelength starting from a given initial polarization state.

#### 5.3.1 Wavelength dependence of Mueller matrix eigenvectors

Mueller matrices are spectral matrices, with one Mueller matrix for each measured wavelength. This gives, therefore, the capacity to plot spectral evolutions of the eigenvectors of each Mueller matrices for each stage of the aggregation. As we showed in chapter

3, the eigenvectors of a Mueller matrix can help revealing hidden symmetries of an optical medium. We apply here this methodology to our chiral supramolecular self-assembly system.

However, as shown above, an experimental Mueller matrix measured on J-aggregates is generally depolarizing. Since the symmetry properties that we are interested in are mainly to be associated with non-depolarizing quantities, the Mueller matrix eigenvectors have to be extracted, at each stage of the aggregation, from the closest non-depolarizing Mueller matrix (the same as the one used for extracting the polarimetric observables). For each wavelength, we will follow the relative configurations between the 2 eigenvectors  $\mathbf{v}_{\pm}$  and their evolutions throughout the self-assembly process. As explained in chapter 3, this approach is interesting when looking at chiral signatures of a medium, here in particular looking at their dynamical evolutions with wavelength noted as  $\mathbf{v}_{\pm}(\lambda)$ . The results of this analysis ( $\mathbf{v}_{\pm}(\lambda)$ ) are plotted for the aggregation stage 2 to 5 in Fig. 5.7. Regarding stage 1, its Mueller matrix is very close to the identity matrix. This implies that the eigenvectors are not well defined and thus not represented here.

Fig. 5.7 reveals that along the direction of the self-assembly, the wavelength-dependent distribution of the eigenvectors evolves from a dispersed conformation to a relatively closed conformation, before becoming dispersed again in the last stage of aggregation. According to the Mueller matrix eigenvector analysis presented in chapter 3, the only non-chiral conformation for the 2 eigenvectors is when they are distributed collinearly on the  $S_1OS_2$  plane of the Poincaré sphere. For all other conformations, the medium possesses at least one type of chirality (planar chirality or optical activity). It is remarkable to see that, compared with the polarimetric observables extracted in the same aggregation stage, the chiral characteristics of the medium described by the eigenvector configurations do not necessarily follow the same evolution of the CD or CB signals that, conventionally, are taken as reflecting the basic chiral properties. Indeed, as it can be seen on Fig. 5.7(a) which displays the wavelength dependence of the eigenvector configuration of the sample in stage 2, the eigenvectors show an obvious chiral response while the CD signal extracted in the same stage is very weak according to Fig. 5.4(G). In contrast, Fig. 5.7(c) for the sample in stage 4 displays eigenvector configurations that correspond to a quasi-absence of chiral feature, while this time, the CD signal is measured to be strong according to Fig. 5.4(I).

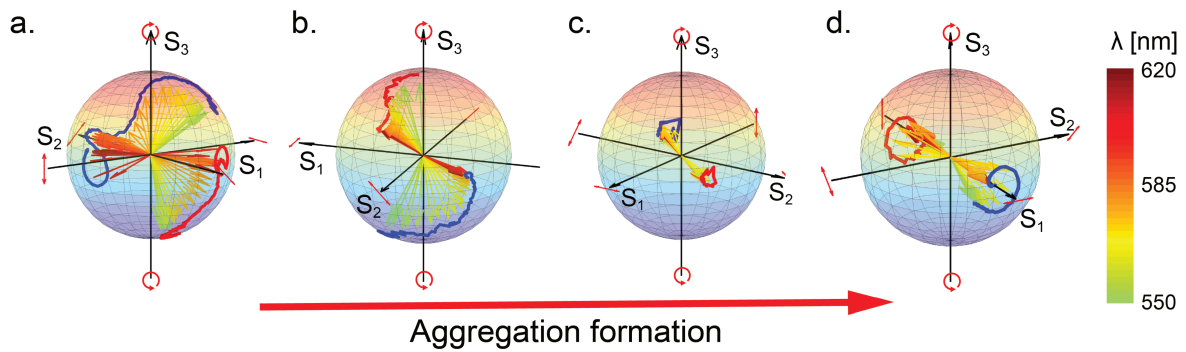


FIGURE 5.7: (a)-(d) show the wavelength distribution of the 2 eigenvectors of the non-depolarizing Mueller matrix extracted at each stage of the aggregation process, going from stage 2 to stage 5. The different colors of the eigenvectors correspond to wavelengths varying from 550 nm (green) to 620 nm (red). The blue and red curves show the trajectory of the tip of each of the two Mueller matrix eigenvectors evolving from 550 nm to 620 nm.

These contrasted results stem from the fact that the eigenvectors yield a global polarimetric view on the sample combining different polarimetric features like CD (CB) but also LD (LB). Therefore when the LD (LB) is much smaller or of the same order of magnitude of the CD (CB), chiral features can easily be revealed looking at the eigenvector conformation. However, when there is a large source of linear anisotropy (like for a linear macrostructure) in the sample so that the LD (LB) signal dominates over the CD (CB) one, the eigenvector conformations will be dominated by the LD (LB) signal. Hence, the results in Fig. 5.7 can be explained by comparing the CD and LD signals at each stage. This shows how the eigenvector conformation approach is an alternative measure of the chirality of the medium and how it yields complementary information with respect to conventional polarimetric measurements.

### 5.3.2 Polarization dynamics in the Poincaré sphere for light passing through a homogeneous sample

Then, once the Mueller matrices are acquired for each stage of the self-assembly, it also becomes possible to visualize in the Poincaré sphere the evolution of the polarization states throughout the assembly at different wavelength. This type of polarization dynamics representation has been applied on different optical systems, for instance on non linear anisotropic fibers [118] or on new types of metamaterials [20]. In principle, the polarization dynamics through a homogeneous sample is described in Eq. (3.115). According to this expression and the discussion in chapter 3, under the framework of  $SO^+(1,3)$  group, the generator for such polarization dynamics are: rotations (related only to birefringence),

boosts (only to dichroism), and generalized Lorentz boosts (to both birefringence and dichroism).

Again being interested only in non-depolarizing quantities here, the Mueller matrix involved in this representation of the polarization dynamics is the closest non-depolarizing Mueller matrix extracted from the experimental Mueller matrix. At this point however, in order to reveal the dynamics more clearly, we expand artificially the optical path from 1mm (the experimental cuvette path length) to 1cm following to Eq.(2.213) and Eq.(2.215). This expansion is done by just extending the parameters of the  $SO^+(1, 3)$  generators and will not change the nature of the dynamics induced by these generators. Fig. 5.8 reveal the polarization dynamics for a sample in stage 5. Picking up 6 representative wavelengths reveals different dynamics with their corresponding optical observables (birefringences and dichroisms) shown in Fig. 5.8(a).

Fig. 5.8(b) and (c) show the polarization dynamics at 550 nm and 572 nm. They look like distorted generalized Lorentz boosts which combine a rotation and a boost with a non-collinear Stokes eigenvector pair. We note that the direction of rotation is reversed when the linear birefringence (both LB and LB') changes sign at 550 nm and at 572 nm, according to Fig. 5.8(a). This effect is clearer by looking at the dynamics from 600 nm to 610 nm in Fig. 5.8(d)-(f) since the amplitude of both linear birefringence and dichroism signals are larger and the 2 Stokes eigenvectors are almost collinear (orthogonal eigenstates) due to the predominance of LD (LD') and LB (LB'). Specifically, at 600 nm and 610 nm, the dynamics corresponds to generalized Lorentz boost with opposite rotation directions but with the same boost direction, corresponding that between these two wavelengths, the linear birefringence changes sign while the linear dichroism maintains its sign. We note a special wavelength in the vicinity of 605 nm, where the linear birefringence is nearly zero. In this case, the polarization dynamics of the end of one eigenvector follows only the boost as shown in Fig. 5.8(e). Finally, the dynamics at 630 nm is driven by the fast decay of the linear dichroism, much faster than the decay of the linear birefringence as wavelength increases according to Fig. 5.8(a). As a consequence, the dynamics only rotate around the eigenvectors as shown in Fig. 5.8(g).

This example clearly shows that the Poincaré sphere representation can be very useful when aiming at visualizing the polarization dynamics involved between the incident and transmitted Stokes vectors at a given wavelength once a full Mueller matrix is measured through the molecular system. As such, it constitutes an obvious alternative for displaying and visualizing the optical information contained within the Mueller matrix.

But fundamentally, this way of representing the polarization dynamics throughout a homogeneous medium at one chosen stage of the self-assembly reveal how the generators of the  $SO^+(1, 3)$  group can actually be experimentally realized. This approach therefore

sheds an interesting light on the Poincaré representation of complex molecular hierarchies in relation with the underlying structure of the Mueller algebra. These connections certainly deserve to be further explored.

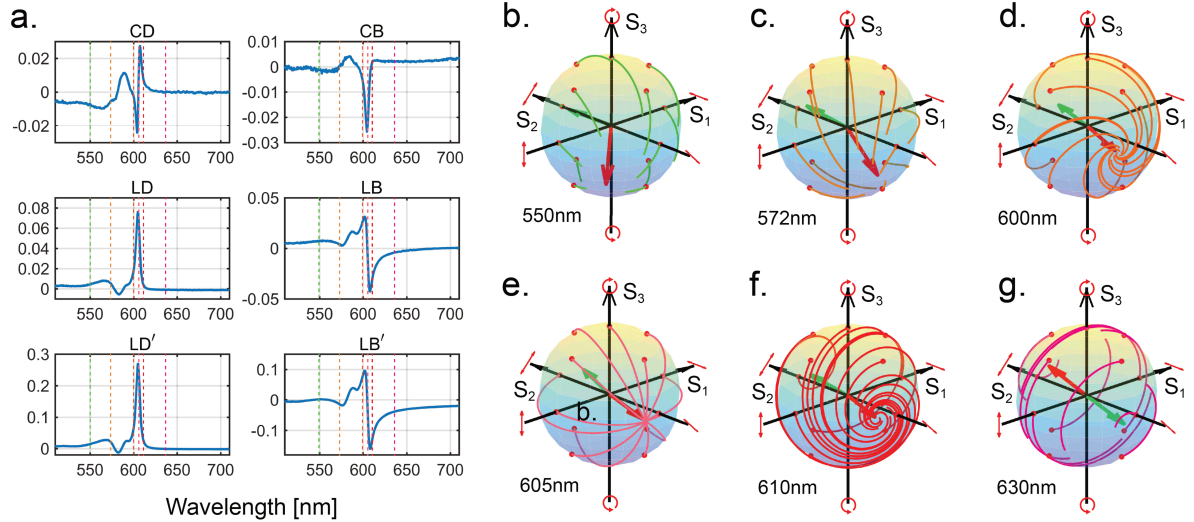


FIGURE 5.8: (a) displays all polarimetric properties of our sample in its stage 5 (with a ratio (v/v) between C8O3 (0.3 mM) in ethanol and aqueous NaOH of 1:4.2). (b)-(g) show the polarization dynamics of the light with different incident polarization in the Poincaré sphere marked as red dot at the wavelength of 550 nm, 572 nm, 600 nm, 605 nm, 610 nm and 630 nm respectively. The colored markers presented in (a) spot the dynamics shown in (b)-(g) with the corresponding wavelength color code of the dynamic trajectories.

### 5.3.3 Polarization dynamics of a reconstructed evolution of polarimetric observables along the self-assembly

We can now extend this analysis, since we have measured the Mueller matrix of every stage of the aggregation. This will allow us to add one dimension, the aggregation stage, to the parameter space and visualize the complex polarization dynamics. The idea here is to describe the polarization dynamics as if it were proceeding from a system that evolves along an optical axis defined by the propagation direction of light probing the system and transmitted through it as shown in Fig 5.9. As presented in Chapter 4, the polarization dynamics through a homogeneous medium can be described analytically as Eq. (3.115). However, the dynamics becomes more complex when  $\mathbf{N}_M$  is not constant along light propagation. In our case, the dynamic equation of a Stokes vector to be investigated writes

$$\frac{d\mathbf{S}(z)}{dz} = \mathbf{N}_M(z)\mathbf{S}(z) = \mathbf{N}_M[\phi(z)]\mathbf{S}(z). \quad (5.12)$$

This expression states that a sample can be reconstructed along the light propagation direction, by a continuous evolution of sublayers corresponding to the aggregation process (with an increasing  $\phi_v$  ratio ( $v/v$ ) between aqueous NaOH (0.02M) and C8O3 (0.3 mM) in ethanol), where each layer displays the polarimetric properties of a given  $\phi_v$  stage as schematized in Fig. 5.9. The differential Mueller matrix  $\mathbf{N}_M$  then becomes a functional of evolving ratio  $\phi_v(z)$ . We investigate, for any input polarization state, the polarization dynamics through this reconstructed medium.

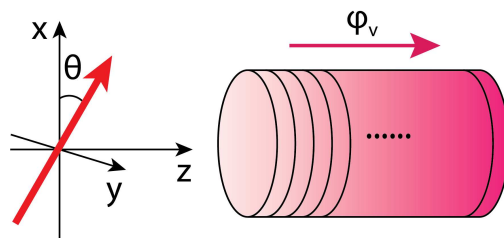


FIGURE 5.9: This schematic shows the setting adopted here for describing the generation of the polarization dynamics through the evolving supramolecular system. The coordinate system chosen fixes  $z$  as the light propagation direction and the red arrow (left-side) indicates the averaged orientation of the linear structure in each layer.

To do so, we need to estimate the evolution of the intrinsic polarimetric properties as a continuous one from the Mueller matrices measured in different aggregation stages. Knowing that linear dichroism (LD, LD') and birefringence (LB, LB') that we extract from the Mueller matrix depend both on the averaged orientation of the tubular self-assembled macrostructures which is randomly distributed between the different samples and the different measurements, we need to extract the total LD and LB in order to compare the samples at different stages with same standard. To do this, we rotate the experimentally measured Mueller matrix to the reference frame of the macrostructure where the tubular structure are aligned to  $Ox$  axis. This angle of rotation is obtained by the ratio between LD and LD' from the initially measured Mueller matrix, according to Eq.(5.10). Once the intrinsic, total LD and LB, are measured, we use a smooth interpolation between the existing stages in order to get the continuous evolution of the polarimetric properties.

In practice, here, we select the data for a sample with ratio 1:  $\phi_v$  ( $v/v$ ) between C8O3 (0.3 mM) in ethanol and aqueous NaOH (0.02M) of 1: 2.2, 1: 2.6, 1: 2.8, 1: 3, 1: 3.5, 1:3.8 and 1:4.2. The polarimetric observables, namely LD, LB, CD and CB for those sample with selected mixing ratio are shown in Fig. 5.10(a),(d),(g) and (j). The evolutions of the polarimetric observables after the smooth interpolation procedure are shown in the last two panels in each box in Fig. 5.10.

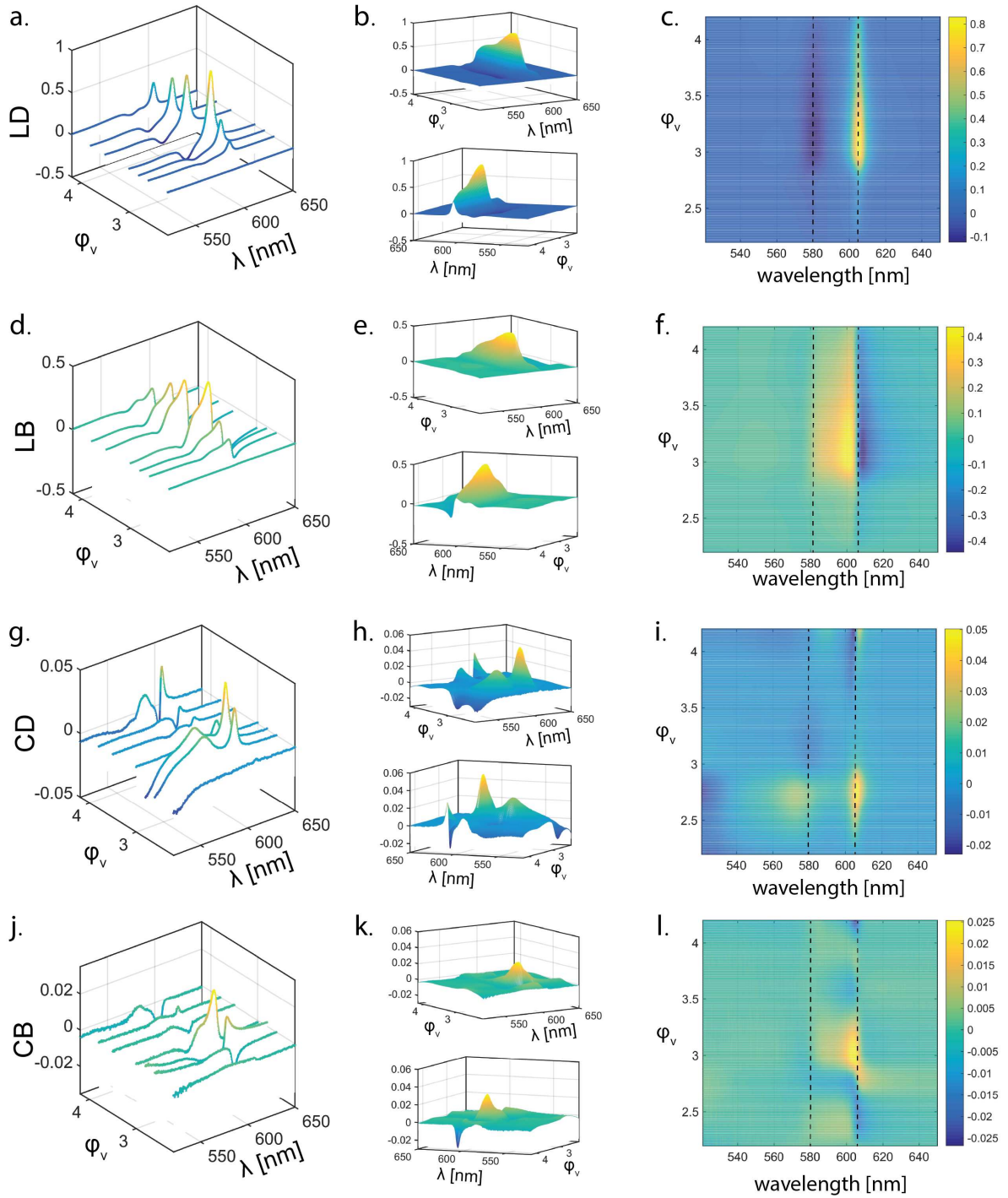


FIGURE 5.10: (a)-(c), (d)-(f), (g)-(i) and (j)-(l) display respectively the spectral evolution of the LD, LB, CD and CB with the aggregation stage as  $\varphi_v$  increases, while the last 2 panels in each box show the front, back and top views of this evolution after interpolation.

Here we stress that the interpolation just gives an ideal estimation based on the existing measurements but does not necessarily correspond to the real situation at one specific stage of the aggregation process. However, throughout the whole aggregation process, the interpolation certainly gives a reasonable estimation for the evolution of the observables.



For the LD signature, we can see an increase of the signal from the ratio 1:2.2 to 1:3 which reveals the growth of the aggregate. Then once all monomers have aggregated, the LD signal gradually decreases, revealing a reduction of the concentration of the aggregate solution as more NaOH solution is added. From the evolution of the CD signal, we can also see the increase of the CD as the tubular structure forms from the ratio 1:2.2 to 1:3. Finally, we clearly observe the progressive transition of the monotonic CD signal to the bisignated CD and the further growth of the bisignated signal due to the increase in the tubular structure bundling.

Once the evolution of these polarimetric properties is drawn, we can build the differential Mueller matrices associated with each intermediate stages of the self-assembly  $\mathbf{N}_M[\phi_v(z)]$  as mentioned in Eq. (5.12). The system thus probed is divided into several layers, each sublayer determined by a Mueller matrix corresponding to certain ratio  $\phi_v$ . The layers are arranged along a linearly increasing order of  $\phi_v$  (from 2.2 to 4.2) with the evolution along  $z$  as

$$\phi_v(z) = \frac{2}{l}z + 2.2 \quad (5.13)$$

with  $l$  the total path length of the reconstructed medium.

First of all, we investigate the simple situation where  $\theta$  (averaged orientation of linear structures) is the same for all layers which is aligned with x axis ( $\theta = 0$ ). The dynamic equation at a given wavelength in this case is described explicitly as

$$\frac{d\mathbf{S}(z)}{dz} = \begin{pmatrix} 0 & -LD[\phi_v(z)] & 0 & CD[\phi_v(z)] \\ -LD[\phi_v(z)] & 0 & CB[\phi_v(z)] & 0 \\ 0 & -CB[\phi_v(z)] & 0 & -LB[\phi_v(z)] \\ CD[\phi_v(z)] & 0 & LB[\phi_v(z)] & 0 \end{pmatrix} \cdot \mathbf{S}_z \quad (5.14)$$

The polarization dynamics in this situation is plotted in Fig. 5.11 at wavelength 530 nm, 580 nm, 600 nm, 605 nm, 610 nm and 625 nm. We can see that this dynamics is not exactly the same as the one we showed above for a uniform sample. This type of dynamics cannot be simply analyzed using a constant generalized Lorentz boost. It rather consists of many segments of generalized Lorentz boosts defined with constant parameters. Since the dominant polarization properties (LD and LB) are monotonically evolving, the polarization dynamics is similar to that of a uniform system.

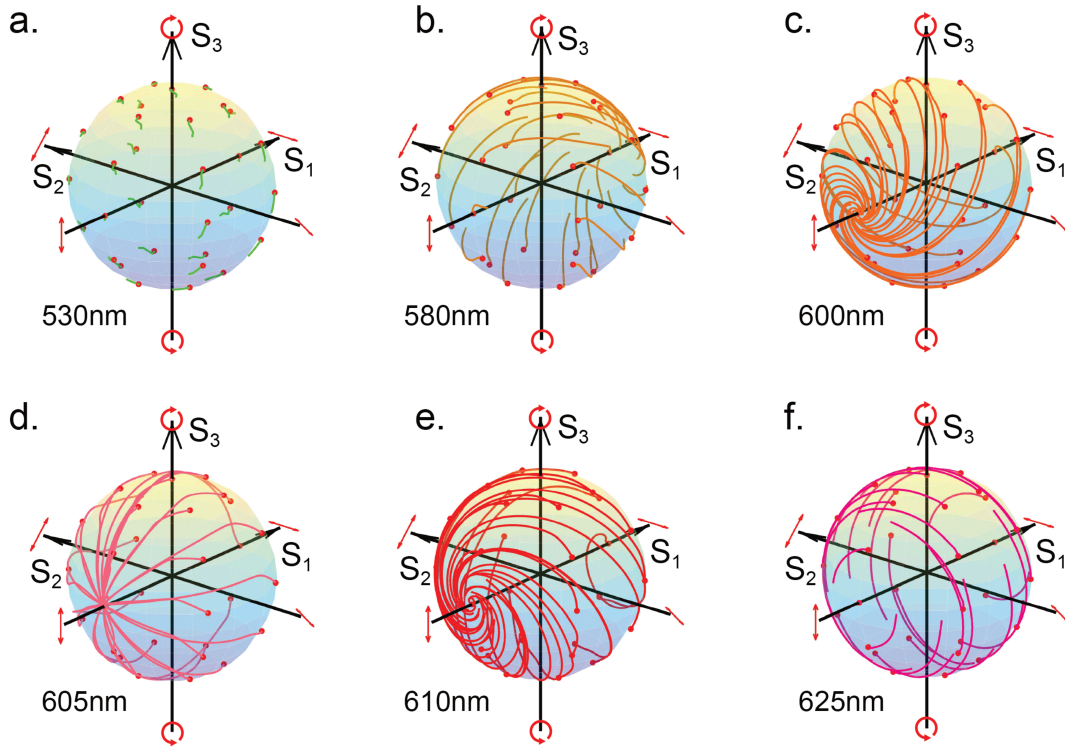


FIGURE 5.11: (a)-(f) show the polarization dynamics in an evolving system according to Fig. 5.9 from the monomer to the aggregated phases with all structures aligned with the same orientation, starting from different incident polarization state marked as red dot in the Poincaré sphere at the wavelengths of 530 nm, 580 nm, 600 nm, 605 nm, 610 nm and 625 nm, respectively.

Although this opens fascinating perspectives, it is important for our work to emphasize that the polarization dynamics shown in Fig. 5.11 does not reflect the actual situation since in reality, the tubular structures are randomly distributed in the volume along the optical axis. Therefore, in order to be more realistic, instead of aligning all the tubular structure in the same direction, we add a random fluctuation on the orientation  $\theta(z)$  along the light propagation direction  $z$  so that the dynamic equation becomes

$$\frac{d\mathbf{S}(z)}{dz} = \begin{pmatrix} 0 & -LD[\phi_v(z)] \cos \theta(z) & LD[\phi_v(z)] \sin \theta(z) & CD[\phi_v(z)] \\ -LD[\phi_v(z)] \cos \theta(z) & 0 & CB[\phi_v(z)] & -LB[\phi_v(z)] \sin \theta(z) \\ LD[\phi_v(z)] \sin \theta(z) & -CB[\phi_v(z)] & 0 & -LB[\phi_v(z)] \cos \theta(z) \\ CD[\phi_v(z)] & LB[\phi_v(z)] \sin \theta(z) & LB[\phi_v(z)] \cos \theta(z) & 0 \end{pmatrix} \cdot \mathbf{S}_z \quad (5.15)$$

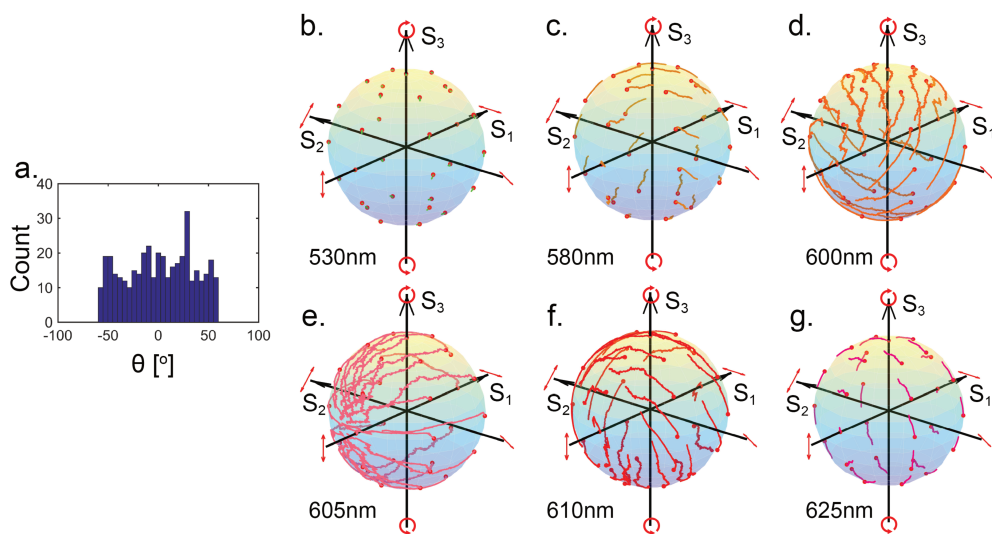


FIGURE 5.12: (a) shows the distribution of the random orientation  $\theta$  indicated in Fig. 5.9 along the optical axis generated from a uniform distribution from  $-60^\circ$  to  $60^\circ$ . (b)-(g) show the polarization dynamics through the evolving system from the monomer to the aggregated phases with all the tubular structures in each layer randomly distributed starting with different incident polarizations in the Poincaré sphere marked as red dots at wavelengths 530 nm, 580 nm, 600 nm, 605 nm, 610 nm and 625 nm, respectively.

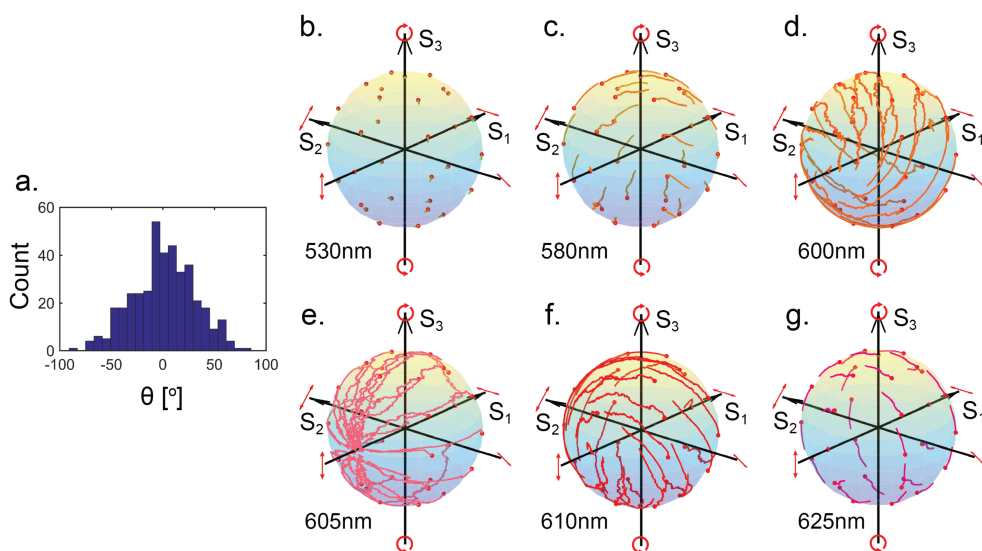


FIGURE 5.13: (a) shows the distribution of the random orientation  $\theta$  indicated in Fig. 5.9 along the optical axis generated from a normal distribution with a variance of  $30^\circ$ . (b)-(g) show the polarization dynamics through the evolving system from the monomer to the aggregated phases with all the tubular structures in each layer randomly distributed starting with different incident polarizations in the Poincaré sphere marked as red dots at wavelengths 530 nm, 580 nm, 600 nm, 605 nm, 610 nm and 625 nm, respectively.

We illustrate this by 2 situations where the random orientation is generated either by a uniform distribution (Fig. 5.12) or by a normal distribution (Fig. 5.13). We can see first that the random fluctuation of the orientation leads to more complex polarization dynamics. This complexity can be understood as caused by a stochastic dynamics superimposed on a deterministic one. Despite this added complexity and within certain limits of fluctuations, the dynamic features of linear birefringence and dichroism can be still recognized. If however the orientation fluctuation becomes much stronger, the polarization dynamics progressively becomes fully stochastic.

### 5.3.4 Evolution of the output Stokes vector $\mathbf{S}_{out}$ as a function of the aggregation stage

We can also investigate an other degree of freedom in the Poincaré sphere. Let us consider again the output polarization state  $\mathbf{S}_{out}$  passing through an homogeneous medium in an aggregation phase characterized by a given ratio  $\phi_v$  determining the differential Mueller matrix  $\mathbf{N}_M(\phi_v)$  as

$$\mathbf{S}_{out} = \exp(z\mathbf{N}_M(\phi_v)) \cdot \mathbf{S}_{in}. \quad (5.16)$$

The evolution of  $\mathbf{S}_{out}$  along  $z$  for a given  $\phi_v$  has been discussed above and referred to as  $\mathbf{S}_{out}$  polarization dynamics. We now look at the evolution of the final polarization state  $\mathbf{S}_{out}$  along  $\phi_v$  (formation of aggregates) for a given path length  $z$ . For a given incident polarization state  $\mathbf{S}_{in}$  on the surface of Poincaré sphere, we plot the tip of the Stokes vectors of the final polarization states for samples at different stages of aggregation. This draws giving a trajectory on the Poincaré sphere shown in Fig. 5.14. We select the wavelength at 530 nm, 580 nm, 600 nm, 605 nm, 610 nm and 625 nm in order to illustrate the different behaviors with the different polarimetric properties. We can see that trajectories starting with different  $\mathbf{S}_{in}$  at different wavelengths can give very different topologies. Some of them form single closed circles (or almost closed curve), while other form closed or quasi-closed lemniscates. The trajectory topology may depend implicitly on the polarimetric property evolution and the polarization state of the incident light. In other words, the possibility to generate in this parameter space closed trajectories on the Poincaré sphere points towards the concept of geometric phases that has many connections in fundamental optics. This indicates further here that molecular complexity and associated hierarchies can lead to complex optical responses, topologically rich in the context of polarization.

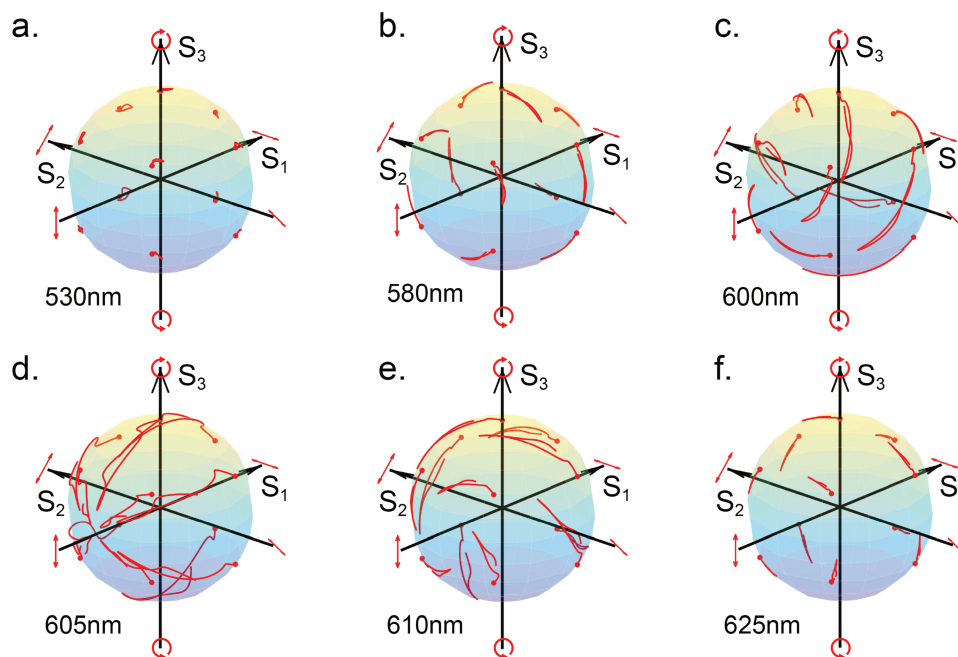


FIGURE 5.14: (a)-(f) show the evolution of the tip of the final polarization Stokes vector  $\mathbf{S}_{out}$  with initial polarization states  $\mathbf{S}_{in}$  marked as red dots at wavelengths 530 nm, 580 nm, 600 nm, 605 nm, 610 nm and 625 nm, respectively.

## 5.4 Conclusion

In this chapter, we have seen how Mueller polarimetry in transmission can be exploited as an efficient tool for evaluating the chiroptical properties of C8O3 hierarchical supramolecular assemblies. By carefully controlling the self-assembly process, a primary chiral nucleation event has been identified. The initial ordering of C8O3 molecules, triggered by the hydrophobic interaction of the alkyl chain, appears to be deterministically determined in this initial mirror symmetry breaking process. The chirality has been observed to be then transferred and amplified to cylindrical J-aggregates, in a later stage of the self-assembly, which handedness is determined by a secondary nucleation event. Bundling of the tubular structures at the final stage of assembly facilitates the coupling of chiral excitons, yielding bisignated circular dichroism signals. The formation, growth, and bundling of tubular structures has also been visualized by tracking the evolution of the linear dichroism and the degree of depolarization through the sample, thereby providing a new tool for monitoring and analyzing supramolecular self-assembly processes.

In the second part of the chapter, Poincaré sphere representation is used for visualizing the symmetry of the system and the polarization dynamics for light passing through such a homogeneous medium. We represented then the chiroptical evolution extracted from

---

the measured Mueller matrices in the Poincaré sphere. This representation has revealed rich polarization dynamics closely related to the hierarchical evolution of the supramolecular system. As shown in the end of the chapter, it is even possible to emulate complex polarization dynamics by literally building up an optical system which polarization response evolves along a chosen optical axis. This leads us to envision how one can harness molecular complexity for proposing new optical signatures and potentially new optical systems.



## Chapter 6

# Mueller matrices for molecular fluorescence polarimetry

In this chapter, we apply Mueller polarimetry for characterizing the polarization properties of molecular fluorescence signals. We will compare Mueller polarimetry to the standard methodology that evaluates polarization ratio and emission anisotropies for common molecular systems. We will stress that for some specific cases, such as when supramolecular systems are involved, resorting to Mueller matrix is necessary, not only because it offers a full characterization of the polarization states relation between excitation and emission, but also because it gives ways to identify and eliminate artifacts in the fluorescence polarization measurements. We will illustrate these capacities when discussing artifacts due to internal filtering effects in fluorescence measurements using the same J-aggregates supramolecular system as the one studied in Chapter 5. As we will see, such artifacts are crucial to be account for circular polarized luminescence (CPL) measurements. We will also discuss other perspectives offered by Mueller polarimetry in emission. Finally despite the fact that Mueller polarimetry in emission has many advantages, we will not avoid presenting some limitations of the method and some remaining difficulties when aiming at generalizing the approach to any type of molecular system.

### 6.1 Standard polarization analysis of molecular fluorescence

In this section, we review the standard approach used for characterizing polarization states in molecular emission, looking at fluorescence anisotropies and polarization ratio parameters. Looking into the dependence of such parameters, our aim is to compare this approach to Mueller polarimetry, from which we stress the importance of Mueller polarimetry as a complete characterization method for studying molecular emission from a polarization point of view.



### 6.1.1 Molecular fluorescence and polarization

In a molecule, the absorption of photons of wavelength  $\lambda_a$  corresponds to a given molecular transition and is followed by dynamic, internal relaxation processes. These lead to the emission of photons from a different transition, and thus to fluorescence at different wavelengths  $\lambda_e$ . This absorption-to-emission process is described in Fig. 6.1 in what is known as the Jablonski diagram.

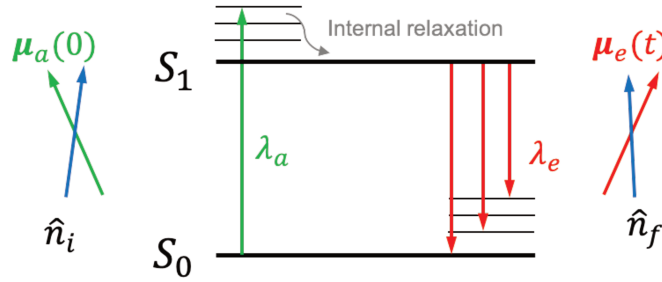


FIGURE 6.1: Energetic diagram describing absorption-to-emission process. The absorption and emission transition dipole moments are shown projected along the direction of polarization in excitation  $\hat{n}_i$  and analysis  $\hat{n}_f$ . The wavelength difference between  $\lambda_e$  and  $\lambda_a$  ( $\lambda_e > \lambda_a$ ) is known as the Stokes shift.

Following this mechanism, a fluorescence polarization experiment proceeds from the following steps, well described in [119]

- 1) A light beam linearly polarized along  $\hat{n}_i$  at wavelength  $\lambda_a$  is absorbed by the molecule. The probability of absorption is proportional to  $|\mu_a(0) \cdot \hat{n}_i|^2$ , where  $\mu_a(0)$  is the absorption transition dipole moment evaluated at  $t = 0$  time of the absorption.
- 2) Internal relaxation processes result in fluorescence from a different transition characterized by a wavelength  $\lambda_e$  and a emission transition dipole moment  $\mu_e(t)$  evaluated at a time  $t > 0$  corresponding to internal relaxation duration.
- 3) The emission polarization is given by the orientation of emission dipole  $\mu_e(t)$ . A linear polarizer oriented along  $\hat{n}_f$  analyzes the emitted fluorescence, which intensity therefore is proportional to  $|\mu_e(t) \cdot \hat{n}_f|^2$ .

Eventually then, the intensity of the fluorescence signal analyzed along the  $\hat{n}_f$  polarization direction and generated using an excitation beam linearly polarized along  $\hat{n}_i$  reads as

$$I_{if}(t) \propto \langle |\mu_a(0) \cdot \hat{n}_i|^2 |\mu_e(t) \cdot \hat{n}_f|^2 \rangle, \quad (6.1)$$

where  $\langle \cdot \rangle$  is an angular average taken over the (random) orientations of the molecules.

In contrast with absorption, emission transition dipole moments will be the same for all excited molecules since they generally correspond to the transition from the lowest excited state to ground state (Kasha's rule). They therefore depend only on the orientation of the molecule itself regardless of the excitation polarization and the excited state reached upon the excitation.

We stress that the emission transition dipole moment  $\mu_e$  is not necessarily aligned with the absorption transition dipole moment  $\mu_a$ . This can be due to intrinsic misalignments between the emission and transition moments of different excited states, internal motion and inter-molecular energy transfer during the life time of the excited state, Brownian diffusion occurring during the time of internal relaxation, etc. It is essentially the aim of fluorescence polarization measurements to access such alignment mismatches (between absorption and emission dipole moments) by measuring the induced anisotropy in the fluorescence polarization signal. Such measurement have proven to be extremely useful. In 1926 for instance, Francis Perrin was able to determine the lifetimes of molecular excited states by looking at the impact of Brownian diffusion of the emission transition dipole moment on polarization fluorescence anisotropy [120]. Other examples include studies in molecular mobility [121], structural properties (conformation [122], size [123, 124], flexibility [125, 126]) and order parameters [127]. More specifically, circular polarized luminescence (CPL) analysis, for chiral systems, can provide valuable information on the symmetry properties, electronic and molecular structure of chiral molecules in the excited states [128, 129].

In order to characterize linear anisotropy in emission, using a linearly polarized excitation, one can define the so-called polarization ratio  $p_V$  written as :

$$p_v = \frac{I_{\parallel} - I_{\perp}}{I_{\parallel} + I_{\perp}}, \quad (6.2)$$

where  $v$  indicates vertically linear polarization excitation, as shown in Fig. 6.2, and  $I_{\parallel}$  and  $I_{\perp}$  are the emission intensity measured respectively in parallel and perpendicular directions with respect to the excitation polarization (also shown in Fig. 6.2) along the observation direction.  $I_{\parallel}$  and  $I_{\perp}$  can be directly measured by analyzing the emission light by vertical and horizontal polarizer. According to Fig. 6.2, the total intensity of the fluorescence is

$$I_{tot} = I_x + I_y + I_z, \quad (6.3)$$

with  $I_x$ ,  $I_y$  and  $I_z$  the emission intensities associated with their polarizations along the  $x$ ,  $y$  and  $z$  directions.

Here we consider a molecular medium homogeneous and isotropic. According to Curie's symmetry principle, we can write that  $I_x = I_z = I_{\perp}$  (shown in Fig. 6.2(a)). This corresponds to the fact that the excitation being polarized along the  $y$ -axis, emission

must be symmetric around this axis since we assume isotropy of the molecular medium. The total intensity thus reads as:

$$I_{tot} = I_{\parallel} + 2I_{\perp}. \quad (6.4)$$

Therefore, we can define a global parameter involving the total intensity: the emission anisotropy  $r_v$  that writes as:

$$r_v = \frac{I_{\parallel} - I_{\perp}}{I_{tot}} = \frac{I_{\parallel} - I_{\perp}}{I_{\parallel} + 2I_{\perp}}. \quad (6.5)$$

These 2 parameters ( $p_v$  and  $r_v$ ) are related:

$$r_v = \frac{2p_v}{3 - p_v}. \quad (6.6)$$

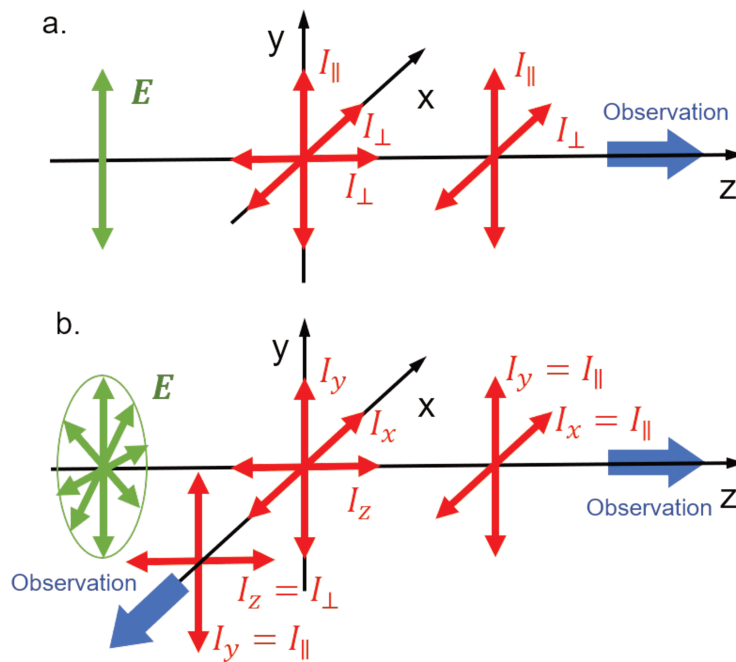


FIGURE 6.2: (a) shows the geometric relation between a linearly polarized excitation with an electric field  $\mathbf{E}$  (green) and the emission intensity in parallel and perpendicular polarization components along an observation direction defined along the  $z$ -axis (blue arrow). (b) shows the geometric relations between a fully non-polarized excitation and emission intensities in different polarization components where  $I_y$  and  $I_x$  are the parallel components and  $I_z$  is the perpendicular component measured along the  $x$ -axis.

For a non-chiral isotropic medium, the fluorescence intensity along the  $x, y$  and  $z$  components can be written by projecting the total intensity on the 3 axis as

$$I_x = I_{tot}\alpha_x^2 \quad (6.7)$$

$$I_y = I_{tot}\alpha_y^2 \quad (6.8)$$

$$I_z = I_{tot}\alpha_z^2 \quad (6.9)$$

with  $\alpha_x^2 + \alpha_y^2 + \alpha_z^2 = 1$  and  $\alpha_x^2 = \alpha_z^2$ . The emission anisotropy can then be rewritten as :

$$r_v = \frac{I_{\parallel} - I_{\perp}}{I_{tot}} = \frac{I_y - I_x}{I_{tot}} = \alpha_y^2 - \alpha_x^2 = \frac{3\alpha_y^2 - 1}{2}. \quad (6.10)$$

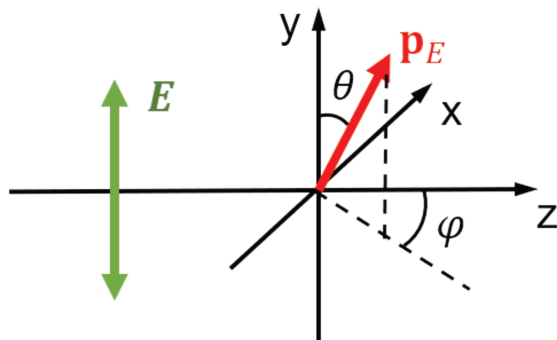


FIGURE 6.3: The geometric relation between a linear excitation and the emission transition moment.

Since  $\alpha_y^2 = \langle \cos^2 \theta_E \rangle$  where  $\theta_E$  is the angle between the excitation electric field and the orientation of the emission transition dipole moment  $\mathbf{p}_E$  as shown in Fig. 6.3 and averaged over the molecular orientations,  $r_v$  writes finally as:

$$r_v = \frac{3 \langle \cos^2 \theta_E \rangle - 1}{2}, \quad (6.11)$$

revealing the relation between the emission anisotropy and the angular distribution of the emission transition dipole moment with respect to the excitation linear polarization.

Moreover, we can define another observable related to emission anisotropy when using a fully non-polarized excitation beam. In this case, parallel components become  $I_x$  and  $I_y$  and  $I_z$  corresponds to the perpendicular component as shown in Fig. 6.2(b). In this case, the anisotropy can only be investigated at a  $90^\circ$  angle with respect to the excitation axis.

For chiral systems, CPL measurements are more interesting to perform. CPL basically measures the emission intensity difference between left and right circularly polarized

excitation light. When it comes to characterize chiral molecular system, the most convenient method is to perform (electronic) CD measurements. But this should not hide that CPL measurements have some advantages over CD characterization. For instance: CPL directly probes the chirality of molecular excited states so that CPL combined with CD measurements can give detailed informations associated with geometric and symmetry differences between ground and excited states [128]. Despite their assets, CPL measurements have limitations too, the most obvious one being that CPL requires molecules with relatively high quantum yields.

Traditionally, the primary parameter characterizing CPL is the emission circular intensity difference (ECID)

$$\Delta I = I_L - I_R \quad (6.12)$$

defined directly from the different intensity measured in the left and right circularly polarized components of emission noted respectively as  $I_L$  and  $I_R$ . We can see that the ECID is actually the  $S_3$  component of the emission Stokes vector. Another parameter is the emission dissymmetry factor

$$g_{lum} = \frac{2\Delta I}{I_{tot}} = 2 \frac{I_L - I_R}{I_L + I_R}, \quad (6.13)$$

extensively used in chiroptical spectroscopy [3]. In order to measure experimentally the CPL, the most commonly used technique is shown in Fig. 6.4. The setup measures the circularly polarized components of the emission light using a circular analyzer composed of a photoelastic modulator (PEM) followed by a linear polarizer (LP) oriented at  $45^\circ$  with respect to the fast axis of the PEM. Since in general, the dissymmetry factor of a chiral molecule is very weak ( $g_{lum} < 10^{-2}$ ), reaching a resolution for weak  $g_{lum}$  of the order of  $10^{-4}$  demands using a lock-in amplifier with the PEM driven at a relatively high modulation frequency  $f_m$  (usually  $f_m \sim 50$  kHz). This configuration can be analyzed using Mueller calculus by writing the final Stokes vector  $\mathbf{S}_f$  after the LP and PEM as

$$\mathbf{S}_f = \mathbf{M}_{LP} \mathbf{M}_{PEM} \mathbf{S}_e, \quad (6.14)$$

where  $\mathbf{S}_e$  is the emission Stokes vector with its  $S_3$  component to be measured. The complete matrix writes

$$\begin{pmatrix} S_f^{(0)} \\ S_f^{(1)} \\ S_f^{(2)} \\ S_f^{(3)} \end{pmatrix} = \frac{1}{2} \begin{pmatrix} 1 & 0 & 1 & 0 \\ 0 & 0 & 0 & 0 \\ 1 & 0 & 1 & 0 \\ 0 & 0 & 0 & 0 \end{pmatrix} \begin{pmatrix} 1 & 0 & 0 & 0 \\ 0 & 1 & 0 & 0 \\ 0 & 0 & \cos \delta(t) & \sin \delta(t) \\ 0 & 0 & -\sin \delta(t) & \cos \delta(t) \end{pmatrix} \begin{pmatrix} S_e^{(0)} \\ S_e^{(1)} \\ S_e^{(2)} \\ S_e^{(3)} \end{pmatrix} \quad (6.15)$$

and yields the resulting intensity  $I_f$  measured in emission as:

$$I_f = S_f^{(0)} = 1 - S_e^{(2)} \cos \delta(t) - S_e^{(3)} \sin \delta(t), \quad (6.16)$$

where  $\delta(t)$  is the time evolution of the driven PEM retardance. In order to analyze circular polarizations,  $\delta$  is set oscillating as

$$\delta(t) = A \sin(2\pi f_m t) \quad (6.17)$$

with a fixed amplitude  $A = \pi/2$  that turns the PEM into an oscillating quarter-wave plate. In this way, if  $S_e^{(3)}$  is non-zero, the signal will oscillate with the frequency  $f_m$  while the term related to a linear component  $S_e^{(2)}$  will be oscillating at  $2f_m$ . With the lock-in amplifier combined with a photomultiplier tube (PMT) recording intensity signals, a precise measurement of  $S_f^{(0)}$  is obtained, allowing to reach high resolution levels for  $g_{lum}$ .

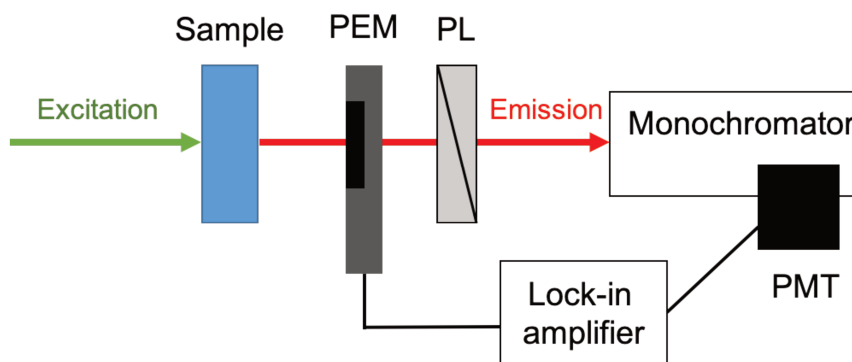


FIGURE 6.4: The schematic setup for a traditional CPL measurement. The light emitted from the sample after an excitation passes through the circular analyzer composed by a PEM and a linear polarizer (PL). The PEM is driven at a given frequency  $f_m$  while the signal is acquired by a photomultiplier tube (PMT) coupled with a monochromator, and synchronized in-phase with the PEM at the same frequency  $f_m$  using the lock-in amplifier.

One strong limitation of these standard methods is that they all are based on the assumption of homogeneity and isotropy of the medium. This implies that they can not be applied to many chemical complex systems where anisotropy and inhomogeneity are present, such as the supramolecular assemblies studied in the previous chapter. Specifically, the mere presence of a linear anisotropy forces a preferred direction for the spatial distribution of transition dipoles. In this case, the parameters  $r_v$  and  $p_v$  become extrinsic since there is no longer invariance with respect to the sample's in-plane rotation and the Curie's symmetry principle breaks down. For CPL, serious artifacts can also arise, for instance when linear birefringence in the system is present (which we will discuss in the next section). Also since the polarization of excitation is not controlled, the contribution

of circular polarization components in the emission can not be discriminated from the excitation polarization. Therefore, more complete characterizations are needed in order to access the "intrinsic" polarization properties of the emission signal, accessible even if the molecular medium becomes heterogeneous and anisotropic.

### 6.1.2 Mueller polarimetry for molecular emission

This is precisely here that Mueller polarimetry methodology becomes relevant. Fluorescence polarization studies of anisotropic molecular media have been pursued in the group of N. Ghosh [130–132], together with a theoretical understanding of how to probe an intrinsically anisotropic system using Mueller polarimetry made by S. Saha and colleagues of IISER, Kolkata [133].

Here, we apply the methods presented in Chapter 4 in order to set a Mueller polarimetry of the emission process. As introduced in Chapter 2 in Eq. (2.226), a Mueller matrix of emission  $\mathbf{M}_E$  relates the polarization states of excitation at a pump wavelength  $\lambda_{pump}$  to the polarization states of photoluminescence at a wavelength  $\lambda_{pl}$ . Fig. 6.5 schematizes the procedure.

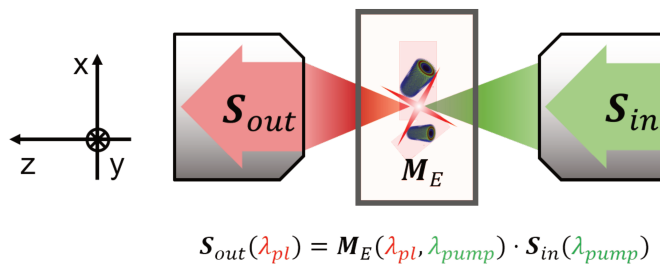


FIGURE 6.5: Schematic representation of the interaction configuration for an emission Mueller matrix measurement. The key point here is that  $\lambda_{pl} \neq \lambda_{pump}$  for reasons exposed in Fig. 6.1

Mueller polarimetry thus relates any excitation polarization state to a resulting emission polarization state in a given frame. It can be applied to any sample, regardless of whether the medium is isotropic or anisotropic. We now derive the observables that can be extracted from such an emission Mueller matrix.

For the case of an isotropic sample, we can directly relate the fluorescence anisotropy parameters ( $p_v$  and  $r_v$ ) presented above to the Mueller matrix elements. Take as an example a non-chiral, anisotropic medium observed at  $0^\circ$  (i.e. along the  $z$ -axis). We first excite this medium with fully non-polarized light characterized by the incident Stokes vector  $\mathbf{S}_{in} = (1, 0, 0, 0)^T$ . The resulting emission Stokes vector writes in terms of the

Mueller matrix elements as:

$$S_{out} = \mathbf{M}_E \cdot \begin{pmatrix} 1 \\ 0 \\ 0 \\ 0 \end{pmatrix} = \begin{pmatrix} S_{out}^{(0)} \\ S_{out}^{(1)} \\ S_{out}^{(2)} \\ S_{out}^{(3)} \end{pmatrix} = \begin{pmatrix} m_{00} \\ m_{10} \\ m_{20} \\ m_{30} \end{pmatrix}. \quad (6.18)$$

According to Fig. 6.2, this emission observed along the  $z$ -axis should not display any polarization contrast since the components along 2 orthogonal directions ( $x/y$  and  $+45^\circ/-45^\circ$ ) are the same, thus  $m_{10} = m_{20} = 0$ . Because the system is achiral, one also enforces  $m_{30} = 0$ . The first column there of this Mueller matrix is zero. Now if we pump the system with a vertical linearly polarized light ( $\mathbf{S}_{in} = (1, -1, 0, 0)^T$ ), the resulting Stokes vectors is changed into:

$$S_{out} = \mathbf{M}_E \cdot \begin{pmatrix} 1 \\ -1 \\ 0 \\ 0 \end{pmatrix} = \begin{pmatrix} S_{out}^{(0)} \\ S_{out}^{(1)} \\ S_{out}^{(2)} \\ S_{out}^{(3)} \end{pmatrix} = \begin{pmatrix} m_{00} - m_{01} \\ -m_{11} \\ -m_{21} \\ -m_{31} \end{pmatrix}. \quad (6.19)$$

In that case, the fluorescence polarization  $p_v$  reads easily as:

$$p_v = \frac{I_{\parallel} - I_{\perp}}{I_{\parallel} + I_{\perp}} = \frac{I_V - I_H}{I_V + I_H} = -\frac{S_{out}^{(1)}}{S_{out}^{(0)}} = \frac{m_{11}}{m_{00} - m_{01}}, \quad (6.20)$$

according to the definition of Stokes parameters. Since the excitation along the vertical axis should not give a preferred linear polarization in another direction,  $m_{21} = 0$ . Following Curie's symmetry principle, this fluorescence polarization ratio  $p_v$  is then the same for a  $45^\circ$  linearly polarized excitation ( $\mathbf{S}_{in} = (1, 0, 1, 0)^T$ ). By the same way, we write  $p_v$  upon a  $45^\circ$  linearly polarized excitation as

$$p_v = \frac{m_{22}}{m_{00} - m_{02}}, \quad (6.21)$$

and  $m_{12} = 0$  accordingly. As introduced in Chapter 2, the first line of the matrix  $m_{0i}$  corresponds to the contrast of the emission intensity with respect to the excitation polarization. Since in the present case, there is no anisotropy in the system,  $m_{0i} = 0$  for all  $i = 1, 2, 3$ . Normalizing as always the Mueller matrix in order to have its  $m_{00} = 1$ , the fluorescence polarization ratio will be written directly as

$$p_v = m_{11} = m_{22}. \quad (6.22)$$



So far, within the conditions we chose, the Mueller matrix of emission writes as :

$$\mathbf{M}_E = \begin{pmatrix} 1 & 0 & 0 & 0 \\ 0 & p_v & 0 & m_{13} \\ 0 & 0 & p_v & m_{23} \\ 0 & m_{31} & m_{32} & 0 \end{pmatrix}. \quad (6.23)$$

Again, due to isotropy, this matrix should be invariant with respect to a in-plane rotation, imposing  $m_{13} = m_{31} = m_{23} = m_{32} = 0$ . Finally, the Mueller matrix of emission in an isotropic molecular system along the  $0^\circ$  axis of observation can be obtained as

$$\mathbf{M}_E = \begin{pmatrix} 1 & 0 & 0 & 0 \\ 0 & p_v & 0 & 0 \\ 0 & 0 & p_v & 0 \\ 0 & 0 & 0 & 0 \end{pmatrix}. \quad (6.24)$$

This matrix is a diagonal matrix with only one parameter which is the aforementioned fluorescence polarization ratio  $p_v$ . This is the reason why for an isotropic medium, performing Mueller polarimetry analysis is not that interesting since it does not provide more informations than those obtained by a polarization anisotropy measurement. We give here as an example the emission Mueller matrix of the molecule C8O3 in its monomeric phase -see Chapter 5- which can be considered as an isotropic phase. The results are shown in Fig. 6.6 and reveal that the experimental  $\mathbf{M}_E$  matrix has the same form as Eq. (6.24) with only 2 non-zero identical elements at  $m_{11}$  and  $m_{22}$ . From these 2 non-zero matrix elements, the fluorescence polarization ratio  $p_v$  can be extracted directly from these elements by taking the mean value of  $m_{11}$  and  $m_{22}$  as shown in Fig. 6.6, measuring the averaged angular distribution of the emission dipole with respect to the excitation polarization direction.

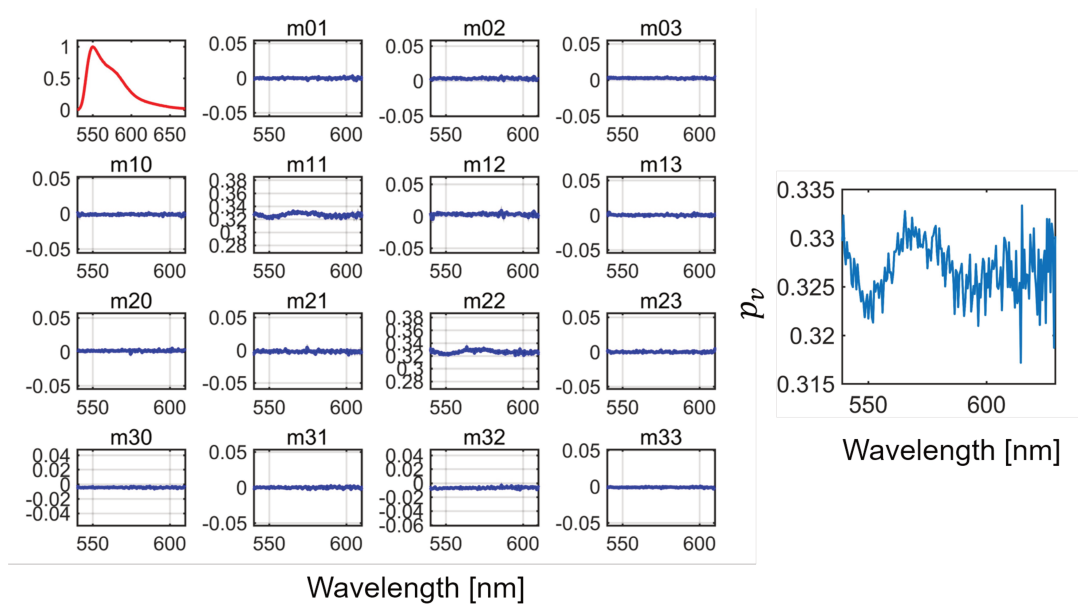


FIGURE 6.6: The Mueller matrix of emission of the molecule C8O3 in its monomeric phase with an excitation set at 520 nm. This matrix is normalized to 1 with the emission spectrum shown at the position of  $m_{00}$ . The panel on the right displays the polarization ratio of the fluorescence extracted from this matrix.

More generally, if we include all directions of observation, the Mueller matrix (noted  $\mathbf{F}$  by Arteaga in [134]) derived by the pioneer work of Soleillet [135]<sup>1</sup> and Perrin [120] on fluorescence scattering in a system containing only linear dipoles, can be written as

$$\mathbf{F}(\phi) = \begin{pmatrix} a - b \sin^2 \varphi & -b \sin^2 \varphi & 0 & 0 \\ -b \sin^2 \varphi & b(1 + \cos^2 \varphi) & 0 & 0 \\ 0 & 0 & 2b \cos \varphi & 0 \\ 0 & 0 & 0 & 2c \cos \varphi \end{pmatrix}, \quad (6.25)$$

with  $\varphi$  the scattering angle shown in Fig. 6.7 and parameters  $a$  and  $b$  defined in this case as

$$a = \frac{1}{2}(1 + \langle \cos^2 \theta_E \rangle) \quad (6.26)$$

$$b = \frac{1}{4}(3 \langle \cos^2 \theta_E \rangle - 1) \quad (6.27)$$

where  $\theta_E$  is the angle between the excitation polarization direction and emission transition moment orientation. The parameter  $c$  is related to the fluorescence anisotropy for circularly polarized excitation associated with optically active dipoles (i.e. combining collinear electric and magnetic dipoles).

<sup>1</sup>P. Soleillet was professor at the Institut de Physique of Strasbourg

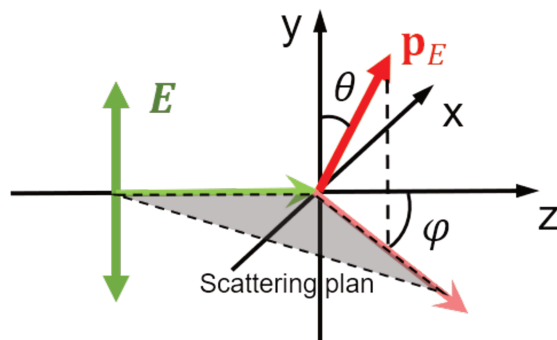


FIGURE 6.7: The schematic representation of the fluorescence scattering configuration for a linear dipole, taken from [134].

We can verify that the form in Eq. (6.25) is consistent with the matrix of emission measured at  $0^\circ$  along the  $z$ -axis by setting  $\phi = 0$  and normalizing  $m_{00}$  to 1.

In that same theoretical work [134], the Stokes-Mueller formalism in emission is extended to chiral isotropic medium. These authors model the total Mueller matrix of emission  $\mathbf{M}_E$  into a product of 3 matrices describing 3 stages of the emission process as:

$$\mathbf{M}_E = \mathbf{M}_1 \mathbf{F} \mathbf{M}_0, \quad (6.28)$$

where  $\mathbf{M}_0$  describes the polarization modifications upon excitation of the molecules in their ground states while  $\mathbf{M}_1$  describes the polarization modification on emission by the molecules in their excited state. Accordingly, this analysis gives a clear interpretation of other matrix elements associated with CPL ( $m_{30}$ ) and fluorescence detected circular dichroism (FDCD) ( $m_{03}$ ) measurements.

Finally, for the most general case where the system is both anisotropic and chiral, the polarization relation between excitation and emission is more complex. Here, a Mueller formalism is clearly needed in order to provide the complete information related to the different contributions from the excitation polarization to the emission polarization. Since a chiral anisotropic system is difficult to analyze by the decomposition proposed in Eq.(6.28), we prefer to investigate directly the different elements of the emission Mueller matrix. Our example is the emission Mueller matrix measured for C8O3 in its the J-aggregated phase, with an interpretation of each element shown in Fig. 6.8. As introduced in chapter 4, the first column of the matrix gives the polarization of emission with a fully non-polarized light revealing purely the excited state property as marked by the red box in Fig. 6.8. Specifically, the  $m_{30}$  gives a measure of the intrinsic CPL while  $m_{10}$  and  $m_{20}$  give a measure of intrinsic linearly polarized luminescence. Similar to the LD measurement discussed in Chapter 5, they also yield a measure of the angular orientation of the emission transition dipole moment. The first line of the matrix marked by the blue box in Fig. 6.8 gives a measure of fluorescence detected dichroism, revealing the ground

state properties. The other elements correspond to polarization state-to-state conversions between the excitation and the emission.

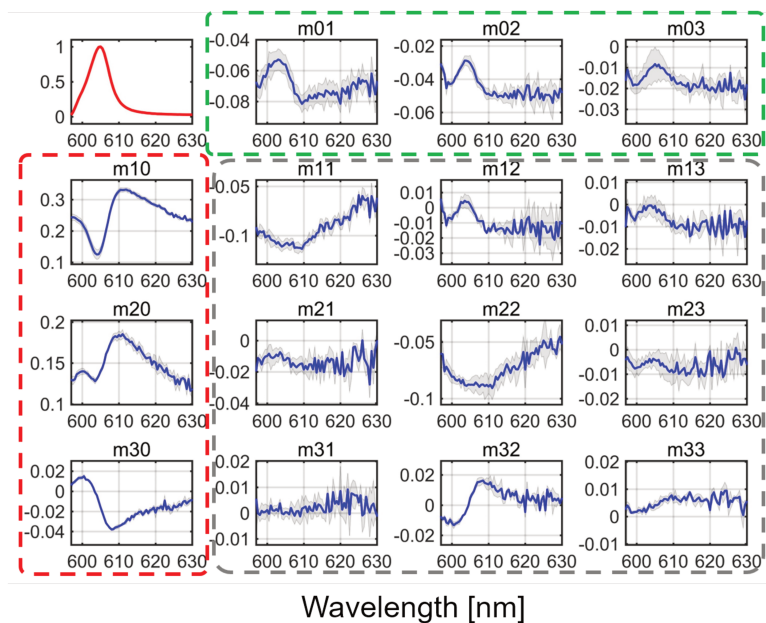


FIGURE 6.8: A normalized emission Mueller matrix measured in an anisotropic system formed by J-aggregates (stage 5) of C8O3 molecules. The meaning of the 3 boxes is given in the main text.

In such an anisotropic system, all elements of Mueller matrix contribute to the knowledge of the fluorescence polarization properties. As the Mueller matrix of emission isolates the different contributions coming from excitation polarizations to emission ones, the properties extracted from the matrix elements can be considered as intrinsic to the medium. Once the matrix is known, additional basic fluorescence polarization properties can also be built from manipulating the Mueller matrix and incident Stokes vectors, as for instance done above with  $p_v$  and  $r_v$ .

Another advantage of a Mueller polarimetry for fluorescence is that since the Mueller formalism is a product calculus, it is well adapted for performing blank corrections of the type discussed earlier in Eq.(4.33). Eliminating artifacts induced by the setup itself when measuring fluorescence is crucial in CPL characterizations for instance. Indeed, uncontrolled linear birefringence in the system can give rise to circularly polarized components in emission although starting with a purely linearly polarized luminescence. Other sources of optical artifacts influencing CPL measurements have been discussed by Nakagawa [136] and Dekker *et. al* [137]. By directly resorting to Mueller polarimetry for measuring fluorescence polarization properties, these artifacts can be identified and thus setup-related artifacts easily corrected. Of course, many other situations can induce artifacts in CPL measurements, other than the setup itself. This will be shown in the next section where we will reveal a new artifact which is solely related to the polarization dynamics internal

to the molecular system, i.e. not related to any setup issue. Because this artifact is in this sense "intrinsic", it can lead to strong misinterpretations of possible CPL measurements, just like linear dichroism was recognized, in transmission polarization studies, to spoof circular dichroism.

## 6.2 Internal filtering effect in supramolecular CPL measurements

This section is devoted to the analysis of a strong artifact induced in CPL measurements when the system under study has strong linear birefringence and dichroism at an emission band. This combination can give to the emission polarization a strong CPL signal after being modified by an internal filtering effect that we will describe here. We have identified this effect by using emission Mueller polarimetry and we stress in this section that it is one source for a strong artifact in CPL measurements that can easily become problematic when performing CPL measurements on supramolecular systems.

### 6.2.1 Supramolecular emission

We use here the same J-aggregates formed in self-assembly from C8O3 monomers as in Chapter 5. Here, we focus on the emission properties monitored throughout the aggregation process. The emission spectra for 3 typical stages in the self-assembly are shown in Fig. 6.9. The emission spectra in stage 2 shown in Fig. 6.9(a) mainly corresponds to the emission band of the monomer molecule (C8O3) at  $\sim 550$  nm. The ones at stages 3 and 5 displayed in Fig. 6.9(b)-(c) reveal a very narrow emission band at 606 nm corresponding to the emission band of the J-aggregate which is almost identical to the J-absorption band. Small Stokes shifts are typical features of J-aggregate systems. We will chose this emission band and study its polarization properties.

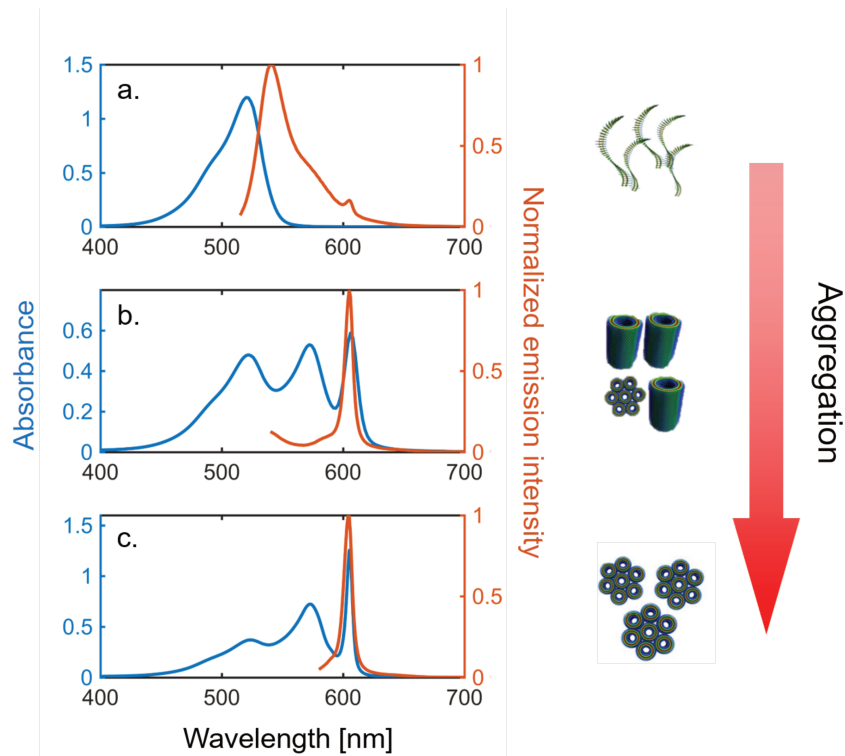


FIGURE 6.9: (a)-(c) display the absorption (blue line) and emission (red line) spectra of C8O3 in 3 stages of the self-assembly with ratio(v/v) (a) 1:2.2, (b) 1:2.6 (d) 1:4 between C8O3 (0.3 mM) in ethanol and aqueous NaOH (0.02 M). The corresponding conformations are shown on the right-hand side. The emission spectra from (a)-(c) are recorded using an excitation wavelength of 500 nm, 530 nm and 560 nm, respectively.

## 6.2.2 Measurement configuration

We first introduce the interaction configuration corresponding to our measurements. As explained in Chapter 4, the usual measurement configuration for emission is in transmission, along the  $0^\circ$  axis of observation for the fluorescence. The configuration is detailed in Fig. 6.10. The excitation beam is focused by a microscope objective so that only the molecules in the vicinity of its focal point are excited. Another microscope objective is used to collect the emission around the focal point of the first objective within a very thin depth-of-field in the so-called telescope configuration. In this case, the polarization of the excitation at wavelength  $\lambda_p$  and of the emission at  $\lambda_{pl}$  are related by a total emission Mueller matrix  $\mathbf{M}_{tot}(\lambda_{pl}, \lambda_p)$  that can be decomposed into 3 different parts (configuration shown in Fig. 6.10) as:

$$\mathbf{M}_{tot}(\lambda_{pl}, \lambda_p) = \mathbf{M}_{T_{pl}}(\lambda_{pl})\mathbf{M}_E(\lambda_{pl}, \lambda_p)\mathbf{M}_{T_p}(\lambda_p) \quad (6.29)$$

with  $\mathbf{M}_{T_p}(\lambda_p)$  characterizing the medium in the sample before the focal plane at the excitation wavelength,  $\mathbf{M}_{T_{pl}}(\lambda_{pl})$  characterizing the medium after the focal plane at the

emission wavelength  $\mathbf{M}_E(\lambda_{pl}, \lambda_p)$  corresponds to the real Mueller matrix of the sample emission. Since the molecules away from the focal point are not excited, they are simply described by the transmission Mueller matrix of the molecule determined in Chapter 5. Given that the transmission Mueller matrix recorded over an optical path length  $l$  is given by:

$$\mathbf{M}_t = \exp(l\mathbf{N}_M), \quad (6.30)$$

the matrix  $\mathbf{M}_{Tp}$  defined over the path length  $l_p$  writes as:

$$\mathbf{M}_{Tp} = \exp(l_p\mathbf{N}_M), \quad (6.31)$$

and the matrix  $\mathbf{M}_{Tpl}$  defined over a path length  $l_{pl}$  reads as:

$$\mathbf{M}_{Tpl} = \exp(l_{pl}\mathbf{N}_M), \quad (6.32)$$

where  $\mathbf{N}_M$  represents the differential Mueller matrix of the transmission Mueller matrix  $\mathbf{M}_t$ . Since  $\mathbf{N}_M$  shows significant polarization signatures only at the absorption bands, this matrix is close to an identity matrix at other wavelengths. Therefore, for a large Stokes shift emissive system where no absorption bands are present at  $\lambda_{pl}$ ,  $\mathbf{M}_{Tpl}(\lambda_{pl})$  will not modify the emission polarization state. Therefore, this total measured emission Mueller matrix  $\mathbf{M}_{tot}(\lambda_{pl}, \lambda_p)$  can give a relatively close estimate of the real emission Mueller matrix.

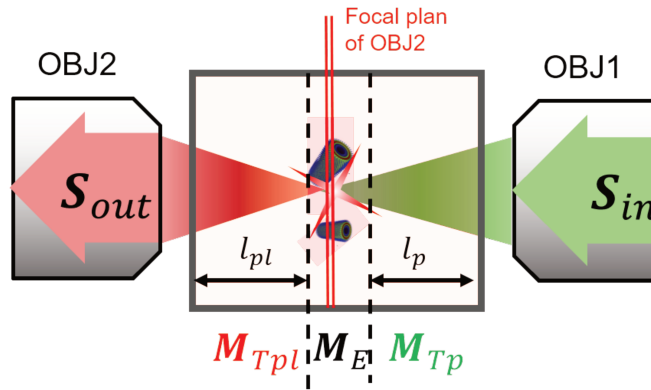


FIGURE 6.10: A schematic representation of the measurement configuration involved for Mueller polarimetry of emission. The excitation polarization noted as  $\mathbf{S}_{in}$  is focused by an objective (OBJ1) and the emission polarization state noted as  $\mathbf{S}_{out}$  is collected by second objective (OBJ2) within the depth-of-field at its focal plane (between red double line). The Mueller matrix characterizing the medium before the focal plane at the excitation wavelength is noted as  $\mathbf{M}_{Tp}$  defined over a path length  $l_p$  while the one for the medium after the focal plane at emission wavelength is noted as  $\mathbf{M}_{Tpl}$  defined over  $l_{pl}$  with the real Mueller matrix characterizing the emission process noted as  $\mathbf{M}_E$ .

However for systems with small Stokes shifts where emission spectra overlap with absorption bands,  $\mathbf{M}_{T_{pl}}(\lambda_{pl})$  may induce polarimetric features that modify the polarization states in emission. This means that, the total measured emission Mueller matrix can (and will) be affected by such transmission polarimetric features. We call this effect an "internal filtering effect". Usually, this undesired effect can be attenuated by diluting the solution and/or using a thinner cuvette. However, in many cases, since the molecular quantum yield is not high enough, dilution is not an option if one needs sufficient emission intensity in order to keep the signal-to-noise ratio at acceptable levels. As we show now, this effect even induces artifacts in CPL measurements, as it can be seen by varying the optical path  $l_{pl}$  via moving the sample along the optical axis while analyzing the signal using Mueller polarimetry.

### 6.2.3 Results and discussion

In this section, the emission Mueller matrix measurements are shown for the C8O3 J-aggregates, highly sensitive to the "internal filtering" artifact that impacts CPL characterization. By combining these measurements with measurements in transmission, the source of this artifact can be precisely analyzed.

As we discussed in the previous section, the total measured emission Mueller matrix under a given excitation wavelength  $\lambda_p$  writes as:

$$\mathbf{M}_{tot}(\lambda_{pl}, \lambda_p) = \exp[l_{pl} \cdot \mathbf{N}_M(\lambda_{pl})] \cdot \mathbf{M}_E(\lambda_{pl}, \lambda_p) \cdot \exp[l_p \cdot \mathbf{N}_M(\lambda_p)]. \quad (6.33)$$

A straight forward "sanity check" determining whether the CPL signal extracted from the measured emission Mueller matrix is biased by some internal filtering effects or not, is according to Eq.(6.33), to check whether the experimental total Mueller matrix (and its CPL signal) are different for different emission optical path lengths  $l_{pl}$  in the sample. This can be realized by moving the sample along the optical axis. Doing so, the relative position of the focal plane with respect to the sample will be shifted. Here, in order to show the contrast between such 2 situations, we choose 2 extreme cases where  $l_{pl}$  takes the minimum and the maximum values, as illustrated in Fig. 6.11(a) and (c). In the case of minimum  $l_{pl}$  value, almost no effect of internal filtering is expected while for the case of maximum  $l_{pl}$ , an obvious internal filtering effect should be observed. The cuvette in this case has a path length of 1 mm. The total Mueller matrices of emission for these 2 cases are shown in Fig. 6.11(b) and (d). By comparing these 2 emission Mueller polarimetry measurements and the transmission Mueller matrices shown in Fig. 6.12, we can extract several informations relevant to this internal filtering effect on the emission polarization dynamics.



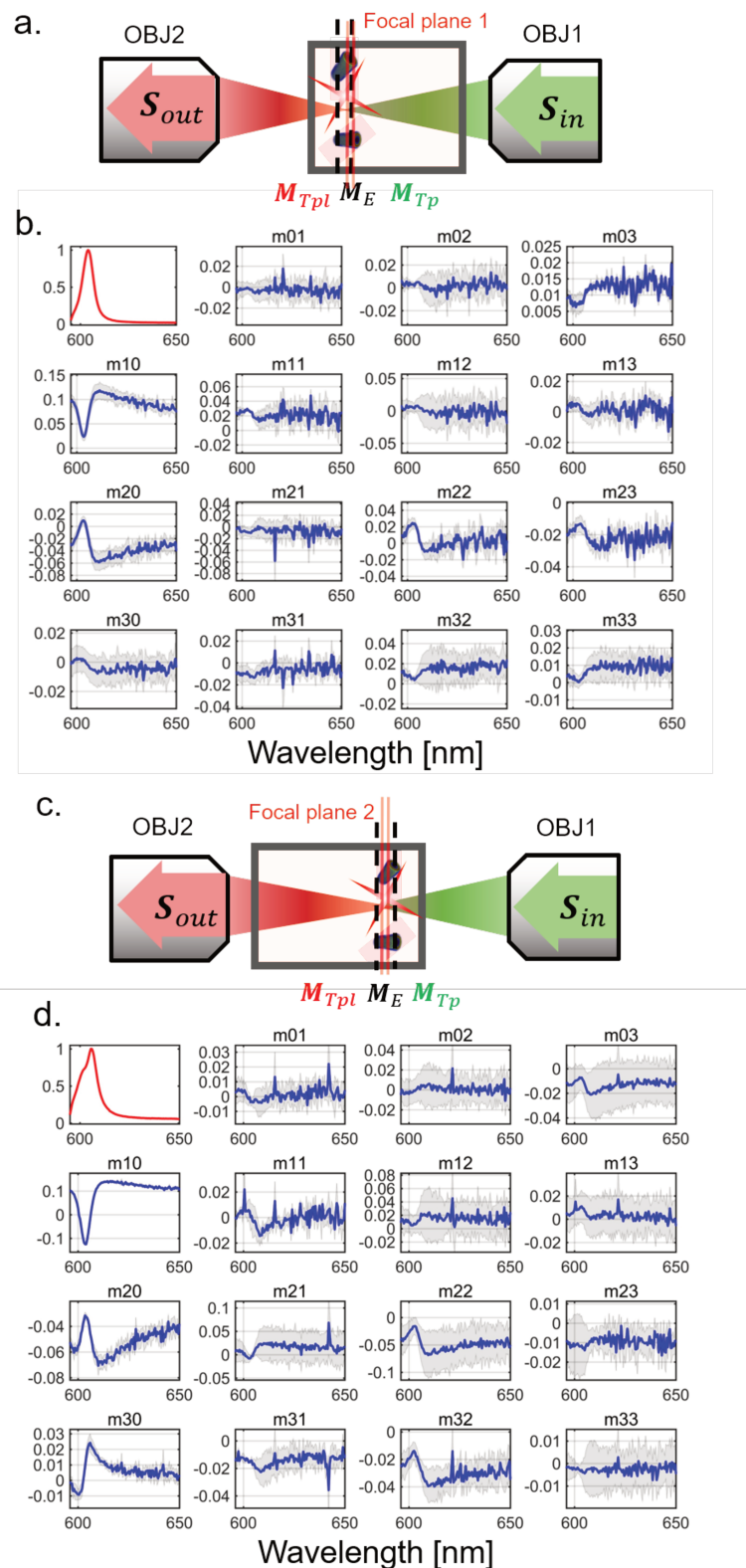


FIGURE 6.11: (a) shows the measurement configuration for the minimum emission optical path length with the corresponding Mueller matrix shown in (b). (c) shows the one for the maximum emission optical path length with the corresponding Mueller matrix shown in (d). The sample is made of C8O3 J-aggregates in stage 5 of the self-assembly, using a cuvette of 1 mm path length at a 570 nm excitation wavelength.

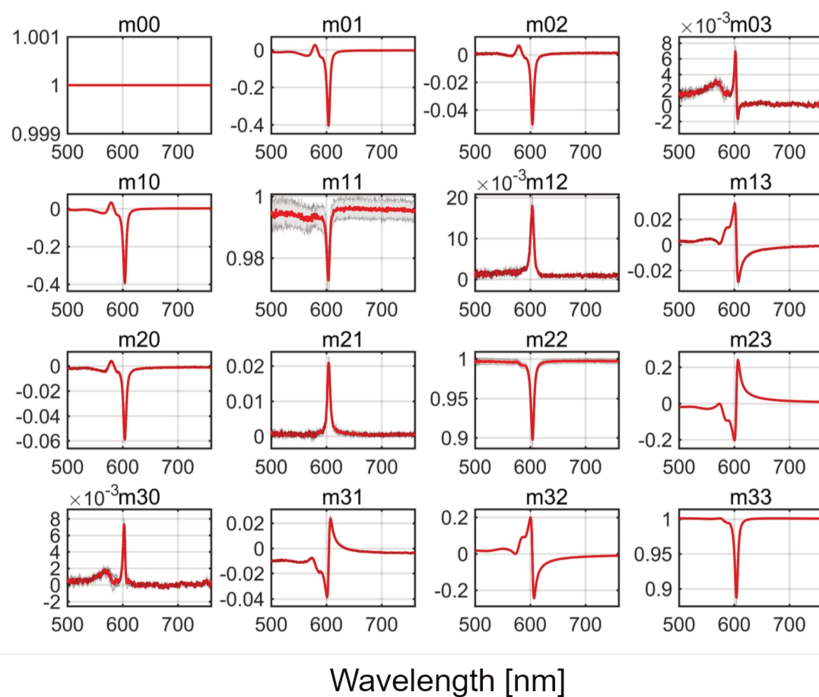


FIGURE 6.12: The transmission Mueller matrix recorded through the same sample of C8O3 J-aggregates used for measuring the emission Mueller matrix displayed in Fig. 6.11 with the error-bar given by standard error marked by grey zone.

First we investigate the CPL signal as provided by the  $m_{03}$  element. From our results, we can see that the matrix with a long emission optical path length within the sample (the situation shown in Fig. 6.11(c)) gives a much more significant signal than that for a short emission signal path length (the situation shown in Fig. 6.11(a)). More precisely, the measurement with a short  $l_{pl}$  gives nearly a zero  $m_{30}$  (CPL) within the detection limit given by the error-bar signal, while the one with long  $l_{pl}$  gives a well-defined  $m_{30}$  (CPL) signal. If one does not check therefore the measurements between the 2 different focal plane positions, the second situation might be misinterpreted by considering that the chiral emission is due to coupled chiral excitons associated with the bisignated feature observed in absorption, as discussed in Chapter 5. This interpretation would make sense, but is seriously challenged by the artifact coming into play here.

A detailed explanation can be proposed here by taking into account the measured emission Mueller matrix given by Eq. (6.33). From it, we obtain the explicit expression of  $m_{03}$  in the total Mueller matrix of emission. Here, we neglect the effect of  $\mathbf{M}_{Tp}(\lambda_p)$  because the excitation is monochromatic. In this case, it is a constant matrix that does not evolve with the emission wavelength and does not determine the spectral features of the final Mueller matrix. When this is so, the measured CPL signal associated with the  $m_{30}$  element of the total Mueller matrix of emission noted as  $m_{30}^{tot}$  is written as a function of the  $\mathbf{M}_{Tp}(\lambda_p)$  matrix elements noted  $m_{ij}^t$  and of the real emission Mueller matrix  $\mathbf{M}_E(\lambda_p)$

elements noted  $m_{ij}^e$ , as:

$$\begin{aligned} m_{30}^{tot} &= \sum_{i=0}^3 m_{3i}^t m_{i0}^e = m_{30}^t m_{00}^e + m_{31}^t m_{10}^e + m_{32}^t m_{20}^e + m_{33}^t m_{30}^e \\ &= m_{30}^t m_{00}^e + m_{31}^t m_{10}^e + m_{32}^t m_{20}^e + m_{33}^t \cdot CPL \end{aligned} \quad (6.34)$$

where  $CPL$  corresponds to the real CPL signal extracted from the  $m_{30}^e$  element of the real emission Mueller matrix  $\mathbf{M}_E$ . This expression clearly shows that, as soon as the first 3 terms are non-zero and  $m_{33}^t$  is not constant, the measured CPL can not correspond to the CPL given by  $m_{30}^e$ . Each term of this CPL artifact series can be analyzed. In the first term  $m_{30}^t m_{00}^e$ ,  $m_{30}^t$  is dominated by the CD of the medium according to differential decomposition (see Chapter 2) and  $m_{00}^e$  is in general taken as 1 from the normalization. This term therefore describes the contribution of the CD inside the sample to the CPL artifact. The second and third terms  $m_{31}^t m_{10}^e$  and  $m_{32}^t m_{20}^e$ , are connected to  $m_{31}^t$  and  $m_{32}^t$  mainly contributed by linear birefringence and  $m_{10}^e$  and  $m_{20}^e$  representing the linearly polarized luminescence. They describe therefore the contribution to the CPL from linearly polarized luminescence (LPL) due to the presence of linear birefringence in the system. This can easily be understood: a linear polarized light will have circular polarization components after passing through a linear birefringent medium if the initial polarized light is not aligned with the linear birefringence axis. This effect will be maximized when the emission dipole moment is in  $45^\circ$  with respect to the linear birefringence direction of internal filtering effect. In the last term, if  $m_{33}^t$  that corresponds to the depolarization of the circularly polarized light is not constant, the real CPL signal defined from  $m_{30}^e$  will be modulated by a prefactor that also induce a kind of artifact.

This analysis shows that our sample, presenting CD and LB terms (non-zero elements  $m_{30}$ ,  $m_{31}$  and  $m_{32}$  in the transmission Mueller matrix) from the transmission Mueller matrix (see Fig. 6.12) and presenting intrinsic linearly polarized luminescence (non-zero elements  $m_{10}$ ,  $m_{20}$  of the emission Mueller matrix shown in Fig. 6.11) is clearly impacted by this CPL artifact issue. The 3 first terms in Eq. (6.34) can not always be zero when  $l_{pr}$  is not small enough. The CD presents in this system will give non-zero  $m_{30}^t m_{00}^e$  element, and because the molecular system is in solution, the linear macrostructures can not all be aligned along the same direction. This implies that the emitter transition dipoles are not necessarily aligned with the linear birefringence axis of the medium yielding non-zero  $m_{31}^t m_{10}^e$  and  $m_{32}^t m_{20}^e$  elements. Therefore, it is clear that the CPL measured in configuration of Fig. 6.11(c), i.e. extracted from the matrix shown in Fig. 6.11(d), is affected by this artifact series revealing how the internal filtering effect can impact the measurement.

Apart from CPL measurement, we also see that LPL signal revealed by  $m_{10}$  and  $m_{20}$

is affected by the internal filtering effect, too. This is so because they present a dip at the peak of the LD (LD') wavelength which is opposite to the base amplitude. This can be analyzed in a similar way as the CPL artifact series by writing the elements  $m_{10}^{tot}$  and  $m_{20}^{tot}$  according to Eq. (6.33) as

$$\begin{aligned} m_{10}^{tot} &= \sum_{i=0}^3 m_{1i}^t m_{i0}^e = m_{10}^t m_{00}^e + m_{11}^t m_{10}^e + m_{12}^t m_{20}^e + m_{13}^t m_{30}^e \\ &= m_{10}^t m_{00}^e + m_{11}^t \cdot LPL + m_{12}^t m_{20}^e + m_{13}^t m_{30}^e \end{aligned} \quad (6.35)$$

$$\begin{aligned} m_{20}^{tot} &= \sum_{i=0}^3 m_{2i}^t m_{i0}^e = m_{20}^t m_{00}^e + m_{21}^t m_{10}^e + m_{22}^t m_{20}^e + m_{23}^t m_{30}^e \\ &= m_{20}^t m_{00}^e + m_{21}^t m_{10}^e + m_{22}^t \cdot LPL' + m_{23}^t m_{30}^e \end{aligned} \quad (6.36)$$

where  $LPL$  and  $LPL'$  correspond to real LPL signal along  $0^\circ/90^\circ$  basis and  $\pm 45^\circ$  basis respectively, extracted from the  $m_{10}^e$  and  $m_{20}^e$  elements of the real emission Mueller matrix  $\mathbf{M}_E$ . From these expressions, we can see that if the sample presents a strong LD (LD') contributing mainly to  $m_{10}^t$  ( $m_{20}^t$ ), the measured total LPL signal will be strongly affected and be different from  $m_{10}^e$  ( $LPL$ ). By comparing 2 matrices measured in different focal planes, we observe that the amplitude of this modulation in LPL and LPL' is different precisely where the emission Mueller matrix in Fig. 6.11(d) shows strong modulations.

Finally, we note that this internal filtering effect, even though it is analyzed by the Mueller formalism, can not be experimentally corrected by the transmission Mueller matrix exploiting matrix products. This because the emission and transmission Mueller matrix are taken at different times, including a lag during which the macrostructures diffuse and change in the averaged orientation angles, that eventually change the anisotropy. Therefore, as long as the transmission and emission Mueller matrix can not be measured simultaneously and on the same region, such artifact series can not be corrected properly.

A solution that mitigates these problems and issues is to simply use a thinner cuvette. In order to show this, we perform again the same measurements with 2 different focal planes for a 0.5 mm path length. The emission Mueller matrix with the corresponding configurations are shown in Fig. 6.13. We can see that these two Mueller matrices measured in different focal plane are quite similar. In particular, the  $m_{30}$  elements revealing CPL signals are almost identical within our limit of detection. Compared to the results shown for a cuvette of 1 mm path length, the  $m_{10}$  and  $m_{20}$  elements recorded here show less modulations induced by the internal filtering effect, with a single peak in the signal. Therefore, these data verify that the decrease in the cuvette path length is a way to reduce the influence of the internal filtering effect and fluorescence polarization measurement artifacts.

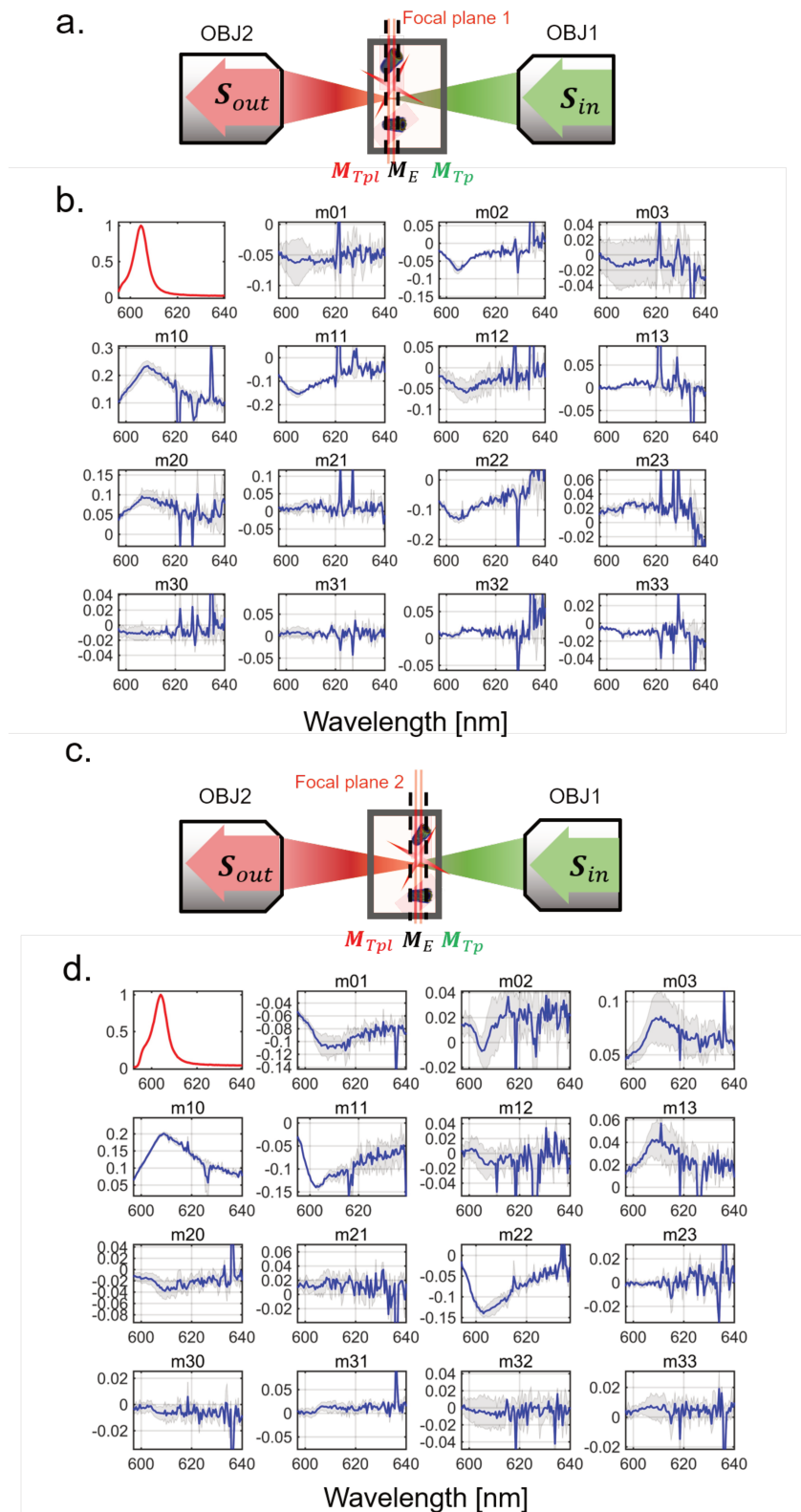


FIGURE 6.13: (a) shows the measurement configuration for the minimum emission optical path length with the corresponding Mueller matrix shown in (b). (c) shows the one for the maximum emission optical path length with the corresponding Mueller matrix shown in (d). The sample is made of C8O3 J-aggregates in stage 5 of the self-assembly, using a thin cuvette with a 0.5 mm path length at a 570 nm excitation wavelength.

Our analysis is therefore raising some potential concerns related to CPL measurements, in particular for molecules with small Stokes shifts, and displaying CD and LB in absorption and LPL in emission. Such a situation is actually very common: chiral J-aggregates have in general minimal Stokes shift and by forming tubular aggregates, they also induce LB and LPL together. This stresses how important it is, when measuring CPL in such systems, to detail and control the conditions of the experiment that must be carefully verified before reaching any conclusion regarding CPL.

## 6.3 Other results

Apart from this artifact issue raised in the previous section, Mueller matrix in emission can yield insight in relation with many other aspects. In this section, we give some examples that illustrate the potentialities of such a polarimetric methodology in the context of emissive chiral molecular systems.

### 6.3.1 Poincaré sphere representation of emission polarization states

The emission Mueller matrix, as a Stokes realizable Mueller matrix, connects the incident to the emergent Stokes vectors. Once the emission Mueller matrix is known, we can obtain the resulting polarization state described by  $\mathbf{S}_{out}$  by applying the emission Mueller matrix on a chosen excitation polarization state  $\mathbf{S}_{in}$ . If we inject all polarization states of light at the surface of the Poincaré sphere as generating an ensemble of  $\mathbf{S}_{in}$ , we can obtain the corresponding ensemble of emission polarization states for a given emission wavelength described by all the  $\mathbf{S}_{out}$  in the sphere. This representation can be used in order to visualize the properties of the emission Mueller matrix.

One example is shown in Fig. 6.14 taken from an emission Mueller matrix of C8O3 J-aggregate upon a 570 nm excitation and measured at 600 nm. From this example, we can see that all emission polarization states obtained from pure polarization state excitations are squeezed near the origin in the polarization space corresponding the states that are very close to be fully non-polarized. This immediately reveals the strong depolarizing nature of the fluorescence. But a closer look at the distribution of the resulting emission polarization states  $\mathbf{S}_{out}$  in Fig. 6.14, reveals that the average of all states corresponds to a Stokes vector built from the first column of the emission Mueller matrix at this wavelength (red vector). This means that the emission has a preferred polarization, regardless of the excitation polarization. This observation implies an intrinsic anisotropy of the supramolecular system. The  $S_1$  and  $S_2$  component measure LPL feature and the contribution to emission of the  $S_3$  component corresponds the CPL signal. The dispersion

of the state distribution from the averaged state corresponds to the capacity of the medium to maintain excitation polarization.

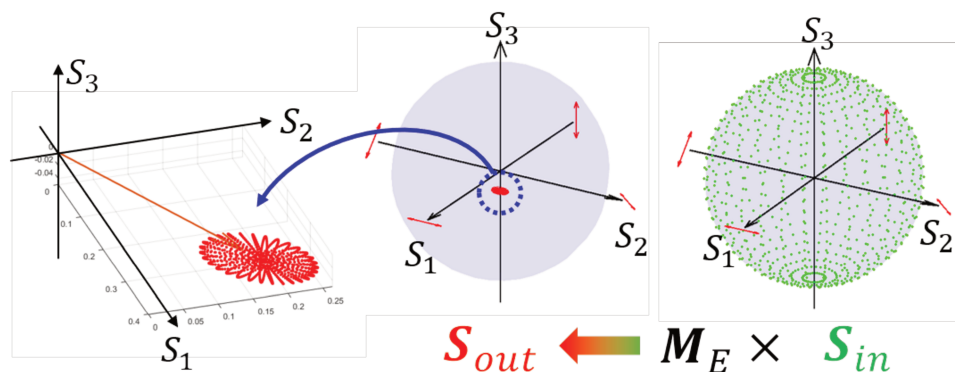


FIGURE 6.14: The Poincaré representation of the emission Mueller matrix for our C8O3 J-aggregate at stage 5 of the self-assembly upon a 570 nm excitation measured at 600 nm (emission wavelength). The green dots represent the excitation polarization states and the red dots are the resulting emission polarization states with a zoom on its detailed distribution in the left panel.

### 6.3.2 2D Mueller matrix for polarization "action spectra"

The experimental results of emission Mueller matrices presented in the previous sections were acquired by fixing the excitation wavelength and displaying the results as a function of the emission wavelengths. However, polarization responses can be different depending on the excitation wavelength since pumping at different absorption bands will couple to different internal relaxation paths, and in this way to different polarimetric dynamics from a change in the absorption transition dipole moment. This is closely analogue to action spectroscopy in photochemistry, and we decided to perform a series of measurements of the same sample under the same conditions (collecting emission from the same focal plane) using different excitation wavelengths. These series of results are arranged using a 2D spectral representation with the x-axis corresponding to the emission wavelength and y-axis to the excitation wavelength displayed in Fig. 6.15. This representation clearly shows the dependence of the matrix elements on the excitation wavelength. We first look at the first column of this 2D Mueller matrix that represents the polarization of emission induced by a fully non-polarized light. This column reveals the anisotropy of the system, as discussed above. Since this anisotropy depends on the averaged orientation of the tubular macrostructures, which is a completely random variable, the signals in the first column do not have any deterministic dependence with respect to the excitation wavelength. It is interesting to see the random nature of the  $m_{30}$  elements. This actually provides a side proof for the CPL signal affected by the internal filtering effect, because in general, CPL is directly related to 3D chirality that does not change for different experiments performed

on the same sample. The only possibility is that this CPL signal is shadowed by the linear anisotropy of the sample, which is itself random. Then, the diagonal elements (in particular the  $m_{11}$  and  $m_{22}$  elements) have a clear dependence with wavelength. First, at a given excitation wavelength, regardless of the signal in  $m_{10}$  and  $m_{20}$ , the  $m_{11}$  and  $m_{22}$  elements give always practically the same signal. By repeating many experiments with the same excitation, this signal does not change significantly. This shows how these elements measure intrinsic properties engaged between the excitation polarization and the emission polarization. We can search for the physical interpretation of these elements by referring to the Mueller matrix of an isotropic medium shown in Eq. (6.24). We can see that these 2 diagonal elements are associated with the fluorescence polarization ratio  $r_v$ . We can thus label these 2 elements ( $m_{11}$  and  $m_{22}$ ) as "intrinsic" polarization ratio, where "intrinsic" means that this quantity does not depend on the intrinsic anisotropy of the system and can not be obtained by a standard fluorescence polarization ratio measurements presented at the beginning of this chapter. This can be easily shown by taking the definition of  $r_v$  in Eq. (6.20) without any constraint on the Mueller matrix elements. One has:

$$r_v = \frac{m_{11} - m_{10}}{m_{00} - m_{01}} \neq m_{11} \quad (6.37)$$

meaning that if we take the traditional fluorescence anisotropy measurement presented in section 6.1 of this chapter for an anisotropic sample, the result will be affected by  $m_{10}$  due to the anisotropy of the sample itself. This example therefore clearly stresses again the relevance and necessity of performing Mueller matrix measurement for the emission of anisotropic systems when aiming at characterizing the polarization properties of the fluorescence signal.



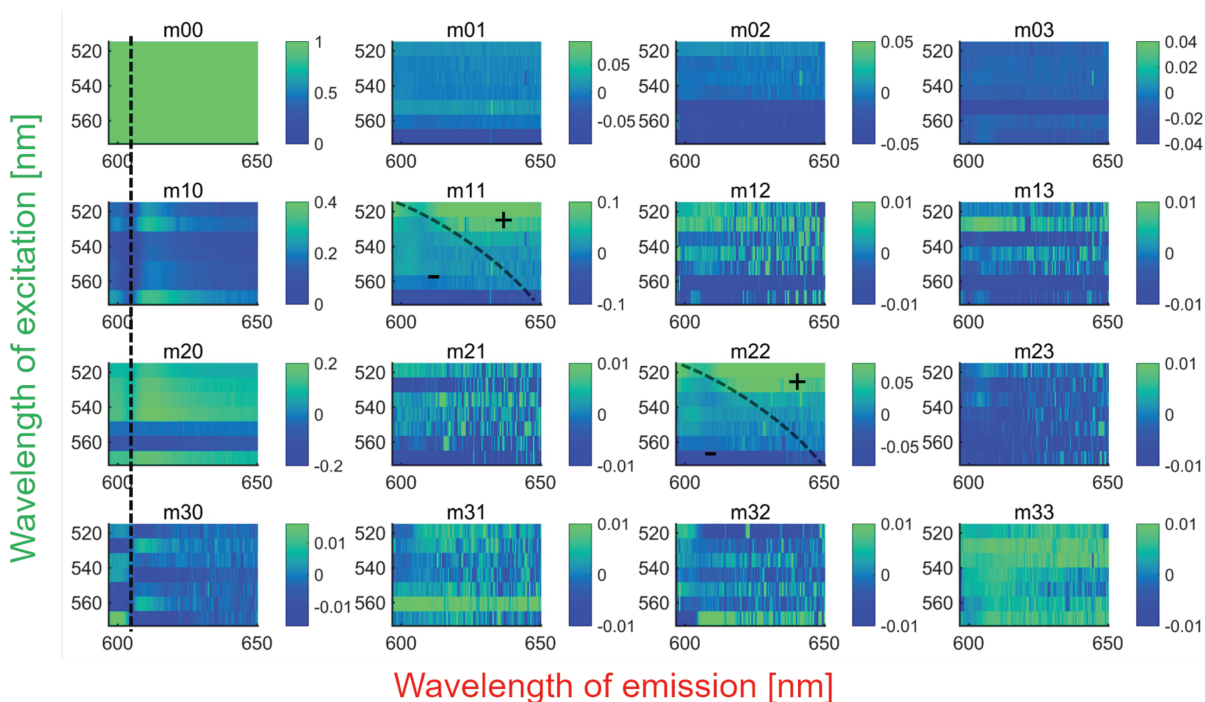


FIGURE 6.15: The 2D Mueller matrix of emission "action spectrum" measured for the C8O3 J-aggregate in stage 5 of the self-assembly. This 2D spectral Mueller matrix is built from all emission Mueller matrices recorded upon excitation wavelengths of 520, 530, 540, 550, 560, 570 and 580 nm displayed as a function of emission wavelength ranging from 595 to 650 nm.

The black dot line in first column shows the emission peak position.

If we look closely at the evolution of the  $m_{11}$  (and  $m_{22}$ ) elements with the excitation wavelength, we can see that from 520 nm to 580 nm, its value shifts gradually from positive to negative. This can be analyzed together with the LD (and LD') signals. Since our C8O3 sample at stage 5 of the self-assembly corresponds to an aggregation process almost complete, the emission is coming from the transition dipole moment associated with the longitudinal exciton along the tubular structure of the J-aggregate (610 nm as discussed in the previous chapter). As 520 nm corresponds to the monomeric absorption band that always displays a LD signal with the same sign as the longitudinal exciton according to Fig. 5.5, these data imply that the exciton at this wavelength (520 nm) is in the same orientation as the longitudinal exciton (at  $\sim 610$  nm), with therefore the absorption transition dipole moment  $\mu_a$  almost aligned with emission transition dipole moment  $\mu_e$  as shown in Fig. 6.16 (a). However, at 580 nm, the excitation falls on the absorption band of the transverse exciton of the aggregate, which is always perpendicular to the longitudinal exciton. In this case, the tubular structure is also revealed by a LD signal but with always an opposite sign (see Fig. 5.5). This means that the absorption transition dipole moment  $\mu_a$  is almost perpendicular to the emission one  $\mu_e$  as shown in Fig. 6.16. It then gives a negative polarization ratio because it converts the excitation

polarization to an orthogonal polarization in emission.

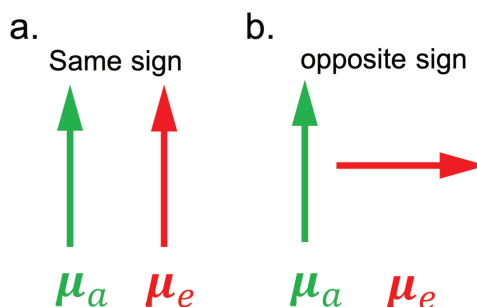


FIGURE 6.16: (a) and (b) display respectively the situation where absorption and emission dipole moments are collinear and perpendicular, giving thus same (a) and opposite (b) signs on the fluorescence polarization ratio.

## 6.4 Conclusion and perspectives

Reviewing the initial motivations of fluorescence polarization measurements using conventional methods such as fluorescence anisotropy and CPL measurements, we introduced the Mueller formalism for characterizing polarization relations in molecular emission processes. For an isotropic medium (being chiral or non-chiral), we related the emission Mueller matrix to the conventional methods, showing that the Mueller approach does not provide more informations than fluorescence anisotropy and CPL measurements. However, for more complex situations for instance when the system is anisotropic, Mueller polarimetry becomes really useful, capable of isolating the different contributions that connect the polarizations of the excitation to those of the emission. Mueller polarimetry thus provides a complete polarization characterization (within the limit of linear optics). With this method, we were able to identify artifacts that threaten conventional fluorescence polarization measurements. This identification lead to the possibility for artifact-free CPL measurements in the context of anisotropic media. We indeed illustrated specifically how artifact in CPL can be raised due to the internal filtering effects induced in small Stokes-shift bi-anisotropic media and we stressed the optimal conditions needed for CPL measurements. Finally, we proposed alternative representations of polarization in emission vs. excitation. We showed how the Poincaré sphere and 2D Mueller matrices can become efficient complementary tools from which more informations can be extracted on polarization dynamics in emission.

As described in this chapter, the emission Mueller matrix methodology offers many advantages with a profound insight in the excitation-to-emission polarization evolutions. But at this stage of thesis, we still remain limited by a rather low signal-to-noise ratio that does not allow us to reach the resolution level needed in the context of molecular

chiroptical spectroscopy. Our measurements are based on sequences of successive spectral acquisitions and the precondition for precise Mueller matrix measurements is that the light source itself must remain very stable throughout the measurement sequence. In transmission, this is not a limiting factor: our high resolution relies on the high stability of our white light source. But in emission, the same high resolution highly relies on the stability of the molecular emission signal requiring that the emission intensity must be stable during the whole experiments, that is over duration of 30 min  $\sim$  1h. In the laboratory, such conditions are very difficult to reach due to the fluctuation of the excitation light, light scattering inside the sample, diffusion and inhomogeneity of the emitter in solution. To solve this, acquiring the emission signal using a lock-in amplifier that filters out the noise at all frequencies different from the modulation frequency  $f_m$  is a known strategy. To improve our signal-to-noise ratio, an efficient approach is to couple Mueller polarimetry with a modulated intensity measurement using a band-pass filter, as exposed for example in [138]. This issue is extremely important for high resolution CPL measurements since CPL signals are in general very weak. With our current setup, the signal of emission itself has a fluctuation of 1% during the measurement time, meaning that without any filter to eliminate other sources of fluctuations, a CPL signal smaller than 1% can not be measured. One clear perspective of this work is thus to improve the signal-to-noise ratio of our setup while exploiting the same methodology based on emission Mueller polarimetry. Doing so will provide measurements that are relevant from a resolution level point of view in the context of molecular chiroptical spectroscopy.

## Chapter 7

# Conclusions and perspectives

### 7.1 Conclusions

We close the thesis in 4 parts that cover both the theoretical work and the experiments presented in the manuscript.

**Theory** In order to understand closely the connections between optical activity and light polarization, we introduced the Stokes-Mueller formalism perfectly suited for describing polarization states interacting with chiral, anisotropic media. We then reviewed the methods available for extracting polarimetric quantities from an experimental Mueller matrix generally depolarizing. These methods are based on Cloude's and differential decompositions. Thanks to the infinitesimal form of Mueller matrices for differential decomposition, we introduced the concept of Lie algebra under the framework of group-like algebraic structures. With this concept at hand, we identified 2 main substructures out of the ensemble of all physically realizable Mueller matrices: the  $SO+(1,3)$  Lie group for all non-singular, non-depolarizing Mueller matrices and a Lie monoid for all non-singular Mueller matrices with  $SU(4)$  Lie algebra. This led us to better understand the implications of the differential decomposition method on depolarizing Mueller matrices and this way polarization dynamics in the Poincaré sphere. We were then able to relate the symmetries of conformation of Mueller matrix eigenvectors in the Poincaré sphere to the symmetries of the medium characterized by the corresponding Mueller matrix. This drew a clear and original method for designing optical media with specific symmetries and polarization responses.

**Experiments** The core experimental work of the thesis was the construction of a broadband Mueller polarimeter working on the principle of dual rotating quarter wave-plate. We verified carefully that the homogeneous elliptical birefringent modeling of quarter wave-plates provided a very good accuracy for Mueller matrix measurements within detection limits precisely assessed through a dedicated statistical analysis of the noise. We proposed a standard procedure for data processing for both passive and active samples together with

a well-controlled reference correction method. We also illustrated other experimental configurations for measuring transmission, reflection and emission, and for performing spectral Mueller imaging in both real and Fourier spaces.

**Mueller polarimetry in transmission configuration** We applied Mueller polarimetry to the detailed study of the evolution of polarization states in the course of an amphiphilic cyanine J-aggregation self-assembly. By carefully controlling the self-assembly process from achiral monomeric to chiral aggregated phases, we identified primary and secondary chiral nucleation events where chirality, once emerged, is amplified in the formation of macroscopic chiral tubular supramolecular assemblies. The formation, growth, and bundling of such chiral tubular assemblies have also been visualized by tracking the evolution of the circular and linear dichroism and the degree of depolarization extracted from Mueller matrix in each stage of self-assembly. A Poincaré sphere representation of the Mueller eigenvectors associated with this supramolecular system was exploited in order to visualize and follow the evolution of the symmetries of the system. Moreover, by reconstructing the evolutions of the chiroptical quantities extracted from the Mueller matrices measured at different stages of aggregation, we showed rich optical hierarchies closely following the hierarchy at play in the supramolecular self-assembly. This allowed us to emulate non-trivial polarization dynamics by constructing an optical system from the evolving molecular response.

**Mueller polarimetry in emission configuration** Conventional fluorescence anisotropy measurements were compared with the emission Mueller approach for characterizing polarization relations in molecular emission processes. We showed in the case of an isotropic medium, that both conventional and Mueller approaches are comparable. But for anisotropic systems, Mueller polarimetry becomes useful, providing a full polarization assessment, capable of isolating the different contributions from the polarization of the excitation to those of the emission and capable of identifying artifacts that can easily spoil conventional fluorescence polarization measurements. We showed how artifacts of circularly polarized luminescence can be induced in anisotropic molecular systems, in particular when characterized by small Stokes shifts as it is the case for supramolecular aggregates. Such artifacts are perfectly identified in emission Mueller polarimetry, that provides therefore a genuine "sanity check" for standard circularly polarized luminescence measurements. We finally showed how Mueller polarimetry of molecular fluorescence can be complemented by Poincaré sphere representations of the polarization dynamics and by the development of "action spectra" bi-dimensional Mueller matrices.

## 7.2 Perspectives

Two pressing perspectives for this work can be identified:

**Designing-building optical media with specific symmetries** Chapter 3 proposed a method for building a medium with specific symmetries and specific polarization responses via the analysis of Mueller matrix eigenvectors. This method could be tested and further explored with real systems such as layer stacking of heterostructures which relative orientations could be governed by our construction rules. For instance, considering that planar chirality has been a topic of very active research in material science and nano-optics recently, our rules also give ways to construct media with specific planar chirality and that are both non-depolarizing (time-reversal symmetric) and depolarizing (time-reversal non-symmetric).

**High resolution Mueller polarimetry for fluorescence** As described in Chapter 6, although emission Mueller polarimetry gives many advantages for understanding the relationship between excitation and emission polarizations, the associated detection resolution for polarization signal turns out to be too low for our current setup to be implemented on all types of chiral emissive molecular samples. Reaching a high resolution of detection will demand a change in the acquisition/detection sequence. One solution would be to modulate the acquisition at a given frequency, in order to filter out all noise spectral contributions falling next to this frequency. This would immediately lead to increase largely the signal-to-noise ratio of an experiment. To reach such a high resolution level in fluorescence Mueller polarimetry, a direct route is to replace, in our dual rotating quarter wave-plate configuration, the polarization state analyzer stage by a system consisting of a harmonically driven PEM and linear polarizer and couple this system to a highly sensitive photomultiplier via a lock-in amplifier. The amplifier will serve as a high resolution polarization analyzer for measuring the output Stokes vector from which circularly polarized luminescent signals can be acquired even when generated by molecules that display only weak chirality in their emission spectrum. Finally, combining the output Stokes vectors with precisely controlled input Stokes vectors will eventually lead to measure the entire Mueller matrix in emission with the highest level of resolution possible. This modification of our current setup will upgrade our capacities and will correspond to one important step taken when aiming at harnessing molecular complexity for proposing new optical features and potentially new optical devices.



## Chapter 8

# Résumé de thèse

### 8.1 Contexte

Depuis l'observation pionnière de la formation spontanée de cristallites de tartrate de gauche et de droite par Luis Pasteur, les composés chiraux ont été intensivement étudiés en physique, chimie et biologie. D'un point de vue énergétique, les énantiomères gauchers et droitiers d'un composé asymétrique ont une probabilité égale de formation, ce qui entraîne normalement des mélanges racémiques [6]. Cependant, l'homochiralité, où un énantiomère prévaut sur l'autre énantiomère, est observée dans nombreux organismes vivants. Pour cette raison de couture et inexplicée, il reste un sujet d'activités intenses combinant de nombreuses disciplines différentes [7–9]. Physiquement parler, l'émergence d'excès d'un énantiomère chiral par rapport à l'autre est identifiée comme un événement de brisure de symétrie du miroir spontané, qui est également observé dans le processus de cristallisation de molécules telles que NaClO [11, 12], cristaux liquides [13, 14], et systèmes d'autoassemblages supramoléculaires [15, 16].

Le but de la thèse est d'étudier tels phénomènes de brisure spontanée de symétrie de miroir. Pour faire ça, nous avons décidé d'utiliser aux outils optiques qui est les plus adaptés pour mesurer l'émergence progressive de signaux chiroptiques induits au cours d'un processus d'autoassemblage supramoléculaire. D'un point de vue moléculaire, nous avons sélectionné des colorants carbocyanines amphiphiles achirales qui peuvent s'auto-assembler en gros agrégats J chiraux tubulaires. Optiquement parler, nous avons choisi la polarimétrie Mueller comme la méthodologie qui s'avère le plus appropriée pour sonder l'émergence de la chiralité.

Ces choix de méthode et de système relie notre thèse aux efforts de recherche actuels qui exploitent des assemblages supramoléculaires pour le développement de nouveaux dispositifs optiques, et / ou l'élaboration de nouveaux outils de spectroscopie chiroptique et d'imagerie applicables à une grande variété de systèmes chiraux moléculaire, biologique ou artificiel.

En ce qui concerne ce deuxième aspect, la polarimétrie Mueller, parmi toutes les méthodologies de caractérisation de polarisation existantes, offre une capacité unique de



déchiffrer la dynamique de tous les types d'états de polarisation de la lumière. Ceci est reconnu depuis longtemps et la polarimétrie Mueller est aujourd'hui un outil essentiel largement exploité chaque fois que la polarisation est pertinente pour étudier les processus physiques, chimiques et biologiques. Cette pénétration de la polarimétrie Mueller dans de nombreux domaines de recherche s'est accompagnée de vastes travaux théoriques qui est largement concernés par la mise en relation d'une mesure de matrice de Mueller avec les observables chiroptiques standard utilisés en spectroscopie chiroptique traditionnelle. Cette question centrale sera au cœur de cette thèse et nous expliquerons comment elle est basée sur certains articles théoriques spécifiques et importants dans ce domaine.

Une fois cette relation est établie, la polarimétrie Mueller offre de nombreux atouts pour analyser et comprendre les propriétés optiques de systèmes chiraux complexes. Par exemple, Bart Kahr, Oriol Arteaga et leurs collègues ont exploité la polarimétrie Mueller, à la fois expérimentalement et théoriquement, avec une grande maîtrise et profusion [17]. L'imagerie de Mueller les a amenés à mesurer des retards circulaires différenciés à différents stades de croissance de la cristallisation. Un tel travail est représentatif comme la contribution de la polarimétrie Mueller à la science des matériaux chiraux.

La polarimétrie Mueller a également été exploitée dans le domaine de la nano-optique, où la variété des nanostructures métalliques artificielles conçues a conduit à la génération et au contrôle de nouveaux types de modes optiques et d'excitations. Comme souvent, les propriétés optiques uniques de ces systèmes optiques nanostructurés sont codées dans leur dynamique de polarisation parfaitement révélée et surveillée à l'aide de la polarimétrie Mueller. Dans ce contexte par exemple, des études récentes réalisées dans le groupe de J. Bellessa à Lyon et dans le groupe de A. Drezet à Grenoble donnent des exemples clairs de la méthode. En particulier, ces auteurs ont souligné la capacité de la polarimétrie Mueller à révéler comment de légères déviations dans le processus de lithographie des nanostructures conçues symétriquement peuvent en fait conduire à de puissants effets chiroptiques, combinant des effets chiraux bi- et tridimensionnels [19]. Dans ce sens et précisément pour sa sensibilité vis-à-vis des aspects de symétrie, S.Fan et ses collègues ont récemment promu l'utilisation de la représentation de sphère de Poincaré dans le contexte de métamatériaux non réciproques qui obéissent à la symétrie d'inversion du temps. Comme nous le verrons dans la thèse, la polarimétrie Mueller est en effet un outil intéressant à utiliser pour explorer les liens entre chiralité, réciprocité et inversion du temps. La notion de hiérarchie jouera également un rôle important dans la thèse. Elle a été centrale dans des articles récents (Y. Battie à Metz, E. Pouget à Bordeaux, M. Pauly et G. Decher à Strasbourg par exemple) impliquant des nanoparticules plasmoniques colloïdales chirales. Dans un article récent, ces auteurs ont utilisé des techniques de pulvérisation par incidence rasante afin d'organiser hiérarchiquement les dispersions colloïdales de nanohélices d'or chirales. Comme clairement démontré en utilisant la polarimétrie Mueller, ces colloïdes

organisés présentent des propriétés chiroptiques collectivement remarquables [21].

La possibilité de créer de nouvelles fonctions optiques à l'aide d'assemblages chiraux à l'échelle nanométrique est actuellement un moteur important de la chimie supramoléculaire. Là, un défi majeur est la capacité à contrôler les autoassemblages supramoléculaires afin de générer des fonctions spécifiques. Ce lien entre architectures supramoléculaires et fonctions est particulièrement bien exploré dans le contexte de l'optique avec pour objectif d'utiliser de tels systèmes supramoléculaires comme de véritables matériaux optiques permettant de nouvelles fonctions. Dans ce contexte, les films supramoléculaires d'hélicène ont été reconnus comme particulièrement prometteurs. Verbiest et al. a montré comment la chiralité de tels systèmes peut améliorer les propriétés optiques non linéaires par rapport à la réponse non linéaire des mélanges d'hélicène racémate [22].

Récemment, J. Crassous et ses collègues à Rennes ont développé des commutateurs chiroptiques à base d'hélicène où les fonctions chimiques sont transférées dans des fonctionnalités optiques [23]. La possibilité de contrôler l'équilibre dynamique entre les formes chirales bistables de l'hélicène à l'aide de déclencheurs lumineux, redox ou pH a conduit à la démonstration de commutateurs optiques, ouvrant la voie à de nombreuses applications dans le contexte de portes logiques et de mémoires purement optiques.

Ces commutateurs fonctionnent à la fois sur les modulations spectrales et d'amplitude de la luminescence à polarisation circulaire (CPL). La CPL est très intéressante pour sonder la structure électronique des molécules chirales, mais elle est aussi particulièrement intéressante dans le cadre de la spintronique, de la bio-imagerie, de la synthèse asymétrique, etc. Ceci explique pourquoi les sources chimiques de CPL sont recherchées depuis longtemps. Dans un domaine essentiellement axé sur les complexes de lanthanides qui présentent des contrastes CPL élevés, Fuchter et al. a réalisé que les assemblages supramoléculaires peuvent en fait conduire à une grande amélioration des dissymétries CPL [25] qui revigore tout un champ visant à exploiter les assemblages supramoléculaires chiraux pour la génération de lumière chirale [26]. La dernière partie de la thèse tente de s'insérer dans cette ligne de recherche, en promouvant les systèmes supramoléculaires chiraux comme nouveaux supports optiques, au niveau desquels la hiérarchie chimique est imprimée dans des signatures de polarisation hiérarchique qui peuvent conduire à des optiques topologiquement non triviales et donc des dynamiques optiques fascinantes.

## 8.2 Résultat et discussion

### 8.2.1 Analyse théorique du formalisme de Mueller

Nous avons choisi d'étudier ces relations dans le formalisme de Stokes-Mueller qui permet une analyse complète des états de polarisation d'un champ optique, y compris des

effets de dépolarisation (fluctuations de polarisation, entropie, etc.). Dans ce formalisme, l'état de polarisation est décrit par un quadrivecteur de Stokes qui vit dans un espace de Minkowski et qui peut être représenté dans une sphère de rayon 1 appelé sphère de Poincaré. La matrice de Mueller quant à elle décrit les transformations induites sur les états de polarisation du champ optique interagissant avec un milieu donné. Un point très important est la capacité du formalisme de Mueller de décrire tout système dépolarisant en quoi consiste la plupart des systèmes moléculaires. Dans ce cas, le vecteur Stokes est écrit sous la forme d'une valeur moyenne de deuxièmes moments du champ électromagnétique qui peuvent être directement des mesurables et que nous étudions en détail. C'est dans ce contexte que nous étudions également les conditions de réalisabilité physique de la matrice de Mueller et nous montrons comment ces conditions donnent une contrainte physique pour la matrice expérimentalement mesurée. Enfin, nous analysons différentes méthodes de décomposition d'une matrice Mueller pour extraire le plus fidèlement possible des observables correspondant aux propriétés chiroptiques que nous souhaitons pouvoir caractériser avec une grande précision. Nous nous intéressons en particulier à la décomposition différentielle basée sur le groupe de Lie qui permet d'accéder aux propriétés polarimétriques non-dépolarisantes et aux contributions différentes de dépolarisation du milieu étudié. Spécifiquement, la chiralité de forme différent est représentée par la conformation de vecteur propre de la matrice de Mueller comme montré dans Fig. 8.1. Nous montrons également comment les approches basées sur la théorie des groupes permettent des interprétations géométriques de la polarimétrie, facilitant la visualisation et l'analyse des états propres de polarisation d'un milieu. A partir de ce formalisme, nous proposons une approche originale pour construire ab initio des milieux optiques capables de manipuler de manière contrôlée un état de polarisation donné.

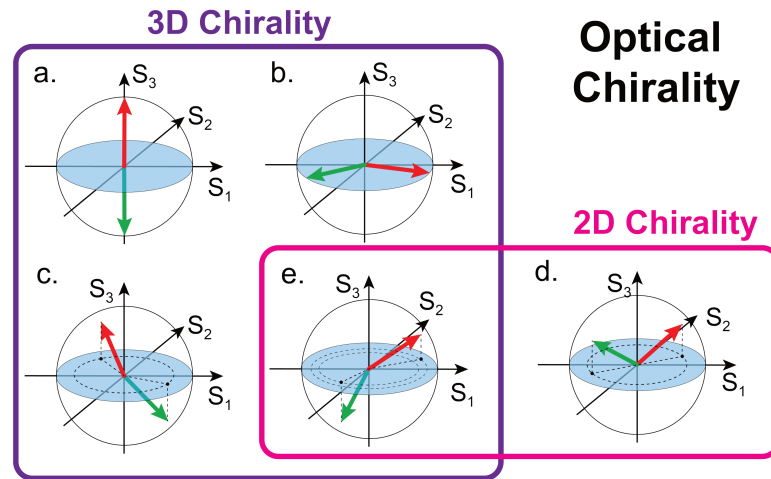


FIGURE 8.1: Conformations différentes de vecteur propre pour le milieu optiquement actif à l'aide de l'analyse de théorie de groupe. (a)-(c) montre la conformation typique de vecteur propres d'un milieu avec purement activité optique (3D). (d) montre la conformation de vecteur propres d'un milieu de chiralité 2D. (e) montre le cas le plus général ayant en le même temps la chiralité 3D et 2D.

### 8.2.2 Construction expérimentale du polarimètre de Mueller

Ce travail théorique fonde notre réalisation expérimentale du polarimètre de Mueller montré dans Fig. 8.2 adapté aux échantillons moléculaires, avec des modes d'opération permettant l'étude de systèmes passifs ou actifs, transparents ou absorbants. Notre banc expérimental fonctionne sur un spectre optique large et avec un excellent rapport signal à bruit, le constituant en un outil expérimental très utile et très souple vis-à-vis des contraintes de signal. Nous avons adapté à toutes ces contraintes et configurations les algorithmes de la polarimétrie Mueller en choisissant une approche par rotation de lames quart d'onde. Nous avons couplé ce montage en mode imagerie, nous permettant de réaliser une microscopie résolue en polarisation à la fois dans l'espace direct de l'échantillon et dans l'espace Fourier. Dans ce dernier cas, nous obtenus une capacité d'analyse des effets de polarisation angulaires particulièrement important à maîtriser et mesurer dans le contexte de la chiralité optique.

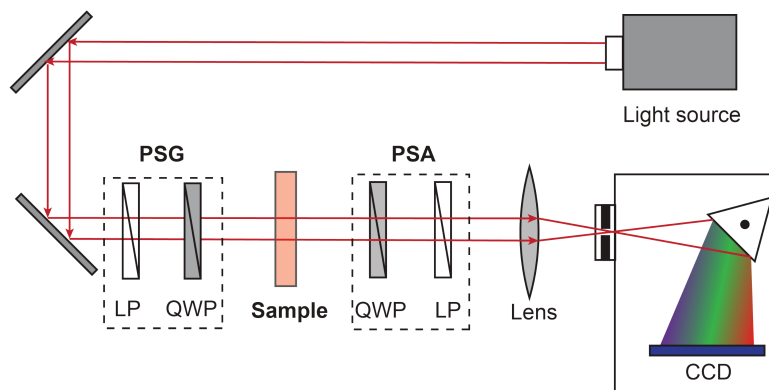


FIGURE 8.2: La représentation schématique de notre montage de polarimétrie Mueller où PSA et PSG représentent le générateur et analyseur d'état de polarisation composé par un polariseur linéaire (LP) fixé et une lame quart-d'onde (QWP) respectivement.

### 8.2.3 Expérience de transmission de polarimétrie Mueller

Dans un premier travail, nous avons choisi d'étudier le système en agrégat J de la molécule de cyanine C8O3, molécule achirale mais peut s'auto-assembler en agrégats hélicoïdaux tubulaires chiral en fonction du pH de la solution. Pour ce processus, l'assemblage hiérarchique parcourt une brisure de symétrie miroir dont on peut contrôler chaque étape avec une valeur définie de pH. Chaque étape peut alors être analysée par une mesure de matrice de Mueller, permettant de suivre optiquement l'émergence de la chiralité et d'étudier la hiérarchisation du signal chiroptique.

Pour la première fois, l'induction initiale de brisure de symétrie miroir a pu être observée où les monomères forment des structures préliminaires avec une chiralité définie avant le début de formation des agrégats. Cette chiralité préliminaire sert de nucléation chirale provoquée par l'interaction hydrophobique de chaînes alkyles des monomères qui transfèrent la chiralité à tout l'assemblage final illustré dans notre publication « Mueller Polarimetry of Chiral Supramolecular Assembly » en « Journal of Physical Chemistry C ». La polarimétrie Mueller des propriétés chiroptiques associées nous a permis de déduire la conformation de chaque étape d'assemblage tel que montré en Fig. 8.3. On peut y voir clairement comment la hiérarchie d'assemblage est encodées par la hiérarchie des propriétés polarimétriques tels que le dichroïsme circulaire (CD). La conformation liée au regroupement des structures tubulaires peut être déduite du signal CD bi-signé dans les 2 dernières étapes en Fig. 8.3. Par ailleurs, le dichroïsme linéaire (LD) mesuré indique la formation et la croissance de la structure tubulaire. La polarimétrie Mueller apparaît donc comme un outil idéal pour suivre et analyser in situ un processus d'assemblage supramoléculaire spontané en solution.

Pour mieux visualiser l'évolution de ces propriétés chiroptiques, nous proposons dans cette thèse une nouvelle approche basée sur le suivi des vecteurs propres de la matrice

de Mueller mesurée pour chaque étape d'agrégation dans la sphère Poincaré. à l'aide de la théorie des groupes, nous montrons comment cette analyse de vecteurs propres peut également servir à l'analyse fine de l'émergence de chiralité.

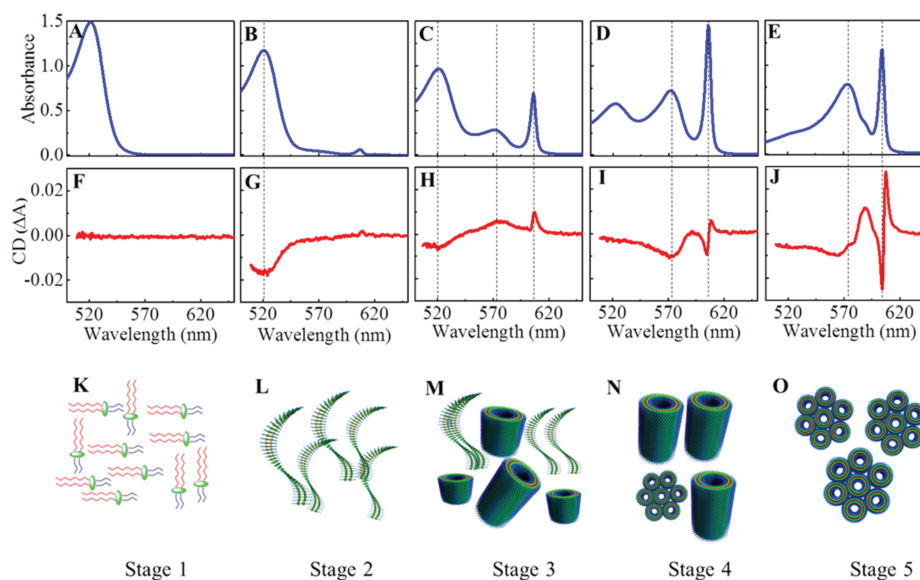


FIGURE 8.3: (A-E) Spectre d'absorption de monomère de carbocyanine (C8O3) au cours des différentes de formation des agrégats J. (F-J) montre l'évolution du spectre CD mesurée par la polarimétrie Mueller. (K-O) montre la représentation schématique de conformations moléculaire associées aux spectres d'absorption et CD obtenus par polarimétrie Mueller. (K) représente l'étape monomérique, (L) indique l'étape ou la brisure de symétrie miroir s'engage au stade de première nucléation. (M) montre la formation de d'agrégats J de C8O3 chiral. (N) indique la croissance de la structure tubulaire auto-assemblée et (O) montre au final le regroupement de structure déduit par le CD bi-signé lié au couplage excitonique chiral. Résultats tirés de notre publication en « Journal of Physical Chemistry C ».

### 8.2.4 Expérience d'émission

Pour générer des états de polarisation complexes en particulier chiraux à partir d'un système chimique complexe excité, il s'agit d'abord effectuer la mesure de la matrice de Mueller en émission avec la conformation montrée dans Fig. 8.4 (a) reliant la polarisation de lumière d'excitation et à la polarisation de la photoluminescence (PL). Cette matrice donne donc des informations importantes sur la contribution de la polarisation d'excitation sur la polarisation de PL (avec un exemple montré en Fig. 8.4 (b)) et cette matrice peut être présentée par la sphère Poincaré. En représentant l'état de polarisation sur la surface de la sphère Poincaré comme l'état incident, l'application de la matrice de Mueller en émission nous fait obtenir l'ensemble des états émergents en PL et qui composent une sphère déformée décrivant tout l'espace d'état de polarisation d'émission. Pour

ce faire, nous devons pouvoir identifier un système supramoléculaire approprié capable de générer de l'émission en polarisation circulaire (CPL). Nos premiers essais ont été effectués sur l'agrégat J de cyanine (C8O3) utilisé précédemment. Des mesures extrêmement précises nous ont permis de constater que le facteur de dissymétrie de C8O3 est très faible et de mettre en évidence un artefact important. En effet, parce que pour cet agrégat, à longueur d'onde d'émission reste une bande absorption optiquement active, le phénomène de ré-absorption se couple à la mesure CPL. En déplaçant le point de collection de la PL à travers l'échantillon, le signal de CPL disparaît graduellement. Cet effet montre comment un signal CPL peut parfois être simplement induit par l'absorption de l'échantillon lui-même et ne rien avoir affaire avec une éventuelle chiralité optique générée par les états moléculaires excités. Ces précautions étant prises, nous avons pu vérifier la validité de notre méthodologie de polarimétrie Mueller pour des mesure en émission et terminons notre travail sur la mesure de CPL sur d'autres systèmes chimiques potentiellement intéressants.

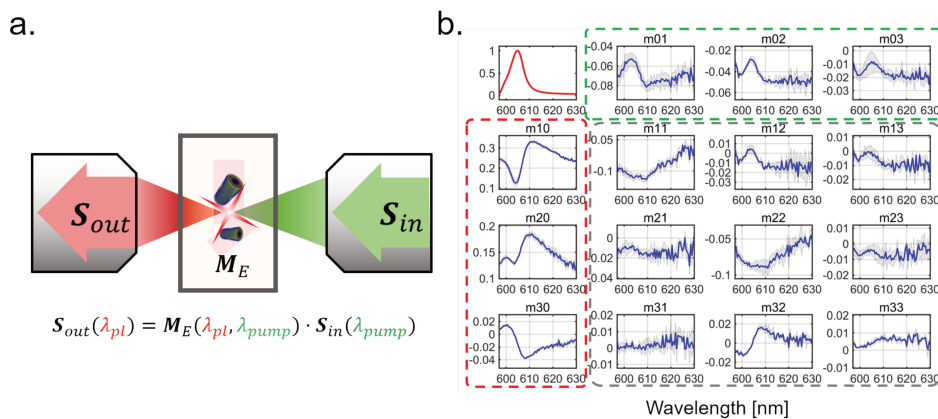


FIGURE 8.4: (a) montre le schéma logique d'interaction d'une matrice de Mueller en émission dans notre montage de mesure. (b) illustre un exemple de matrice de Mueller en émission pour un agrégat J où le cadre rouge représente les mesures de propriété polarimétrique d'état excité et le cadre vert représente les mesures de propriété polarimétrique d'état fondamentale.

### 8.3 Conclusion générale et perspectives

**Conclusions théoriques** Afin de bien comprendre les liens entre l'activité optique et la polarisation de la lumière, nous avons introduit le formalisme de Stokes-Mueller parfaitement adapté pour décrire les états de polarisation interagissant avec les milieux chiraux et anisotropes. Nous avons ensuite passé en revue les méthodes disponibles pour extraire des quantités polarimétriques à partir d'une matrice de Mueller expérimentale qui est généralement dépolarisante. Ces méthodes sont basées sur les décompositions de Cloude et différentielles. Grâce à la forme infinitésimale des matrices de Mueller pour

la décomposition différentielle, nous avons introduit le concept d'algèbre de Lie dans le cadre de structures algébriques de type groupe. Avec ce concept, nous avons identifié 2 sous-structures principales de l'ensemble de toutes les matrices Mueller physiquement réalisables : le groupe de Lie  $SO^+(1,3)$  pour toutes les matrices de Mueller non singulières et non dépolarisantes et un monoïde de Lie pour toutes les matrices de Mueller singulières avec  $SU(4)$  Algèbre de Lie. Ceci nous a conduit à mieux comprendre les implications de la méthode de décomposition différentielle sur la dépolarisation des matrices de Mueller et ainsi la dynamique de polarisation dans la sphère Poincaré. Nous avons alors pu relier les symétries de conformation des vecteurs propres de la matrice de Mueller dans la sphère de Poincaré aux symétries du milieu caractérisé par cette matrice de Mueller correspondante. Cela a dessiné une méthode claire et originale pour concevoir des supports optiques avec des symétries et des réponses de polarisation spécifiques.

**Conclusions expérimentales** Le travail principal expérimental de la thèse était la construction d'un polarimètre Mueller à lumière blanche fonctionnant sur le principe de la double lame quart-d'onde rotative. Nous avons vérifié soigneusement que la modélisation biréfringente elliptique homogène des lames quart-d'onde fournissait une très bonne précision pour les mesures de la matrice de Mueller dans des limites de détection qui est précisément évaluées par une analyse statistique dédiée du bruit stochastique. Nous avons proposé une procédure standard pour le traitement des données pour les échantillons passifs et actifs ainsi qu'une méthode de correction de référence bien contrôlée. Nous avons également illustré d'autres configurations expérimentales pour mesurer la transmission, la réflexion et l'émission, et pour réaliser l'imagerie spectrale de Mueller dans les espaces réels et de Fourier.

Nous avons appliqué la polarimétrie Mueller à l'étude détaillée de l'évolution des états de polarisation au cours d'un auto-assemblage amphiphile cyanine J-agrégation. En contrôlant soigneusement le processus d'auto-assemblage des phases monomères achirales aux phases agrégées chirales, nous avons identifié des événements de nucléation chirale primaire et secondaire où la chiralité, une fois émergée, est amplifiée dans la formation d'assemblages supramoléculaires tubulaires chiraux macroscopiques. La formation, la croissance et le regroupement de tels assemblages tubulaires chiraux ont également été visualisés en suivant l'évolution du dichroïsme circulaire et linéaire et le degré de dépolarisation extrait de la matrice de Mueller à chaque étape de l'auto-assemblage. Une représentation en sphère Poincaré des vecteurs propres de Mueller associés à ce système supramoléculaire a été exploitée afin de visualiser et suivre l'évolution des symétries du système. De plus, en reconstruisant les évolutions des grandeurs chiroptiques extraites des matrices de Mueller mesurées à différents stades d'agrégation, nous avons montré de riches hiérarchies optiques suivant de près la hiérarchie en jeu dans l'auto-assemblage



supramoléculaire. Cela nous a permis d'émuler une dynamique de polarisation non triviale en construisant un système optique à partir de la réponse moléculaire en évolution.

Les mesures conventionnelles d'anisotropie de fluorescence ont été comparées avec l'approche de polarimétrie Mueller d'émission pour caractériser les relations de polarisation dans les processus d'émission moléculaire. Nous avons montré dans le cas d'un milieu isotrope, que les approches conventionnelles et de matrice de Mueller sont comparables. Mais pour les systèmes anisotropes, la polarimétrie Mueller devient utile, fournissant une évaluation de polarisation complète, parce qu'il est capable d'isoler les différentes contributions de la polarisation de l'excitation à celles de l'émission et capable d'identifier les artefacts qui peuvent facilement gâcher les mesures de polarisation de fluorescence classiques. Nous avons montré comment des artefacts de luminescence à polarisation circulaire peuvent être induits dans les systèmes moléculaires anisotropes, en particulier quand le système présente petits déplacements de Stokes comme le cas des agrégats supramoléculaires. Ces artefacts sont parfaitement identifiés dans la polarimétrie Mueller d'émission, qui fournit donc un véritable contrôle de pureté pour les mesures de luminescence à polarisation circulaire standard. Nous avons enfin montré comment la polarimétrie Mueller de la fluorescence moléculaire peut être complétée par des représentations de sphère Poincaré pour visualiser la dynamique de polarisation et par le développement de matrices de Mueller bi-dimensionnelles de type "spectres d'action".

**Perspectives** Le chapitre 3 a proposé une méthode pour construire un milieu avec des symétries spécifiques et des réponses de polarisation spécifiques via l'analyse des vecteurs propres de la matrice de Mueller. Cette méthode pourrait être testée et explorée plus avant avec des systèmes réels tels que l'empilement de couches d'hétérostructures dont les orientations relatives pourraient être régies par nos règles de construction. Par exemple, étant donné que la chiralité planaire a été un sujet de recherche très active récemment en science des matériaux et en nano-optique, nos règles donnent également des moyens de construire des médias avec une chiralité planaire spécifique et qui sont à la fois non dépolarisants (symétrique à inversion de temps) et dépolarisante (inversion du temps non symétrique).

Comme décrit au chapitre 6, bien que la polarimétrie Mueller d'émission offre de nombreux avantages pour comprendre la relation entre les polarisations d'excitation et d'émission, la résolution de détection associée pour le signal de polarisation s'avère trop faible pour que notre configuration actuelle puisse être mise en œuvre sur tous les types de molécules émissives chirales. Atteindre une haute résolution de détection nous impose des changements dans la séquence d'acquisition / détection. Une solution serait de moduler l'acquisition à une fréquence donnée, afin de filtrer toutes les contributions spectrales de bruit tombant autre que cette fréquence. Cela conduirait immédiatement

à augmenter considérablement le rapport signal sur bruit d'une expérience. Pour atteindre un niveau de résolution aussi élevé en polarimétrie Mueller en fluorescence, une voie directe consiste à remplacer, dans notre configuration à double lame quart d'onde rotative, l'étage d'analyseur d'état de polarisation par un système constitué d'un PEM piloté harmoniquement accompagné avec un polariseur linéaire et de coupler ce système à un photomultiplicateur très sensible via un amplificateur de verrouillage. L'amplificateur servira d'analyseur de polarisation à haute résolution pour mesurer le vecteur de Stokes de sortie à partir duquel des signaux luminescents à polarisation circulaire peuvent être acquis même lorsqu'ils sont générés par des molécules qui ne présentent qu'une faible chiralité en émission. Enfin, la combinaison des vecteurs Stokes de sortie avec des vecteurs Stokes d'entrée contrôlés avec précision conduira à terme à mesurer toute la matrice de Mueller en émission avec le plus haut niveau de résolution possible. Cette modification de notre configuration actuelle améliorera nos capacités et correspondra à une étape importante franchie dans le but d'exploiter la complexité moléculaire pour proposer de nouvelles fonctionnalités optiques et potentiellement de nouveaux dispositifs optiques.



## Appendix A

# Matrix calculus

### A.1 Relations for the trace of matrices

A trace of a square matrix  $\mathbf{M}$ , denoted  $\text{Tr}(\mathbf{M})$ , is defined to be the sum of the main diagonal elements of  $\mathbf{M}$ . For an  $n$ -dimensional square matrix, the trace writes

$$\text{Tr}(\mathbf{M}) = \sum_{i=1}^n m_{ii} \quad (\text{A.1})$$

With this definition, we note usually the Frobenius norm of matrix by a trace as

$$\|\mathbf{M}\|_F^2 \equiv \sum_{i=1}^n \sum_{j=1}^n m_{ij}^2 \equiv \text{Tr}(\mathbf{M}^T \mathbf{M}). \quad (\text{A.2})$$

Clearly, the trace operation is linear and the trace for the transpose of a matrix is equal to its initial matrix:

$$\text{Tr}(\mathbf{M}) = \text{Tr}(\mathbf{M}^T) \quad (\text{A.3})$$

For a product of two matrices  $\mathbf{A}$  and  $\mathbf{B}$ , one can show

$$\text{Tr}(\mathbf{AB}) = \text{Tr}(\mathbf{BA}) \quad (\text{A.4})$$

More general, the trace of a matrix has the cyclic property which reads

$$\text{Tr}(\mathbf{ABC}) = \text{Tr}(\mathbf{CAB}) = \text{Tr}(\mathbf{BCA}) \quad (\text{A.5})$$

With this relation, one can show trace is invariant with respect to matrix similarity. This can be derived for 2 similar matrix  $\mathbf{A}$  and  $\mathbf{B}$  related by

$$\mathbf{A} = \mathbf{PBP}^{-1} \quad (\text{A.6})$$

as

$$\text{Tr}(\mathbf{A}) = \text{Tr}(\mathbf{PBP}^{-1}) = \text{Tr}(\mathbf{P}^{-1}\mathbf{PB}) = \text{Tr}(\mathbf{B}) \quad (\text{A.7})$$

This property can imply that matrix trace is also equal to the sum of its eigenvalues, written as

$$\text{Tr}(\mathbf{M}) = \sum_{i=1}^n \lambda_i \quad (\text{A.8})$$

with  $\lambda_i$  the  $i$ th eigenvalue of matrix  $\mathbf{M}$ , since a matrix is always similar to its diagonalized matrix. Besides, due to the property of matrix power and its eigenvalue, for any integer  $m$ , we have

$$\text{Tr}(\mathbf{M}^m) = \sum_{i=1}^n \lambda_i^m \quad (\text{A.9})$$

## A.2 Relations for Kronecker product

A kronecker product is generally not commutative, but has the property of bilinearity and associativity. For matrix transpose and inversion, one have

$$(\mathbf{A} \otimes \mathbf{B})^T = \mathbf{A}^T \mathbf{B}^T \text{ and } (\mathbf{A} \otimes \mathbf{B})^{-1} = \mathbf{A}^{-1} \mathbf{B}^{-1} \quad (\text{A.10})$$

For the mixed-product with matrix product, one have the relation

$$(\mathbf{A} \otimes \mathbf{B})(\mathbf{C} \otimes \mathbf{D}) = (\mathbf{AC}) \otimes (\mathbf{BD}) \quad (\text{A.11})$$

In addition, one can define a Kronecker sum, for a  $n \times n$  matrix  $\mathbf{A}$  and a  $m \times m$  matrix  $\mathbf{B}$  as

$$\mathbf{A} \oplus \mathbf{B} = \mathbf{A} \otimes \mathbf{I}_m + \mathbf{I}_n \otimes \mathbf{B} \quad (\text{A.12})$$

where  $\mathbf{I}_k$  is the  $k$ -dimensional identity matrix. We have then the following formula for a matrix exponential

$$\exp(\mathbf{A} \oplus \mathbf{B}) = \exp(\mathbf{A}) \otimes \exp(\mathbf{B}) \quad (\text{A.13})$$

This formula is very useful for numerical analysis. Also, the discussion on the relation between Jones and Mueller differential matrix ( $\mathbf{N}_J$  and  $\mathbf{N}_M$ ) in Eq. (2.212) can be derived directly by this formula.

As the abstract properties, for square matrices  $\mathbf{A}$  and  $\mathbf{B}$  with their non zeros eigenvalues  $\lambda_1 \dots \lambda_n$  and  $\mu_1 \dots \mu_m$ , the eigenvalue of matrix given by  $\mathbf{A} \otimes \mathbf{B}$  are  $\lambda_i \mu_j$ . Therefore, the number of eigenvalue is  $n \times m$ . And the trace of a Kronecker product follows

$$\text{Tr}(\mathbf{A} \otimes \mathbf{B}) = \text{Tr}(\mathbf{A})\text{Tr}(\mathbf{B}) \quad (\text{A.14})$$

Since the rank of a matrix is equal to the number of non-zero eigenvalue, we have

$$\text{rank}(\mathbf{A} \otimes \mathbf{B}) = \text{rank}(\mathbf{A})\text{rank}(\mathbf{B}) \quad (\text{A.15})$$

For rectangular matrices, we consider the singular values. Given rectangular matrices  $\mathbf{A}$  and  $\mathbf{B}$  with their non zeros singular  $\sigma_{\mathbf{A},1}\dots\sigma_{\mathbf{A},N}$  and  $\sigma_{\mathbf{B},1}\dots\sigma_{\mathbf{B},M}$ , the eigenvalue of matrix given by  $\mathbf{A} \otimes \mathbf{B}$  are  $\sigma_{\mathbf{A},i}\sigma_{\mathbf{B},j}$ . Since the rank of a matrix is equal to the number of singular number, for rectangular matrices, we also have the relation mention above in Eq.(A.15).

### A.3 Baker-Campbell-Hausdorff formula

The Baker-Campbell-Hausdorff formula is an important relation for the matrix exponential or more general for Lie algebra. For  $X$  and  $Y$  in the Lie algebra of a Lie group, the solution for  $Z$  determined by

$$e^Z = e^X e^Y \quad (\text{A.16})$$

is given according to Baker-Campbell-Hausdorff formula as

$$Z = X + Y + \frac{1}{2}[X, Y] + \frac{1}{12}([X, [X, Y]] + [Y, [Y, X]]) - \frac{1}{24}[Y, [X, [X, Y]]] + \dots \quad (\text{A.17})$$

where  $[\cdot, \cdot]$  represents the commutation operation.

### A.4 Lie-Trotter-Kato formula

Lie-Trotter-Kato formula also known as Lie product formula or Trotter product formula states for  $A$  and  $B$  in Lie algebra of a Lie group,

$$e^{A+B} = \lim_{N \rightarrow \infty} (e^{A/N} e^{B/N})^N \quad (\text{A.18})$$

This relation can be proven based on the lemma

$$e^{A+B} = e^A e^B + O(\det(A)\det(B)) \quad (\text{A.19})$$

using concept of infinitesimal.

### A.5 Eigenvector of a matrix transpose

This section focus on investigating the relation between the eigenvector of a matrix and its transpose. For a matrix  $\mathbf{A}$ , it can be diagonalized as

$$\mathbf{P}_{\mathbf{A}}^{-1} \mathbf{A} \mathbf{P}_{\mathbf{A}} = \mathbf{D} = \text{diag}(\lambda_1, \dots, \lambda_n) \quad (\text{A.20})$$

with  $\lambda_i$  its  $i$ th eigenvalue and matrix  $\mathbf{P}_A$  built by corresponding eigenvector  $\mathbf{v}_{A,n}$  as

$$\mathbf{P}_A = (\mathbf{v}_{A,1}, \dots, \mathbf{v}_{A,n}) \quad (\text{A.21})$$

If we take the transpose of Eq. (A.20)

$$\mathbf{P}_A^T \mathbf{A}^T \mathbf{P}_A^{-1,T} = \mathbf{D}^T = \mathbf{D}, \quad (\text{A.22})$$

and compare to the diagonalization of  $\mathbf{A}^T$  by setting

$$\mathbf{P}_{A^T}^{-1} = \mathbf{P}_A^T, \quad (\text{A.23})$$

we get

$$\mathbf{P}_{A^T}^{-1} \mathbf{A}^T \mathbf{P}_{A^T} = \mathbf{D} = \text{diag}(\lambda_1, \dots, \lambda_n). \quad (\text{A.24})$$

We can see therefore the transposed matrix share eigenvalues with the initial matrix. However, the corresponded eigenvectors are not the same any more. From Eq. (A.23), we have

$$\mathbf{P}_{A^T} \mathbf{P}_A^T = \mathbf{I}. \quad (\text{A.25})$$

Since the  $\mathbf{P}_A$  and  $\mathbf{P}_{A^T}$  is constructed by their corresponding eigenvectors such as Eq.(A.21), Eq.(A.25) become,

$$(\mathbf{v}_{A^T,1}, \dots, \mathbf{v}_{A^T,n})(\mathbf{v}_{A,1}, \dots, \mathbf{v}_{A,n})^T = \mathbf{I} \quad (\text{A.26})$$

yielding thus,

$$\mathbf{v}_{A^T,i} \cdot \mathbf{v}_{A,j} = \delta_{ij} \quad (\text{A.27})$$

meaning that the eigenvectors  $\mathbf{M}$  and  $\mathbf{M}^T$  associated with different eigenvalues are orthogonal. It implies that if we take a transpose of a matrix, the eigenvector will become the one that orthogonal to eigenvectors associated to all other eigenvalues.

## Appendix B

# Wigner rotation

### B.1 Relativistic addition of velocities

In order to introduce the Wigner rotation, let us first look at the relativistic addition of velocity. Considering a Lorentz transform with a velocity  $v$  along  $x$  direction between 2 frames  $\Sigma_0$  and  $\Sigma_1$  (shown in Fig. B.1. (a)) as

$$\begin{pmatrix} ct' \\ x' \\ y' \\ z' \end{pmatrix} = \begin{pmatrix} \gamma & -\gamma\beta & 0 & 0 \\ -\gamma\beta & \gamma & 0 & 0 \\ 0 & 0 & 1 & 0 \\ 0 & 0 & 0 & 1 \end{pmatrix} \begin{pmatrix} ct \\ x \\ y \\ z \end{pmatrix}, \quad (\text{B.1})$$

where  $\gamma$  is the Lorentz factor  $\gamma = (1 - \beta^2)^{-1/2}$  with  $\beta = v/c$ , the velocity of a point P along  $x$ ,  $y$  and  $z$  directions in both frames are then related as

$$u_x = \frac{dx'}{dt'} = \frac{\beta\gamma c dt' + \gamma dx'}{\gamma dt' + \frac{\beta\gamma}{c} dx'} = \frac{u'_x + v}{1 + \frac{\beta}{c} u'_x} \quad (\text{B.2})$$

$$u_y = \frac{dy'}{dt'} = \frac{dy'}{\gamma dt' + \frac{\beta\gamma}{c} dx'} = \frac{u'_y}{\gamma (1 + \frac{\beta}{c} u'_x)} \quad (\text{B.3})$$

$$u_z = \frac{dz'}{dt'} = \frac{dz'}{\gamma dt' + \frac{\beta\gamma}{c} dx'} = \frac{u'_z}{\gamma (1 + \frac{\beta}{c} u'_x)}. \quad (\text{B.4})$$

The total velocity observed in two frames writes

$$\mathbf{u} = u_x \hat{\mathbf{x}} + u_y \hat{\mathbf{y}} + u_z \hat{\mathbf{z}} \quad (\text{B.5})$$

$$\mathbf{u}' = u'_x \hat{\mathbf{x}} + u'_y \hat{\mathbf{y}} + u'_z \hat{\mathbf{z}}, \quad (\text{B.6})$$

respectively with  $\hat{\mathbf{x}}$ ,  $\hat{\mathbf{y}}$  and  $\hat{\mathbf{z}}$  the unitary vector along  $x$ ,  $y$  and  $z$  directions and  $\mathbf{v} = v\hat{\mathbf{x}}$ . By observing the expression in Eq. (B.2)-(B.4), the total velocity can be decomposed into two parts: one is the component along the velocity of the transformation  $\mathbf{u}_{\parallel}$  ( $\mathbf{u}_{\parallel} = u_x \hat{\mathbf{x}}$ ) and the other is the the one perpendicular to the velocity of the transformation  $\mathbf{u}_{\perp}$



( $\mathbf{u}_\perp = u_y \hat{\mathbf{y}} + u_z \hat{\mathbf{z}}$ ). Using Eq. (B.2)-(B.4), the parallel and perpendicular components are written as:

$$\mathbf{u}_\parallel = u_x \hat{\mathbf{x}} = \frac{\mathbf{u}'_\parallel + \mathbf{v}}{1 + \mathbf{u}'_\parallel \cdot \mathbf{v}/c^2} \quad (\text{B.7})$$

$$\mathbf{u}_\perp = u_y \hat{\mathbf{y}} + u_z \hat{\mathbf{z}} = \frac{\mathbf{u}'_\perp}{\gamma \left(1 + \mathbf{u}'_\parallel \cdot \mathbf{v}/c^2\right)}. \quad (\text{B.8})$$

Then the total velocity of point P observed in  $\Sigma_0$  expressed as a function of the velocity of frame  $\Sigma_1$  in  $\Sigma_0$  identified as the transformation velocity  $\mathbf{v}$  and the velocity of P observed in  $\Sigma_1$   $\mathbf{u}'$  writes

$$\mathbf{u} = \mathbf{u}_\parallel + \mathbf{u}_{\text{perp}} = \frac{1}{1 + \mathbf{u}'_\parallel \cdot \mathbf{v}/c^2} \left[ \mathbf{v} + \frac{1}{\gamma} \mathbf{u}' + \left(1 - \frac{1}{\gamma}\right) \mathbf{u}'_\parallel \right] \quad (\text{B.9})$$

using  $\mathbf{u}'_\parallel = \frac{\mathbf{v} \cdot \mathbf{u}'}{\|\mathbf{v}\|^2} \mathbf{v}$  and  $\mathbf{u}'_\parallel \cdot \mathbf{v} = \mathbf{u}' \cdot \mathbf{v}$ ,

$$\mathbf{u} = \frac{1}{1 + \mathbf{u}' \cdot \mathbf{v}/c^2} \left[ \mathbf{v} + \frac{1}{\gamma} \mathbf{u}' + \left(1 - \frac{1}{\gamma}\right) \frac{\mathbf{v} \cdot \mathbf{u}'}{\|\mathbf{v}\|^2} \mathbf{v} \right] = \mathbf{v} \oplus \mathbf{u}', \quad (\text{B.10})$$

with the configuration showing in Fig. B.1 (a) from which can be considered as an addition of velocity between  $\mathbf{v}$  and  $\mathbf{u}'$  related by the relativistic addition of velocity noted as  $\oplus$ . In general, this formula of velocity addition is understood as a velocity  $\mathbf{u}$  measured in the initial frame  $\Sigma_0$  is obtained by a relativistic addition between an arbitrary velocity  $\mathbf{v}_1$  and the velocity  $\mathbf{v}_2$  measured in a co-moving frame with a velocity  $\mathbf{v}_1$  with respect to the initial frame as

$$\mathbf{u} = \mathbf{v}_1 \oplus \mathbf{v}_2 = \frac{1}{1 + \mathbf{v}_1 \cdot \mathbf{v}_2/c^2} \left[ \left(1 + \frac{\gamma_{\mathbf{v}_1}}{c^2(1 - \gamma_{\mathbf{v}_1})} \mathbf{v}_1 \cdot \mathbf{v}_2\right) \mathbf{v}_1 + \frac{1}{\gamma_{\mathbf{v}_1}} \mathbf{v}_2 \right] \quad (\text{B.11})$$

where  $\gamma_{\mathbf{v}_1}$  is the Lorentz factor associated with  $\mathbf{v}_1$ . From this expression, we can see some properties of relativistic addition of velocities. This addition is not linear, so

$$a_1 \mathbf{v}_1 \oplus a_2 \mathbf{v}_2 \neq a_1 a_2 \mathbf{v}_1 \oplus \mathbf{v}_2, \quad (\text{B.12})$$

we have however

$$(-\mathbf{v}_1) \oplus (-\mathbf{v}_2) = -(\mathbf{v}_1 \oplus \mathbf{v}_2), \quad (\text{B.13})$$

Also this addition is generally not commutable

$$\mathbf{v}_1 \oplus \mathbf{v}_2 \neq \mathbf{v}_2 \oplus \mathbf{v}_1 \quad (\text{B.14})$$

Another important property derived in [139] is that for the norm of the addition, one has

$$\|\mathbf{v}_1 \oplus \mathbf{v}_2\|^2 = \|\mathbf{v}_2 \oplus \mathbf{v}_1\|^2. \quad (\text{B.15})$$

Finally, the Lorentz factor  $\gamma$  associated with the relativistic addition  $\mathbf{v}_1 \oplus \mathbf{v}_2$  writes

$$\gamma_{\mathbf{v}_1 \oplus \mathbf{v}_2} = \gamma_{\mathbf{v}_1} \gamma_{\mathbf{v}_2} \left( 1 + \frac{\mathbf{v}_1 \cdot \mathbf{v}_2}{c^2} \right) \quad (\text{B.16})$$

## B.2 2 successive non-collinear Lorentz boosts

Now let us consider the effect of 2 successive non-collinear single Lorentz transformation recognized as a Lorentz boost. First of all, a single Lorentz transformation denoted as a boost matrix  $\mathbf{B}(\mathbf{v})$  associated with a velocity  $\mathbf{v}$  can be written in several ways as

$$\mathbf{B}(\mathbf{v}) = \exp(-\boldsymbol{\zeta} \cdot \mathbf{K}) = \exp\left(-\tanh^{-1}\left(\frac{\mathbf{v}}{c}\right) \cdot \mathbf{K}\right) = \begin{pmatrix} \gamma_{\mathbf{v}} & -\frac{\gamma_{\mathbf{v}}}{c} \mathbf{v}^T \\ -\frac{\gamma_{\mathbf{v}}}{c} \mathbf{v} & \mathbf{I} + \frac{\gamma_{\mathbf{v}}^2}{\gamma_{\mathbf{v}}+1} \frac{\mathbf{v} \mathbf{v}^T}{c^2} \end{pmatrix} \quad (\text{B.17})$$

where  $\boldsymbol{\zeta}$  is the rapidity associated with velocity  $\mathbf{v}$  and  $\mathbf{K}$  represents the generator set vector for boost in  $\text{SO}^+(1,3)$  group ( $\mathbf{K} = (\mathbf{K}_1, \mathbf{K}_2, \mathbf{K}_3)$ ) as shown in Eq. (3.23). With this expression, the result of the 2 successive Lorentz boosts is written as a product of 2 boost matrix with different velocities:  $\mathbf{v}_1$ , the velocity of  $\Sigma_1$  measured in  $\Sigma_0$  and  $\mathbf{v}_2$ , the velocity of  $\Sigma_2$  measured in  $\Sigma_1$ . The general setting of this 2 non-collinear successive Lorentz transformation is shown in Fig. B.1(b). The resulting transformation  $\boldsymbol{\Lambda}$  is then written as

$$\boldsymbol{\Lambda} = \mathbf{B}(\mathbf{v}_2) \mathbf{B}(\mathbf{v}_1) = \begin{pmatrix} \gamma_{tot} & -\mathbf{a}_1^T \\ -\mathbf{a}_2 & \mathbf{M}_3 \end{pmatrix} \quad (\text{B.18})$$

with

$$\gamma_{tot} = \gamma_{\mathbf{v}_1 \oplus \mathbf{v}_2} = \gamma_{\mathbf{v}_1} \gamma_{\mathbf{v}_2} \left( 1 + \frac{\mathbf{v}_1 \cdot \mathbf{v}_2}{c^2} \right) \quad (\text{B.19})$$

$$\mathbf{a}_1 = \frac{\gamma_{tot}}{c} \mathbf{v}_1 \oplus \mathbf{v}_2, \quad \mathbf{a}_2 = \frac{\gamma_{tot}}{c} \mathbf{v}_2 \oplus \mathbf{v}_1 \quad (\text{B.20})$$

$$\mathbf{M}_3 = \gamma_{\mathbf{v}_1} \gamma_{\mathbf{v}_2} \frac{\mathbf{v}_2 \mathbf{v}_2^T}{c^2} + \left( \mathbf{I} + \frac{\gamma_{\mathbf{v}_2}^2}{\gamma_{\mathbf{v}_2}+1} \frac{\mathbf{v}_2 \mathbf{v}_2^T}{c^2} \right) \left( \mathbf{I} + \frac{\gamma_{\mathbf{v}_1}^2}{\gamma_{\mathbf{v}_1}+1} \frac{\mathbf{v}_1 \mathbf{v}_1^T}{c^2} \right) \quad (\text{B.21})$$

From this expression, we can first see that  $\boldsymbol{\Lambda}$  can not be written as a single Lorentz boost shown in Eq.(B.17). Therefore, 2 successive non-collinear Lorentz transformations are not equal to a single Lorentz transformation associated with the relativistic addition of the 2 velocities which reads

$$\mathbf{B}(\mathbf{v}_1 \oplus \mathbf{v}_2) \neq \mathbf{B}(\mathbf{v}_2) \mathbf{B}(\mathbf{v}_1) \quad (\text{B.22})$$

Therefore, we can see that the boost transformation can not itself describe all Lorentz transformations. In order to find the other elementary operations that close the group, we take the exponential expression of the boost transformation shown in Eq.(B.17), and write the product of 2 single boosts as

$$\mathbf{B}(\mathbf{v}_2)\mathbf{B}(\mathbf{v}_1) = \exp(-\boldsymbol{\zeta}_2 \cdot \mathbf{K}) \exp(-\boldsymbol{\zeta}_1 \cdot \mathbf{K}) = \exp(\boldsymbol{\lambda}) \quad (\text{B.23})$$

where  $\boldsymbol{\zeta}_1$  and  $\boldsymbol{\zeta}_2$  are the rapidity associated with  $v_1$  and  $v_2$ , respectively and

$$\boldsymbol{\lambda} = -\boldsymbol{\zeta}_2 \cdot \mathbf{K} + -\boldsymbol{\zeta}_1 \cdot \mathbf{K} + \frac{1}{2}[\boldsymbol{\zeta}_2 \cdot \mathbf{K}, \boldsymbol{\zeta}_1 \cdot \mathbf{K}] + \dots \quad (\text{B.24})$$

according to the Baker-Campbell-Hausdorff formula. This expression then reveals the commutator between the generator of boost  $[\mathbf{K}_i, \mathbf{K}_j]$ , where within the framework of  $\text{SO}^+(1,3)$  group, this commutator gives the generator for rotation as discussed in Chapter 3. Together with the rotation generators, they form a Lie algebra which is closed with respect to commutation. The total Lorentz transformation resulting from 2 successive non-collinear single boosts can be certainly decomposed into a single boost and a rotation called Wigner rotation (also known as Thomas rotation or Thomas Wigner rotation).

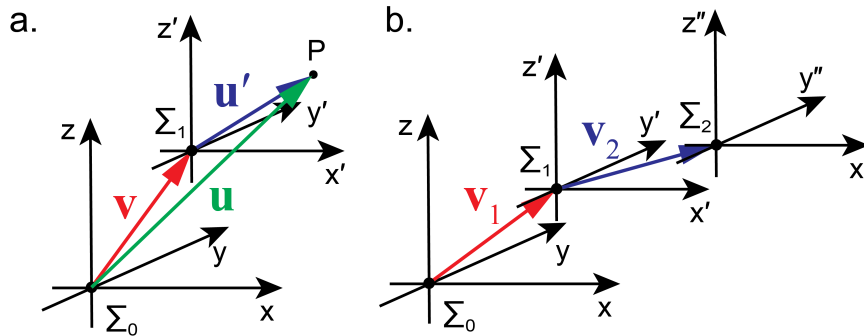


FIGURE B.1: (a) displays the geometric relation among velocity of a point P in frame  $\Sigma_0$  noted  $\mathbf{u}$  and in frame  $\Sigma_1$  noted  $\mathbf{u}'$  and the velocity of the frame  $\Sigma_1$  measured in  $\Sigma_0$ ,  $\mathbf{v}$ . (b) shows the geometric set of 2 successive non-collinear Lorentz transformation with  $\mathbf{v}_1$  the velocity of frame  $\Sigma_1$  measured in frame  $\Sigma_0$  and  $\mathbf{v}_2$  the velocity of frame  $\Sigma_2$  measured in frame  $\Sigma_1$ .

### B.3 Wigner rotation

By introducing rotation operation, Lorentz transformation resulted from 2 successive non-collinear boost can therefore be decomposed either by a boost associated with a velocity  $\mathbf{v}_1 \oplus \mathbf{v}_2$  followed by a rotation  $\mathbf{R}(\boldsymbol{\theta})$  as shown in Fig. B.2 (a) or a rotation  $\mathbf{R}(\boldsymbol{\theta})$  followed by a boost associated with a velocity  $\mathbf{v}_2 \oplus \mathbf{v}_1$  as shown in Fig. B.2 (b), expressed

as [60]

$$\mathbf{B}(\mathbf{v}_2)\mathbf{B}(\mathbf{v}_1) = \mathbf{R}(\boldsymbol{\theta})\mathbf{B}(\mathbf{v}_1 \oplus \mathbf{v}_2) = \mathbf{B}(\mathbf{v}_2 \oplus \mathbf{v}_1)\mathbf{R}(\boldsymbol{\theta}), \quad (\text{B.25})$$

with  $\boldsymbol{\theta} = \theta \hat{\mathbf{n}}$  where  $\theta$  is the angle of rotation calculated according to [140]

$$\theta = \cos^{-1} \left[ \frac{(1 + \gamma_{tot} + \gamma_{\mathbf{v}_1} + \gamma_{\mathbf{v}_2})^2}{(1 + \gamma_{tot})(1 + \gamma_{\mathbf{v}_1})(1 + \gamma_{\mathbf{v}_2})} - 1 \right] \quad (\text{B.26})$$

and  $\hat{\mathbf{n}}$  is the unitary vector of rotation axis

$$\hat{\mathbf{n}} = \frac{\mathbf{v}_1 \times \mathbf{v}_2}{\|\mathbf{v}_1 \times \mathbf{v}_2\|} \quad (\text{B.27})$$

revealing the rotation is in the plane formed by  $\mathbf{v}_1$  and  $\mathbf{v}_2$ .

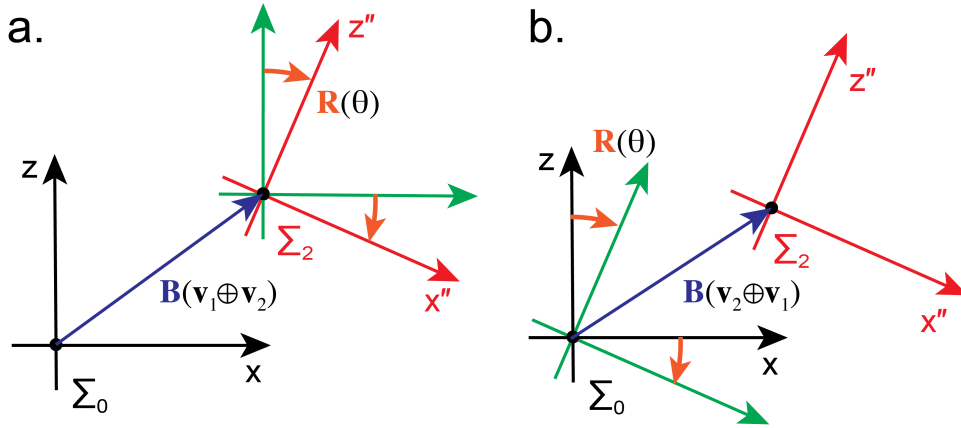


FIGURE B.2: (a) and (b) show the decomposition of a Lorentz transformation resulted from 2 successive non-collinear boost with different order between a boost and a rotation.

Moreover, giving in general a matrix associated with an arbitrary Lorentz transformation with block matrix form written in Eq. (B.18), the decomposition into a rotation and a boost can be written directly with the block matrix parts as

$$\boldsymbol{\Lambda} = \mathbf{B}(\mathbf{v}_2)\mathbf{B}(\mathbf{v}_1) = \mathbf{R}(\boldsymbol{\theta})\mathbf{B}(c\mathbf{a}_1/\gamma) = \mathbf{B}(c\mathbf{a}_2/\gamma)\mathbf{R}(\boldsymbol{\theta}). \quad (\text{B.28})$$

## B.4 Generalization in Lorentz ( $SO^+(1,3)$ ) group

This can be generalized to any matrix in the  $SO^+(1,3)$  group. Any  $SO^+(1,3)$  group matrix

$$\boldsymbol{\Lambda} = \begin{pmatrix} 1 & -\mathbf{a}^T \\ -\mathbf{c} & \mathbf{m}_3 \end{pmatrix}, \quad (\text{B.29})$$

can be decomposed into a rotation type and boost type matrix as

$$\mathbf{\Lambda} = \mathbf{B}_1 \mathbf{R} = \mathbf{R} \mathbf{B}_2 \quad (\text{B.30})$$

where

$$\mathbf{B}_1 = \exp(-(\tanh^{-1} \mathbf{c}) \cdot \mathbf{K}), \quad (\text{B.31})$$

$$\mathbf{B}_2 = \exp(-(\tanh^{-1} \mathbf{a}) \cdot \mathbf{K}) \quad (\text{B.32})$$

and

$$\mathbf{R} = \exp(\tanh^{-1} \mathbf{c} \cdot \mathbf{K}) \cdot \mathbf{\Lambda} = \mathbf{\Lambda} \cdot \exp(\tanh^{-1} \mathbf{a} \cdot \mathbf{K}). \quad (\text{B.33})$$

## Appendix C

# Non-depolarizing and depolarizing planar chirality

In this section, we discuss the difference between non-depolarizing and depolarizing planar (2D) chirality. As we discussed in Chapter 3, a non-depolarizing 2D chirality can be built by a differential Mueller matrix with non-collinear linear birefringence and dichroism vectors. The differential Mueller matrix of a typical 2D chiral medium is presented in Table. 3.1

$$m_{2D,nd} = \begin{pmatrix} 0 & a & k_1a & 0 \\ a & 0 & 0 & k_2b \\ k_1a & 0 & 0 & -b \\ 0 & -k_2b & b & 0 \end{pmatrix} \quad (\text{C.1})$$

with the birefringence vector  $\mathbf{b}$  and dichroism vector  $\mathbf{d}$  written as

$$\mathbf{b} = (b, k_2b, 0)^T, \quad \mathbf{d} = (-a, -k_1a, 0)^T. \quad (\text{C.2})$$

The general form of depolarizing 2D chirality is

$$\begin{aligned} m_{2D,d} &= \begin{pmatrix} 0 & a & k_1a & -q \\ a & -p_1 & \mu & k_2b \\ k_1a & \mu & -p_2 & -b \\ q & -k_2b & b & -p_3 \end{pmatrix} \\ &= \begin{pmatrix} 0 & a & k_1a & 0 \\ a & 0 & 0 & k_2b \\ k_1a & 0 & 0 & -b \\ 0 & -k_2b & b & 0 \end{pmatrix} + \begin{pmatrix} 0 & 0 & 0 & -q \\ 0 & -p_1 & \mu & 0 \\ 0 & \mu & -p_2 & 0 \\ q & 0 & 0 & -p_3 \end{pmatrix} = \mathbf{m}_{nd} + \mathbf{m}_d \end{aligned} \quad (\text{C.3})$$

which can be decomposed into a non-depolarizing part and a depolarizing part.

For a depolarizing medium caused by spatial inhomogeneity, the non-depolarizing part  $\mathbf{m}_{nd}$  results from the average of this inhomogeneity as discussed in Chapter 3 in Eq. (3.71). By engineering the inhomogeneity, we can make the  $\mathbf{m}_{nd}$  matrix to be zero matrix at the

same time  $q$  is non-zero, yielding the total matrix purely depolarizing. An example is shown in Chapter 3 (Fig. 3.9) and we look at this example in detail here. First, the "L" shaped structure is a typical elementary 2D chiral structure modeled by non-collinear linear birefringence and dichroism vector as mentioned in Eq. (C.2). Now let consider the construction of inhomogeneity. The simplest way is, instead of arranging the elementary 2D chiral structure along the same orientation, to arrange them with different orientation. So the rotated birefringence and dichroism vector with an angle  $\theta_d$  is then written as

$$\mathbf{d}_d = \begin{pmatrix} a \cos 2\theta_d + k_1 a \sin 2\theta_d \\ -a \sin 2\theta_d + k_1 a \cos 2\theta_d \\ 0 \end{pmatrix}, \mathbf{b}_d = \begin{pmatrix} b \cos 2\theta_d + k_2 b \sin 2\theta_d \\ -b \sin 2\theta_d + k_2 b \cos 2\theta_d \\ 0 \end{pmatrix} \quad (\text{C.4})$$

In order to make the non-depolarizing part to be a zero matrix, the average of the  $\cos 2\theta_d$  and  $\sin 2\theta_d$  within the beam cross section is zero. One simple case is to form a cycle of  $N$  elementary 2D structure with each time a rotation of  $\pi/N$ . For example, we set a 2D chiral medium resulted from a total linear birefringence ( $LB$ ) of 0.8, and total linear dichroism ( $LD$ ) of 0.6 and the angle between the birefringence and dichroism vector of  $30^\circ$ . The non-depolarizing cumulative differential and total Mueller matrix of a homogeneous arrangement of this elementary 2D structure is

$$\mathbf{m}_{2D,nd} = \begin{pmatrix} 0 & -0.6000 & 0 & 0 \\ -0.6000 & 0 & 0 & -0.2438 \\ 0 & 0 & 0 & 0.7619 \\ 0 & 0.2438 & -0.7619 & 0 \end{pmatrix}, \quad (\text{C.5})$$

$$\mathbf{M}_{2D,nd} = \exp(\mathbf{m}_{2D,nd}) = \begin{pmatrix} 1.0000 & -0.5324 & -0.0155 & 0.0604 \\ -0.5324 & 0.9755 & -0.0767 & -0.1967 \\ -0.0155 & -0.0767 & 0.6120 & 0.5767 \\ -0.0604 & 0.1967 & -0.5767 & 0.5874 \end{pmatrix}, \quad (\text{C.6})$$

which corresponds to a typical 2D non-depolarizing Mueller matrix. And if we set the inhomogeneity by a cycle of 4 elementary 2D structures with each time a  $45^\circ$  ( $\pi/4$ ) rotation, the depolarizing Mueller matrix of 2D chirality here writes,

$$\mathbf{m}_{2D,d} = \begin{pmatrix} 0 & 0 & 0 & 0.2078 \\ 0 & -0.2500 & 0 & 0 \\ 0 & 0 & -0.2500 & 0 \\ -0.2078 & 0 & 0 & -0.5000 \end{pmatrix}, \quad (\text{C.7})$$

$$\mathbf{M}_{2D,d} = \exp(\mathbf{m}_{2D,d}) = \begin{pmatrix} 1.0000 & 0 & 0 & 0.1654 \\ 0 & 0.7934 & 0 & 0 \\ 0 & 0 & 0.7934 & 0 \\ -0.1654 & 0 & 0 & 0.6020 \end{pmatrix}. \quad (\text{C.8})$$

Compared to the non-depolarizing 2D chirality, this depolarizing 2D chiral medium has an in-plane rotation symmetry which means this medium is isotropic. It provides also completely different polarization dynamics with the non-depolarizing one. Especially, for a fully non-polarized incident light, this depolarizing 2D chiral medium can give a depolarized purely circular polarized light without linear component.





## Appendix D

# General multivariate linear regression

In this appendix, we introduce the standard procedure for solving and evaluating a Multivariate linear regression.

### D.1 General form

Considering here the form of general linear dependence,

$$y = a_0 + a_1x_1 + \dots + a_px_p + \epsilon \quad (\text{D.1})$$

where  $y$  depends on  $p$  different variables  $x_i$  with their associated parameter  $a_i$  and  $\epsilon$  gives the residue. And the expected value of  $y$  is

$$E(y) = a_0 + a_1x_1 + \dots + a_px_p \quad (\text{D.2})$$

giving the theoretical prediction of the linear regression. In this case, the variable associated with an observables  $y_i$  is a vector  $(1, x_{1i}, \dots, x_{1p})$ . In order to facilitate the notation, the matrix representation of this regression for different observable  $y_i$  is then written as

$$\mathbf{y} = \mathbf{X}\mathbf{a} + \boldsymbol{\epsilon} \quad (\text{D.3})$$

with

$$\mathbf{y} = \begin{pmatrix} y_1 \\ y_2 \\ \vdots \\ y_n \end{pmatrix}, \mathbf{X} = \begin{pmatrix} 1 & x_{11} & \cdots & x_{1p} \\ 1 & x_{21} & \cdots & x_{2p} \\ \vdots & \vdots & \ddots & \vdots \\ 1 & x_{n1} & \cdots & x_{np} \end{pmatrix}, \mathbf{a} = \begin{pmatrix} a_1 \\ a_2 \\ \vdots \\ a_b \end{pmatrix}, \boldsymbol{\epsilon} = \begin{pmatrix} \epsilon_1 \\ \epsilon_2 \\ \vdots \\ \epsilon_n \end{pmatrix} \quad (\text{D.4})$$

where  $\epsilon_i \sim N(0, \sigma^2)$ ,  $\text{rank}(\mathbf{X}) = p + 1$  and  $x_1 \dots x_p$  are not random variables.

## D.2 Least square estimation

To get the estimate of parameter vector  $\mathbf{a}$  noted as  $\hat{\mathbf{a}}$  from Eq.(D.3), we use the least square estimation by minimizing the residue  $\boldsymbol{\rho}^T \boldsymbol{\rho}$  where  $\boldsymbol{\rho}$  results from a given set of parameter vector estimate  $\hat{\mathbf{a}}$  as

$$\boldsymbol{\rho} = \mathbf{y} - \mathbf{X}\hat{\mathbf{a}}. \quad (\text{D.5})$$

Therefore, in order to let

$$\boldsymbol{\rho}^T \boldsymbol{\rho} = (\mathbf{y} - \mathbf{X}\hat{\mathbf{a}})^T \cdot (\mathbf{y} - \mathbf{X}\hat{\mathbf{a}}), \quad (\text{D.6})$$

be minimum, the derivative with respect to the parameter vector of this expression must be zero,

$$d [(\mathbf{y} - \mathbf{X}\mathbf{a})^T \cdot (\mathbf{y} - \mathbf{X}\mathbf{a})] = 0 \quad (\text{D.7})$$

that is:

$$(\hat{\mathbf{a}}^T \mathbf{X}^T \mathbf{X} - \mathbf{y}^T \mathbf{X}) \cdot d\hat{\mathbf{a}} + d\hat{\mathbf{a}}^T \cdot (\mathbf{X}^T \mathbf{X}\hat{\mathbf{a}} - \mathbf{X}^T \mathbf{y}) = 0 \quad (\text{D.8})$$

leading to

$$\hat{\mathbf{a}} = (\mathbf{X}^T \mathbf{X})^{-1} \mathbf{X}^T \cdot \mathbf{y}, \quad (\text{D.9})$$

where  $\hat{\mathbf{a}}$  is the final least square estimation of  $\mathbf{a}$  which can be obtained directly by left-multiply the matrix  $(\mathbf{X}^T \mathbf{X})^{-1} \mathbf{X}^T$ , on the observable vector  $\mathbf{y}$ . Here we can define a matrix called hat matrix (projection matrix)  $\mathbf{H}$

$$\mathbf{H} = \mathbf{X}(\mathbf{X}^T \mathbf{X})^{-1} \mathbf{X}^T, \quad (\text{D.10})$$

so that the regression relation become

$$\mathbf{y} = \mathbf{X}\hat{\mathbf{a}} + \boldsymbol{\rho} = \mathbf{H}\mathbf{y} + \boldsymbol{\rho}. \quad (\text{D.11})$$

And we can see this  $\mathbf{H}$  matrix is symmetric ( $\mathbf{H}^T = \mathbf{H}$ ) and  $\mathbf{H}^n = \mathbf{H}$ .

## D.3 Unbiased estimation of variance

Now we investigate the unbiased estimation of total variance  $\sigma^2$  which is determined by the intrinsic residue vector as

$$\sigma^2 = \frac{1}{n} \sum_{i=1}^n \epsilon_i^2 = \frac{1}{n} \boldsymbol{\epsilon}^T \boldsymbol{\epsilon} = \langle \boldsymbol{\epsilon}^T \boldsymbol{\epsilon} \rangle. \quad (\text{D.12})$$

To get the unbiased estimate of  $\sigma^2$ , we need to establish the relation between the total residue  $\boldsymbol{\rho}^T \boldsymbol{\rho}$  and the  $\boldsymbol{\epsilon}^T \boldsymbol{\epsilon}$ . Starting from

$$\begin{aligned} \boldsymbol{\rho}^T \boldsymbol{\rho} &= (\mathbf{y} - \mathbf{X}\hat{\mathbf{a}})^T (\mathbf{y} - \mathbf{X}\hat{\mathbf{a}}) = (\mathbf{y} - \mathbf{H}\mathbf{y})^T (\mathbf{y} - \mathbf{H}\mathbf{y}) \\ &= \mathbf{y}^T (\mathbf{I} - \mathbf{H})^T (\mathbf{I} - \mathbf{H}) \mathbf{y} = \mathbf{y}^T (\mathbf{I} - \mathbf{H}) \mathbf{y}, \end{aligned} \quad (\text{D.13})$$

by substituting  $\mathbf{y} = \mathbf{X}\mathbf{a} + \boldsymbol{\epsilon}$

$$\begin{aligned} \boldsymbol{\rho}^T \boldsymbol{\rho} &= (\mathbf{X}\mathbf{a} + \boldsymbol{\epsilon})^T (\mathbf{I} - \mathbf{H}) (\mathbf{X}\mathbf{a} + \boldsymbol{\epsilon}) \\ &= \mathbf{a}^T \mathbf{X}^T (\mathbf{I} - \mathbf{H}) \mathbf{X} \mathbf{a} + \boldsymbol{\epsilon}^T (\mathbf{I} - \mathbf{H}) \mathbf{X} \mathbf{a} + \mathbf{a}^T \mathbf{X}^T (\mathbf{I} - \mathbf{H}) \boldsymbol{\epsilon} + \boldsymbol{\epsilon}^T (\mathbf{I} - \mathbf{H}) \boldsymbol{\epsilon}, \end{aligned} \quad (\text{D.14})$$

as it is easy to show that  $(\mathbf{I} - \mathbf{H})\mathbf{X} = \mathbf{0}$ , we have finally

$$\boldsymbol{\rho}^T \boldsymbol{\rho} = \boldsymbol{\epsilon}^T (\mathbf{I} - \mathbf{H}) \boldsymbol{\epsilon}. \quad (\text{D.15})$$

Then we can take the average over this relation

$$\langle \boldsymbol{\rho}^T \boldsymbol{\rho} \rangle = \langle \boldsymbol{\epsilon}^T (\mathbf{I} - \mathbf{H}) \boldsymbol{\epsilon} \rangle \quad (\text{D.16})$$

Since the final average is a scalar, it is equivalent to take the trace of the product:

$$\langle \boldsymbol{\rho}^T \boldsymbol{\rho} \rangle = \langle \text{Tr}(\boldsymbol{\epsilon}^T (\mathbf{I} - \mathbf{H}) \boldsymbol{\epsilon}) \rangle = \langle \text{Tr}((\mathbf{I} - \mathbf{H}) \boldsymbol{\epsilon} \boldsymbol{\epsilon}^T) \rangle = \text{Tr}((\mathbf{I} - \mathbf{H}) \langle \boldsymbol{\epsilon} \boldsymbol{\epsilon}^T \rangle) \quad (\text{D.17})$$

where  $\langle \boldsymbol{\epsilon} \boldsymbol{\epsilon}^T \rangle$  is the covariance matrix of  $\boldsymbol{\epsilon}$ . As  $\langle \epsilon_i^2 \rangle = \sigma^2$  and  $\langle \epsilon_i \epsilon_j \rangle = \delta_{ij}$ , so the covariance matrix of  $\boldsymbol{\epsilon}$  is  $\sigma^2 \mathbf{I}$ . Therefore,

$$\langle \boldsymbol{\rho}^T \boldsymbol{\rho} \rangle = \sigma^2 \text{Tr}((\mathbf{I} - \mathbf{H})) = \sigma^2 [n - (p + 1)] \quad (\text{D.18})$$

This way, an unbiased estimation ( $\hat{\sigma}^2$ ) of total variance  $\sigma^2$  is given by

$$\hat{\sigma}^2 = \frac{\boldsymbol{\rho}^T \boldsymbol{\rho}}{n - p - 1} \quad (\text{D.19})$$

where  $n$  is the number of observables ( $y_i$ ) and  $p$  is the number of the variable ( $x_j$ ) in this linear relation.

As for the variance for each parameter  $a_i$ , we look at first its covariance matrix. The expected value of the  $\hat{\mathbf{a}}$  is obviously  $\mathbf{a}$ , and the covariance matrix is written as

$$\text{cov}(\hat{\mathbf{a}}) = \langle (\hat{\mathbf{a}} - \mathbf{a})(\hat{\mathbf{a}} - \mathbf{a})^T \rangle, \quad (\text{D.20})$$

knowing that

$$\hat{\mathbf{a}} = (\mathbf{X}^T \mathbf{X})^{-1} \mathbf{X}^T \mathbf{y} \quad (\text{D.21})$$

we have then,

$$\text{cov}(\hat{\mathbf{a}}) = (\mathbf{X}^T \mathbf{X})^{-1} \mathbf{X}^T \cdot \text{cov}(\mathbf{y}) \cdot \mathbf{X} (\mathbf{X}^T \mathbf{X})^{-1}, \quad (\text{D.22})$$

using

$$\text{cov}(\mathbf{y}) = \langle (\mathbf{y} - \langle \mathbf{y} \rangle)(\mathbf{y} - \langle \mathbf{y} \rangle)^T \rangle = \langle (\mathbf{y} - \mathbf{X}\mathbf{a})(\mathbf{y} - \mathbf{X}\mathbf{a})^T \rangle = \langle \boldsymbol{\epsilon}\boldsymbol{\epsilon}^T \rangle = \sigma^2 \mathbf{I}, \quad (\text{D.23})$$

the covariance matrix of the parameter becomes then

$$\text{cov}(\hat{\mathbf{a}}) = \sigma^2 (\mathbf{X}^T \mathbf{X})^{-1}. \quad (\text{D.24})$$

Thus

$$\text{cov}(\hat{a}_i, \hat{a}_j) = \langle (\hat{a}_i - a_i)(\hat{a}_j - a_j) \rangle = \sigma^2 c_{ij}, \quad (\text{D.25})$$

where  $c_{ij}$  is the matrix element of  $(\mathbf{X}^T \mathbf{X})^{-1}$ . Finally, we get the distribution for a given parameter:  $\hat{a}_i \sim N(a_i, c_{ii}\sigma^2)$ , and the unbiased estimation of variance for  $i$ th parameter  $a_i$  is given by

$$\hat{\sigma}_i^2 = c_{ii}\hat{\sigma}^2 = c_{ii} \frac{\boldsymbol{\rho}^T \boldsymbol{\rho}}{n - p - 1}. \quad (\text{D.26})$$

with  $c_{ii}$  the  $i$ th diagonal element of matrix  $(\mathbf{X}^T \mathbf{X})^{-1}$ .

## D.4 Test of significance

Two major tests of significance of the multivariate regression are introduced in this section which is the test for the regression relation and the parameters.

### D.4.1 Significance test of the regression relation

The significance test of the regression relation is to verify if the relation obtained from this regression is valid. In other words, the parameters of in this relation  $a_i$  are not all zero. In this case, we use a test of hypothesis by setting

$$\mathbf{H}_0 : a_1 = a_2 = \dots = a_p = 0$$

$$\mathbf{H}_1 : a_1, a_2, \dots, a_p \text{ are not all zero.}$$

So, using the condition of hypothesis  $\mathbf{H}_0$ , one can show that

$$\frac{SSR}{\sigma^2} \sim \chi^2(p) \quad (\text{D.27})$$

where  $SSR$  is the sum of squares regression calculated as

$$SSR = \sum_{i=1}^n (\hat{y}_i - \bar{y})^2 \quad (\text{D.28})$$

with  $\hat{y}_i = \sum_{j=1}^n x_{ij} \hat{a}_j$  and  $n\bar{y} = \sum_{i=1}^n y_i$ , and

$$\frac{SSE}{\sigma^2} \sim \chi^2(n - p - 1) \quad (\text{D.29})$$

where  $SSE$  sum of squares error which is  $\boldsymbol{\rho}^T \boldsymbol{\rho}$ . As long as  $SSR$  and  $SSE$  are independent, we can built the parameter for F-test

$$F = \frac{SSR/p}{SSE/(n - p - 1)} \sim F(p, n - p - 1). \quad (\text{D.30})$$

By setting a level of significance  $\alpha$ , if the parameter F calculated constructed by Eq. (D.30) is larger than the value of F-distribution  $F_\alpha(p, n - p - 1)$  at this level  $\alpha$ , the hypothesis  $\mathbf{H}_0$  is then rejected meaning that the regression relation is valid and  $\mathbf{y}$  is linearly dependent with  $\mathbf{X}$ .

## D.4.2 Significance test of parameters

Once the significance of the regression relation is validated, we can look at the significance of each parameter. To do this, the test that needs to be performed is to set

$$\mathbf{H}_{0i} : a_i = 0$$

$$\mathbf{H}_{1i} : a_i \neq 0$$

Since we know that  $\hat{a}_i \sim N(a_i, c_{ii}\sigma^2)$ , we need to construct the test for normal distribution. Since the intrinsic variance  $\sigma$  is not known yet, t test is suitable here. According to the estimated variance of its distribution given in Eq. (D.26), the degree of freedom is  $n - p - 1$ , t-distribution to evaluate and the associated parameter  $t_j$  are

$$t_i = \frac{\hat{a}_i}{\sqrt{c_{ii}\hat{\sigma}}} \sim t(n - p - 1) \quad (\text{D.31})$$

If the  $t_i$  is larger than the corresponding value of  $t(n - p - 1)$  distribution at certain confidence level, the  $\mathbf{H}_0$  is then rejected.

## D.5 Goodness-of-fit

Finally, we can also quantify the quality of the regression, which is the goodness-of-fit. One important parameter is the coefficient of determination  $R^2$  defined as

$$R^2 = \frac{SSR}{SST} \quad (\text{D.32})$$

where  $SST$  is the sum of squares total represent the squared differences between the observables  $y_i$  and its mean as

$$SST = \sum_{i=1}^n (y_i - \langle y_i \rangle)^2. \quad (\text{D.33})$$

The closer to 1  $R^2$  is, the better is the regression.

## Appendix E

# Systematic error and accuracy

The systematic error of our Mueller polarimetry setup can be estimated through the process of solving the Mueller matrix according to the principle of multivariate linear regression. This error on each matrix element is calculated by Eq.(D.26), which will not be eliminated through any number of averaging. The systematic error is different from the statistical error which stems from random fluctuation of the signal during an experiment. Thus the statistical error gives a value for the noise level and the experimental resolution. The systematic error gives a measurement of the level of accuracy of a given experiment.

We show first a comparison of intensity traces between the detected intensity  $I_{out}^k$  and the residue  $\rho_k$  through the experimental protocol (64 acquisitions) in Fig. E.1 (a). With this residue, the systematic error is calculated using Eq. (D.26) for each matrix element at each wavelength. The results are shown in Fig. E.1 (b).

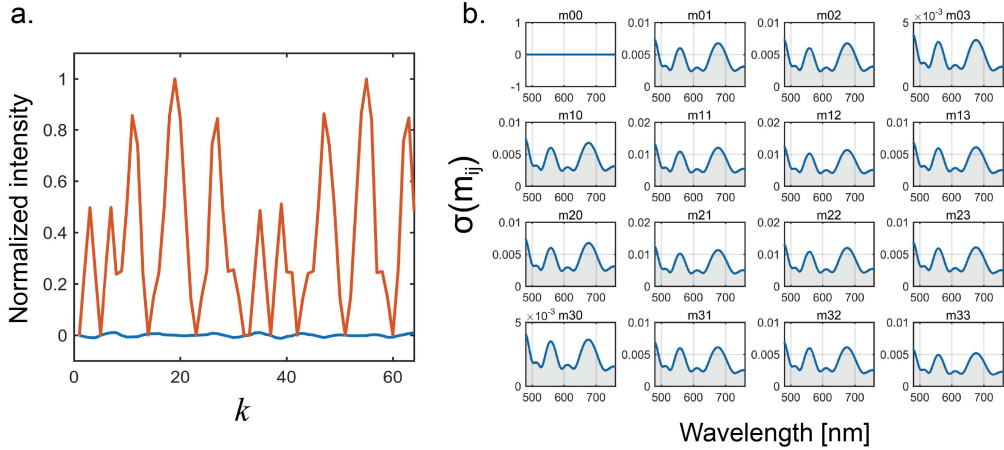


FIGURE E.1: (a) shows the normalized intensity trace of the detected intensity  $I_{out}^k$  (red line) and the residue  $\rho_k$  (blue line) along the time of acquisition  $k$  (from 1 to 64) at wavelength 700 nm. (b) shows the systematic error evaluated by the variance defined in Eq.(D.26) on each matrix element.

We found that using an empty setup, the systematic error is always the same. This error depends on multiple factors but mainly on how polarizers and QWPs are modeled. In our treatment, the polarizer is considered as perfect and the QWPs are modeled by



the HEB approach. However in reality, the real optical components are never perfect and always come with some defects. The theoretical model is implemented in order to approach at best the real case. This is revealed by the deviations of the empty setup matrix from an ideal identity matrix as seen in Fig. 4.8. Therefore, the systematic error depends optical component, as can be seen by looking at the systematic error evaluated for another setup with a different set of polarizers in PSG and PSA, shown in Fig. E.2. We can see that the features in the systematic error are directly associated with the optical components.

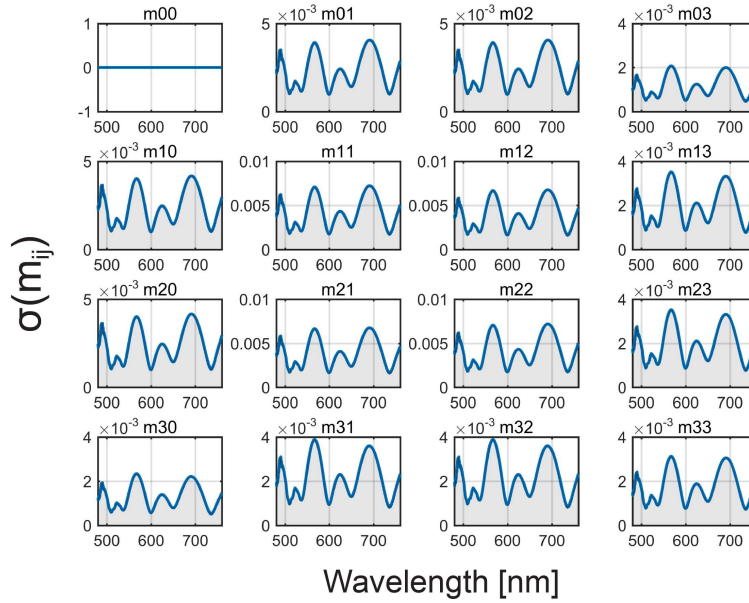


FIGURE E.2: The systematic error evaluated by the variance defined in Eq.(D.26) on each matrix element for a different set of polarizers from the one shown in Fig. E.1.

# Bibliography

- <sup>1</sup>C. Brosseau, *Fundamentals of polarized light: a statistical optics approach* (Wiley-Interscience, 1998).
- <sup>2</sup>C. Huygens, *Treatise on light: in which are explained the causes of that which occurs in reflexion, & in refraction. and particularly in the strange refraction of iceland crystal* (MacMillan and Company, limited, 1912).
- <sup>3</sup>L. D. Barron, *Molecular light scattering and optical activity* (Cambridge University Press, 2009).
- <sup>4</sup>D. H. Goldstein, *Polarized light* (CRC press, 2017).
- <sup>5</sup>W. T. B. Kelvin, *Baltimore lectures on molecular dynamics and the wave theory of light* (CJ Clay and Sons, 1904).
- <sup>6</sup>M. Avalos, R. Babiano, P. Cintas, J. L. Jiménez, and J. C. Palacios, “From parity to chirality: chemical implications revisited”, *Tetrahedron: Asymmetry* **11**, 2845–2874 (2000).
- <sup>7</sup>W Thiemann and W Darge, “Experimental attempts for the study of the origin of optical activity on earth”, in *Cosmochemical evolution and the origins of life* (Springer, 1974), pp. 263–283.
- <sup>8</sup>W. A. Bonner, “Parity violation and the evolution of biomolecular homochirality”, *Chirality: The Pharmacological, Biological, and Chemical Consequences of Molecular Asymmetry* **12**, 114–126 (2000).
- <sup>9</sup>M. M. Green and V. Jain, “Homochirality in life: two equal runners, one tripped”, *Origins of Life and Evolution of Biospheres* **40**, 111 (2010).
- <sup>10</sup>B. Darquié, C. Stoeffler, A. Shelkovnikov, C. Daussy, A. Amy-Klein, C. Chardonnet, S. Zrig, L. Guy, J. Crassous, P. Soulard, et al., “Progress toward the first observation of parity violation in chiral molecules by high-resolution laser spectroscopy”, *Chirality* **22**, 870–884 (2010).
- <sup>11</sup>D. K. Kondepudi, R. J. Kaufman, and N. Singh, “Chiral symmetry breaking in sodium chlorate crystallization”, *Science* **250**, 975–976 (1990).

- <sup>12</sup>C. Viedma, “Chiral symmetry breaking during crystallization: complete chiral purity induced by nonlinear autocatalysis and recycling”, *Physical review letters* **94**, 065504 (2005).
- <sup>13</sup>D. R. Link, G. Natale, R. Shao, J. E. Maclennan, N. A. Clark, E. Körblova, and D. M. Walba, “Spontaneous formation of macroscopic chiral domains in a fluid smectic phase of achiral molecules”, *Science* **278**, 1924–1927 (1997).
- <sup>14</sup>K. Nayani, R. Chang, J. Fu, P. W. Ellis, A. Fernandez-Nieves, J. O. Park, and M. Srinivasarao, “Spontaneous emergence of chirality in achiral lyotropic chromonic liquid crystals confined to cylinders”, *Nature communications* **6**, 1–7 (2015).
- <sup>15</sup>A. R. Palmans and E. e. Meijer, “Amplification of chirality in dynamic supramolecular aggregates”, *Angewandte Chemie International Edition* **46**, 8948–8968 (2007).
- <sup>16</sup>P. J. Stals, P. A. Korevaar, M. A. Gillissen, T. F. de Greef, C. F. Fitié, R. P. Sijbesma, A. R. Palmans, and E. Meijer, “Symmetry breaking in the self-assembly of partially fluorinated benzene-1, 3, 5-tricarboxamides”, *Angewandte Chemie* **124**, 11459–11463 (2012).
- <sup>17</sup>O. Arteaga and B. Kahr, “Mueller matrix polarimetry of bianisotropic materials”, *JOSA B* **36**, F72–F83 (2019).
- <sup>18</sup>M. Tan, W. Jiang, A. T. Martin, A. G. Shtukenberg, M. D. McKee, and B. Kahr, “Polarized light through polycrystalline vaterite helicoids”, *Chemical Communications* (2020).
- <sup>19</sup>A. Pham, Q. Jiang, A. Zhao, J. Bellessa, C. Genet, and A. Drezet, “Manifestation of planar and bulk chirality mixture in plasmonic  $\Lambda$ -shaped nanostructures caused by symmetry breaking defects”, *ACS Photonics* **4**, 2453–2460 (2017).
- <sup>20</sup>S. Buddhiraju, A. Song, G. T. Papadakis, and S. Fan, “Nonreciprocal metamaterial obeying time-reversal symmetry”, *Phys. Rev. Lett.* **124**, 257403 (2020).
- <sup>21</sup>J. Gao, W. Wu, V. Lemaire, A. Carvalho, S. Nlate, T. Buffeteau, R. Oda, Y. Battie, M. Pauly, and E. Pouget, “Tuning the chiroptical properties of elongated nano-objects via hierarchical organization”, *ACS nano* **14**, 4111–4121 (2020).
- <sup>22</sup>T. Verbiest, S. Van Elshocht, M. Kauranen, L. Hellemans, J. Snauwaert, C. Nuckolls, T. J. Katz, and A. Persoons, “Strong enhancement of nonlinear optical properties through supramolecular chirality”, *Science* **282**, 913–915 (1998).
- <sup>23</sup>H. Isla and J. Crassous, “Helicene-based chiroptical switches”, *Comptes Rendus Chimie* **19**, 39–49 (2016).

- <sup>24</sup>H. Isla, M. Srebro-Hooper, M. Jean, N. Vanthuyne, T. Roisnel, J. L. Lunkley, G. Muller, J. G. Williams, J. Autschbach, and J. Crassous, “Conformational changes and chiroptical switching of enantiopure bis-helicenic terpyridine upon Zn 2+ binding”, *Chemical communications* **52**, 5932–5935 (2016).
- <sup>25</sup>J. R. Brandt, X. Wang, Y. Yang, A. J. Campbell, and M. J. Fuchter, “Circularly polarized phosphorescent electroluminescence with a high dissymmetry factor from pholeds based on a platinahelicene”, *Journal of the American Chemical Society* **138**, 9743–9746 (2016).
- <sup>26</sup>M. Liu, L. Zhang, and T. Wang, “Supramolecular chirality in self-assembled systems”, *Chemical reviews* **115**, 7304–7397 (2015).
- <sup>27</sup>R. C. Jones, “A new calculus for the treatment of optical systems: i. description and discussion of the calculus”, *J. Opt. Soc. Am.* **31**, 488–493 (1941).
- <sup>28</sup>R. C. Jones, “A new calculus for the treatment of optical systems: v. a more general formulation, and description of another calculus”, *J. Opt. Soc. Am.* **37**, 107–110 (1947).
- <sup>29</sup>H. Müller, *The foundation of optics* (1948).
- <sup>30</sup>G. G. Stokes, “On the composition and resolution of streams of polarized light from different sources”, *Transactions of the Cambridge Philosophical Society* **9**, 399–416 (1851).
- <sup>31</sup>H. Poincaré, *Théorie Mathématique de la Lumière*, Vol. II (1892).
- <sup>32</sup>E. Wolf et al., *Introduction to the theory of coherence and polarization of light* (Cambridge University Press, 2007).
- <sup>33</sup>E. S. Fry and G. W. Kattawar, “Relationships between elements of the stokes matrix”, *Appl. Opt.* **20**, 2811–2814 (1981).
- <sup>34</sup>J. J. Gil and E. Bernabeu, “Depolarization and polarization indices of an optical system”, *Optica Acta: International Journal of Optics* **33**, 185–189 (1986).
- <sup>35</sup>J. J. Gil and E. Bernabeu, “A depolarization criterion in Mueller matrices”, *Optica Acta: International Journal of Optics* **32**, 259–261 (1985).
- <sup>36</sup>C. R. Givens and A. B. Kostinski, “A simple necessary and sufficient condition on physically realizable Mueller matrices”, *Journal of Modern Optics* **40**, 471–481 (1993).
- <sup>37</sup>S. R. Cloude, “Conditions for the physical realisability of matrix operators in polarimetry”, in *Polarization considerations for optical systems ii*, Vol. 1166 (International Society for Optics and Photonics, 1990), pp. 177–187.
- <sup>38</sup>R. Sridhar and R. Simon, “Normal form for Mueller matrices in polarization optics”, *Journal of modern optics* **41**, 1903–1915 (1994).

- <sup>39</sup>S. R. Cloude, “Physical interpretation of eigenvalue problems in optical scattering polarimetry”, in *Polarization: measurement, analysis, and remote sensing*, Vol. 3121 (International Society for Optics and Photonics, 1997), pp. 88–99.
- <sup>40</sup>F. Boulvert, G. Le Brun, B. Le Jeune, J. Cariou, and L. Martin, “Decomposition algorithm of an experimental Mueller matrix”, *Optics communications* **282**, 692–704 (2009).
- <sup>41</sup>D. G. Anderson and R. Barakat, “Necessary and sufficient conditions for a Mueller matrix to be derivable from a Jones matrix”, *JOSA A* **11**, 2305–2319 (1994).
- <sup>42</sup>S. R. Cloude and E. Pottier, “A review of target decomposition theorems in radar polarimetry”, *IEEE transactions on geoscience and remote sensing* **34**, 498–518 (1996).
- <sup>43</sup>S.-Y. Lu and R. A. Chipman, “Interpretation of Mueller matrices based on polar decomposition”, *JOSA A* **13**, 1106–1113 (1996).
- <sup>44</sup>S. R. Cloude, “Group theory and polarisation algebra”, *Optik (Stuttgart)* **75**, 26–36 (1986).
- <sup>45</sup>S. N. Savenkov, “Principles of the Mueller matrix measurements”, in *Light scattering reviews 9* (Springer, 2015), pp. 213–255.
- <sup>46</sup>S. Alali and I. A. Vitkin, “Polarized light imaging in biomedicine: emerging Mueller matrix methodologies for bulk tissue assessment”, *Journal of biomedical optics* **20**, 061104 (2015).
- <sup>47</sup>M. Sun, H. He, N. Zeng, E. Du, Y. Guo, S. Liu, J. Wu, Y. He, and H. Ma, “Characterizing the microstructures of biological tissues using Mueller matrix and transformed polarization parameters”, *Biomedical optics express* **5**, 4223–4234 (2014).
- <sup>48</sup>J. Morio and F. Goudail, “Influence of the order of diattenuator, retarder, and polarizer in polar decomposition of Mueller matrices”, *Opt. Lett.* **29**, 2234–2236 (2004).
- <sup>49</sup>R. Ossikovski, A. D. Martino, and S. Guyot, “Forward and reverse product decompositions of depolarizing Mueller matrices”, *Opt. Lett.* **32**, 689–691 (2007).
- <sup>50</sup>J. Vizet, J. Rehbinder, S. Deby, S. Roussel, A. Nazac, R. Soufan, C. Genestie, C. Haie-Meder, H. Fernandez, F. Moreau, et al., “In vivo imaging of uterine cervix with a Mueller polarimetric colposcope”, *Scientific reports* **7**, 1–12 (2017).
- <sup>51</sup>O. Arteaga and A. Canillas, “Pseudopolar decomposition of the Jones and Mueller-Jones exponential polarization matrices”, *JOSA A* **26**, 783–793 (2009).
- <sup>52</sup>O. Arteaga and A. Canillas, “Analytic inversion of the Mueller-Jones polarization matrices for homogeneous media”, *Opt. Lett.* **35**, 559–561 (2010).
- <sup>53</sup>N. Ortega-Quijano and J. L. Arce-Diego, “Mueller matrix differential decomposition”, *Optics letters* **36**, 1942–1944 (2011).

- <sup>54</sup>A Aiello and J. Woerdman, “Physical bounds to the entropy-depolarization relation in random light scattering”, *Physical review letters* **94**, 090406 (2005).
- <sup>55</sup>S. R. Cloude and E. Pottier, “Concept of polarization entropy in optical scattering”, *Optical engineering* **34**, 1599–1611 (1995).
- <sup>56</sup>R. C. Jones, “A new calculus for the treatment of optical systems. vii. properties of the n-matrices”, *J. Opt. Soc. Am.* **38**, 671–685 (1948).
- <sup>57</sup>V. Moncrief, *Group theory and general relativity: representations of the Lorentz group and their applications to the gravitational field*, 1978.
- <sup>58</sup>R. F. Streater and A. S. Wightman, *Pct, spin and statistics, and all that*, Vol. 52 (Princeton University Press, 2000).
- <sup>59</sup>R. Ossikovski and V. Devlaminck, “General criterion for the physical realizability of the differential Mueller matrix”, *Optics Letters* **39**, 1216–1219 (2014).
- <sup>60</sup>E. Wigner, “On unitary representations of the inhomogeneous Lorentz group”, *Annals of Mathematics* **40**, 149–204 (1939).
- <sup>61</sup>V. Devlaminck, “Physical model of differential Mueller matrix for depolarizing uniform media”, *JOSA A* **30**, 2196–2204 (2013).
- <sup>62</sup>R. Ossikovski and O. Arteaga, “Statistical meaning of the differential Mueller matrix of depolarizing homogeneous media”, *Optics letters* **39**, 4470–4473 (2014).
- <sup>63</sup>R. Ossikovski, “Differential matrix formalism for depolarizing anisotropic media”, *Opt. Lett.* **36**, 2330–2332 (2011).
- <sup>64</sup>N. Ortega-Quijano and J. L. Arce-Diego, “Depolarizing differential Mueller matrices”, *Opt. Lett.* **36**, 2429–2431 (2011).
- <sup>65</sup>O. Arteaga and B. Kahr, “Characterization of homogenous depolarizing media based on Mueller matrix differential decomposition”, *Opt. Lett.* **38**, 1134–1136 (2013).
- <sup>66</sup>R. M. A. Azzam, “Propagation of partially polarized light through anisotropic media with or without depolarization: A differential 4 x 4 matrix calculus”, *J. Opt. Soc. Am.* **68**, 1756–1767 (1978).
- <sup>67</sup>J. Courtial, “Wave plates and the pancharatnam phase”, *Optics communications* **171**, 179–183 (1999).
- <sup>68</sup>A. Niv, G. Biener, V. Kleiner, and E. Hasman, “Manipulation of the pancharatnam phase in vectorial vortices”, *Optics express* **14**, 4208–4220 (2006).
- <sup>69</sup>S. Pancharatnam, “Generalized theory of interference and its applications”, in *Proceedings of the indian academy of sciences-section a*, Vol. 44, 6 (Springer, 1956), pp. 398–417.

- <sup>70</sup>M. V. Berry, “The adiabatic phase and pancharatnam’s phase for polarized light”, *Journal of Modern Optics* **34**, 1401–1407 (1987).
- <sup>71</sup>K. Y. Bliokh, M. A. Alonso, and M. R. Dennis, “Geometric phases in 2D and 3D polarized fields: geometrical, dynamical, and topological aspects”, *Reports on Progress in Physics* **82**, 122401 (2019).
- <sup>72</sup>J. C. Gutiérrez-Vega and G. Rendon, “Pancharatnam–berry phase algorithm to calculate the area of arbitrary polygons on the poincaré sphere”, *J. Opt. Soc. Am. A* **37**, 925–929 (2020).
- <sup>73</sup>A Drezet and C Genet, *Reciprocity and optical chirality* (Pan Stanford Publishing, 2014).
- <sup>74</sup>A. Schönhofer and H.-G. Kuball, “Symmetry properties of the Mueller matrix”, *Chemical physics* **115**, 159–167 (1987).
- <sup>75</sup>F. Arago, *Sur une modification remarquable qu’éprouvent les rayons lumineux dans leur passage à travers certains corps diaphanes, et sur quelques autres nouveaux phénomènes d’optiques: lu le 11 août 1811* (Firmin-Didot, 1812).
- <sup>76</sup>M. Pasteur, “European society for paediatric infectious diseases/European society for paediatric gastroenterology, hepatology, and nutrition evidence-based recommendations for rotavirus vaccination in Europe: executive summary”, *Journal of Pediatric Gastroenterology and Nutrition* **46**, 615–618 (2008).
- <sup>77</sup>E Plum and N. Zheludev, “Chirality and anisotropy of planar metamaterials”, (2011).
- <sup>78</sup>Q. Jiang, A. Pham, M. Berthel, S. Huant, J. Bellessa, C. Genet, and A. Drezet, “Directional and singular surface plasmon generation in chiral and achiral nanostructures demonstrated by leakage radiation microscopy”, *ACS Photonics* **3**, 1116–1124 (2016).
- <sup>79</sup>A. Drezet, C. Genet, J.-Y. Laluet, and T. W. Ebbesen, “Optical chirality without optical activity: how surface plasmons give a twist to light”, *Optics express* **16**, 12559–12570 (2008).
- <sup>80</sup>J. Cheng, G. Le Saux, J. Gao, T. Buffeteau, Y. Battie, P. Barois, V. Ponsinet, M.-H. Delville, O. Ersen, E. Pouget, et al., “Goldhelix: gold nanoparticles forming 3D helical superstructures with controlled morphology and strong chiroptical property”, *ACS nano* **11**, 3806–3818 (2017).
- <sup>81</sup>D. H. Goldstein, “Mueller matrix dual-rotating retarder polarimeter”, *Applied optics* **31**, 6676–6683 (1992).
- <sup>82</sup>A. Thomas, T. Chervy, S. Azzini, M. Li, J. George, C. Genet, and T. W. Ebbesen, “Mueller polarimetry of chiral supramolecular assembly”, *The Journal of Physical Chemistry C* **122**, 14205–14212 (2018).

- <sup>83</sup>Z. Shi, A. Y. Zhu, Z. Li, Y.-W. Huang, W. T. Chen, C.-W. Qiu, and F. Capasso, “Continuous angle-tunable birefringence with freeform metasurfaces for arbitrary polarization conversion”, *Science Advances* **6**, eaba3367 (2020).
- <sup>84</sup>O. Arteaga, B. M. Maoz, S. Nichols, G. Markovich, and B. Kahr, “Complete polarimetry on the asymmetric transmission through subwavelength hole arrays”, *Optics Express* **22**, 13719–13732 (2014).
- <sup>85</sup>R. M. A. Azzam, “Photopolarimetric measurement of the Mueller matrix by fourier analysis of a single detected signal”, *Opt. Lett.* **2**, 148–150 (1978).
- <sup>86</sup>H. Fujiwara, *Spectroscopic ellipsometry: principles and applications* (John Wiley & Sons, 2007).
- <sup>87</sup>M. H. Smith, “Optimization of a dual-rotating-retarder Mueller matrix polarimeter”, *Appl. Opt.* **41**, 2488–2493 (2002).
- <sup>88</sup>I. Damian, *Malus’ law for a real polarizer*, 2006.
- <sup>89</sup>Kazimierz Pietraszkiewicz and Władysław A. Woźniak and Piotr Kurzynowski, “Effect of multiple reflections in retardation plates with elliptical birefringence”, *J. Opt. Soc. Am. A* **12**, 420–424 (1995).
- <sup>90</sup>J. Poirson, T. Lanternier, J.-C. Cotteverte, A. L. Floch, and F. Bretenaker, “Jones matrices of a quarter-wave plate for gaussian beams”, *Appl. Opt.* **34**, 6806–6818 (1995).
- <sup>91</sup>B. Boulbry, B. Bousquet, B. L. Jeune, Y. Guern, and J. Lotrian, “Polarization errors associated with zero-order achromatic quarter-wave plates in the whole visible spectral range”, *Opt. Express* **9**, 225–235 (2001).
- <sup>92</sup>Thorlabs, *Mounted achromatic quarter-wave plate*, <https://www.thorlabs.com/thorproduct.cfm?partnumber=AQWP05M-600>.
- <sup>93</sup>N. R. Draper and H. Smith, *Applied regression analysis*, Vol. 326 (John Wiley & Sons, 1998).
- <sup>94</sup>J. L. Pezzaniti and R. A. Chipman, “Mueller matrix imaging polarimetry”, *Optical engineering* **34**, 1558–1569 (1995).
- <sup>95</sup>J. Qi and D. S. Elson, “Mueller polarimetric imaging for surgical and diagnostic applications: a review”, *Journal of biophotonics* **10**, 950–982 (2017).
- <sup>96</sup>Y. Shindo and M. Nishio, “The effect of linear anisotropies on the cd spectrum: is it true that the oriented polyvinylalcohol film has a magic chiral domain inducing optical activity in achiral molecules?”, *Biopolymers: Original Research on Biomolecules* **30**, 25–31 (1990).



- <sup>97</sup>Z. El-Hachemi, O. Arteaga, A. Canillas, J. Crusats, C. Escudero, R. Kuroda, T. Harada, M. Rosa, and J. M. Ribó, “On the mechano-chiral effect of vortical flows on the dichroic spectra of 5-phenyl-10, 15, 20-tris (4-sulfonatophenyl) porphyrin J-aggregates”, *Chemistry–A European Journal* **14**, 6438–6443 (2008).
- <sup>98</sup>A. Drezet, C. Genet, J.-Y. Laluet, and T. W. Ebbesen, “Optical chirality without optical activity: how surface plasmons give a twist to light”, *Optics express* **16**, 12559–12570 (2008).
- <sup>99</sup>Y. Gorodetski, A. Drezet, C. Genet, and T. W. Ebbesen, “Generating far-field orbital angular momenta from near-field optical chirality”, *Physical review letters* **110**, 203906 (2013).
- <sup>100</sup>Y. Gorodetski, K. Bliokh, B Stein, C Genet, N Shitrit, V. Kleiner, E. Hasman, and T. Ebbesen, “Weak measurements of light chirality with a plasmonic slit”, *Physical review letters* **109**, 013901 (2012).
- <sup>101</sup>X. Cui, A. G. Shtukenberg, J. Freudenthal, S. Nichols, and B. Kahr, “Circular birefringence of banded spherulites”, *Journal of the American Chemical Society* **136**, 5481–5490 (2014).
- <sup>102</sup>X. Cui, S. M. Nichols, O. Arteaga, J. Freudenthal, F. Paula, A. G. Shtukenberg, and B. Kahr, “Dichroism in helicoidal crystals”, *Journal of the American Chemical Society* **138**, 12211–12218 (2016).
- <sup>103</sup>H.-M. Ye, J. Xu, J. Freudenthal, and B. Kahr, “On the circular birefringence of polycrystalline polymers: polylactide”, *Journal of the American Chemical Society* **133**, 13848–13851 (2011).
- <sup>104</sup>E. Gunn, R. Sours, J. B. Benedict, W. Kaminsky, and B. Kahr, “Mesoscale chiroptics of rhythmic precipitates”, *Journal of the American Chemical Society* **128**, 14234–14235 (2006).
- <sup>105</sup>H Von Berlepsch, C Böttcher, A Quart, C. Burger, S Dähne, and S Kirstein, “Supramolecular structures of J-aggregates of carbocyanine dyes in solution”, *The Journal of Physical Chemistry B* **104**, 5255–5262 (2000).
- <sup>106</sup>S. Kirstein and S. Daehne, “J-aggregates of amphiphilic cyanine dyes: self-organization of artificial light harvesting complexes”, *International Journal of Photoenergy* **2006** (2006).
- <sup>107</sup>U. De Rossi, S. Dähne, S. C. Meskers, and H. P. Dekkers, “Spontaneous formation of chirality in J-aggregates showing davydov splitting”, *Angewandte Chemie International Edition in English* **35**, 760–763 (1996).

- <sup>108</sup>A. Pawlik, S. Kirstein, U. De Rossi, and S. Daehne, “Structural conditions for spontaneous generation of optical activity in J-aggregates”, *The Journal of Physical Chemistry B* **101**, 5646–5651 (1997).
- <sup>109</sup>S. Kirstein, H. von Berlepsch, C. Böttcher, C. Burger, A. Quart, G. Reck, and S. Dähne, “Chiral J-aggregates formed by achiral cyanine dyes”, *ChemPhysChem* **1**, 146–150 (2000).
- <sup>110</sup>V. Avetisov and V. Goldanskii, “Mirror symmetry breaking at the molecular level”, *Proceedings of the National Academy of Sciences* **93**, 11435–11442 (1996).
- <sup>111</sup>S. Azeroual, J. Surprenant, T. D. Lazzara, M. Kocun, Y. Tao, L. A. Cuccia, and J.-M. Lehn, “Mirror symmetry breaking and chiral amplification in foldamer-based supramolecular helical aggregates”, *Chemical Communications* **48**, 2292–2294 (2012).
- <sup>112</sup>N. Harada and K. Nakanishi, “Exciton chirality method and its application to configurational and conformational studies of natural products”, *Accounts of Chemical Research* **5**, 257–263 (1972).
- <sup>113</sup>S. Matile, N. Berova, K. Nakanishi, J. Fleischhauer, and R. W. Woody, “Structural studies by exciton coupled circular dichroism over a large distance: porphyrin derivatives of steroids, dimeric steroids, and brevetoxin b”, *Journal of the American Chemical Society* **118**, 5198–5206 (1996).
- <sup>114</sup>M. R. Hicks, J. Kowalski, and A. Rodger, “LD spectroscopy of natural and synthetic biomaterials”, *Chemical Society Reviews* **39**, 3380–3393 (2010).
- <sup>115</sup>A. Rodger, G. Dorrington, and D. L. Ang, “Linear dichroism as a probe of molecular structure and interactions”, *Analyst* **141**, 6490–6498 (2016).
- <sup>116</sup>A. Narayanan, S. Chandel, N. Ghosh, and P. De, “Visualizing phase transition behavior of dilute stimuli responsive polymer solutions via Mueller matrix polarimetry”, *Analytical chemistry* **87**, 9120–9125 (2015).
- <sup>117</sup>J. Parkash, J. H. Robblee, J. Agnew, E. Gibbs, P. Collings, R. F. Pasternack, and J. C. De Paula, “Depolarized resonance light scattering by porphyrin and chlorophyll a aggregates”, *Biophysical journal* **74**, 2089–2099 (1998).
- <sup>118</sup>A. Komarov, K. Komarov, D. Meshcheriakov, F. Amrani, and F. Sanchez, “Polarization dynamics in nonlinear anisotropic fibers”, *Physical Review A* **82**, 013813 (2010).
- <sup>119</sup>B. J. Berne and R. Pecora, *Dynamic light scattering: with applications to chemistry, biology, and physics* (Dover Publications, 2000).
- <sup>120</sup>F. Perrin, “Phys. Radium 1926, 7, 390”, *Ann. Phys.(Paris)* **12**, 0022–3654 (1929).

- <sup>121</sup>S. Urano, M. Matsuo, T. Sakanaka, I. Uemura, M. Koyama, I. Kumadaki, and K. Fukuzawa, "Mobility and molecular orientation of vitamin E in liposomal membranes as determined by <sup>19</sup>F NMR and fluorescence polarization techniques", *Archives of Biochemistry and Biophysics* **303**, 10–14 (1993).
- <sup>122</sup>A. J. Lapen and W. R. Seitz, "Fluorescence polarization studies of the conformation of soil fulvic acid", *Analytica Chimica Acta* **134**, 31–38 (1982).
- <sup>123</sup>W. A. Lea and A. Simeonov, "Fluorescence polarization assays in small molecule screening", *Expert opinion on drug discovery* **6**, 17–32 (2011).
- <sup>124</sup>E. Keh and B. Valeur, "Investigation of water-containing inverted micelles by fluorescence polarization. Determination of size and internal fluidity", *Journal of Colloid and Interface Science* **79**, 465–478 (1981).
- <sup>125</sup>J. N. Forkey, M. E. Quinlan, and Y. E. Goldman, "Protein structural dynamics by single-molecule fluorescence polarization", *Biology at the Single Molecule Level* **1** (2001).
- <sup>126</sup>J. N. Forkey, M. E. Quinlan, M. A. Shaw, J. E. Corrie, and Y. E. Goldman, "Three-dimensional structural dynamics of myosin V by single-molecule fluorescence polarization", *Nature* **422**, 399–404 (2003).
- <sup>127</sup>W. Van Blitterswijk, R. Van Hoeven, and B. Van der Meer, "Lipid structural order parameters (reciprocal of fluidity) in biomembranes derived from steady-state fluorescence polarization measurements", *Biochimica Et Biophysica Acta (BBA)-Biomembranes* **644**, 323–332 (1981).
- <sup>128</sup>J. P. Riehl and F. S. Richardson, "Circularly polarized luminescence spectroscopy", *Chemical Reviews* **86**, 1–16 (1986).
- <sup>129</sup>K. Dhbaibi, L. Favereau, M. Srebro-Hooper, C. Quinton, N. Vanthuyne, L. Arrico, T. Roisnel, B. Jamoussi, C. Poriel, C. Cabanetos, et al., "Modulation of circularly polarized luminescence through excited-state symmetry breaking and interbranched exciton coupling in helical push–pull organic systems", *Chemical science* **11**, 567–576 (2020).
- <sup>130</sup>J. Soni, H. Purwar, H. Lakhotia, S. Chandel, C. Banerjee, U. Kumar, and N. Ghosh, "Quantitative fluorescence and elastic scattering tissue polarimetry using an eigenvalue calibrated spectroscopic Mueller matrix system", *Optics express* **21**, 15475–15489 (2013).
- <sup>131</sup>K. Maji, S. Saha, R. Dey, N. Ghosh, and D. Haldar, "Mueller matrix fluorescence spectroscopy for probing self-assembled peptide-based hybrid supramolecular structure and orientation", *The Journal of Physical Chemistry C* **121**, 19519–19529 (2017).

- <sup>132</sup>J Jagtap, S Chandel, N. Das, J Soni, S Chatterjee, A Pradhan, and N Ghosh, “Quantitative Mueller matrix fluorescence spectroscopy for precancer detection”, *Optics letters* **39**, 243–246 (2014).
- <sup>133</sup>S. Saha, J. Soni, S. Chandel, N. Ghosh, and U. Kumar, “Probing intrinsic anisotropies of fluorescence: Mueller matrix approach”, *Journal of biomedical optics* **20**, 085005 (2015).
- <sup>134</sup>O. Arteaga, S. Nichols, and B. Kahr, “Mueller matrices in fluorescence scattering”, *Optics letters* **37**, 2835–2837 (2012).
- <sup>135</sup>P. Soleillet, “Sur les paramètres caractérisant la polarisation partielle de la lumière dans les phénomènes de fluorescence”, *AnPh* **10**, 23–97 (1929).
- <sup>136</sup>Y. Shindo, M. Nakagawa, and Y. Ohmi, “On the problems of cd spectropolarimeters. ii: artifacts in cd spectrometers”, *Applied spectroscopy* **39**, 860–868 (1985).
- <sup>137</sup>H. P. Dekkers, P. F. Moraal, J. M. Timper, and J. P. Riehl, “Optical artifacts in circularly polarized luminescence spectroscopy”, *Applied spectroscopy* **39**, 818–821 (1985).
- <sup>138</sup>O. Arteaga, J. Freudenthal, B. Wang, and B. Kahr, “Mueller matrix polarimetry with four photoelastic modulators: theory and calibration”, *Applied optics* **51**, 6805–6817 (2012).
- <sup>139</sup>L. D. Landau, *The classical theory of fields*, Vol. 2 (Elsevier, 2013), p. 37.
- <sup>140</sup>A. J. Macfarlane, “On the restricted Lorentz group and groups homomorphically related to it”, *Journal of Mathematical Physics* **3**, 1116–1129 (1962).



# Mueller polarimetry for probing supramolecular and optical chiralities

## Résumé

Cette thèse applique de manière détaillée le formalisme de Stokes-Mueller dans un contexte de mesures de propriétés chiroptiques d'échantillons supramoléculaires. Ce travail nous a permis de suivre l'émergence progressive de la chiralité au cours d'une procédure d'autoassemblage moléculaire spontané. En développant une polarimétrie Mueller en émission, nous avons pu révéler et contourner certains artefacts potentiels associés à la mesure de signaux chiraux en émission générés par des systèmes moléculaires chiraux excités. Les éléments théoriques et expérimentaux rassemblés dans ce travail fournissent une base solide pour poursuivre cette thématique de recherche visant à explorer les liens intimes et subtils entre la chiralité moléculaire et la chiralité optique.

**Mots clés** : Polarimétrie Mueller – Propriétés chiroptiques – Chiralité – Systèmes supramoléculaires

## Résumé en anglais

This thesis applies detailly the Stokes-Mueller formalism in the context of measurement of chiroptical properties in supramolecular system. This work allowed us to follow progressive emergence of chirality during the spontaneous self-assembly process through a transmission polarimetry measurement. Then, by developing Mueller polarimetry in emission, we have been able to identify and circumvent some potential artefacts on the measurement of chiral emission signals generated by excited chiral molecular systems. The theoretical and experimental elements brought together in this work provide a solid basis to pursue this research theme, aiming at exploring the intimate and subtle links between molecular chirality and optical chirality.

**Keywords** : Mueller polarimetry – Chiroptical properties – Chirality – Supramolecular systems